

STAR Analysis Note:
Forward $A_{LL}^{\pi^0}$ in the FMS for $\sqrt{s} = 510$ GeV pp
Collisions during RHIC Runs 12 and 13

Christopher Dilks

Submitted: January 9, 2018

Revised: April 1, 2018

Abstract

The STAR Collaboration reports measurements of the longitudinal double-spin asymmetry, A_{LL} , for neutral pions produced at forward directions in polarized proton-proton collisions, at a center-of-mass energy of 510 GeV. Results are given for transverse momenta in the range $2 < p_T < 10$ GeV/c and two regions in the pseudorapidity range $2.65 < \eta < 3.90$. The observed asymmetries are less than $\pm 5 \cdot 10^{-3}$ and are sensitive to the polarized gluon parton distribution function, $\Delta g(x)$, down to the region of Bjorken $x \sim 10^{-3}$. When combined with other measurements as part of a global analysis, these data will help constrain the contribution to the spin of the proton from polarized gluons at low- x .

Contents

1	Introduction	1
1.1	Analysis Links	1
1.2	A_{LL} Definition	1
1.3	A_{LL} In Terms Of Yield	2
1.4	Simulation of Parton Kinematic Reach of FMS Acceptance	3
2	Experimental Apparatus	4
2.1	The Forward Meson Spectrometer	4
2.1.1	Electromagnetic Showers in the FMS	5
2.1.2	Pion Event Reconstruction Summary	6
2.2	FMS Trigger	8
2.2.1	General Trigger Logic and Data Flow	8
2.2.2	FMS DSM Tree	9
2.2.3	FMS Trigger Set	13
2.3	Data Set and Quality Assurance	17
2.4	Radiation Damage	21
3	Event Selection	22
3.1	π^0 Kinematics and FMS Acceptance	22
3.2	Inner and Outer Pseudorapidity Regions	23
3.3	Event Reconstruction	26
3.3.1	Trigger Matching	26
3.3.2	Shower Shapes	27
3.3.3	Clustering Algorithm	29
3.3.4	Energy Dependence of the Mass	31
3.4	Gain Corrections	31
3.4.1	Time-Dependent Corrections – The LED Flasher System	31
3.4.2	Nonlinear Energy-Dependent Response Correction	33

3.4.2.1	Nonlinear Gain Correction Model	33
3.4.2.2	Including Radiation Damage	35
3.4.2.3	Application of the Correction	39
3.5	Hot Tower Masking	42
3.6	Pion Event Selection	48
3.6.1	Kinematic Cuts	48
3.6.2	p_T Threshold Cut	49
3.6.3	Mass Cut	51
3.6.4	Kinematics Distributions	57
4	Relative Luminosity	62
4.1	Basic Computation Algorithm	62
4.2	Accidentals and Multiples Corrections	65
4.2.1	CDF Accidentals Correction	66
4.2.2	CDF Multiple Interactions Correction	67
4.2.3	Rate-Safe Accidentals and Multiples Corrections	70
4.3	R_3 Results	73
4.4	R_3 Cross-Checks	78
4.5	Miscellaneous	89
4.5.1	Anomalous Bunch Crossings	89
4.5.2	N_{bx} vs. Bunch Crossing	89
5	Systematic Uncertainties	91
5.1	Relative Luminosity Systematic	91
5.1.1	Direct VPD and ZDC Comparison: Δ_{R_3} Method	92
5.1.2	Comparison of $A_{LL}^{\pi^0}$ via VPD and ZDC: $\delta_{A_{LL}}$ Method	94
5.1.3	Intrinsic Scaler Double-Spin Asymmetries: $\Delta_{S_{LL}}$ Method	96
5.1.3.1	Bunch Fitting Algorithm	96
5.1.3.2	Scaler Asymmetry Measurement	97
5.1.4	Scaler Self-Consistency via A_N Cross Ratio: Δ_{D_N} Method	100
5.1.5	Correlations of Run 13 Δ_{R_3} and S_{LL} with Spin Patterns	103
5.1.6	Summary of Relative Luminosity Systematics	111
5.2	Polarization Transverse Component Systematic	111
5.2.1	STAR Local Polarimetry	112
5.2.2	Relating Local Polarimetry to A_{LL} Systematic	114
5.2.3	Transverse Component Systematic Result	115
5.3	p_T Uncertainty	119

5.3.1	Energy Uncertainty	120
5.3.1.1	Energy Resolution	120
5.3.1.2	Calibration Anchor Point	122
5.3.1.3	Nonlinear Response	123
5.3.2	Position Uncertainty	124
5.3.3	Vertex Uncertainty	126
5.3.4	Correlation Terms in p_T Uncertainty	127
5.3.5	p_T Uncertainty Result	128
5.4	Summary of Systematic Uncertainties	130
6	$A_{LL}^{\pi^0}$ Analysis	131
6.1	Kinematic Binning and Means	131
6.2	Polarization	132
6.2.1	Scale Systematic on $A_{LL}^{\pi^0}$	133
6.3	Maximum Likelihood Method A_{LL} Computation	133
6.4	Background Corrections	136
6.4.1	Implementation	136
6.4.2	Signal and Background Fitting	138
6.4.3	Purity Results	140
6.5	Preliminary $A_{LL}^{\pi^0}$ Results	147
6.6	Final $A_{LL}^{\pi^0}$ Results	149
Appendices		149
A Decay Kinematics of $\pi^0 \rightarrow \gamma + \gamma$		151
A.1	Invariant Mass	151
A.2	Note on Small Angles from π^0 Decay Cones	157
B Spin Asymmetries and their Relative Luminosities		158
B.1	Notation	158
B.2	Nine Asymmetries and Relative Luminosities	159
C Decomposing Cross-Sections in terms of Spin Asymmetries		161
C.1	Longitudinal Components	161
C.2	Transverse Components	164
C.3	Application: Systematic Uncertainty on A_{LL} due to Nonzero Transverse Polarization	165

D Rate-Safe Counting Derivation	166
D.1 Event Classes	166
D.2 Hit Probabilities	166
D.3 Probabilities for Detecting Zero Hits	167
D.4 Rate-Safe Correction Equation	168
D.5 Note on Accidental	169
D.6 Statistical Uncertainty Propagation	169
E Bunch-Fitting Algorithm	172
F Polarization Uncertainties	175
F.1 Single Beam Polarization	175
F.2 Beam Polarization Product	177
F.3 Combining Uncertainties over Two Run Periods	179
F.4 Results	180
G Including Photon Uncertainties in p_T Uncertainty	183
H Maximum Likelihood Method for A_{LL} Measurement	185
H.1 Gaussian probability distributions	185
H.2 MLM value for A_{LL}	187
I Curing Radiation Damage in the FMS	189
I.1 Sunlight Exposure	189
I.2 UV-LED Curing	191

List of Figures

1.1	Simulation of partonic x accessible within FMS acceptance	3
2.1	FMS geometry schematic	5
2.2	Isolation cone sizes	8
2.3	FMS channel to QT board map	11
2.4	FMS DSM tree	12
2.5	FMS jet patch regions	13
2.6	Trigger overlap matrix	16
2.7	Rescaled trigger counts f_T vs. run index	19
2.8	Ratio of f_T to local mean vs. run index	20
3.1	Scattering coordinates notation	23
3.2	M vs. η and η boundaries	25
3.3	FMS schematic and pseudorapidity boundaries	26
3.4	35 mrad cone size with respect to FMS	30
3.5	Photon pair α vs. E with M contours	32
3.6	Photon pair M vs. E with α contours	32
3.7	M vs. E and M vs. α for π^0 s and η -mesons; before $g(E)$ correction	34
3.8	M vs. E and M vs. α for π^0 s and η -mesons; after $g(E)$ correction	35
3.9	$g(E)$ model	36
3.10	Pseudorapidity factor $\lambda(\eta)/\lambda_0$ vs. η	38
3.11	Slope factor $R(t)$ vs. days of radiation damage	38
3.12	E_t vs. E_o via $g(E)$ correction	38
3.13	Day-0 Δp_T vs. p_{T_o} and Δp_T distributions	41
3.14	Day-D Δp_T vs. p_{T_o} and Δp_T distributions	41
3.15	Hot spot search algorithm	43
3.16	Hot spot identification result for Run 12 outer region	45
3.17	Hot spot identification result for Run 12 inner region	46
3.18	Hot spot identification result for Run 13 outer region	47

3.19	Hot spot π^0 -masking algorithm	48
3.20	p_T vs. run index for Run 12 outer region	50
3.21	p_T vs. run index for Run 12 inner region	50
3.22	p_T vs. run index for Run 13 outer region	51
3.23	Photon pair M distributions in E bins for outer region	53
3.24	Photon pair M distributions in E bins for inner region	54
3.25	π^0 mass windows vs. runset index for Run 12 outer region	55
3.26	π^0 mass windows vs. runset index for Run 13 outer region	55
3.27	π^0 mass windows vs. runset index for Run 12 inner region	56
3.28	$\pi^0 p_T$ vs. E	58
3.29	$\pi^0 y$ -position vs. x -position	59
3.30	$\pi^0 Z$ distribution	60
3.31	$\pi^0 p_T$ distribution and bin boundaries for outer region	61
3.32	$\pi^0 p_T$ distribution and bin boundaries for inner region	61
4.1	Scaler bit counts	65
4.2	CDF accidentals and multiples corrections schematic	66
4.3	Scale and physical process probabilities schematic	67
4.4	Fractional change in CDF corrected counts	69
4.5	Fractional change in rate-safe corrected counts	72
4.6	R_3 from ZDC for Run 12	74
4.7	R_3 from VPD for Run 12	75
4.8	R_3 from ZDC for Run 13	76
4.9	R_3 from VPD for Run 13	77
4.10	Comparison of R_3 via CDF and rate-safe correction methods for Run 12 . .	79
4.11	Comparison of R_3 via CDF and rate-safe correction methods for Run 13 . .	80
4.12	Comparison of R_3 from ZDC and VPD for Run 12	81
4.13	Comparison of R_3 from ZDC and VPD for Run 13	82
4.14	Comparison of R_3 from E and W for Run 12	83
4.15	Comparison of R_3 from E and W for Run 13	84
4.16	Comparison of R_3 from E and X for Run 12	85
4.17	Comparison of R_3 from E and X for Run 13	86
4.18	Comparison of R_3 from W and X for Run 12	87
4.19	Comparison of R_3 from W and X for Run 13	88
4.20	N_{bx} vs. bunch crossing number	90
5.1	$R_3^{\text{ZDC}} - R_3^{\text{VPD}}$ distribution for Run 12	92

5.2	$R_3^{\text{ZDC}} - R_3^{\text{VPD}}$ distribution for Run 13	92
5.3	Comparison of A_{LL} via R_3^{ZDC} and R_3^{VPD} for Run 12 outer region	95
5.4	Comparison of A_{LL} via R_3^{ZDC} and R_3^{VPD} for Run 12 inner region	95
5.5	Comparison of A_{LL} via R_3^{ZDC} and R_3^{VPD} for Run 13 outer region	95
5.6	Spin patterns for Run 12	98
5.7	Spin patterns for Run 13	98
5.8	S_{LL} via VPD/ZDC for Run 12	99
5.9	S_{LL} via VPD/ZDC for Run 13	99
5.10	D_N distributions	102
5.11	Bunch crossing distributions showing afterpulsing	104
5.12	Deconvolved afterpulse signal	106
5.13	Deconvolved afterpulse signal noise	106
5.14	Afterpulse effect correlation to post-abort gap removals	108
5.15	Afterpulse effect correlation to pre-abort gap removals	108
5.16	S_{LL} distributions for post-abort gap removals for Run 12	109
5.17	S_{LL} distributions for post-abort gap removals for Run 13	110
5.18	Run 12 ϵ_T in ZDC-SMD local polarimeter	117
5.19	Run 12 ϵ_L in ZDC-SMD local polarimeter	117
5.20	Run 13 ϵ_L in ZDC-SMD local polarimeter	118
5.21	A_Σ vs. p_T from Run 11	118
5.22	p_T uncertainty schematic	120
5.23	FNAL PMT-to-Pb-glass optical coupling test results	122
5.24	p_T distribution comparison for day-0 and day- D	124
5.25	Vertex distribution	127
5.26	p_T uncertainty σ_{p_T} vs. p_T	129
6.1	Polarization vs. run index for Run 12	134
6.2	Polarization vs. run index for Run 13	135
6.3	Sample M distribution signal+background fits for outer region	141
6.4	Sample M distribution signal+background fits for inner region	142
6.5	π^0 purities for p_T bin 1	143
6.6	π^0 purities for p_T bin 2	143
6.7	π^0 purities for p_T bin 3	144
6.8	π^0 purities for p_T bin 4	144
6.9	Overall π^0 purities for each p_T bin	145
6.10	$A_{LL}^{\pi^0}$ background correction implementation for outer region	146

6.11	$A_{LL}^{\pi^0}$ background correction implementation for inner region	146
6.12	Preliminary Measurement of $A_{LL}^{\pi^0}$ vs. E	148
6.13	Preliminary Measurement of $A_{LL}^{\pi^0}$ vs. p_T	148
A.1	α vs. E plane with M contours for fixed Z	153
A.2	M vs. E plane with α contours for fixed Z	154
A.3	M vs. Z plane with α contours for fixed E	155
A.4	E_2 vs. E_1 and E vs. Z planes with α contours for $M = M_{\pi^0}$	156
A.5	E_2 vs. E_1 and E vs. Z planes with α contours for $M = M_\eta$	156
I.1	Light source spectrum used for Pb-glass transmission spectra	190
I.2	Pb-glass transmittance spectra with and without radiation damage	190
I.3	Pb-glass transmittance spectra ratios	191
I.4	UV-LED curing tests	192
I.5	Radiation damage vs. η	193
I.6	UV-LED array schematic	193
I.7	UV-LED array power distribution schematic	194
I.8	UV-LED and FMS HV controller screenshot	195
I.9	UV-LED FMS curing result	196

List of Tables

2.1	FMS trigger bit locations	14
3.1	Shower shape fit parameters	29
3.2	$g(E)$ model parameters	36
3.3	$g(E)$ model radiation damage parameters	39
3.4	Hot spot search parameters	44
4.1	Scaler bit recombinations	64
4.2	Consistent R_3 measurement requirements	89
5.1	Double-spin patterns	93
5.2	Double-spin state differences for post-abort bunch crossings	107
5.3	Summary of relative luminosity systematic uncertainties	111
5.4	p_T systematic uncertainty contribution G	125
5.5	W and X_0 values for FMS Pb-glass	126
5.6	Summary of $A_{LL}^{\pi^0}$ systematic uncertainties	130
6.1	Kinematic binning for $A_{LL}^{\pi^0}$	131
6.2	Kinematic bin means for $A_{LL}^{\pi^0}$	132
6.3	Overall polarizations and uncertainties	133

Chapter 1

Introduction

1.1 Analysis Links

Before anything else, here is a collection of relevant hyperlinks:

- Paper Draft Webpage:

http://www.star.bnl.gov/protected/spin/dilks/paper_FMS_aLL_510GeV/index.html

- Analysis Code

- Information:

<https://drupal.star.bnl.gov/STAR/blog/dilks/all-analysis-code>

- Documentation:

<http://www.star.bnl.gov/protected/spin/dilks/spinlongDoc/README.html>

- PWGC Preview:

<https://drupal.star.bnl.gov/STAR/blog/dilks/all-fms-pi0s-pp510-runs-12-and-13-paper-proposal>

- Preliminary Results:

<https://drupal.star.bnl.gov/STAR/blog/dilks/spin-2014-slideshow>

1.2 A_{LL} Definition

The longitudinal double spin asymmetry, $A_{LL}^{\pi^0}$, measured for the production of π^0 s, is defined as

$$A_{LL}^{\pi^0} = \frac{1}{P_B P_Y} \frac{(\sigma_{++} + \sigma_{--}) - (\sigma_{+-} + \sigma_{-+})}{(\sigma_{++} + \sigma_{--}) + (\sigma_{+-} + \sigma_{-+})}, \quad (1.1)$$

where P_B and P_Y are the polarizations of “blue” (westbound) and “yellow” (eastbound) proton beams and $\sigma_{h_B h_Y}$ is the cross section for the production of π^0 s with the helicity states of the initial-state protons as h_B and h_Y . Note that the blue beam faces the FMS.

Assuming factorization validity, $A_{LL}^{\pi^0}$ may be written in terms of PDFs $f_i(x)$, hard scattering cross section $\hat{\sigma}$, and fragmentation functions D_{π^0} as

$$A_{LL}^{\pi^0} = \frac{\sum_{f_a,b \in \{q,\bar{q},g\}} \Delta f_a \otimes \Delta f_b \otimes \Delta \hat{\sigma}_{f_a f_b \rightarrow f' X} \otimes D_{\pi^0}^{f'}}{\sum_{f_a,b \in \{q,\bar{q},g\}} f_a \otimes f_b \otimes \hat{\sigma}_{f_a f_b \rightarrow f' X} \otimes D_{\pi^0}^{f'}} \quad (1.2)$$

where $\Delta f = f_{++} + f_{--} - f_{+-} - f_{-+}$ is the polarized PDF and $\Delta \hat{\sigma} = \hat{\sigma}_{++} + \hat{\sigma}_{--} - \hat{\sigma}_{+-} - \hat{\sigma}_{-+}$ is the polarized hard scattering cross-section. The \otimes symbol represents convolution, defined by

$$[f \otimes g](z) = \int dx dy f(x) g(y) \delta(xy - z) \quad (1.3)$$

Of all the quantities in equation 1.2, the least constrained quantity is $\Delta g(x)$, which is the gluon helicity distribution. According to [1], it is positive at high- x , but largely unconstrained at small- x . The FMS is ideal for measuring low- x gluons, since the dominant subprocess which produces forward hadrons is the asymmetric $qg \rightarrow qg$ process where the quark at mid-to-high- x scatters off a low- x gluon [2].

1.3 A_{LL} In Terms Of Yield

In order to measure A_{LL} , it is easier to measure the π^0 yields for each of the initial proton spin states. The cross sections can be rewritten as

$$\sigma_{h_B h_Y} = \frac{N_{h_B h_Y}}{\Omega_{h_B h_Y} \cdot L_{h_B h_Y}}, \quad (1.4)$$

where N is the π^0 yield, Ω is the product of acceptance and efficiency, and L is the luminosity. Assuming that Ω is independent of initial proton spin, A_{LL} can be rewritten as

$$A_{LL}^{\pi^0} = \frac{1}{P_B P_Y} \frac{(N_{++} + N_{--}) - R_3(N_{+-} + N_{-+})}{(N_{++} + N_{--}) + R_3(N_{+-} + N_{-+})}, \quad (1.5)$$

where the quantity R_3 is defined as the relative luminosity:

$$R_3 = \frac{L_{++} + L_{--}}{L_{+-} + L_{-+}}. \quad (1.6)$$

The suffix “3” on the relative luminosity is a STAR convention, where 8 other stan-

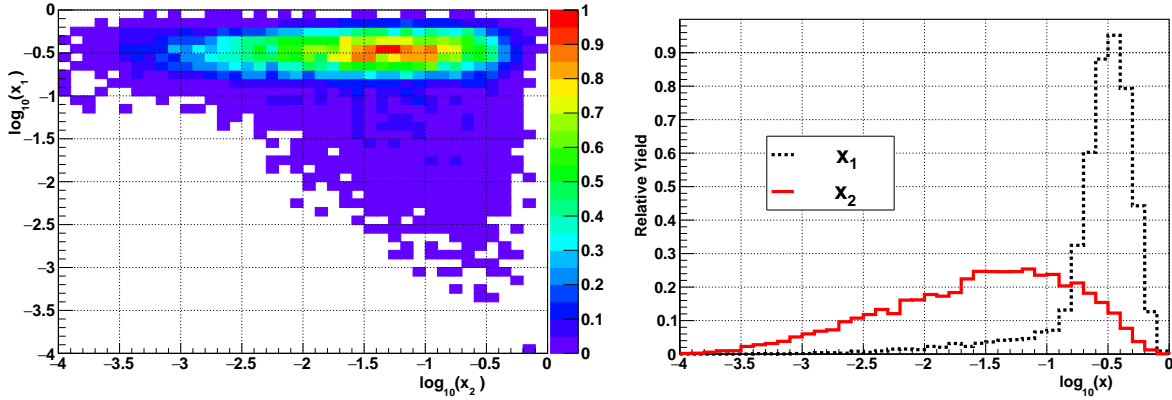


Figure 1.1: Monte Carlo (PYTHIA) simulations of x_1 and x_2 from $\sqrt{s} = 510$ GeV proton-proton collisions, constrained to π^0 s produced within the acceptance applicable to this $A_{LL}^{\pi^0}$ analysis. The forward direction (*i.e.*, toward the FMS) is given by parton 1.

dard relative luminosities can be defined for single-spin asymmetries and the so-called “false asymmetries.” For other definitions and their associated asymmetries, see appendix E.

1.4 Simulation of Parton Kinematic Reach of FMS Acceptance

Since the FMS occupies a forward pseudorapidity range of approximately 2.5 to 4.2, it is sensitive to collisions which are dominated by a hard (high- x) quark interacting with a soft (low- x) gluon. Figure 1.1 shows results of a Pythia simulation of the values of x_1 and x_2 reached, for π^0 s produced within the FMS kinematic acceptance. Parton 1 is the forward-going (*i.e.*, toward the FMS) parton, thus x_2 is likely that of the soft gluon. For details, see:

- http://www.star.bnl.gov/protected/spin/trent/fms_theory/theory.html

Chapter 2

Experimental Apparatus

2.1 The Forward Meson Spectrometer

The FMS is an electromagnetic calorimeter, composed of 1,264 lead-glass cells, each coupled to photomultiplier tubes (PMTs). It is situated at a pseudorapidity (η) range of approximately $2.6 < \eta < 4$. Figure 2.1 shows the transverse geometry of the FMS, along with rings of constant η . Black lines indicate divisions between sections of the FMS which are considered for the trigger, and the grey colored lines divide the individual cells. Grey-colored cells, which are along the outer edges of the FMS, are not considered in the trigger system logic. The green square indicates the boundary between the outer large cells, measuring $5.8\text{ cm} \times 5.8\text{ cm} \times 60\text{ cm}$ each, and the inner small cells, measuring $3.8\text{ cm} \times 3.8\text{ cm} \times 45\text{ cm}$ each; the FMS itself is approximately $2\text{ m} \times 2\text{ m}$ and situated about 7 m from the nominal beam collision point, the vertex. The RHIC beam passes through the cyan square in the center.

The primary observable in the FMS is the decay of the neutral pion into two photons: $\pi^0 \rightarrow \gamma\gamma$. The π^0 is a pseudoscalar meson with quark composition $|\pi^0\rangle = (|u\bar{u}\rangle - |d\bar{d}\rangle)/\sqrt{2}$. Its fundamental properties [3] are:

- Primary decay modes: $\gamma\gamma$ (98.82%), $e^+e^-\gamma$ (1.17%), and others with branching ratios less than 6×10^{-4}
- Mass: 135 MeV
- Spin: $S = 0$
- Charge: $Q = 0$
- Parity: $P = -1$

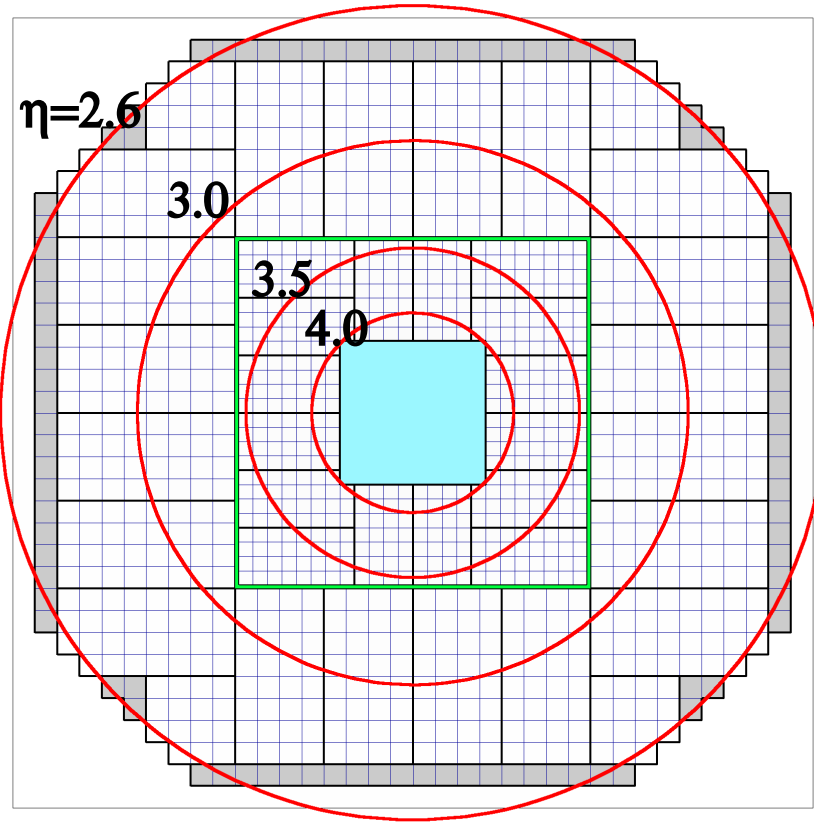


Figure 2.1: FMS geometry schematic; see text for legend

- Lifetime: $\tau = 8.5 \times 10^{-17}$ s

Note that in this document, natural units with $c = \hbar = 1$ are used.

2.1.1 Electromagnetic Showers in the FMS

Since the primary observable in the FMS is photon pairs from π^0 decays, consider a single photon incident on a Pb-glass cell; at STAR the photon energies are typically 15-30 GeV. As the incident photon passes near a heavy Pb nucleus (or other heavy nucleus in the glass), it will pair-produce an electron-positron pair. The nucleus will absorb the necessary momentum in order properly conserve momentum, since while in the rest frame of the electron-positron pair the net momentum is zero, there is no rest frame of the photon where its momentum is zero; instead the photon scatters off the electromagnetic field of a nucleus, which provides the necessary momentum absorption. This pair production probability increases as a function

of approximately Z^2 , where Z is the atomic number of the nucleus (82 for Pb).

Electrons and positrons which have been pair-produced then pass by more Pb atoms (as well as other atoms in the glass) and re-radiate photons via the bremsstrahlung process: the electrons and positrons interact with the electromagnetic field surrounding the heavy atoms and are deflected, radiating the energy lost as photons. These bremsstrahlung photons can, in turn, pair-produce, thereby repeating the cycle. This cascade of electrons, positrons, and photons is called an electromagnetic shower.

The shower proceeds until enough energy is lost such that the photons can no longer pair-produce; this energy is at least twice the electron or positron mass, $M_{e^{+(-)}} \approx 0.51$ MeV. Both the large and small FMS cells are 18-19 radiation lengths long, where a radiation length is defined as roughly 7/9 of the mean free path of a photon before pair-production, or the distance an electron or positron travels before losing a fraction $1/e$ of its energy due to bremsstrahlung. The longitudinal length of the Pb-glass cells is sufficient for most of the electromagnetic shower to develop; some of the energy does, however, leak into neighboring cells.

While the electromagnetic shower is developing, the electrons and positrons are moving faster than the speed of light can in the Pb-glass, which has index of refraction $n \approx 1.65$. They therefore radiate Cherenkov radiation in the blue-to-ultraviolet region of the electromagnetic spectrum. This Cherenkov radiation (and other photons of similar energy) is within the spectral sensitivity range of the photomultiplier tubes (PMTs), where a single PMT is optically coupled to the back face of every FMS cell.

When a photon of sufficient energy is incident on the front face photo-cathode of a PMT, the photo-electric effect will cause electrons to be emitted from its surface. These photo-electrons are attracted to an electrode in the PMT (under vacuum), and upon interacting with it, cause secondary emission of more electrons, which in turn are attracted to another electrode. These electrodes, called dynodes, are arranged in stages such that after ~ 10 stages, the original photo-electric signal is amplified enough to be measured as an electric current; the time integral of the overall current signal generated from the part of the electromagnetic shower which is sampled by the PMT can then be directly related to the incident high-energy photon energy.

2.1.2 Pion Event Reconstruction Summary

Neutral pions are identified as two nearby electromagnetic showers, initiated by two decay photons from the π^0 . The invariant mass of the two photons is a function of the energies of the photons and their decay opening angle; these parameters are measurable by analyzing

the electromagnetic shower relative positions and energy depositions, therefore the original π^0 mass can be reconstructed from energy deposition measurements in clusters of FMS cells. The invariant mass $M_{\gamma\gamma}$ of a two photon decay seen in the FMS is determined by

$$M_{\gamma\gamma} \approx \frac{E_{\gamma\gamma} D_{xy}}{2R_z} \sqrt{1 - Z_{\gamma\gamma}^2}, \quad (2.1)$$

where, given E_1 and E_2 as the photon energies, $E_{\gamma\gamma} = E_1 + E_2$ is the total energy, D_{xy} is the transverse distance between the detected photon pair, R_z is the distance between the FMS and the interaction point (~ 7 m), and $Z_{\gamma\gamma} = |E_1 - E_2| / E_{\gamma\gamma}$ is the energy imbalance. For further details on π^0 decay kinematics and the derivation of equation 2.1, see section 3.1 or appendix A.

The identification of photon events in the FMS begins with the observation of a distribution of energy, where typically $\sim 80\%$ of the photon energy is deposited into a single cell and the remaining $\sim 20\%$ is deposited within the adjacent cells. The distribution of energy in the cells which are considered (along with factoring in a low-energy noise cutoff) is compared to a shower shape, which models the fraction of energy deposited as a function of transverse distance from the location where the incident photon initiated the shower. If the energy distribution is similar to the expectation from the shower shape model, the photon is then considered valid; its point of entry in the FMS is accurate to within 1/10th of a cell width. See section 3.3.2 for more details.

After one valid photon is identified in a single event readout, more photons are searched for within an “isolation cone” of the first photon. This isolation cone is used to select between event topologies ranging from very isolated to the more “jetty” photons which are less isolated. In this analysis, two isolation cones were used for STAR preliminary results: 35 mrad and 100 mrad; for final publication results, only the 35 mrad cone radius is presented. Figure 2.2 shows a picture of the isolation cones compared to the FMS. A new photon which is found within the isolation cone is then added to a growing list of found photons and the center of the isolation cone used for this event characterization moves to the centroid of the list of photons. After all the photons within the isolation cone have been identified, the event is written out to an analysis tree, along with the number of photons found. Naturally, to reconstruct π^0 events, the two-photon events are the primary observable. For more details on photon reconstruction, see section 3.3.3 as well as [4].

Looking more carefully at equation 2.1, one sees that the energy dependence of the opening angle α of the photons is approximately

$$\alpha \approx \frac{M_{\gamma\gamma}}{\sqrt{E_1 E_2}} \quad (2.2)$$

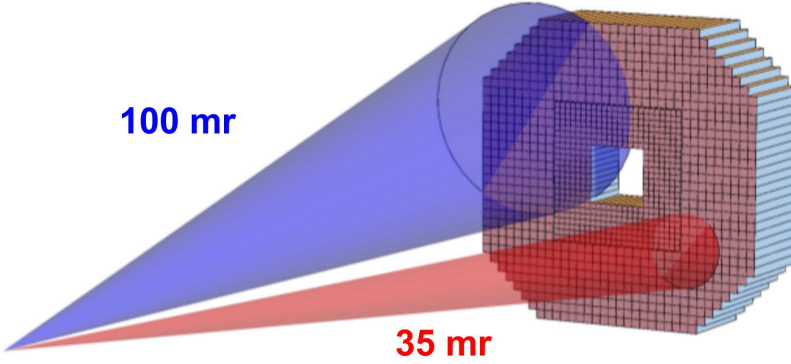


Figure 2.2: Two π^0 isolation cones used in this analysis compared to the FMS geometry; red is 35 mrad and blue is 100 mrad

Thus higher energy π^0 s have smaller opening angles. Within the large cells, two-photon clusters begin to merge for energies above approximately 50 GeV, whereas within small cells, they merge above approximately 80 GeV. This cluster merging turns out to be one of the major obstacles of π^0 reconstruction, as it is non-trivial to distinguish between a single photon cluster and a two-photon cluster. More on this will be discussed in section 3.3.4.

2.2 FMS Trigger

The RHIC bunch crossing rate is approximately 9.38 MHz, that is, there is a possible collision at STAR every 107 ns. Since detector data-taking times are typically on the time scale of milliseconds, a fast trigger system is implemented to cull collision observations which appear to be suitable for physics analyses. Multiple trigger levels are in place, such that each level must “accept” the event before passing it onto the next. Each successive level is capable of analyzing more information about the event than the previous level, but it is also more time-consuming. If the highest trigger level accepts the event, then the data from the detectors involved in the trigger are saved to disk. This section will explain the STAR trigger system, published in [5] with updates summarized in [6], followed by an explanation of the FMS triggers used in this analysis.

2.2.1 General Trigger Logic and Data Flow

Raw data from all detectors used in the trigger are first sent into trigger level 0, which is able to make a decision whether or not to keep the event within 1.5 μ s. For all detector subsystems used as triggering detectors, level 0 contains a tree of Data Storage and Manipulation (DSM) boards, which are capable of performing fast bitwise operations. The first layer of the DSM

tree takes multiple inputs from the associated detector(s), performs mathematical operations to compress the amount of information needed, and then latches a set of output bits; this layer of the DSM tree is capable of passing information to the next in time for the next bunch crossing. Other operations which occur include pedestal subtraction and gain normalization. Each DSM layer has less output bits than input bits, such that the final layer of the DSM tree simply outputs a single bit associated with each trigger. All trigger bits are then passed into the Trigger Control Unit (TCU).

The TCU is given information as to whether or not the detector is live, *i.e.*, not recovering from dead-time due to slower digitization (analog-to-digital conversion, as described in the next section), detector recovery, *etc*. It also is capable of “prescaling” a trigger, this is, given a prescale factor ρ , it will accept only a fraction $1/\rho$ of the events; this prescale scales with the desired trigger rate, instantaneous luminosity, and with the overall RHIC clock rate. If a trigger is accepted, it is issued by the TCU to the rest of the trigger system and the next level trigger processing occurs.

The next trigger level trigger is actually level 2; a trigger level 1 was designed and tested, but eventually was abandoned. Level 2 takes \sim 10 ms to complete and includes jet, di-jet, J/ψ , upsilon, ultra-peripheral collision triggers, *et al.* By the time trigger level 2 makes a decision, the digitized data arrives at the Data Acquisition (DAQ) system; if level 2 decides to reject the event, the data are simply deleted at the DAQ level.

If level 2 accepts the event, trigger level 3 processing begins, which takes \sim 100 ms, the scale of time needed to “build” each event in the DAQ system. Level 3 includes track reconstruction in the central calorimeter, vertex finding, *etc*. Like level 2, if level 3 decides to reject the event, it is simply deleted from the DAQ system. By the time level 3 decides to accept the event, the event will be built and ready to be packaged with all other events in the data-taking period in order to be sent to the High Performance Storage System (HPSS).

In 2012 and 2013, STAR was able to acquire data at a rate of about 1 kHz, with 300-400 Hz of the bandwidth dedicated to the FMS. Improvements to the trigger and DAQ systems are always underway between RHIC runs; DAQ rates in the 2017 run were as high as 6 kHz overall.

2.2.2 FMS DSM Tree

The FMS triggering information is first handled by four QT “crates”, where the acronym “QT” stands for charge (Q) from time (T) integration of current. The current which is integrated comes from the PMTs; the resultant charge is “digitized” to a 12-bit integer ranging from 0 to 4,095, denoted as number of ADC (Analog-to-Digital Conversion) counts.

The time interval over which the integrals of the PMT signals are taken is phase-locked to the RHIC bunch crossing rate and long enough to contain the typical PMT pulse widths. Each of the four QT crates is associated with a single quadrant of the FMS; the trigger logic explained below is replicated for each crate.

Each QT crate contains 11 QT “boards”, 10 of which are used in the FMS trigger; all FMS channels are mapped into the QT boards. Each QT board contains 4 cards, called “QT8 cards”, with 8 inputs each. PMT signals are directly connected to the QT8 card inputs through a patch panel, which provides a mapping “dictionary” between the FMS channels and the trigger system.

Figure 2.3 shows a diagram of the FMS mapping into the QT system. The bold black lines separate channels which are mapped into QT boards, which are labelled with a letter from A to J. Within each QT board, the stripes separated by dashed lines denote QT8 cards and are labeled with a number from 0 to 3 for each QT board. Note that the outermost rows and columns as well as 3 cells in each corner are not in the trigger and are colored grey in the diagram; their PMT signals are still sent to the 11th QT board for digitization, however.

The output of the QT boards is sent into the DSM tree, as shown in figure 2.4; each QT board outputs to the DSM tree 32 bits, composed of 5 bits representing a truncated ADC sum from each QT8 card, plus 12 bits encoding the ADC and channel number of the cell with the highest ADC, called the High Tower (HT).

These 32-bits from all 40 QT boards are then sent into layer 0 of the DSM tree, which, for each quadrant, consists of 3 DSM boards: one associated with QT boards A-D, another with E-H, and the third with I-J. Layer 0 DSM boards sum together QT8 ADC sums in various combinations of 4 adjacent QT8 stripes:

- sum over all QT8 cards of each QT board individually:
 - sumA, sumB, sumC, sumD, sumE, sumF, sumG, sumH, sumI, sumJ
- sums split between adjacent QT boards (4 adjacent QT8 cards):
 - $\text{sumBC} = \text{B}_2 + \text{B}_3 + \text{C}_0 + \text{C}_1$
 - $\text{sumCD} = \text{C}_2 + \text{C}_3 + \text{D}_0 + \text{D}_1$
 - $\text{sumEF} = \text{E}_2 + \text{E}_3 + \text{F}_0 + \text{F}_1$
 - $\text{sumGH} = \text{G}_2 + \text{G}_3 + \text{H}_0 + \text{H}_1$
 - $\text{sumIJ} = \text{I}_2 + \text{I}_3 + \text{J}_0 + \text{J}_1$

This “board sum” technique is essentially a very fast but very crude, low-level cluster finding algorithm. Layer 0 also compares the HT ADC to two thresholds and ORs the results

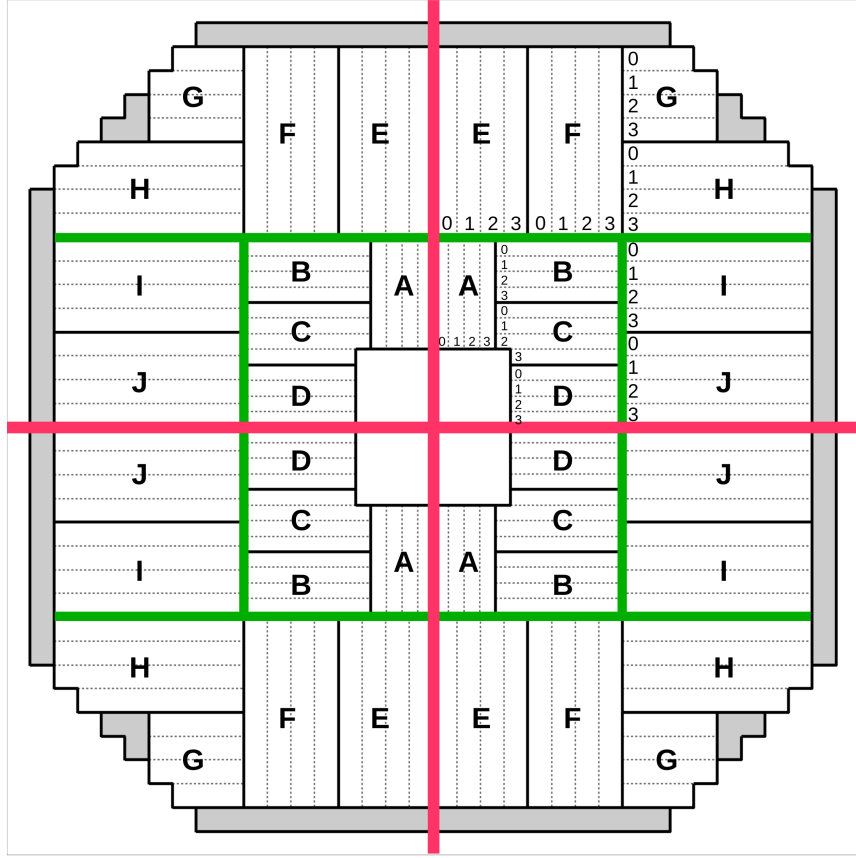


Figure 2.3: Assignment of FMS channels to QT boards (labelled by letters A-J, divided by solid black lines) and to QT8 cards within each board (labelled by numbers 0-3, divided by dotted black lines). Red lines divide quadrants and green lines divide regions within each quadrant associated to DSM layer 0. Grey cells along the outer edges are not in the trigger.

together. In total, the 12 layer 0 DSM boards each output 32 bits encoding the QT8 sums and the HT threshold comparisons.

The 12×32 -bit trigger data stream from layer 0 is then sent to 3 layer 1 DSM boards: one for the south large cells, one for the north large cells, and one for all the small cells. The HT threshold bits are ORed together from all four quadrants and compared to thresholds, forming the HT trigger. Sums of QT8 sums within FMS sectors are also taken and compared to cluster thresholds, forming the large and small board sum triggers and the basis of the jet patch trigger. The sector sums are then latched for output as well as their comparisons to cluster thresholds. In total, 32 bits are output from the small cells and 64 bits from the large cells (32 bits for both north and south).

The layer 2 DSM boards are responsible for combining all the data into a final 16-bit output trigger output word. In this layer, quadrant sums are combined in various ways to form 6 overlapping Jet Patch (JP) sums, shown in figure 2.5. Other high-level triggers can

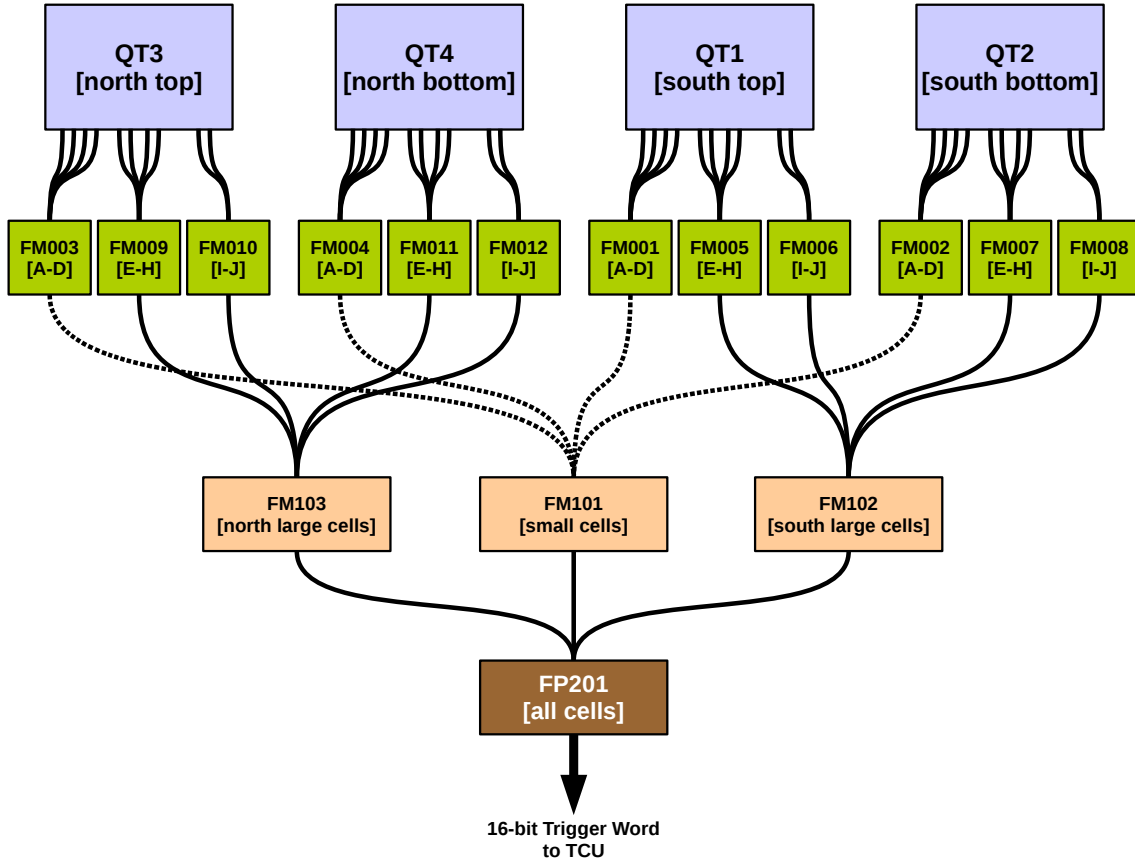


Figure 2.4: FMS DSM tree. Analog data enter the QT boards at the top of the diagram, where 11 boards are housed per QT crate (QT1-QT4). 10 QT boards in each quadrant output logic data to DSM layer 0 (FM001-FM012), which output to layer 1 (FM101-FM103), then finally to layer 2 (FP201), whose output is a 16-bit word sent to the TCU. All connectors between boards transmit a 32-bit logic signal.

also be defined here, such as the di-jet trigger (not used in this analysis). The final 16-bit trigger word is composed of comparisons of ADC sums to various thresholds: 2 HT bits, 2 small cell board sum bits, 3 large cell board sum bits, 3 jet patch bits, and the di-jet bit. Since layer 2 is the last DSM in the tree, these bits are forwarded to the TCU. These comparisons make up 11 bits, where the other 5 bits of the 16-bit word were not used in this analysis or were reserved for coincidences with other detectors.

The FMS data are not manipulated by any higher level triggers. If the event is ultimately determined to be valid, the digitized data are written out to the “trigger files,” as well as the trigger word which was sent to the TCU and the prescaled (and dead-time corrected) trigger word from trigger level 2, called the “L2 sum.” These trigger words are then used in

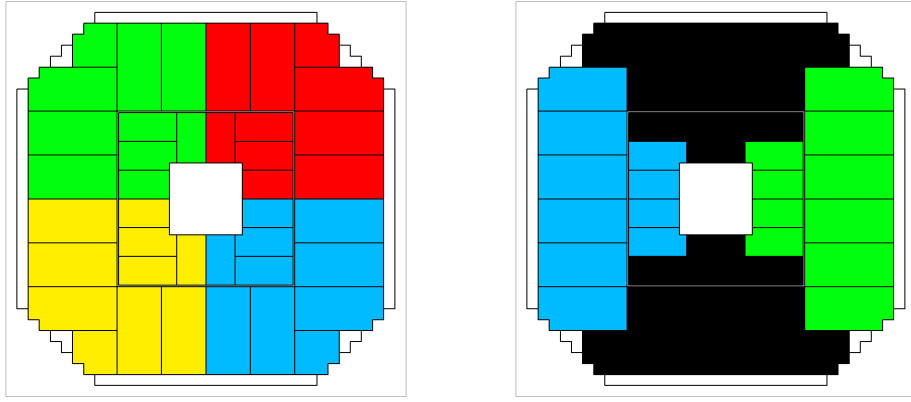


Figure 2.5: The 6 regions (colored) of the FMS which are summed together as jet patch sums; the top and bottom sectors in the right-hand figure are not included as jet patches.

data analysis to filter events of interest.

An additional trigger that comes from the FMS but is not particularly used in overall trigger decisions is the FMS LED trigger. In front of every channel of the FMS is the output of a fiber optic cable, which is connected to an LED flasher system, configured to flash at 1 Hz. Looking at FMS LED events helps track time-dependence of the gain of the PMTs as well as radiation damage. The LED trigger is configured on an independent DSM board, which is used for other miscellaneous triggers in STAR.

2.2.3 FMS Trigger Set

In total, 9 FMS triggers were defined in Runs 12 and 13:

- Jet Patch (JP) Triggers
 - JP1
 - JP2 (take-all)
- Large Board Sum (LgBS) Triggers
 - LgBS0
 - LgBS1 (take-all)
- Small Board Sum (SmBS) Triggers
 - SmBS0

- SmBS1 (take-all)
- High Tower (HT) Trigger (take-all)
- Di-jet (DJ) Trigger (take-all)
- LED Trigger (take-all)

The “take-all” triggers are those which are not prescaled, *i.e.*, $\rho = 1$. The fact that there are two JP, SmBS, and LgBS triggers is because two thresholds are used: the take-all triggers have higher ADC sum thresholds than their associated prescaled triggers.

In the data files, for every event the ADC counts for every channel is available as well as the trigger word which was sent into the TCU, denoted “lastDSM,” and the trigger word after prescaling, denoted “L2sum,” since it is determined at trigger level 2. In order to filter events with specific triggers, naturally the L2sum variable is preferable; this variable is composed of two 32-bit integers forming a 64-bit trigger mask. There was a software bug present in 2012 and 2013, however, in which the lower 32 bits of L2sum was simply copied into the upper 32 bits; only the lower 32 bits are correct. Fortunately, the only triggers which were defined in the upper 32-bit half were take-all triggers, and hence one can instead use the lastDSM trigger words for those triggers, since their prescale factors are unity. Table 2.1 shows a summary of the triggers and which trigger bits define them. L2sum is given as a hexadecimal trigger mask, representing a single bit out of the 64 bits (divided into upper and lower 32 bits), whereas lastDSM is given as which DSM output channel the trigger bit occupies. The right-most column states which trigger bit mask is ultimately used in order to filter events in analysis.

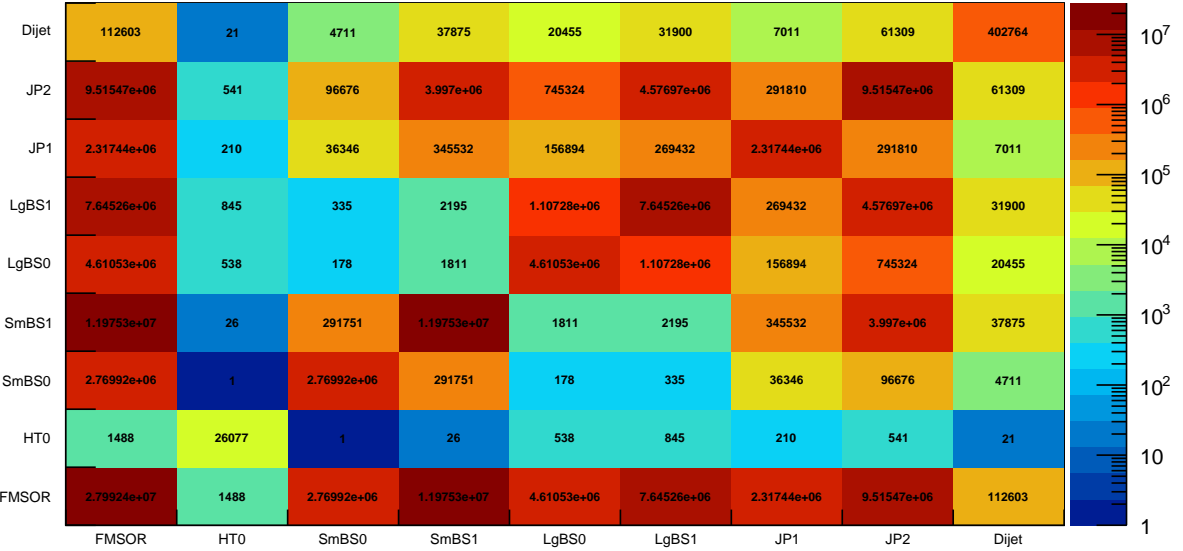
Trigger	L2sum high bitmask	L2sum low bitmask	lastDSM bit	Take-all?	Which trigger bit mask to use
HT	0x0	0x1000000	0	no	L2sum
SmBS0	0x0	0x4000000	2	no	L2sum
SmBS1	0x2000	0x0	3	yes	lastDSM
LgBS0	0x0	0x8000000	5	no	L2sum
LgBS1	0x1000	0x0	6	yes	lastDSM
JP1	0x0	0x20000000	9	no	L2sum
JP2	0x800	0x0	10	yes	lastDSM
Dijet	0x8000	0x0	11	yes	lastDSM

Table 2.1: Trigger bit locations in the last DSM (FP201) 16-bit output word and the 32+32-bit trigger bitmask from trigger level 2. The state of whether or not each trigger is “take-all” is also shown, along with which trigger bit mask is ultimately used in analysis.

For this $A_{LL}^{\pi^0}$ analysis, we have chosen the following combination of trigger bits: the overall OR of SmBS0, SmBS1, LgBS0, LgBS1, JP0, and JP1. This was chosen to avoid the Dijet and HT triggers, which are not as well-understood as the others, while at the same time maximizing the statistics analyzed. In terms of bit masks, this trigger combination corresponds to an L2sum bit mask of 0x2c00000 on the lower 32 bits for the prescaled triggers, ORed with the OR of bits 3, 6, and 10 on the lastDSM output word for the take-all triggers. In this analysis, this combination of triggers is denoted as “FMSOR.”

Figure 2.6 shows the overlap of the triggers, including FMSOR, for candidate π^0 events (more on π^0 event selection later). The overlap is given as a matrix, where each entry is the number of events satisfying both the trigger on the horizontal axis and that on the vertical axis (hence the matrix is symmetric). The diagonal then represents the overall distribution of triggers. The overlap between SmBS and LgBS is quite small, as expected, while the overlap between the BS and JP triggers is significant. The HT trigger (written in the figure as HT0) has very low statistics, as does the di-jet trigger, neither of which are used in the $A_{LL}^{\pi^0}$ analysis.

π^0 FMS trigger overlap matrix



π^0 FMS trigger overlap matrix

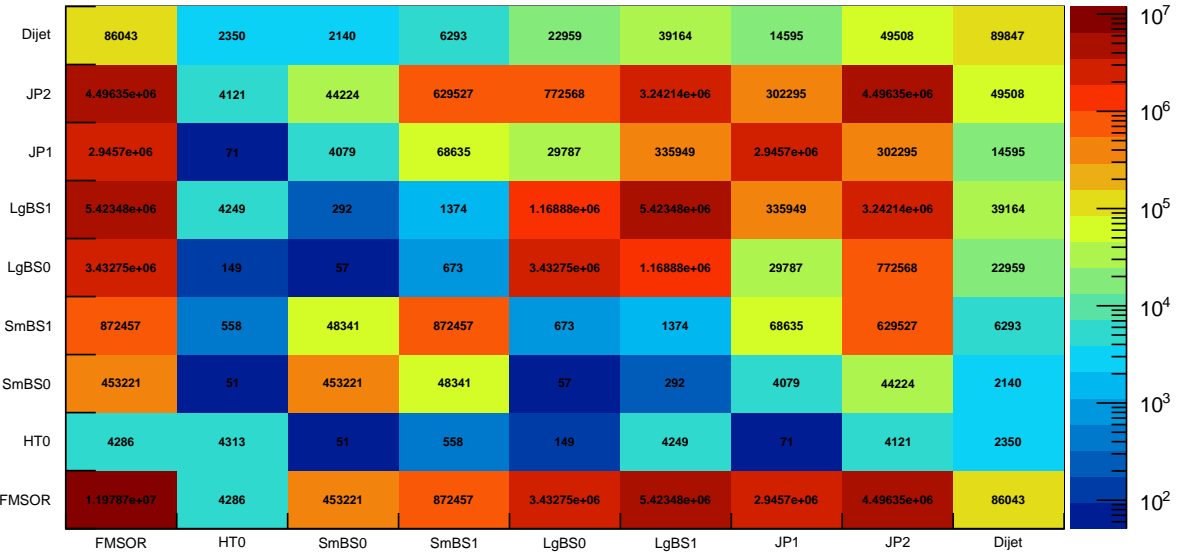


Figure 2.6: Trigger overlap matrix for Run 12 (top) and Run 13 (bottom); color scale is logarithmic and corresponds to the number of times the trigger on one axis is coincident with the trigger on the other axis.

2.3 Data Set and Quality Assurance

The data are typically acquired in 30 minute intervals, called “runs.” These runs allow for the ability to look at the overall data set for an entire RHIC Run (a RHIC Run will henceforth be capitalized, to differentiate it from a 30-minute run) as a time series and cull out any runs which had anomalies, such as abnormally high trigger rates. A basic run Quality Assurance (QA) test was first used to filter runs which are consistent with each other. For each trigger T in each run, the following quantity is computed:

$$f_T = \frac{N_T \cdot \rho_T}{N_{MB} \cdot \rho_{MB}} \quad (2.3)$$

where N is the number of triggers, ρ is the prescale factor of that trigger, and the subscript MB is for a minimum bias trigger, given by the BBC, VPD, or ZDC; in this analysis, the BBC is used as a minimum bias trigger. The ratio f_T is then plotted in figure 2.7 as a function of a run index, in chronological order. Any time there was a major change in the system, such as a threshold change, beam condition change, *et al*, a vertical line was drawn; these vertical lines separate the trigger data into “epochs,” defined as contiguous time periods over which the trigger conditions were the same.

Within each epoch, f_T decreases exponentially as a function of time. Since f_T is proportional to trigger rate (assuming the minimum bias is constant with respect to time), the FMS trigger rate as a whole is decaying. The culprit of this decay is radiation damage within the Pb-glass cells, as will be discussed in the next section. As the Pb-glass cells darken, the amount of light which reaches the PMTs decreases, which in turn causes a reduction in the trigger rates.

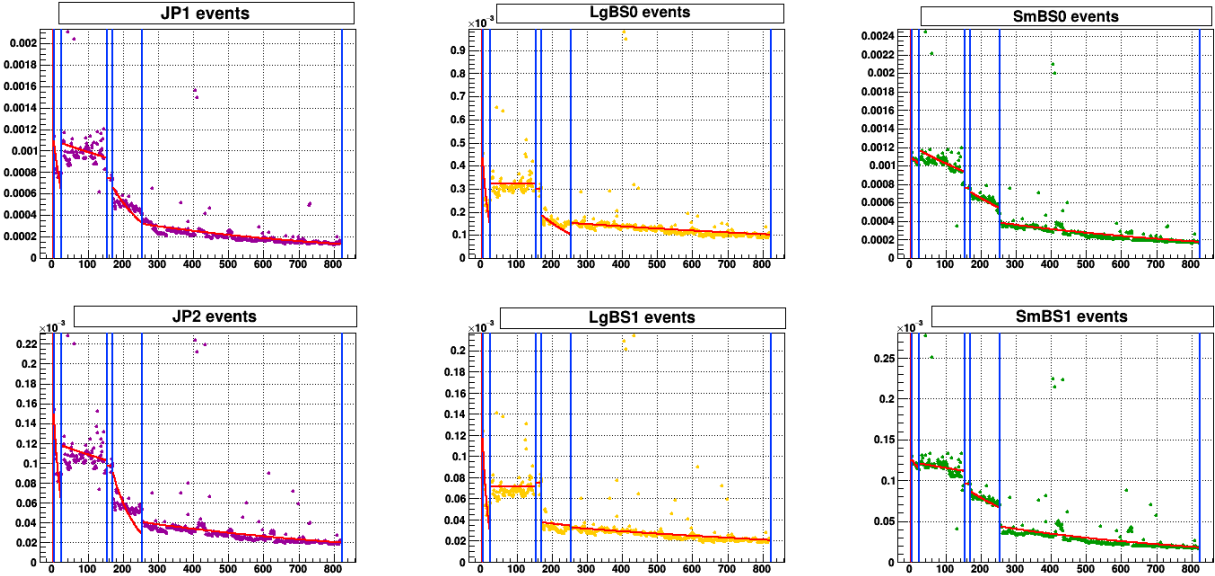
Within each epoch, an exponential fit was performed, as shown by the red curves in figure 2.7. Any epoch with red-colored points was marked bad. In some cases of Run 13, the exponential fit was bad because there were too many outliers.

Figure 2.8 shows the value of f_T normalized to the value given by the fit function for each run and for each epoch fit. The run QA was then performed by visually selecting boundaries around the normalized f_T in order to remove any outliers; runs within these boundaries pass the QA test are defined as “good.” These boundaries are drawn in figure 2.8 as horizontal lines. Although this is more of a qualitative QA method, it is sufficient to cull a more reasonable and consistent data set from the whole and serves as a decent starting point for analysis.

The final run lists which were used in this analysis are found in the “good runs” tables of the following pages:

- Run 12: <http://www.star.bnl.gov/protected/spin/dilks/trgmon12/500/runs.html>
- Run 13: <http://www.star.bnl.gov/protected/spin/dilks/trgmon13/500/runs.html>

Run 12 f_T vs Run Index:



Run 13 f_T vs Run Index:

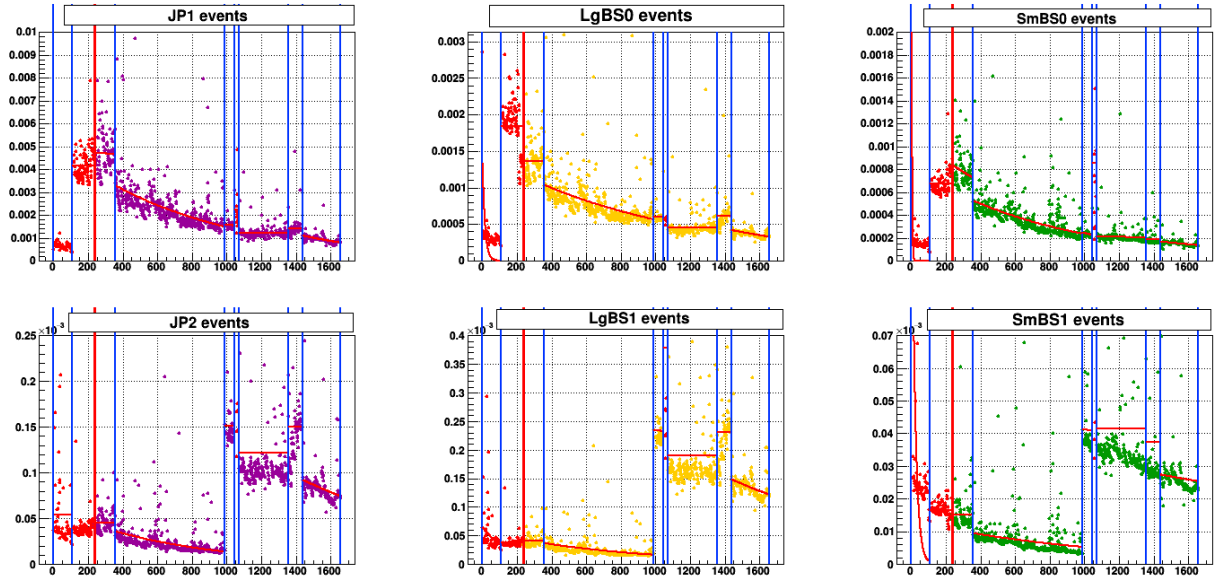
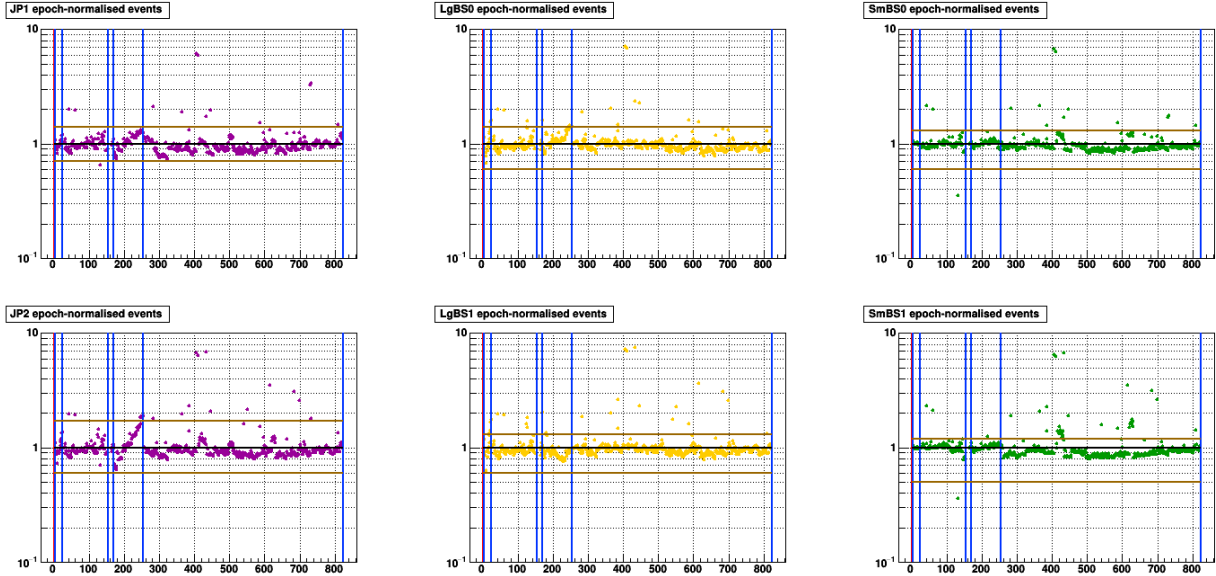


Figure 2.7: f_T vs. data-taking run index (chronological order) for each trigger used in $A_{LL}^{\pi^0}$ analysis for Run 12 (top) and run 13 (bottom). The data points are colored according to trigger: f_{JP} is purple, f_{LgBS} is yellow, and f_{SmBS} is green. Red-colored points are epochs which are marked bad; vertical lines divide epochs.

Run 12 Epoch-normalized f_T vs Run Index:



Run 13 Epoch-normalized f_T vs Run Index:

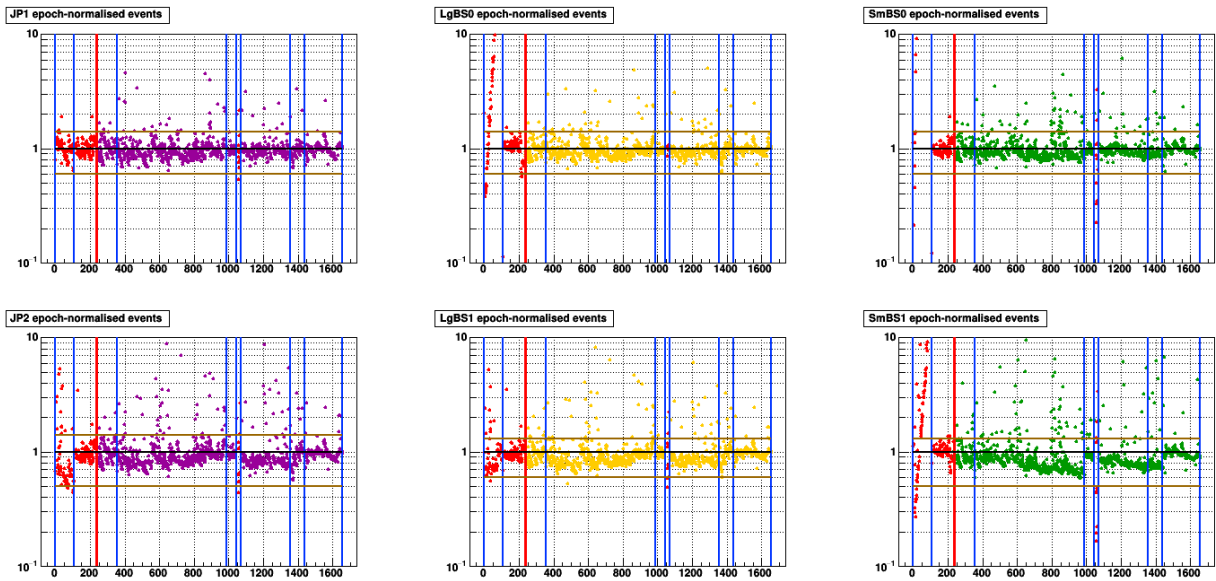


Figure 2.8: f_T divided by epoch exponential fit vs. data-taking run index for each trigger used in $A_{LL}^{\pi^0}$ analysis for Run 12 (top) and run 13 (bottom). Vertical axis is log scale, a bold black horizontal line is drawn at unity, and the brown horizontal lines represent the QA cuts. A run is “good” if it is within the brown horizontal lines.

2.4 Radiation Damage

As electromagnetic radiation passes through the Pb-glass, electrons can become trapped in defects in the crystal called anionic vacancies: these are negative-charge “holes” where an anion would normally expected to be. These trapped electrons are called F-centers (F for *farbe*, German for color), and typically absorb photons in the visible part of the spectrum. The accumulation of F-centers is proportional to the shower density, hence a relative darkening or “browning” of the Pb-glass proportional to the longitudinal shower development is observed in highly exposed cells.

In all RHIC Runs up to Run 13, the FMS accumulated radiation damage, causing an overall monotonic reduction in the trigger rate. After Run 13, the Pb-glass was unstacked and all cells were exposed to direct sunlight. The UV part of the solar emission spectrum is just energetic enough such that trapped electrons are excited out of the anionic vacancies; the number of F-centers exponentially decays and Pb-glass becomes visibly transparent. After 48 hours of sunlight exposure during the summer of 2013, all FMS cells were transparent and cured. For more details, see appendix I.

When the FMS was stacked and operational again in Run 15, the higher luminosity was found to cause the Pb-glass to accumulate radiation damage more rapidly than before. Since unstacking the FMS, exposing all cells to sunlight, and re-stacking the glass is a very labor intensive task, we sought an alternative solution. Several damaged blocks were exposed to various sources of UV radiation, ranging from tanning bed lights, bug lights, UV lasers, and UV-LEDs.

It turned out that the most effective curing method came from UV-LEDs, which were shown to fully cure the glass within approximately 48 hours. The optimal wavelength was determined to be 375 nm, and an array of roughly 1,000 such UV-LEDs was built. Because of design restrictions, the array had to be built in small modules and then be connected after installation; furthermore, the UV-LEDs needed to be cooled. All LEDs were mounted on aluminum plates which are embedded with copper pipes carrying cooling water. The entire array was installed facing the front face of the Pb-glass, with higher LED densities closer to the higher-radiation region near the beam pipe. This UV-LED array was built and installed prior to Run 17 and ultimately turned out to be a successful method to keep the radiation damage minimal during the entire Run.

Chapter 3

Event Selection

This chapter outlines the data selection procedure, which aims for a clean and well-understood sample of π^0 s while maximizing the overall statistics.

3.1 π^0 Kinematics and FMS Acceptance

Consider a π^0 with energy E which decays into two photons of energies E_+ and E_- , and with a decay opening angle of α . These energy variables (E_+, E_-) of the 2-photon system can be transformed into two variables (E, Z) , associated with the π^0 : the total energy $E = E_+ + E_-$ and the energy imbalance

$$Z := \frac{E_+ - E_-}{E} \tag{3.1}$$

The subscripts “+” and “−” were chosen so that $E_{\pm} = E(1 \pm Z)/2$. The invariant mass, M , depends on the photon energies and opening angle as

$$M = 2 \cdot \sqrt{E_+ E_-} \cdot \sin \frac{\alpha}{2} = E \cdot \sqrt{1 - Z^2} \cdot \sin \frac{\alpha}{2} \tag{3.2}$$

For further details on π^0 decay kinematics, see appendix A.

In addition to the π^0 E , Z , and α , two angles are also needed to fully describe the π^0 momentum p : the azimuthal angle ϕ and the scattering angle θ . Referring to figure 3.1, let the positive z -axis be along the proton beam, pointing toward the FMS, and the y -axis point upward, with the origin centered at the nominal proton-proton interaction point (IP). The azimuth ϕ is defined as the angle between the positive x -axis and transverse momentum vector p_T , which is the projection of the momentum vector p on the xy -plane. The scattering angle θ , defined as the angle between p and the positive z -axis, is more commonly given as

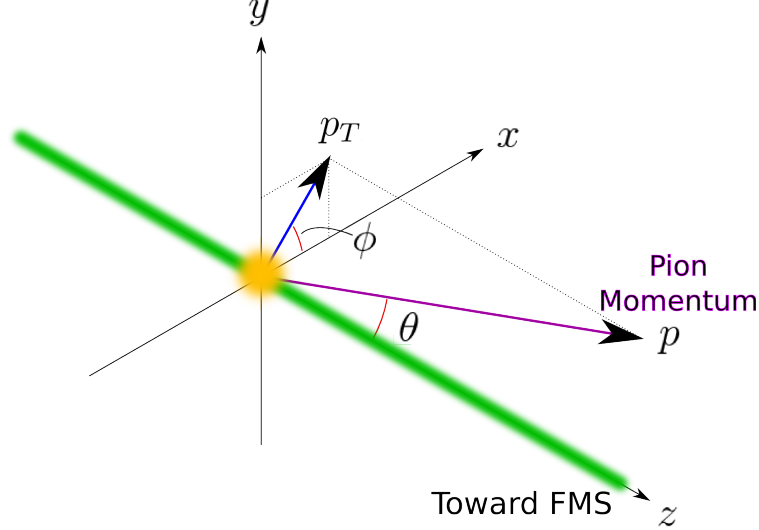


Figure 3.1: Scattering coordinates notation

the pseudorapidity η , defined as

$$\eta := -\ln \left(\tan \frac{\theta}{2} \right) \quad (3.3)$$

In practical data analysis, the variables used to classify π^0 s are $\{E, Z, M, p_T, \eta, \phi\}$.

The FMS is situated about 7.2 m from the nominal IP, and occupies almost a 2 m \times 2 m transverse size, so it is sensitive to π^0 s (and other particles) with $\eta \in [2.5, 4.2]$ over full azimuth. Note that the outer boundary of the FMS is octagonal and that the inner boundary is square; thus the η boundary rings listed here are only approximate bounds of the FMS geometry boundaries. Given typical values of $\sqrt{s} \in \{200, 510\}$ GeV as well as trigger thresholds and reconstruction limitations, typical energy and momentum ranges of π^0 s are $E \in [10, 100]$ GeV and $p_T \in [2, 10]$ GeV. An upper limit on Z is also typically employed, in order to omit high-energy photons which could have been mis-identified as a π^0 ; a typical constraint is $Z < 0.8$.

3.2 Inner and Outer Pseudorapidity Regions

Before discussing specific kinematic cuts, it is worth mentioning that the $A_{LL}^{\pi^0}$ analysis is separated into two η regions which approximately separate the large cells and the small cells. Figure 3.2 shows the distribution of 2-photon invariant mass plotted versus their pseudorapidity (of their parent π^0 , eta, *et al*). The outer black vertical lines represent overall η cuts of 2.65 and 3.9. The events selected here have all of the nominal π^0 kinematic

cuts (omitting the mass cut), which will be discussed in this chapter.

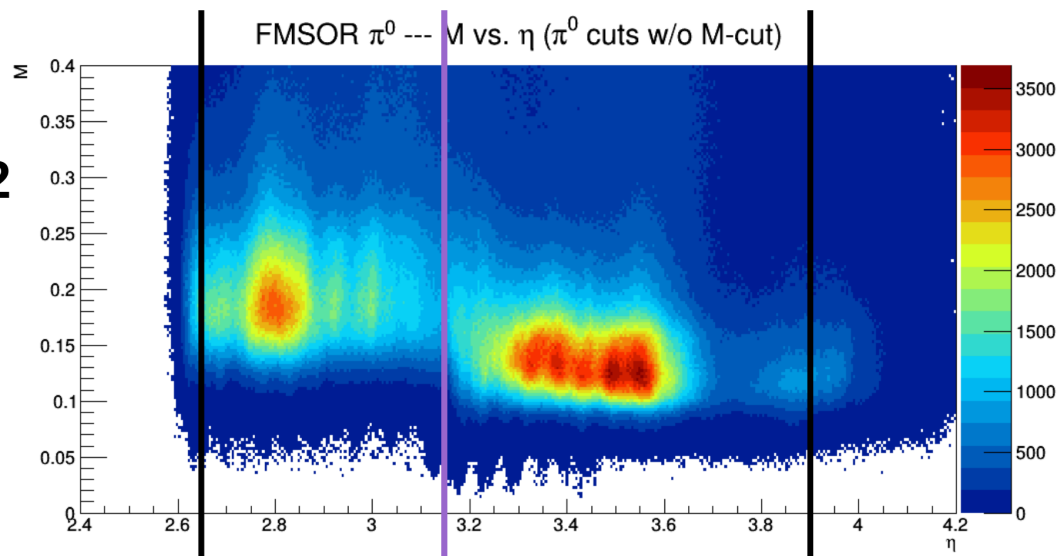
Although the FMS is composed of large cells and small cells taken together, the large cells and small cells behave differently, due to their PMT differences, glass cell size differences, and different exposures to radiation damage. They are therefore calibrated a bit differently, and the two corresponding pseudorapidity regions can be discerned from figure 3.2. Looking at Run 12, $\eta = 3.15$ was chosen as an appropriate boundary, and was also applied to Run 13, since the two Runs need to have the same η constraints in order to merge them into one $A_{LL}^{\pi^0}$ analysis. Furthermore, for Run 13, the small cells were too heavily damaged from radiation and were consequently omitted from the analysis. Therefore, the event selection is broken down in the following manner:

- Outer region: $2.65 < \eta < 3.15$ – mostly large cells – analyzed Runs 12 and 13
- Inner region: $3.15 < \eta < 3.9$ – mostly small cells – analyzed Run 12 only

Figure 3.3 shows a schematic of the FMS with the above pseudorapidity cuts.

Note that the most dominant part of the mass distribution shown in figure 3.2 is higher than the expected π^0 peak at 0.135 GeV; this is because there is an energy-dependent effect in the π^0 reconstruction, which causes the reconstructed mass to rise as a function of energy. This effect will be discussed in detail later.

Run 12 M vs η



Run 13 M vs η

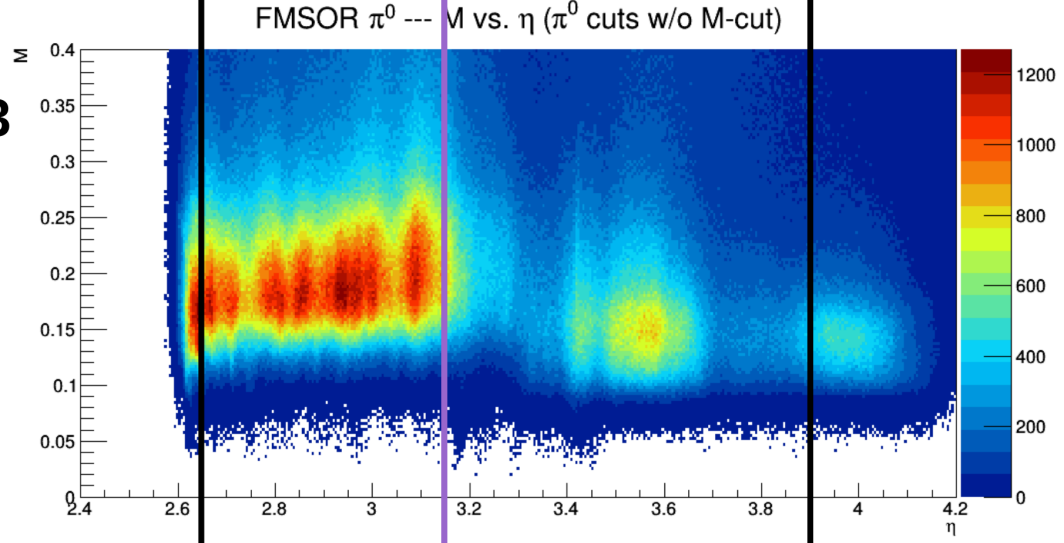


Figure 3.2: 2-photon invariant mass vs. pseudorapidity for run 12 (top) and run 13 (bottom) Outer black vertical lines represent overall η cuts, and the inner magenta vertical line represents the inner/outer regions' boundary

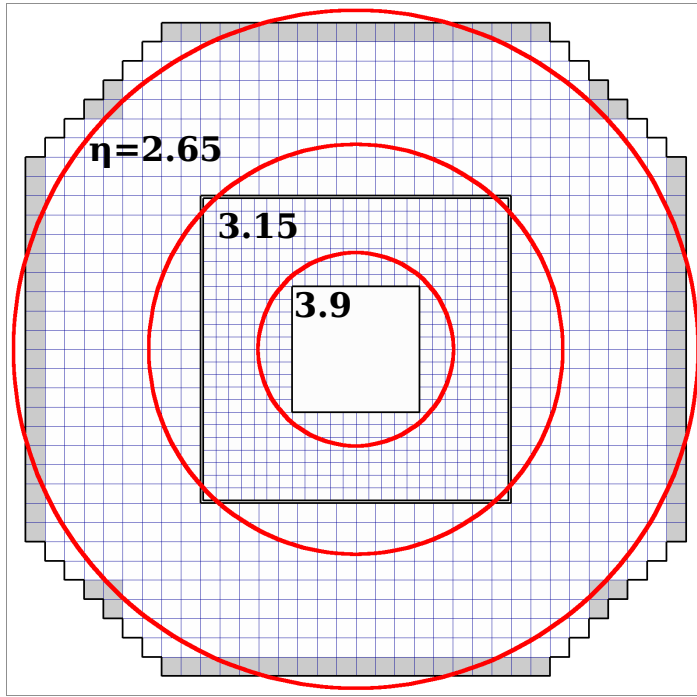


Figure 3.3: FMS schematic and pseudorapidity boundaries

3.3 Event Reconstruction

We now turn to how π^0 events are reconstructed from photon hits. This section describes the photon-finding and clustering algorithms, and how π^0 candidates are selected from the results.

3.3.1 Trigger Matching

Events which satisfy an FMS trigger are those which have “clusters” of cells with nonzero ADC counts; for example, a single photon that hits the center of one FMS cell will deposit $\sim 80\%$ of its energy in that cell and the remaining $\sim 20\%$ in the surrounding cells. Essentially, the trigger will fire if one of these clusters will cause a subsequent ADC sum (in a higher DSM layer) to be above threshold, so it does not matter which cluster or set of clusters actually fired the trigger: the clusters are basically “ORed” together.

A given trigger, either Board Sum (BS) or Jet Patch (JP), is defined in a geometric segmentation of the FMS, as in figures 2.3 (BS) and 2.5 (JP). The segmentation divides the

FMS into “patches”, for example, in figure 2.3 each letter corresponds to a single BS patch; note that patches in general can overlap with each other, so that any cluster is very likely fully contained in some patch.

Each patch contains some number of cells, and for a given event, each cell will report an ADC count. The sums of the cells’ ADC counts in a given patch is called the “patch sum”. Depending on the trigger algorithm, these patches could then be further combined into “patches of patches”, which then have their sums (of sums). This combination of sums forms the tree structure of the DSM tree (see figure 2.4). The last layer of the DSM tree contains the final set of ADC sums which are then compared to thresholds (defined during data-taking), each which returns a boolean 1 for sum above threshold or a 0 otherwise. The key point here is that the OR of all of these booleans is taken: so as long as at least one of the patches had something trigger-worthy in it, the overall trigger is satisfied. This OR result then defines the output trigger Level 0 bit (one for each trigger), defined as 1 if the trigger fired and 0 if not.

These output trigger bits, which are the output of trigger Level 0, go through the TCU and prescaling etc., resulting with the Level 2 output trigger bits. It is these level 2 output bits which we use to filter for FMS-triggered events.

Event reconstruction is done on all trigger events, and one can of course impose a restriction on FMS triggers only. Kinematic cutoffs (minimum E and p_T) are applied, which approximately match what was defined in the original trigger thresholds, but since the trigger threshold applies in “ADC space” and then ADC counts for each cells are converted to E (and p_T etc.), the actual trigger threshold gets smeared in E (or p_T) space.

The trigger thresholds are hard cutoffs in ADC values, however when the ADC values are converted to E and p_T , the actual threshold is smeared by the fact that there is a variation on the gains throughout the whole detector. In particular, the FMS is calibrated such that the target gains are a function of η . In the reconstruction algorithm, we apply a soft energy cutoff as well as a $p_T > 1.5$ GeV cut so that only clusters which very likely satisfied the trigger DSM algorithm are considered. In the $A_{LL}^{\pi^0}$ analysis, tighter constraints on p_T and E are made, ensuring that all of the photon pairs considered for π^0 s candidates satisfied the trigger.

3.3.2 Shower Shapes

Consider a point source of light at a distance b from a plane. Let (x, y) represent the coordinates of a point on the plane, where $(0, 0)$ is the point that is a distance b from the source. If the point source emits photons uniformly, the probability density distribution

$f(x, y; b)$ of photons hitting the plane follows a Cauchy distribution:

$$f(x, y; b) = \frac{1}{2\pi} \frac{b}{(b^2 + x^2 + y^2)^{3/2}} \quad (3.4)$$

If the plane were to be segmented into squares, each with side length d , one can determine the fraction of light seen in each square. Assume the coordinate system is aligned with the square boundaries. Consider a square which is centered about (x_c, y_c) ; the square ranges from $(x_c - d/2, y_c - d/2)$ at one corner to $(x_c + d/2, y_c + d/2)$ at the opposite. To evaluate the total probability of photons hitting this square, one uses the cumulative distribution function of $f(x, y; b)$:

$$\begin{aligned} F(x, y; b) &= \int_{-\infty}^x \int_{-\infty}^y d\hat{x} d\hat{y} f(\hat{x}, \hat{y}; b) = \\ &= \frac{1}{4} + \frac{1}{2\pi} \left[\arctan\left(\frac{x}{b}\right) + \arctan\left(\frac{y}{b}\right) + \arctan\left(\frac{xy}{b\sqrt{b^2 + x^2 + y^2}}\right) \right] \end{aligned} \quad (3.5)$$

The total fraction of light (of which would hit the plane) that is detected in this square is then

$$\begin{aligned} G(x_c, y_c) &= F\left(x_c + \frac{d}{2}, y_c + \frac{d}{2}; b\right) - F\left(x_c - \frac{d}{2}, y_c + \frac{d}{2}; b\right) - \\ &\quad - F\left(x_c + \frac{d}{2}, y_c - \frac{d}{2}; b\right) + F\left(x_c - \frac{d}{2}, y_c - \frac{d}{2}; b\right) \end{aligned} \quad (3.6)$$

These four terms correspond to the four corners of the square.

The shower shape model which is employed in FMS photon reconstruction is a linear combination of Cauchy distributions

$$f_\Sigma(x, y) = \sum_{i=1}^N a_i f(x, y; b_i) \quad (3.7)$$

and the aforementioned detector squares correspond to individual FMS cells. To maintain normalization, $\sum_i a_i = 1$ is enforced. A fit was performed by [7] with $N = 3$ terms; this used the equivalent of FMS small cells with $d = 4$ cm and the resulting fit parameters are given in table 3.1.

The geometrical interpretation of b_i as a longitudinal source distance was never enforced in the fit. It is suspected that this variable could help correct for asymmetric shower shapes which occur with high incident angles photons; however, such attempts only resolve photons

i	a_i	b_i
1	0.8	0.8 cm
2	0.3	0.2 cm
3	-0.1	7.6 cm

Table 3.1: Fit parameters of the shower shape model described in [7]

which, given the FMS geometry, are up to a conservative maximum of 0.5 cm away from the symmetric shower shape photon reconstructed positions, which use the parameterization in table 3.1. This difference is a very small correction in the context of other uncertainties which contribute to the $A_{LL}^{\pi^0}$ measurement and is not implemented in this analysis. Instead, the parameterization in table 3.1 is implemented.

At high energies, it becomes difficult to distinguish 2-photon clusters from 1-photon clusters, because the opening angle of 2-photons decreases as a function of energy. One variable which helps separate 1-photon and 2-photon clusters is the second-moment matrix of the cluster’s cells’ log-weighted energy. In particular, the maximum eigenvalue of the second-moment matrix, called σ_{\max} , plotted as a function of cluster energy, reveals two bands: one which is mostly 1-photon clusters and another which is mostly 2-photon clusters. See [4] for more details.

3.3.3 Clustering Algorithm

Given a list of photons for an event, the next step is to start to look for photon pairs in order to begin identifying π^0 candidates; the method used is a type of clustering algorithm, which organizes all photons into groups of photons, called “cone-clusters,” limited in size by “isolation cones.” The isolation cone technique uses a cone of a fixed radius, defining the maximum size of a cone-cluster. If the isolation cone radius is very high, only highly isolated π^0 s will be identified; on the other hand, if the isolation cone radius is too low, splitting of photon pairs between adjacent cone-clusters becomes an issue. Ideally, for an inclusive analysis one wants a cone radius which is low enough such that π^0 s of any level of isolation are found, but high enough such that π^0 s are unlikely to have their photons split between adjacent cone-clusters. An example of a 35 mrad cone with respect to the FMS size is shown in figure 3.4; this particular choice turns out to be the most optimal choice in providing an inclusive-like sample of π^0 s.

The cone-clustering algorithm begins by sorting all photons in the event in descending order of energy. An isolation cone is drawn around the first, highest-E photon, centered on its trajectory; in other words, this photon begins the first cone-cluster. Each subsequent photon on the sorted list is then compared to the current list of cone-clusters, and if the

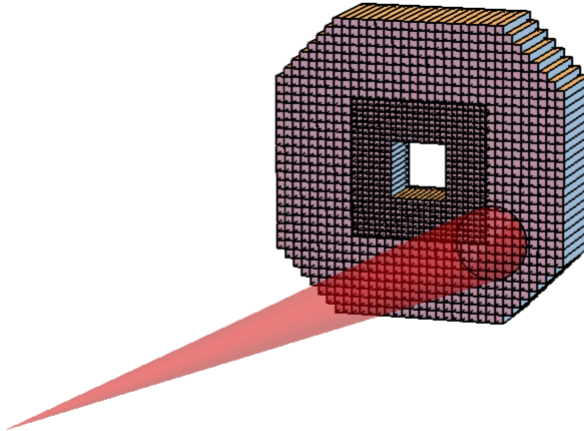


Figure 3.4: Sample 35 mrad isolation cone projected onto the FMS; the vertex of the cone is situated at the nominal IP

photon is within an isolation cone radius of any cone-cluster on that list, then it is added to that cone-cluster; that cone-cluster’s isolation cone is then re-centered on the cone-cluster energy centroid. On the other hand, if the photon is not within an isolation cone radius of any cone-cluster, a new cone-cluster is started for that photon. The algorithm proceeds until all of the photons (with energy greater than a soft energy cutoff) of the event are organized into cone-clusters. Finally, the cone-clusters themselves are sorted by energy and stored in a data tree for that event, along with their kinematics.

Given the sorted list of cone-clusters, one can then begin to search for π^0 s. Only cone-clusters with at least two photons are candidates for containing a π^0 ; of these cone-clusters, the highest energy pair in the highest energy cone-cluster of each event was found to give the cleanest sample of π^0 candidates. For an inclusive measurement, one wants the maximum π^0 mass signal with the minimum background; furthermore, given the clustering algorithm, one must be mindful of cases where the photon pairs are split between adjacent cone-clusters, which cause combinatorial losses of π^0 s. Various samples of photon pairs were compared using a variety of isolation cone sizes, minimum photon energy cutoffs, and minimum pair transverse momentum cutoffs. Looking at the highest energy photon pair in the highest energy cone-cluster of each event, an isolation cone of 35 mrad (figure 3.4), a minimum photon energy of 3 GeV, and a minimum photon pair p_T of 1.5 GeV provided the best inclusive-surrogate sample, when compared to all other tested samples. Combinatorial losses due to pair-splitting between adjacent cone-clusters are limited to 2%. This sample of photon pairs is the closest we are able to get to a “true” inclusive sample of π^0 s and is the sample used for the $A_{LL}^{\pi^0}$ analysis.

3.3.4 Energy Dependence of the Mass

Once pairs of photons have been selected, one may begin to look at their invariant masses; the determination of invariant mass depends on the photon energies as well as their opening angle, as was shown in section 3.1. The fit algorithm for fitting clusters of energy deposits in the FMS to a shower shape has a tendency to overestimate the decay photon opening angle, α , at higher pair energies, E . Figure 3.5 shows shows an example of this effect, where the monochrome histogram is of α vs. E . The red lines in this figure indicate constant M contours (π^0 mass contour is solid) for fixed values $Z = 0$ (left), $Z = 0.44$ (middle), and $Z = 0.8$; while the α vs. E data in these three figures are the same, the position of the $M(\alpha, E)$ contours still has a dependence on Z , thus M contours three values of Z are shown. The data histograms contain data in the range $0 \leq Z \leq 0.8$ in all three plots and show that α decreases as a function of E ; however, the decrease is not as rapid as the contours indicate it should be. These data show a clear overestimation of the value of α , which worsens as the E increases.

Figure 3.6 shows the pair invariant mass, M , as a function of E ; contours of constant α are plotted, again for three values of Z . These contours show that for a specific value of α and Z , the mass increases monotonically with respect to the energy. Since the value of α is not falling rapidly enough with respect to E , the data tend toward following these α contours, rather than remaining flat on a line of constant M . In other words, we see a monotonic increase in the reconstructed M as a function of E , directly associated with the overestimation of α as E increases.

To compensate for this overestimate of α , one could implement an α -dependent dependent correction; this correction could be done in such a way that the E -dependence on the mass would become flat. Instead, however, we decided to simply implement an E -dependent mass cut scheme, as will be discussed in section 3.6.3.

3.4 Gain Corrections

This section outlines the “offline” corrections to the gains of each FMS cell. These corrections arise from radiation damage effects, as well as from a nonlinearity in the response of the FMS PMTs.

3.4.1 Time-Dependent Corrections – The LED Flasher System

The radiation damage caused a time-dependent degradation in the overall PMT response. Furthermore, the PMT responses had a tendency to vary in time during all Runs before Run

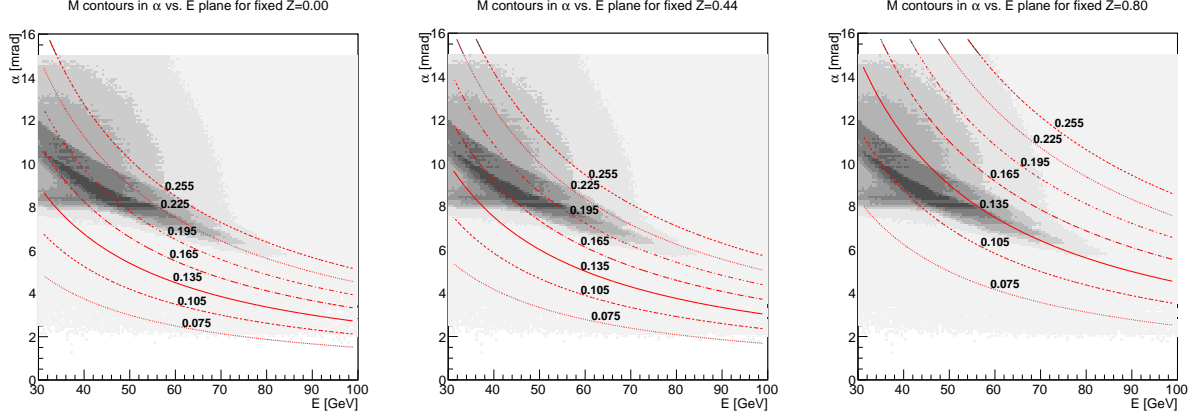


Figure 3.5: Pair opening angle α vs. pair energy E , where Run 12 data are shown in monochrome. The red lines are contours of constant mass M , given a value of $Z = 0$ (left), $Z = 0.44$ (middle), and $Z = 0.8$ (right); the ideal π^0 mass contour is drawn solidly

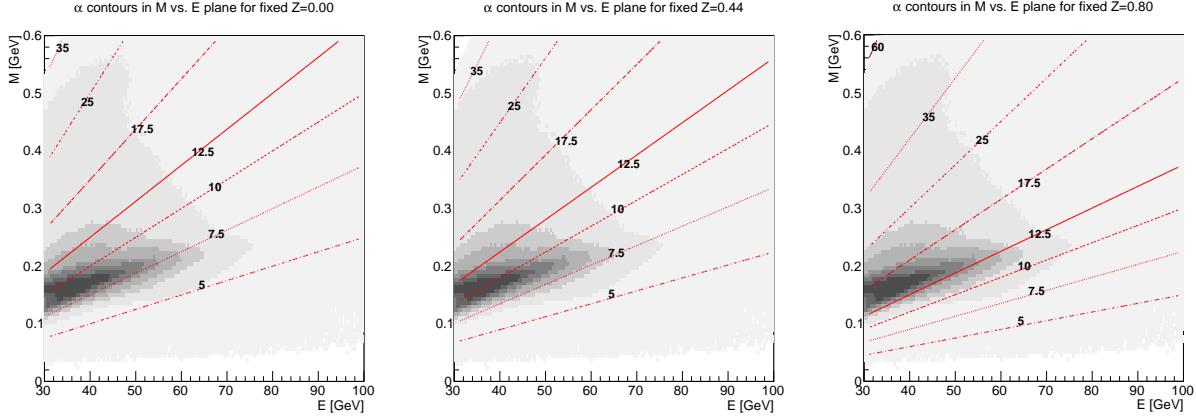


Figure 3.6: Pair mass M vs. pair energy E , where Run 12 data are shown in monochrome. The red lines are contours of constant opening angle α , given a value of $Z = 0$ (left), $Z = 0.44$ (middle), and $Z = 0.8$ (right)

15, due to malfunctioning Zener diodes in the PMT bases. These time-dependent variations in PMT responses, are corrected for by making use of data collected from the FMS LED flasher system. The LED flasher system used in Runs 12 and 13 was composed of a set of LEDs pulsing at 1 Hz, where the LED light outputs were directed into a tree of fiber optic cables, such that each cell had a fiber optic LED light output directed at its transverse center. Although there was an independent STAR trigger used for the LED system, it was more practical to pick the LED events from the overall trigger data by looking for events which had very high ADC sums (over all cells). Since the LED flasher system pulses light into all channels simultaneously, the resultant ADC sum from any LED pulse is much higher than the typical ADC sums seen during usual data taking. The LED events are, therefore,

very easy to identify.

The time-dependent variations in gain of all of the PMTs can be tracked by looking at the time-dependence of the ADC distributions seen from LED events. This tracking gives one the ability to correct for these effects, by simply introducing a time-dependent gain correction.

3.4.2 Nonlinear Energy-Dependent Response Correction

Another piece of the gain correction comes from a nonlinear dependence on energy of the PMT response. This effect is mostly due to the dependence of the electromagnetic shower shape on the depth, z , in the Pb-glass cells; for example, the effective z -position of the shower maximum depends on incident energy and on incident angle. This dependence is the source of different effective attenuation lengths, which in turn causes a nonlinearity in the relationship between the energy measured by the PMT, the “observed energy,” and the energy of the incident photon, the “true energy.” In order to correct for this behavior, an additional nonlinear energy-dependent gain correction is applied.

3.4.2.1 Nonlinear Gain Correction Model

To model the nonlinearity, we first take a closer look at the monotonically increasing dependence of the reconstructed pion mass on the energy. The left panel of figure 3.7 shows reconstructed π^0 masses as a function of one of the photon energies in green, in comparison to η -mesons in black. These data are from Run 15, however, the dependence is similar in Runs 12 and 13; data from Run 15 is shown here since the η meson signal was much cleaner than in Runs 12 and 13. One observes a slow rise in M at low E , relatively flat M at mid-range E , and a slow rise of M at higher E .

The right panel of figure 3.7 shows a ratio of the reconstructed M to the ideal meson M , as a function of the two-photon opening angle, α . The low- E η mesons, with $\alpha \sim 40$ mrad, barely fit into the FMS acceptance, causing a cutoff at high α due to geometry. The low- E π^0 's have a lot of background under the mass peak, however, they are produced with values of α similar to those in high- E $\eta \rightarrow \gamma\gamma$ decays; this region of event overlap is approximately $\alpha \in [20, 30]$ mrad and shows a mis-match of reconstructed mass to meson masses. Modelling the nonlinearities observed in the E -dependence of M could help improve this α -dependence matching.

The high- E π^0 's show a steep rise in the mass ratio as α decreases; this effect is from the aforementioned opening angle overestimation as the photon clusters merge closer and closer. This effect is correctable by dividing the mass by an α -dependent factor, but such a correction

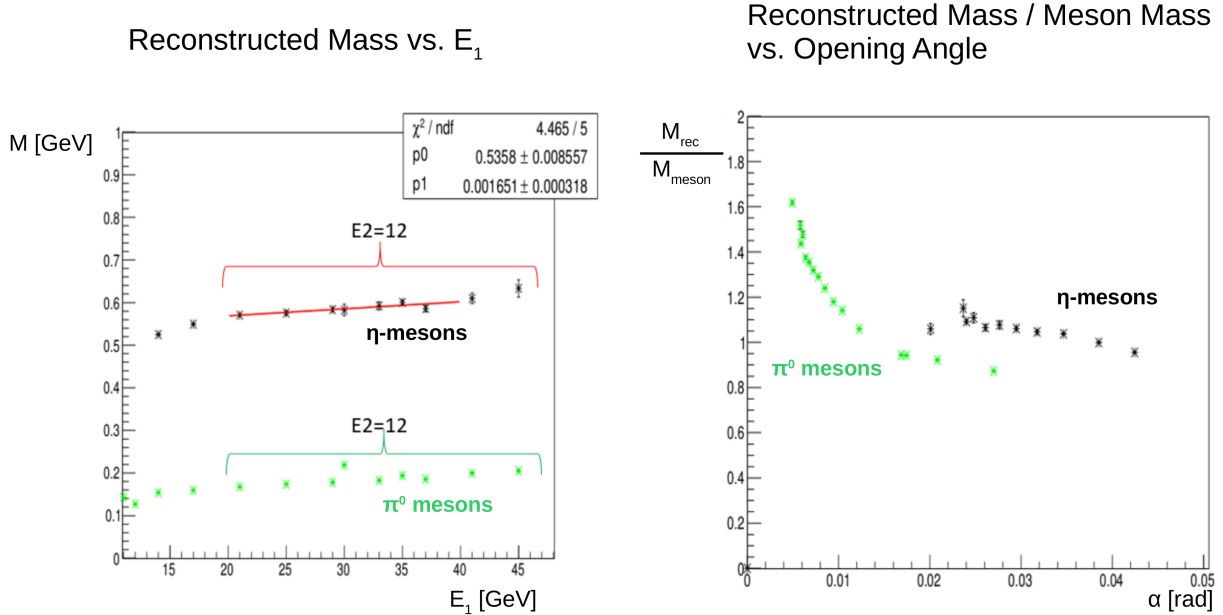


Figure 3.7: Left: reconstructed mass versus energy of one photon (E_1) for π^0 s in green and η mesons in black; in the bracketed region, the energy of the other photon is ~ 12 GeV. Right: ratio of reconstructed mass to true meson mass versus two-photon opening angle

is not implemented in this analysis. Instead, energy-dependent (and time-dependent) mass cut compensates for this by tracking the π^0 mass peak location and width in bins of energy.

The E -dependence of the M in figure 3.7 motivates the following nonlinear E -dependent gain correction. Define this correction as $g(E_t) = E_o/E_t$, where E_o is the observed energy and E_t is the “true” energy, defined as the corrected energy. $g(E_t)$ is modelled as a piecewise linear function over three energy regions $\{A, B, C\}$:

$$g(E_t) = \begin{cases} g_A(E_t) = 1 - (N - K_t^A) \varepsilon_B - (K_t^A - E_t) \varepsilon_A & \forall E_t \leq K_t^A \\ g_B(E_t) = 1 - (N - E_t) \varepsilon_B & \forall K_t^A \leq E_t \leq K_t^C \\ g_C(E_t) = 1 - (N - K_t^C) \varepsilon_B - (K_t^C - E_t) \varepsilon_C & \forall E_t \geq K_t^C \end{cases} \quad (3.8)$$

The parameter N is the normalization energy point, since $g(N) = 1$ and is a fixed value in region B. It can be thought of as 1/2 the π^0 mass calibration anchor energy, where the factor 1/2 originates from assuming that most π^0 s decay to 2 equal- E photons; this assumption is not exactly true since the energy imbalance, Z , is not always 0 and does not average out to 0 either, but this assumption is a sufficient starting anchor point for this $g(E_t)$ model. The energies $\{K_t^A, K_t^C\}$ are boundaries between the energy regions; they are subscripted by t to indicate that these “crossover” energy points represent region boundaries in E_t -space, as

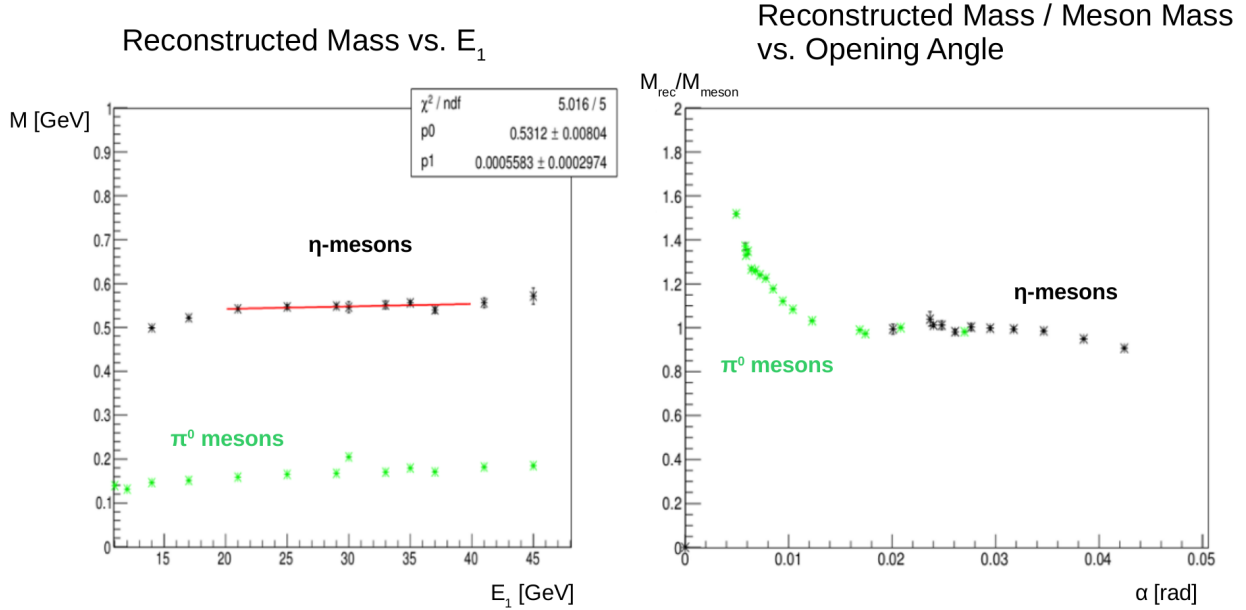


Figure 3.8: Left: reconstructed mass versus energy of one photon (E_1) for π^0 s in green and η mesons in black; in the bracketed region, the energy of the other photon is ~ 12 GeV. Right: ratio of reconstructed mass to true meson mass versus two-photon opening angle. This figure is a repeat of figure 3.7, but with the nonlinear E -dependent gain correction implemented

opposed to boundaries in E_o -space. Finally, the parameters $\{\varepsilon_A, \varepsilon_B, \varepsilon_C\}$ are slopes of $g(E_t)$ in each of the three energy regions.

The effect of an example correction of the form of equation 3.8 is plotted in figure 3.8, which shows the same plots as figure 3.7 showed, but now with the new gain correction implemented. The E -dependence of the mass has flattened out; furthermore, the matching of low- E π^0 s with high- E η mesons has significantly improved. Figure 3.8 is, again, from Run 15 data, but the effect the same in Runs 12 and 13.

The parameters of equation 3.8 were refined using a stand-alone Geant4 simulation of the FMS. By analyzing the photon yield at the photon-cathodes as a function of thrown incident photon energy, the fit parameters given in table 3.2 were obtained. This parameterization is plotted as the solid line in figure 3.9. Region A , the low energy region, has a high slope which corresponds to the fast rising mass at low energy seen in figure 3.7; this is the aforementioned overlap region, where high- α π^0 s overlap with low- α η mesons. On the other hand, regions B and C have flatter E -dependences.

3.4.2.2 Including Radiation Damage

We now turn to considering the effect of radiation damage on this gain correction. The longitudinal dependence of the radiation damage when considered along with the shower

Cells Type	N	K_t^A	K_t^B	ε_A	ε_B	ε_C
Large Cells	12.5 GeV	8.6 GeV	20.1 GeV	0.015	0.0082	0.0023
Small Cells	20 GeV	10.2 GeV	34.1 GeV	0.020	0.0048	0.0020

Table 3.2: Values of parameters in $g(E)$ model

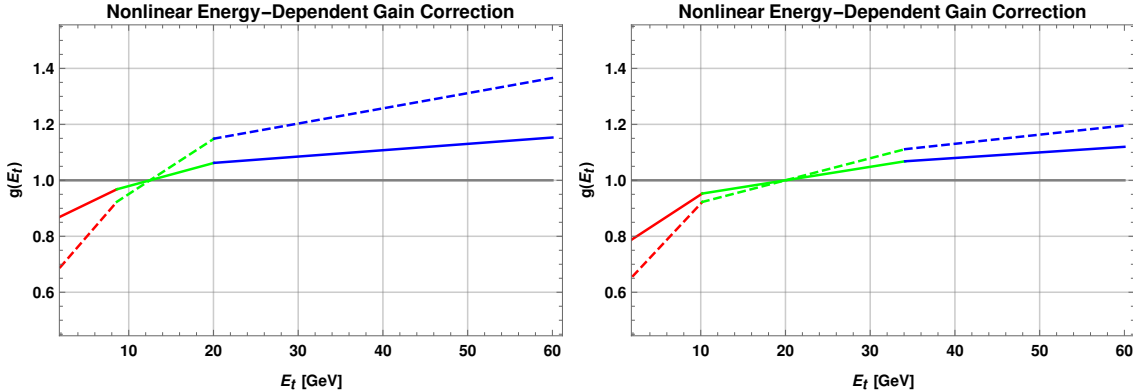


Figure 3.9: Non-linear energy-dependent gain correction model for large cells (left) and small cells (right). Colors red, green, and blue indicate energy regions A , B , and C , respectively. The solid line is the day-0 model, with base-line radiation damage, and the dashed line is the day-300 model, the modified form of $g(E_t)$ after 300 days worth of radiation damage.

shape is the origin of additional nonlinearity in the gain correction, which cannot be factored out directly. As a starting point, we attempt to model the radiation damage accumulation as a function of time. The amount of accumulated radiation damage is proportional to the number of f-centers which have formed; these f-centers are electrons which occupy anionic vacancies in the glass. Assuming the rate of f-center formation is proportional to the number of unfilled anionic vacancies, the rate of radiation damage accumulation decreases linearly with respect to the amount of accumulated radiation damage. Therefore the time-dependence of a general variable R , which characterizes the amount of radiation damage, evolves with respect to time t as

$$\frac{dR}{dt} = \lambda [R_\infty - R(t)] \implies R(t) = R_\infty - (R_\infty - R_0) e^{-\lambda t} \quad (3.9)$$

where $R_0 = R(0)$, $R_\infty = \lim_{t \rightarrow \infty} R(t)$, and $\lambda = 1/\tau$ with τ the time constant.

To evaluate effects of radiation damage, another simulation was performed. The radiation damage longitudinal profile was assumed to match the typical energy deposition longitudinal profiles, which was obtained from minimum-bias PYTHIA events thrown at a model FMS with undamaged, clear Pb-glass. Under this assumption, for any specified amount of radiation damage, the radiation damage in the glass can be simulated by a modification of

the attenuation coefficients. The photon yield as a function of thrown photon energy was assessed for a range of days' worth of radiation damage accumulation and it showed that the relative strength of the nonlinear gain correction increases as a function of accumulated radiation damage.

The simulation was performed for photons thrown at the large cells in an η range of 3.1 ± 0.05 and at the small cells in an η range of 3.9 ± 0.05 ; these values of η are approximate maximum values of η for the large cells and small cells and they represent the regions of highest radiation damage for each cell type. For each simulated day, the photon yield as a function of energy was fit with the $g(E)$ model in equation 3.8, with fixed crossover energies and constrained to unity at the anchor point energies. For all three energy regions, the slopes of the fits were observed to evolve similarly in time; consequently, a time-dependent model of the effect of radiation damage on the nonlinear gain correction can be captured simply by a “slope factor”, which multiplies all slopes in $g(E)$. This slope factor was ultimately chosen as the variable $R(t)$, with time-dependence given in equation 3.9.

The slope factor, $R(t)$, was evaluated for one (small range around a) value of η for large cells and another for small cells, but it can be extrapolated to apply to all pseudorapidities. Cells closer to the beam line will receive more radiation damage than those farther away. This η -dependence can be folded in to the time constant as follows: first assume that at pseudorapidity η_0 the amount of radiation damage was Δt days' worth. The cells with pseudorapidity $\eta < \eta_0$ therefore experienced less than Δt days' worth of damage. Now let the time constant be τ_0 at the value of $\eta = \eta_0$, and let η_0 be where the $g(E)$ fits were performed. For $\eta < \eta_0$, the radiation damage is expected to be less, and consequently the time constant should be longer. Therefore, we assume

$$\lambda \rightarrow \lambda(\eta) = \lambda_0 e^{-h_0 + h_1 \eta} \quad (3.10)$$

where λ_0 , h_0 , and h_1 are fit parameters and are constrained by $\lambda(\eta_0) = \lambda_0$. Their explicit values were determined by looking at ratios in flasher LED amplitudes.

Finally, the full radiation damage parameterization is given table 3.3. Figure 3.10 shows the plot of the psuedorapidity-dependence of the factor $\lambda(\eta)/\lambda_0 = \exp(-h_0 + h_1 \eta)$. This factor is unity at the chosen fit points η_0 , and decreases with decreasing η . Figure 3.11 shows the behavior of $R(t)$ as a function of days worth of radiation damage (using Run 15 luminosities); it is plotted for various values of η . The value of $R(t)$ increases with respect to t and also with respect to η .

The radiation damage accumulation rate was assumed to be a 0.5% degradation per day for the large cells and a 1.5% degradation per day for small cells; these values are specific to

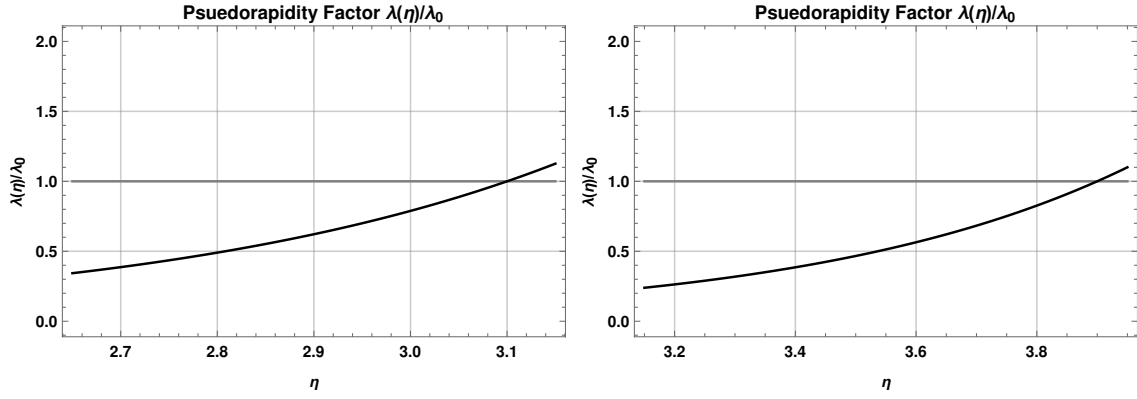


Figure 3.10: Pseudorapidity factor $\lambda(\eta)/\lambda_0$ in equation 3.10 for large cells (left) and small cells (right).

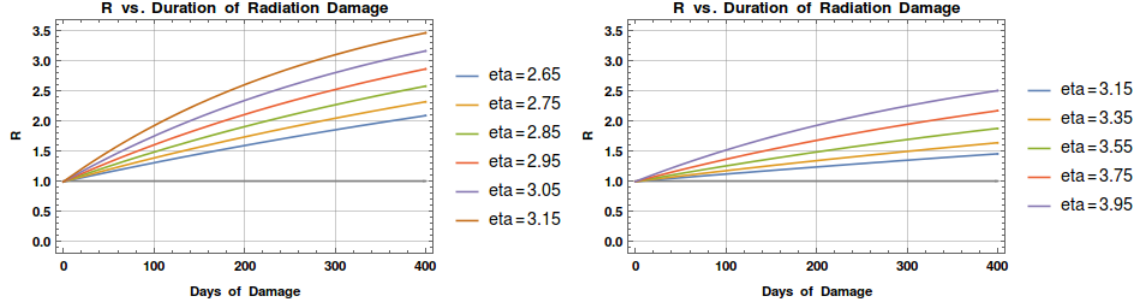


Figure 3.11: Slope factor $R(t)$ in equation 3.9 for large cells (left) and small cells (right), for various values of η

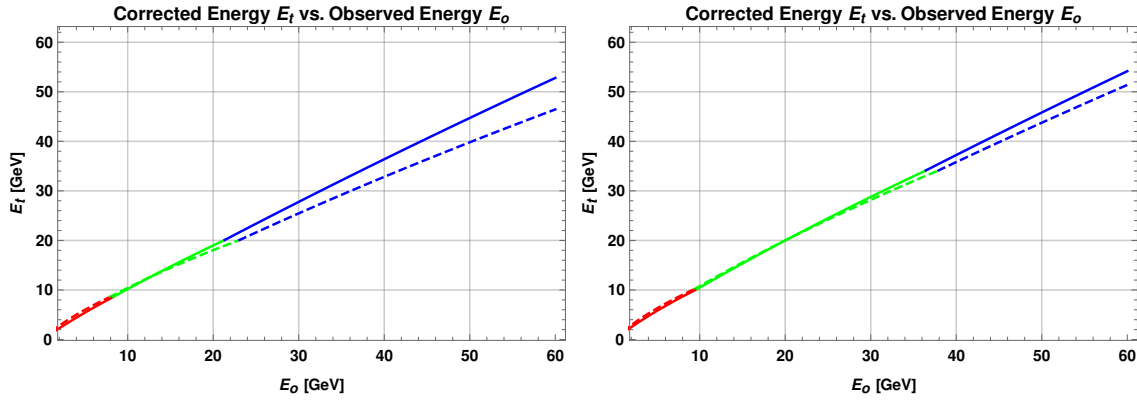


Figure 3.12: Corrected energy E_t , that is, the supposed thrown energy, plotted as a function of observed energy for large cells (left) and small cells (right). Colors red, green, and blue indicate energy regions A , B , and C , respectively. Solid line is day-0 model and dashed line is day-300.

Cells Type	R_∞	R_0	λ_0 [day $^{-1}$]	h_0	h_1
Large Cells	4.46	1.0	0.0028	7.37	2.38
Small Cells	3.44	1.0	0.0022	7.44	1.91

Table 3.3: Values of parameters used in radiation damage extension of $g(E)$ model

Run 15, but it is straightforward to translate a Run 15 day’s worth of radiation damage to a Run 12 or 13 day’s worth. Runs 12 and 13 had approximate delivered luminosities of 4.0 pb $^{-1}$ per day (during the analyzed data period) and Run 15 had about 2.4 pb $^{-1}$ per day. Furthermore, the beam energy for Run 15 was 100 GeV, whereas that for Runs 12 and 13 was 255 GeV; the ratio of these beam energies accounts for different amounts of radiation damage delivered per unit luminosity between Runs 12+13 and Run 15. Therefore, one Run 12 or 13 day corresponds to an estimate of (1 Run 12+13 Day) \times (4.0/2.4) \times (255 GeV/100 GeV) = 4.2 Run 15 days’ worth of radiation damage.

Ultimately, the effects of two forms of the nonlinear gain correction are evaluated. Let $g^0(E_t)$ represent the “day-0” model, that is, the state of the $g(E_t)$ before additional radiation damage accumulated. This $g^0(E_t)$ was plotted as the solid line in figure 3.9 (and since $t = 0$, it does not depend on η). A model after D days’ worth of radiation damage was also considered, called the “day- D ” model and denoted $g^D(E_t)$. For each run in the $A_{LL}^{\pi^0}$ data set, D was set to the number of days of running after the beginning of Run 12, times the aforementioned 4.2 Run 15 days per Run 12+13 day factor; the maximum value of D analyzed was 281. In figure 3.9, the $g^{300}(E_t)$ model is plotted as the dashed line, given the pseudorapidities of 2.9 and 3.5 for the large and small cells, respectively.

3.4.2.3 Application of the Correction

In order to make use of $g(E_t)$, one must obtain $E_t(E_o)$ by solving the quadratic equation $E_o = E_t \cdot g(E_t)$. Letting $I \in \{A, B, C\}$ denote a region, the solution is

$$E_t(E_o) = \frac{1}{2\varepsilon_I} \left[-g_I(0) + \sqrt{4\varepsilon_I E_o + g_I(0)^2} \right] \quad (3.11)$$

and the crossover energy points in E_o -space are $K_o^I = K_t^I \cdot g(K_t^I)$. Figure 3.12 shows the true (thrown) energy as a function of the observed energy, as given in equation 3.11. The fractional difference between the day-0 and day-300 corrected energies can be up to 5%.

In order to assess the impact this gain correction has on π^0 s for the A_{LL} analysis, the

shift in p_T must be measured. The shifted p_T , defined as p_{T_t} , is

$$p_{T_t} = \frac{\sqrt{E_t^2 - M_t^2}}{\cosh \eta} \quad (3.12)$$

where $E_t = E_{1_t}(E_{1_o}) + E_{2_t}(E_{2_o})$ is the corrected total energy and $M_t = M_o/\sqrt{g(E_1)g(E_2)}$ is the corrected mass. The corrected Z is straightforward to compute. Both the corrected η and ϕ are obtained via the sum of the corrected 4-momenta of the photons, but the fractional changes in these values are small.

Given the day-0 and day- D models' corrected p_T values, figures 3.13 and 3.14 respectively show the fractional change in p_T , defined as $\Delta p_T = (p_{T_t} - p_{T_o}) / p_{T_o}$ versus the original p_{T_o} . The day-0 model on average reduces p_T from $\sim 3 - 8\%$ whereas the day- D model reduces it by $\sim 5 - 10\%$.

Outer Region Day-0 Δp_T vs. p_{T_o} **Inner Region Day-0 Δp_T vs. p_{T_o}**

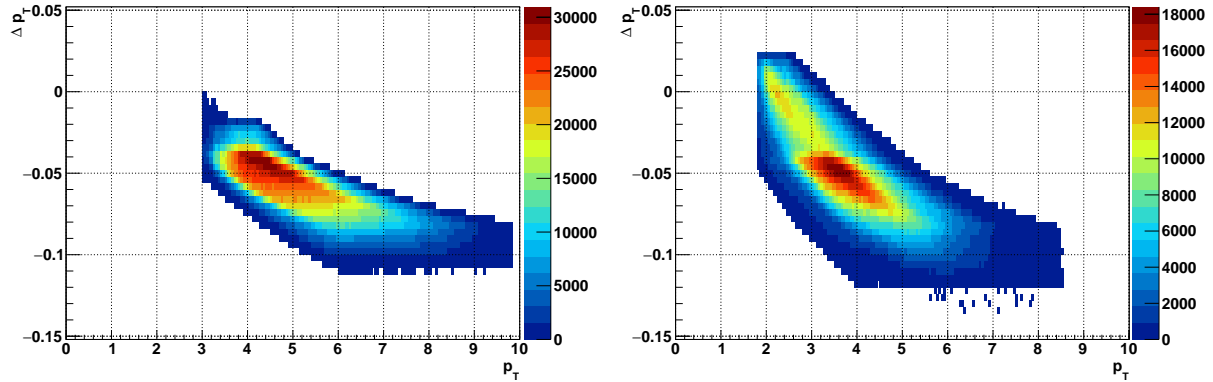


Figure 3.13: Fractional change in p_T (denoted Δp_T) vs p_{T_o} (top) and Δp_T distribution (bottom) for outer region (left) and inner region (right); this is for the day-0 model

Outer Region Day- D Δp_T vs. p_{T_o} **Inner Region Day- D Δp_T vs. p_{T_o}**

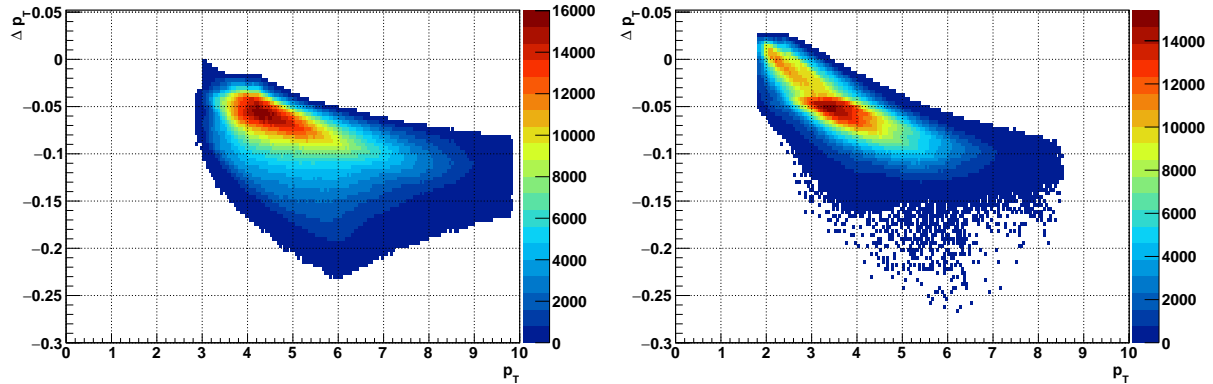


Figure 3.14: Same as figure 3.13, but for day- D

3.5 Hot Tower Masking

After full pion reconstruction was executed, there were some specific, small areas of the FMS geometry (or of kinematics distributions) that had several more events than other regions. Occasionally during the data-taking period, a single PMT gain would change such that it would be dominantly firing the trigger. Such a pathology is called a “hot tower” and during data-taking, monitoring tools enabled detector operators to find and suppress hot towers, but not all could be suppressed in a timely manner. Furthermore, several of the PMTs had time-dependent fluctuations of the voltages, which was the fault of Zener diode failure in the PMT bases due to high temperatures. While the flasher LED system data was sufficient to correct for the time-dependent gain of the PMTs, it was not perfect and still some hot spots remain in the data.

Hot towers primarily appear as sharp peaks in the photon (or pion) position distributions. They can also sometimes appear as single isolated spikes in E , p_T , or even in M distributions. Runs which have a spike in any of these three distributions were excluded from the $A_{LL}^{\pi^0}$ analysis. The majority of all the data, however, have a few such spikes in the photon position distributions, however, and needs a more careful treatment.

Figure 3.15 illustrates the hot spot search algorithm, which takes a photon position distribution (in (x, y) space) and iteratively searches for hot spots; this is done for each runset, which is a set of 5-10 contiguous runs, all of which in the same fill. Some of the hot spot peaks are much higher than others, so the algorithm begins at the highest peak and scans downward. Starting from the highest peak, it is first checked for certain criteria which define a hot spot; if the criteria are satisfied, then this peak is added to the list of hot spots. Whether or not this peak is added to the list of hot spots, it and its small local neighborhood are deleted from the position distribution so that the next highest distribution bin the algorithm finds is not some “foothill” of any peak which was already analyzed. Furthermore, subsequent candidate hot spots must be sufficiently far from any other hot spots already on the list of hot spots.

For each candidate hot spot, defined as the position distribution’s current highest bin, the following metrics are computed:

- i is the number of hot spots added to the list
- H is the number of entries in the hot spot’s tallest bin
- P is the number of entries in a 3 bins \times 3 bins neighborhood centered around the tallest bin; this neighborhood is called the “patch”

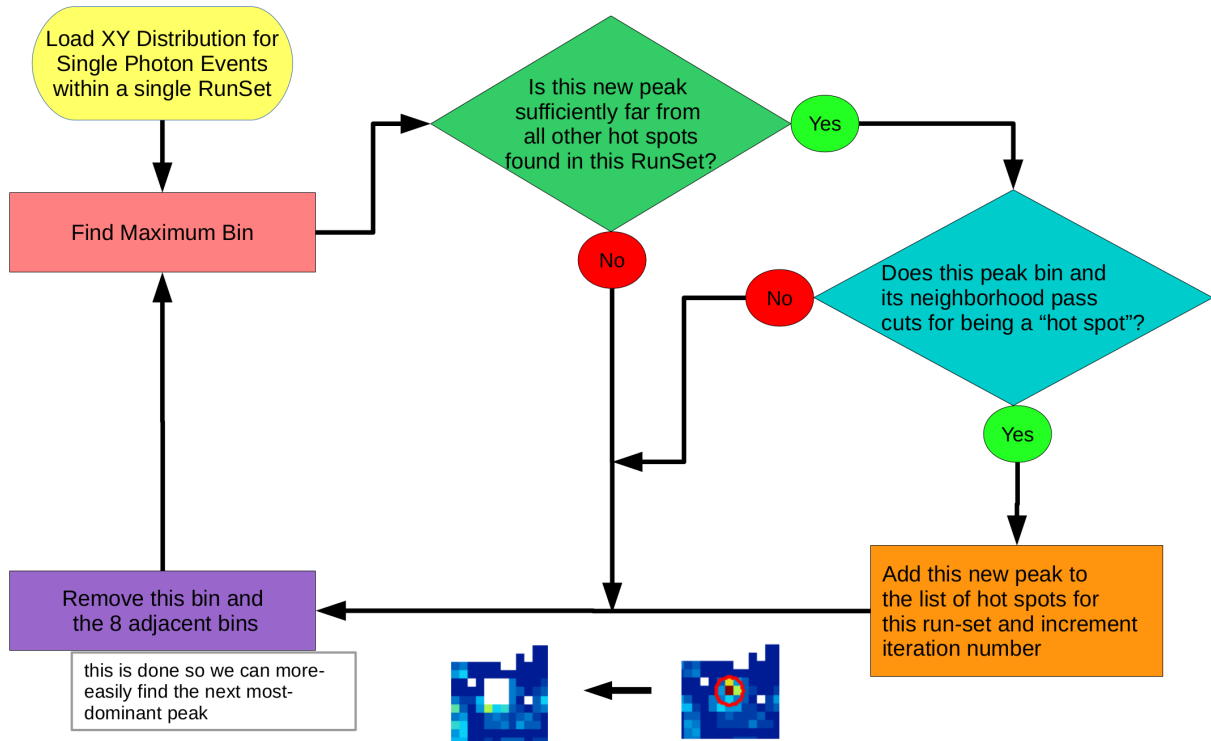


Figure 3.15: Hot spot search algorithm; a sample removal of a hot spot candidate's peak bin and its 8 adjacent bins (*i.e.*, the patch) is shown at the bottom of the figure.

- A is the average number of events over all the nonzero bins in the entire position distribution
- σ_{\max} is the maximum eigenvalue of the moment matrix of the patch and is defined analogously to the σ_{\max} used in single and 2-photon cluster separation (see, for example, [8] or [4]).

Using these metrics, several criteria are defined. First, i should be limited and be no higher than some value i_{\max} , so that only a few hot spots are considered; removing too many causes the algorithm to start identifying local maxima of the usual noise in the position distributions. The sharpness of the peak is roughly given by the ratio of H to P ; if it is too low, then the hot spot candidate peak is rather wide and likely not from a single isolated hot tower. Another characterization of the peak width is given by σ_{\max}^2 and if this value is too high, then the candidate hot spot is too wide; H/P and σ_{\max}^2 are roughly anti-correlated with one-another. Finally, the value of H above the overall distribution average A should be rather high, that is, the peak should be at least $[H/A]_{\min}$ times taller than the distribution average. This last criterion is one which, if satisfied, overrides all the aforementioned criteria; it is rarely satisfied for $i > 5$. The full criterion for a hot spot candidate to be accepted as a hot spot is the boolean

$$(i < i_{\max} \text{ AND } H/P > [H/P]_{\min} \text{ AND } \sigma_{\max}^2 < [\sigma_{\max}^2]_{\max}) \text{ OR } H/A > [H/A]_{\max} \quad (3.13)$$

The values have been tuned to the data and the effects of the algorithm on the hot spot candidate's distributions of σ_{\max}^2 and H/P versus i are shown in figures 3.16-3.18. For all three “data sectors,” defined as Run 12 Outer, Run 12 Inner, and Run 13 Outer, the values used in equation 3.13 are given in table 3.4.

Data Sector	i_{\max}	$[H/P]_{\min}$	$[\sigma_{\max}^2]_{\max}$	$[H/A]_{\min}$
Run 12 Outer	6	0.3	0.8	20
Run 12 Inner	5	0.4	0.8	15
Run 13 Outer	7	0.4	0.7	20

Table 3.4: Values of parameters use to set limits on which hot spots are removed

After a list of hot spots is generated for all runsets in the dataset, a masking algorithm is applied on all candidate π^0 s in the $A_{LL}^{\pi^0}$ analysis. Basically, if either photon which makes the π^0 is too close to a hot tower, its parent π^0 is omitted from the analysis; here “too close” is defined as within a square of side-length $3 \times [\text{cell width}]$ centered around any hot spot. This π^0 masking procedure is summarized in figure 3.19.

Run 12 Outer Region Hot Spot Removal

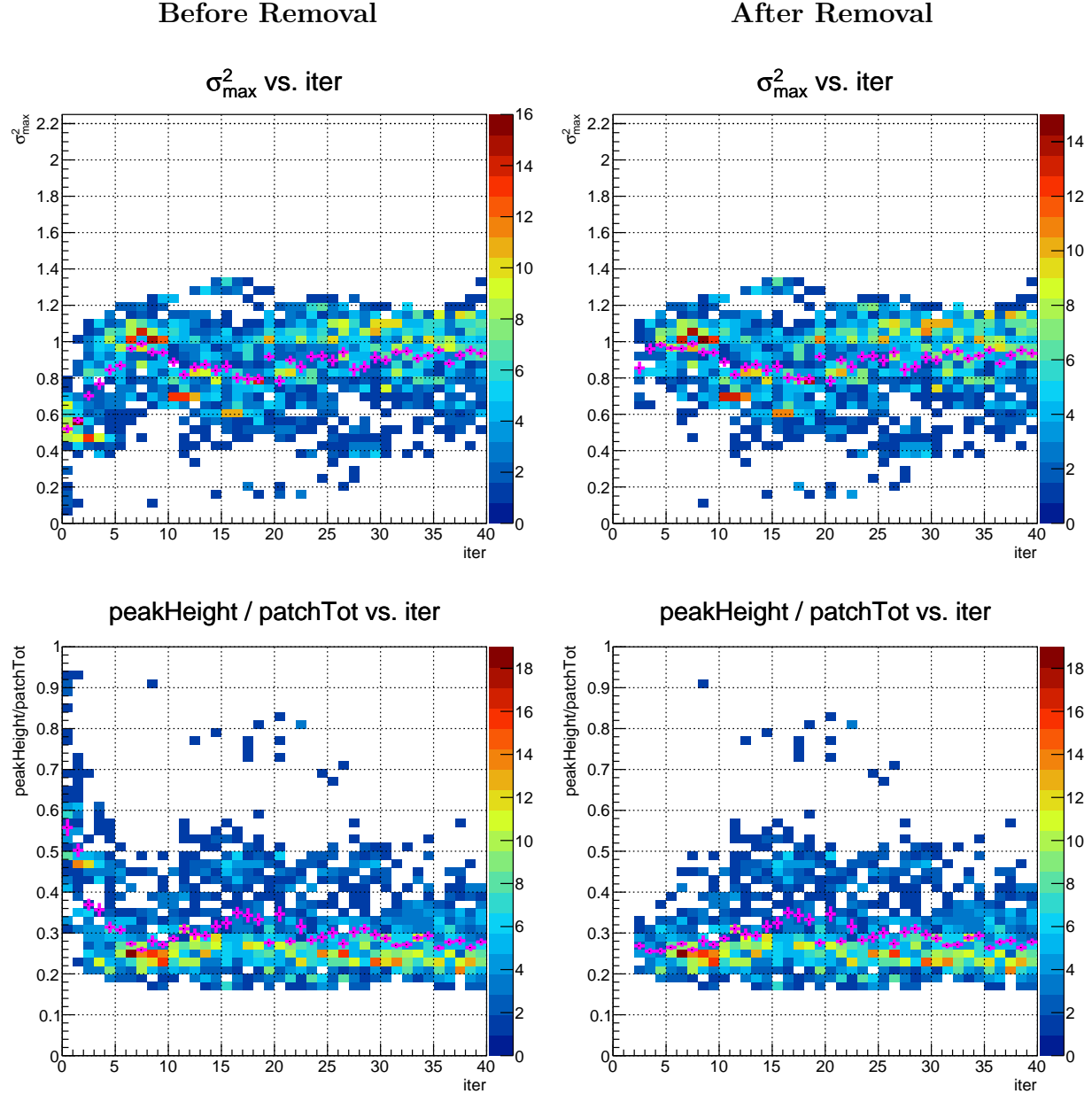


Figure 3.16: For Run 12 outer region, distributions of hot spot candidate σ_{\max}^2 versus i (top) and H/P versus i (bottom) before hot spots are removed (left figures) compared to after hot spot masking (right figures)

Run 12 Inner Region Hot Spot Removal

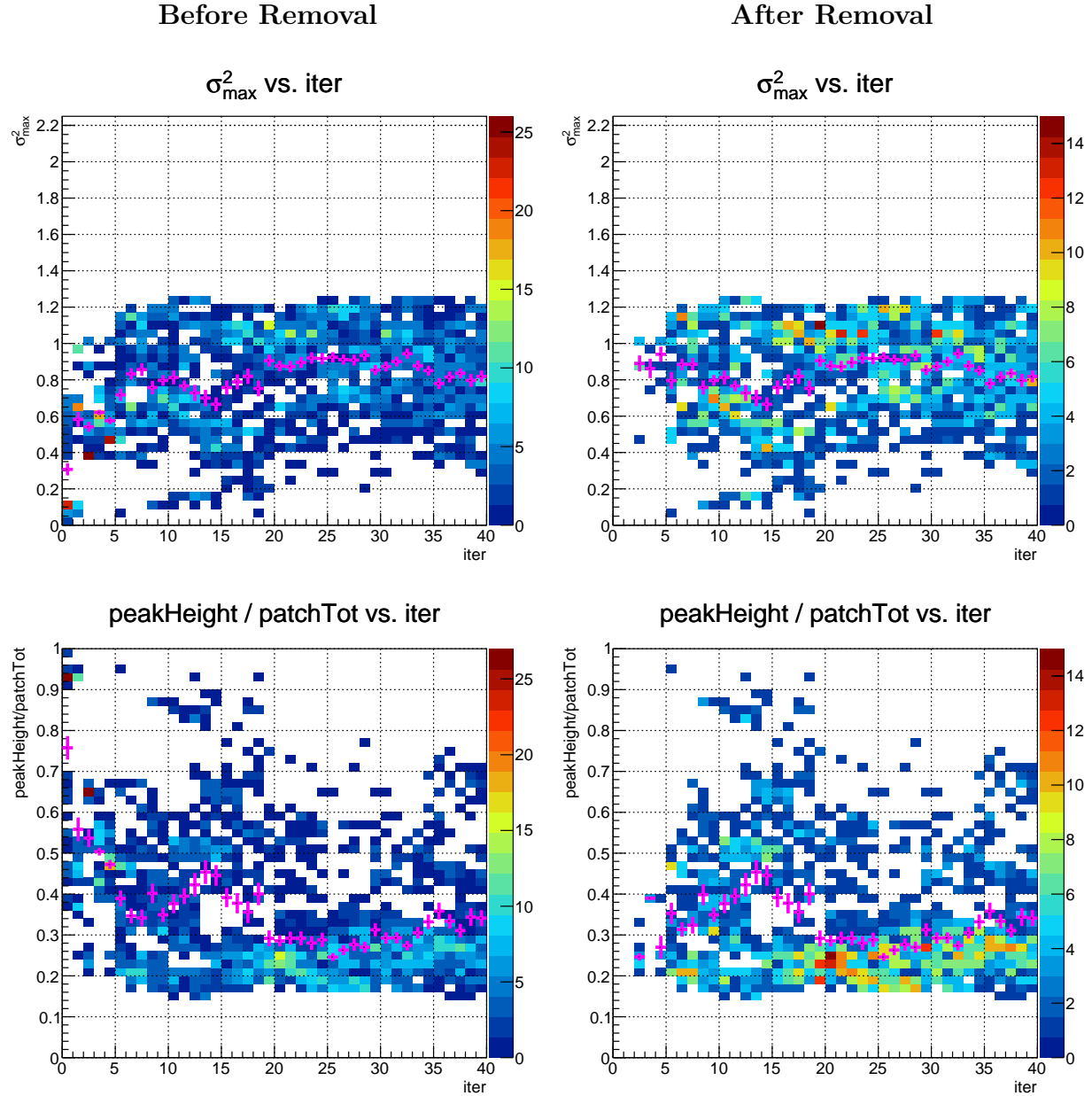


Figure 3.17: For Run 12 inner region, distributions of hot spot candidate σ_{\max}^2 versus i (top) and H/P versus i (bottom) before hot spots are removed (left figures) compared to after hot spot masking (right figures)

Run 13 Outer Region Hot Spot Removal

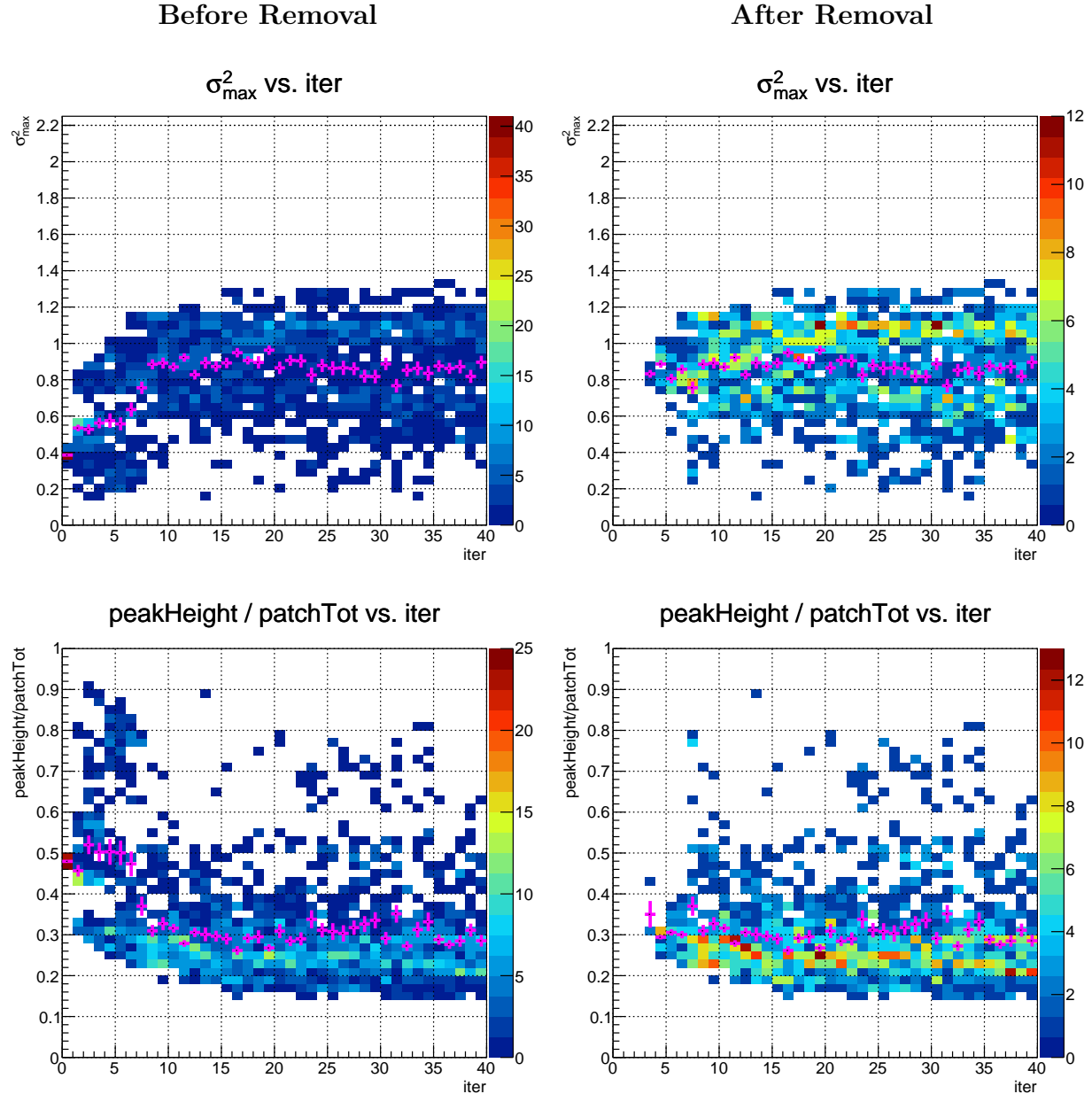


Figure 3.18: For Run 13 outer region, distributions of hot spot candidate σ_{\max}^2 versus i (top) and H/P versus i (bottom) before hot spots are removed (left figures) compared to after hot spot masking (right figures)

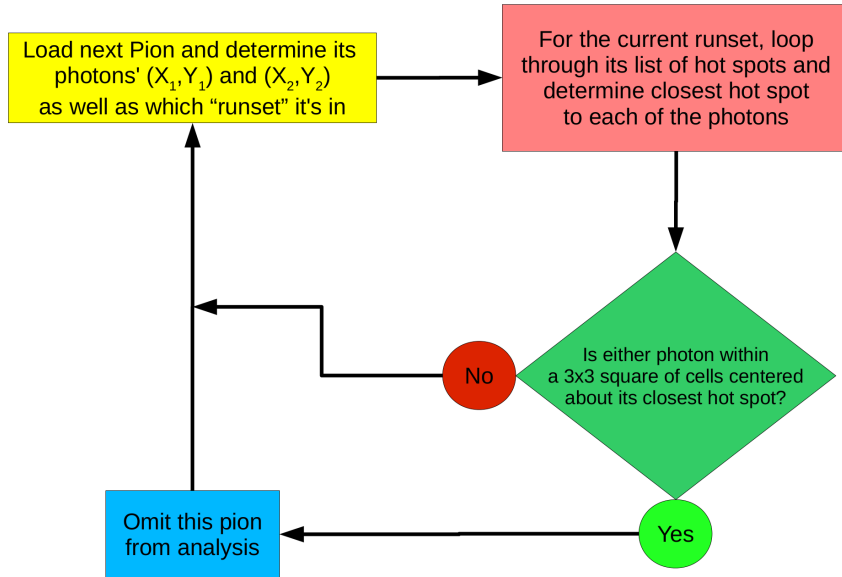


Figure 3.19: Hot spot π^0 -masking algorithm

3.6 Pion Event Selection

3.6.1 Kinematic Cuts

The set of cuts used to identify π^0 s in the $A_{LL}^{\pi^0}$ analysis are:

- Highest energy 2-photon cluster in the event
- Pseudorapidity:
 - Outer Region: $\eta \in [2.65, 3.15]$
 - Inner Region: $\eta \in [3.15, 3.9]$
- Energy:
 - Outer Region: $E \in [30, 70]$ GeV
 - Inner Region: $E \in [30, 100]$ GeV
- Transverse Momentum: p_T greater than time-dependent threshold (details below); the upper limit of p_T is restricted by the lower limit on η and the upper limit on E
 - Outer Region: $p_T \in [p_T^{\text{thresh}}, 9.8]$ GeV
 - Inner Region: $p_T \in [p_T^{\text{thresh}}, 8.6]$ GeV
- Energy Imbalance: $Z \in [0, 0.8]$

- Energy-and-time-dependent Mass Cut (details below)

3.6.2 p_T Threshold Cut

Because of the ever-increasing radiation damage during Runs 12 and 13, several side effects occurred. One of the most noticeable ones in the π^0 kinematics is a slow increase in the overall p_T distribution and threshold. In order to maintain an appropriate lower bound on the π^0 p_T , a time-dependent p_T threshold cut was implemented. Each DAQ run's π^0 p_T distribution was first fit to a Gaussian in order to approximate the rise and fall in p_T just above the nominal threshold. The p_T lower bound was then selected as the p_T value at which the distribution is $2/3$ of the Gaussian fit height, on the low side of the p_T distribution. This algorithm provided a consistent p_T cut for all DAQ runs analyzed.

Figures 3.20-3.22 show p_T distributions on the vertical axis versus DAQ run on the horizontal axis, for all runs analyzed in $A_{LL}^{\pi^0}$; each DAQ run's distribution is normalized and the runs are plotted in chronological order. The black line indicates the p_T lower cutoff as determined by the fits and the magenta dots indicate the distribution means. Both the distribution means and the p_T lower cutoffs increase as a function of time. Sometimes a step up or down in the distributions is observed, for example in run 12 outer region around run index 100; these steps are indicative of trigger threshold adjustments during the data-taking period.

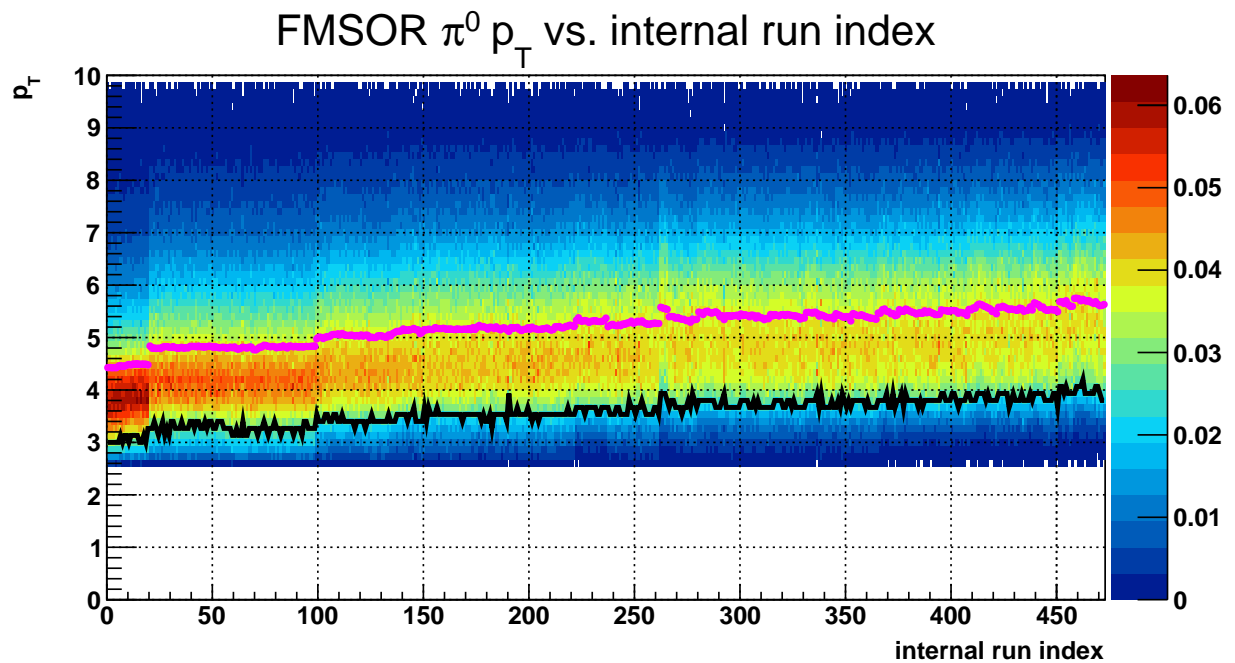


Figure 3.20: $\pi^0 p_T$ normalized distribution vs internal run index for Run 12 outer η region

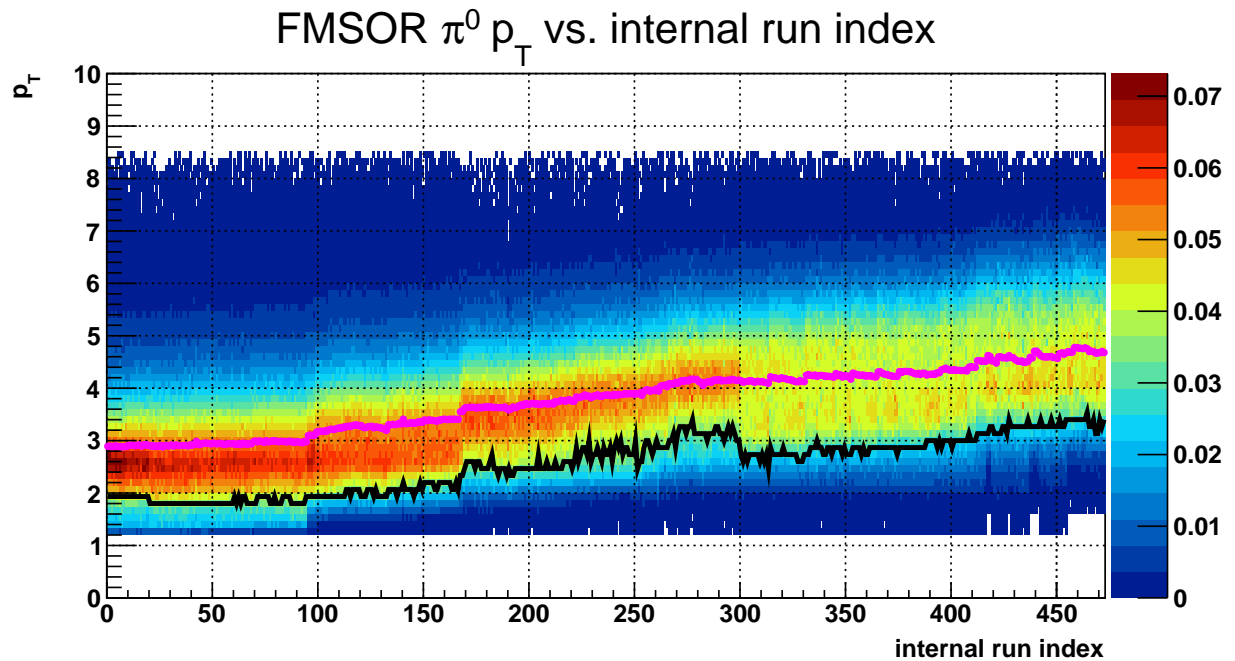


Figure 3.21: $\pi^0 p_T$ normalized distribution vs internal run index for Run 12 inner η region

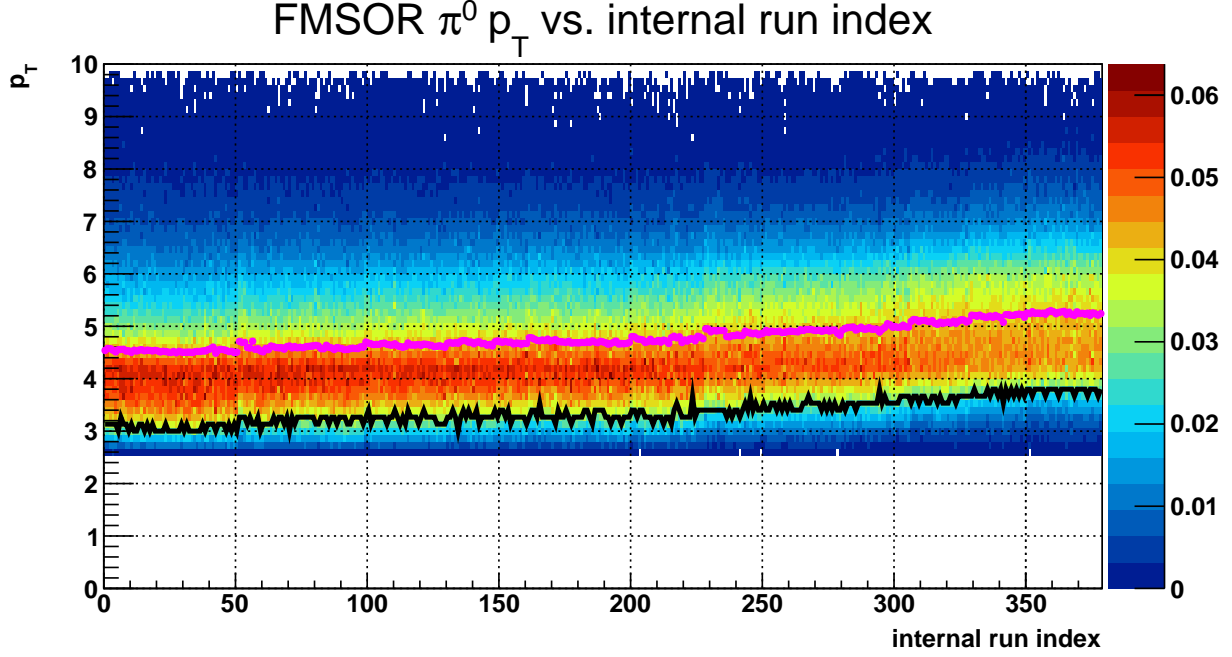


Figure 3.22: $\pi^0 p_T$ normalized distribution vs internal run index for Run 13 outer η region

3.6.3 Mass Cut

Recall that in section 3.3.4 that the source of the energy dependence of the mass is that the fit algorithm for clusters has a tendency to over-estimate the decay photon opening angle, α . Instead of implementing an α -dependent energy correction, the 2-photon sample, which satisfies all π^0 cuts except for the mass cuts, is divided into bins of energy. The invariant mass distribution of 2-photon events within each bin is fit with a skewed Gaussian; this is done on a runset-by-runset basis. The skewed Gaussian is used to determine a value which approximates the π^0 peak maximum, that is, the approximate mode of the mass distribution had it been smoothed; using the fit to determine the peak maximum provides more of a stable maximum than the distribution maximum itself would.

Starting from the maximum of the fit, the lower and upper bounds of the mass window are established by tracing down each side of the skewed Gaussian function until its value is such that the fit function is a fraction f of the value of the distribution maximum; the fraction $f = 0.2$ is used for the lower bound and $f = 0.3$ for the upper bound, for both inner and outer regions. Alternate mass cut determination algorithms were attempted, such as using the fit parameters to determine the skewed Gaussian mean and standard deviation, however, the implemented algorithm provides more of a stable result than other attempts did. The choices of how far one slides on either side were determined empirically and provide a reasonable set of cuts for all E bins, both η regions, for all runsets throughout Runs 12 and

13.

Figures 3.23 and 3.24 show a sample runset's mass distributions for each energy bins, for the outer region and inner region respectively. The energy bins, plotted in order from left-to-right, top-to-bottom, are: [30, 40), [40, 50), [50, 60), [60, 70), [70, 85), [85, 100) GeV, where the last two bins are only plotted for the inner region. The overall mass cuts used in the $A_{LL}^{\pi^0}$ analysis as a function of a chronological runset index is provided in figures 3.25-3.27. The fit maxima are plotted as the points and their error bars represent the full mass window of π^0 's and the energy bins are in order from left-to-right, then top-to-bottom.

A sideband region is also obtained using these mass cuts and the fits. This sideband region is a sample of background events between the π^0 and η -meson mass peaks, which is used to determine a background A_{LL} and later subtracted out of the full $A_{LL}^{\pi^0}$. The upper bound of the π^0 mass window is used as the lower bound of this sideband region. The sideband upper bound is set such that the width of the sideband region is equal to the width of the region between the fit maximum and the π^0 mass window upper bound. Again, these sidebands are defined on a runset-by-runset basis for each E bin.

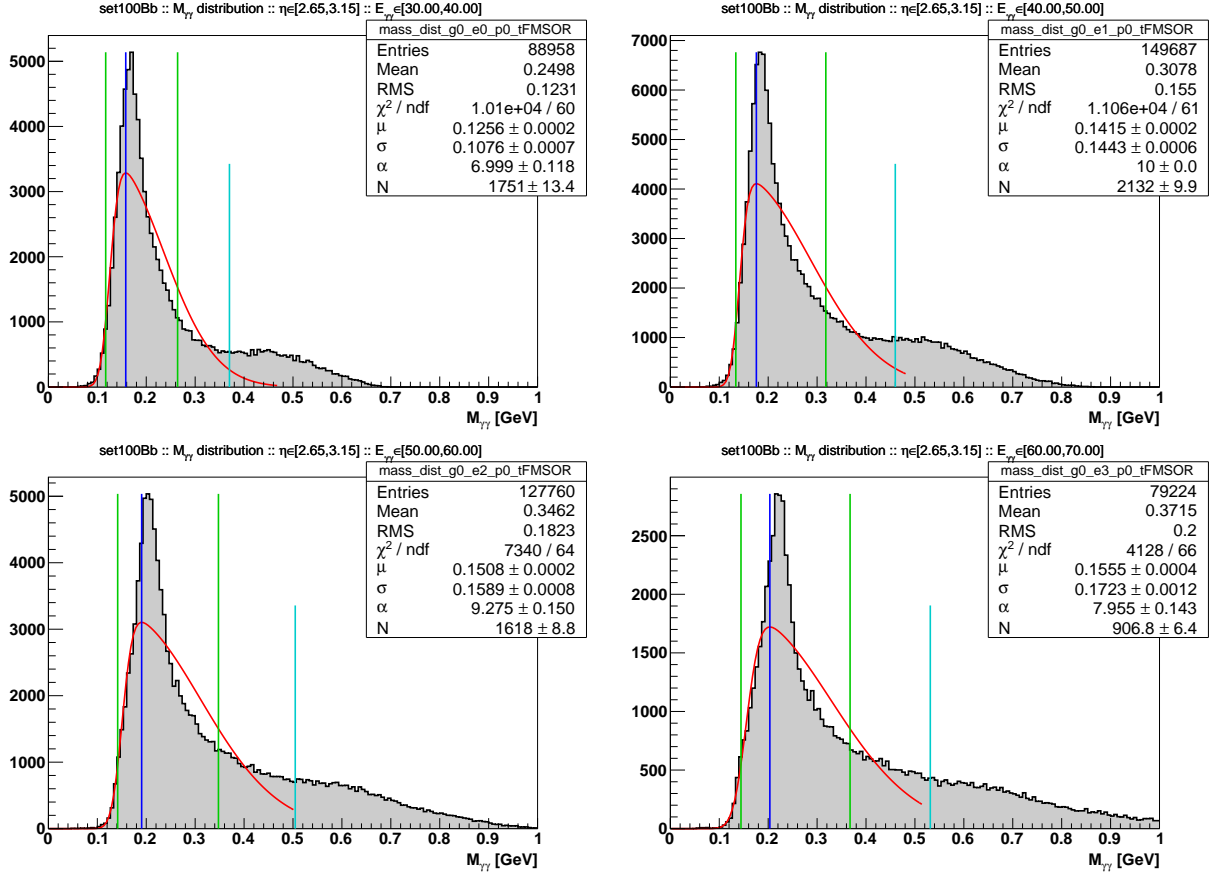


Figure 3.23: Sample 2-photon mass distributions for outer region for various E bins (given in text); tall green lines indicate π^0 mass cuts, in between which is a blue line indicating the distribution maximum as approximated by the fit. The short cyan line is the upper bound of the sideband region.

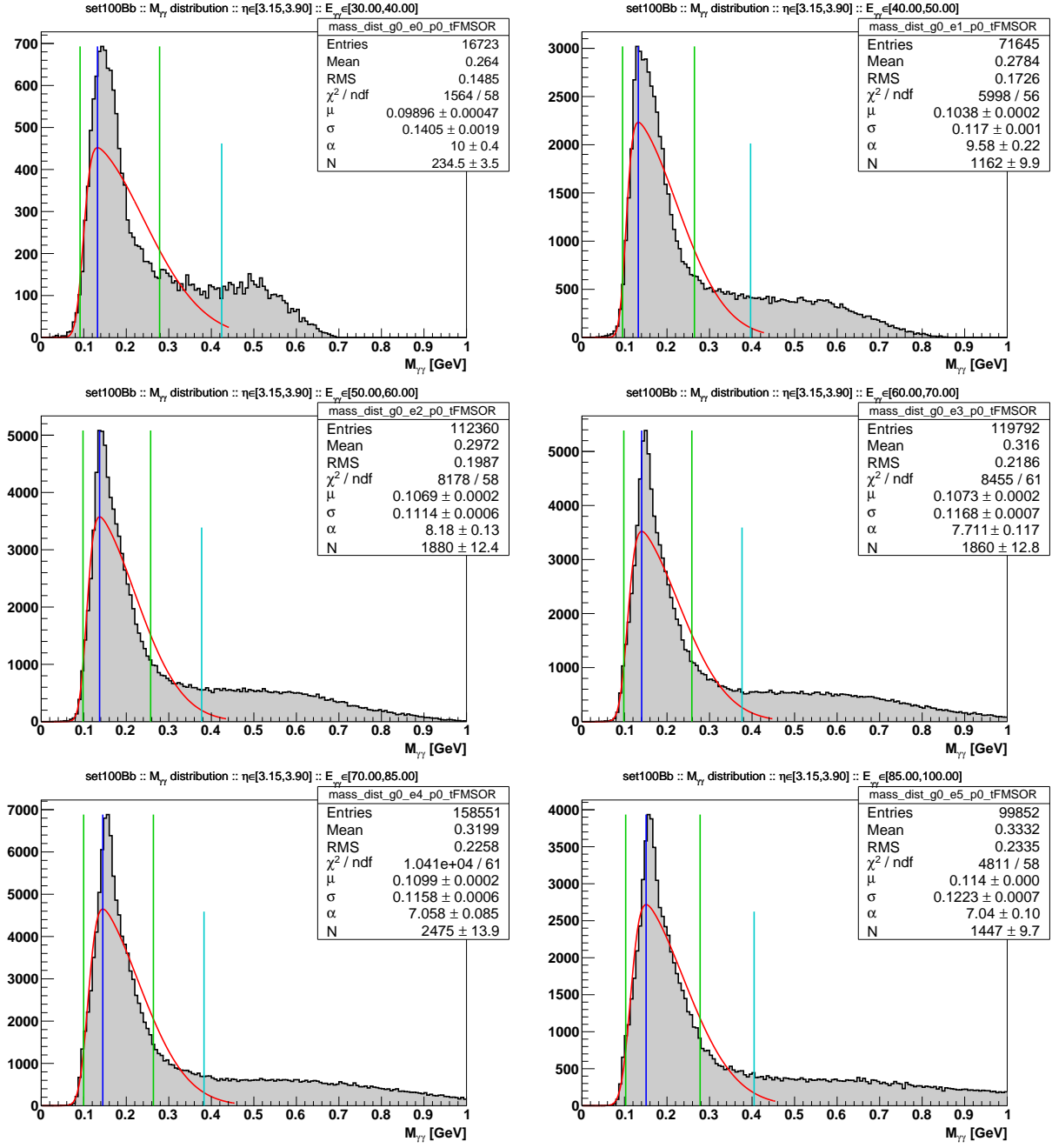


Figure 3.24: Sample 2-photon mass distributions for inner region for various E bins (given in text)

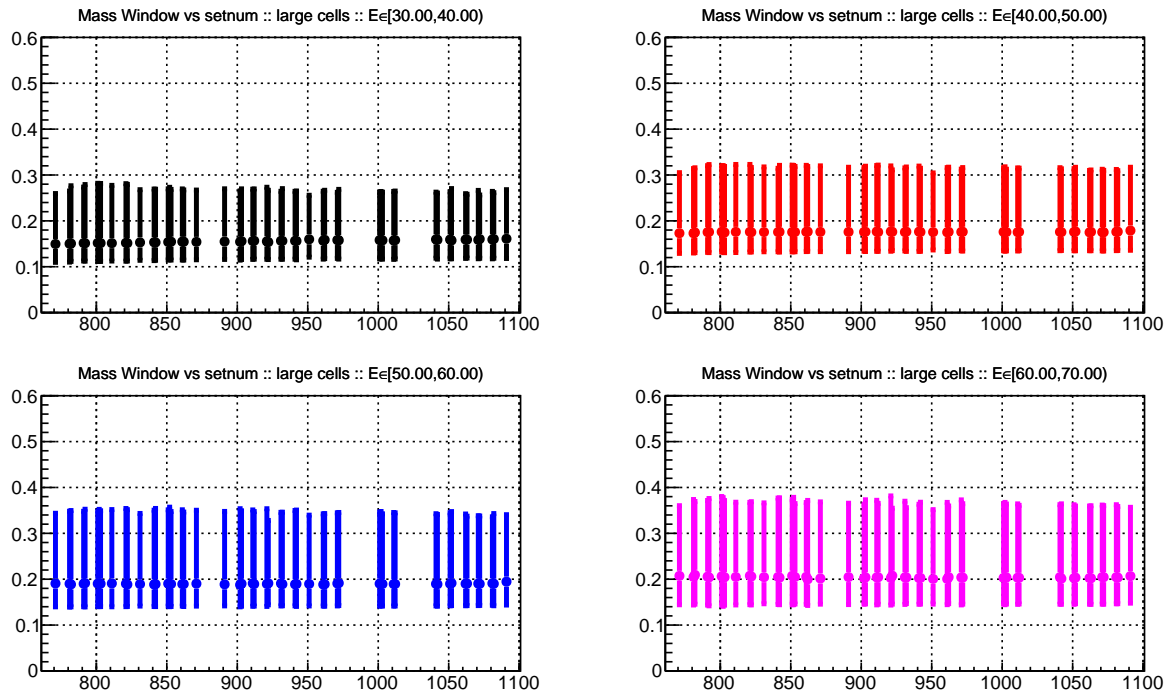


Figure 3.25: π^0 mass windows vs. runset index for Run 12 outer region

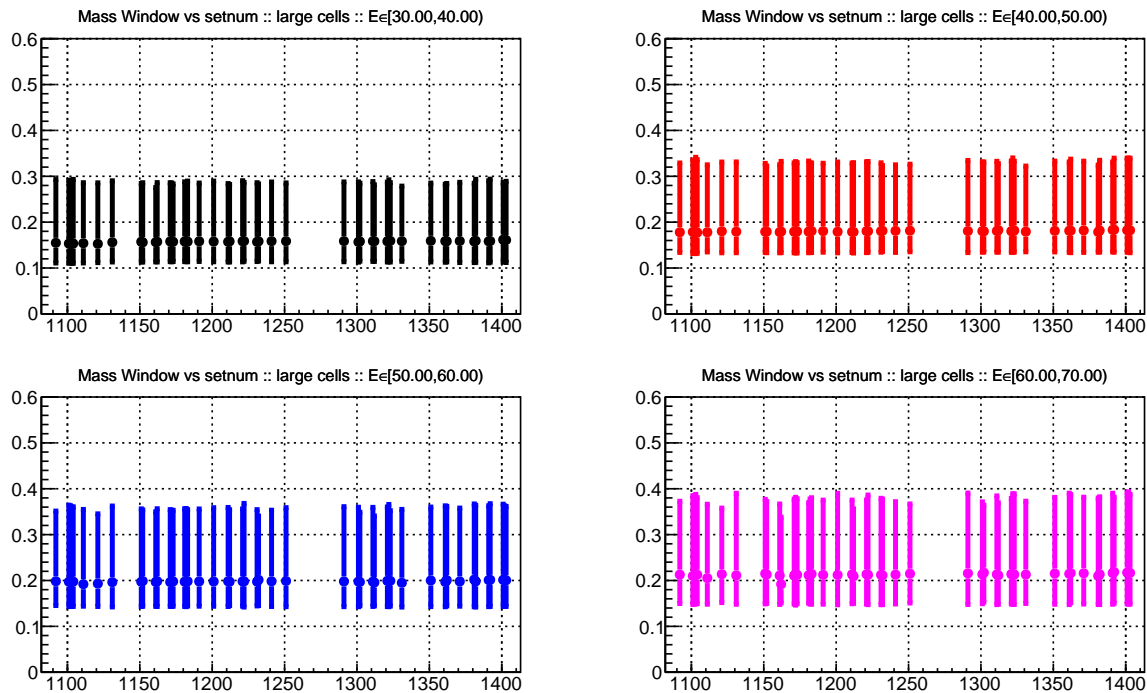


Figure 3.26: π^0 mass windows vs. runset index for Run 13 outer region

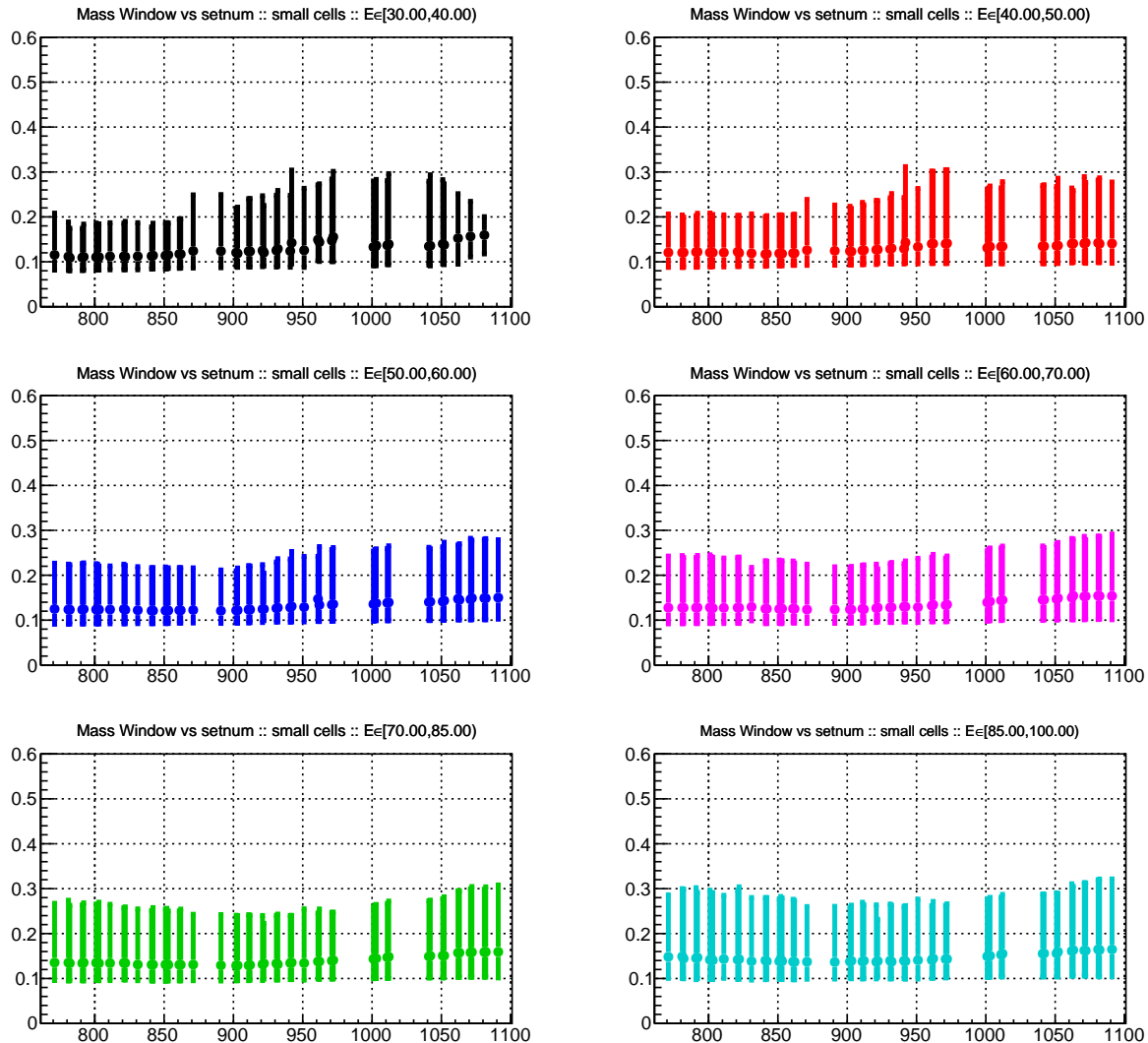


Figure 3.27: π^0 mass windows vs. runset index for Run 12 inner region

3.6.4 Kinematics Distributions

Now that all of the π^0 cuts have been discussed, the resulting π^0 dataset's kinematic distributions are presented. Figure 3.28 shows the $\pi^0 p_T$ vs. E plane. In this plane, bands are visible, which follow lines of constant pseudorapidity. The data in this plot are bounded by two diagonal lines given by the pseudorapidity bounds, a lowest time-dependent p_T threshold minimum, and lower and upper E bounds. The data peaks within a p_T range of $3.5 - 6$ GeV for the outer region and $2.5 - 4.5$ GeV for the inner region.

The position-space distributions of reconstructed π^0 trajectories are plotted in figure 3.29. There are some relatively “warm” areas of the detector, which are small regions which have more than average π^0 hits. These areas have survived the hot tower masking algorithm, which served to remove the worst-case hot towers; removing these warm areas does not meaningfully impact the $A_{LL}^{\pi^0}$ results. In some cases, hot spots persisted for most or all of the $A_{LL}^{\pi^0}$ dataset, and appear as holes in the distributions.

In Run 13, there was a problem with the upper-left quadrant of the detector; figure 3.29 shows that there is much less data there. This was because trigger crate QT3 malfunctioned shortly after the beginning of the data-taking period and was subsequently disabled. For all runs after run number 14113035, data are omitted from the problematic quadrant. Furthermore, $A_{LL}^{\pi^0}$ is not dependent on azimuth and is thus not affected by this data omission.

Figure 3.30 shows the Z -distributions, without the $Z < 0.8$ cut applied. The absolute upper limit on Z is determined by the energy cuts: $Z_{\max} = \left[(E_{\max}^{\pi^0} - E_{\min}^{\gamma}) - E_{\min}^{\gamma} \right] / E_{\max}^{\pi^0}$. In the photon reconstruction algorithm, there is a soft-energy cutoff demanding photon energy be at least $E_{\min}^{\gamma} = 6$ GeV. The values of $E_{\max}^{\pi^0}$ are 70 GeV and 100 GeV for the outer and inner regions, as discussed. Therefore, Z_{\max} is 0.83 for the outer region and 0.88 for the inner region. The $Z < 0.8$ cut impacts the inner region more than the outer region.

Figures 3.31 and 3.32 show the full $A_{LL}^{\pi^0}$ pion p_T distributions as well as the binning used for the $A_{LL}^{\pi^0}$ calculation, indicated by the tall vertical black lines. The $A_{LL}^{\pi^0}$ calculation occurs for four p_T bins over the two η regions, separately, integrating over the other kinematic variables (see section 6.1 for numerical bin boundary values). The p_T binning has been chosen to roughly equalize the pion yields within each bin, rounded to the nearest sensible number. Each bin has a red cross-shaped marker: its horizontal position indicates the p_T bin means and its horizontal extent indicates the bin RMS values. The overall lower bounds are given by the p_T threshold cuts and the overall upper bounds are constrained by kinematics: $p_T^{\max} \approx E_{\max}^{\pi^0} / \cosh \eta_{\min}$. For the outer region, $p_T^{\max} = 9.8$ GeV and for the inner region, 8.6 GeV. The minimum value of p_T allowed by kinematics, $p_T^{\min} \approx E_{\min}^{\pi^0} / \cosh \eta_{\max}$, is below the p_T thresholds over the entire dataset.

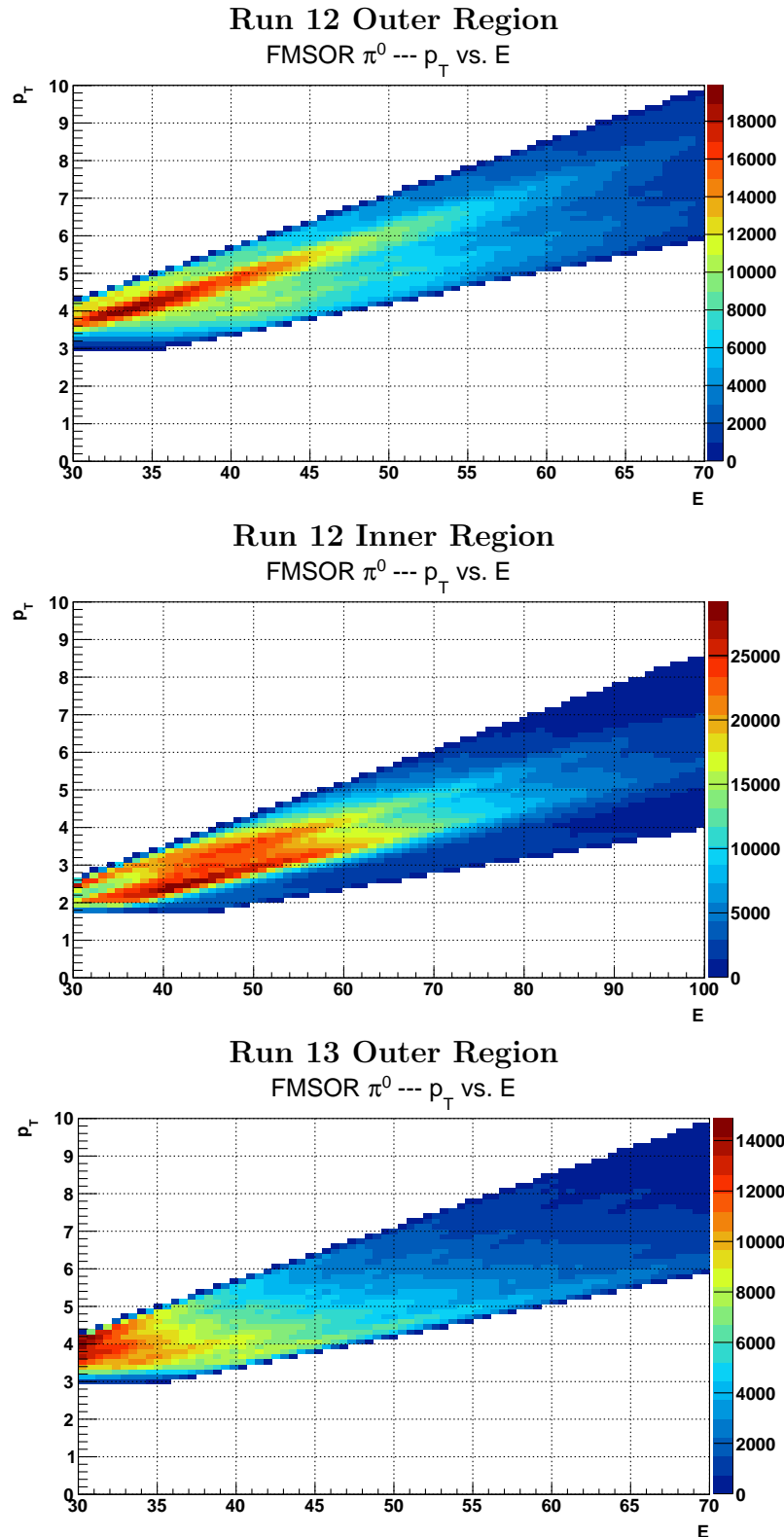


Figure 3.28: $\pi^0 p_T$ vs E for Run 12 outer region (top), Run 12 inner region (middle) and Run 13 outer region (bottom)

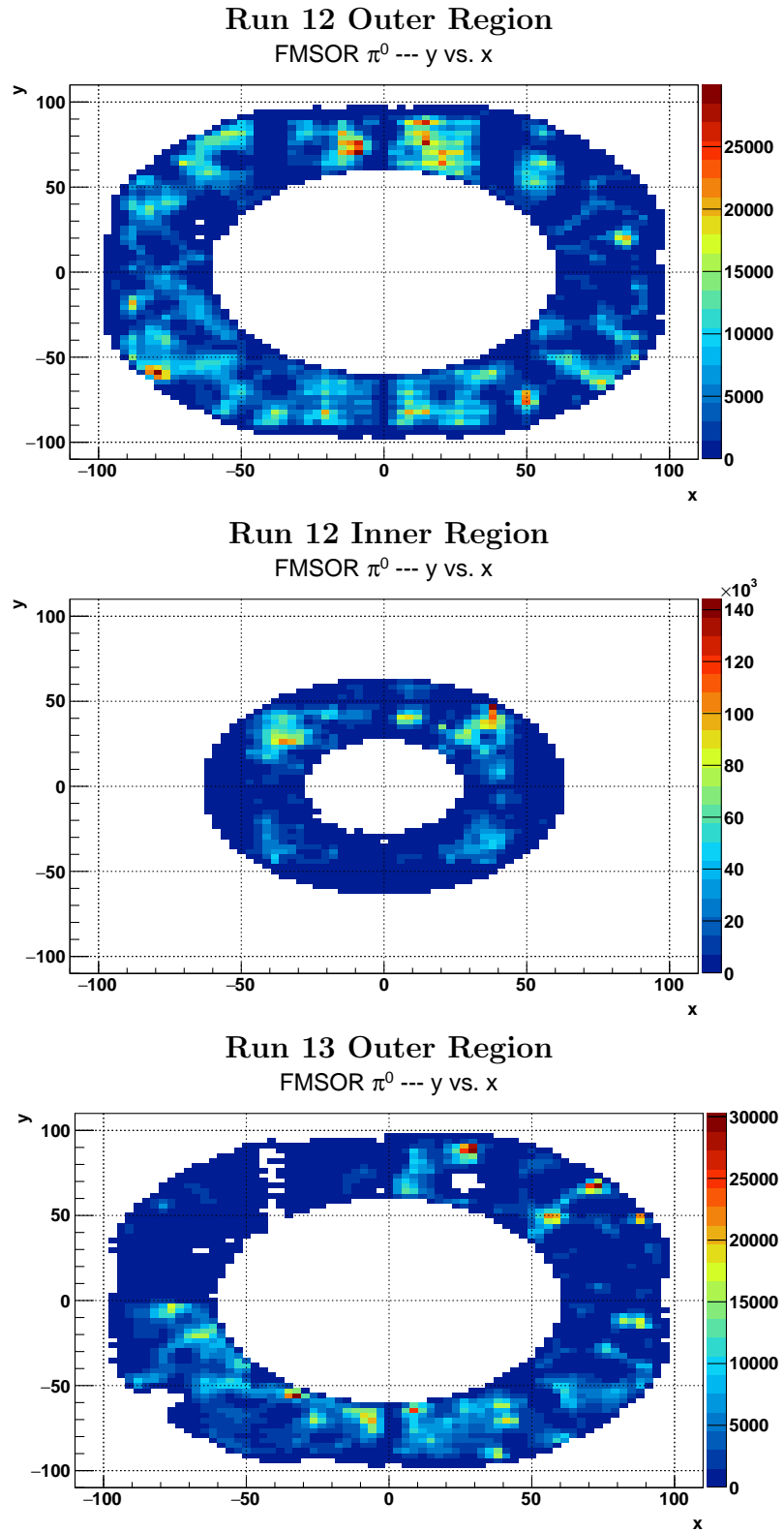


Figure 3.29: π^0 y -position vs x -position for Run 12 outer region (top), Run 12 inner region (middle) and Run 13 outer region (bottom)

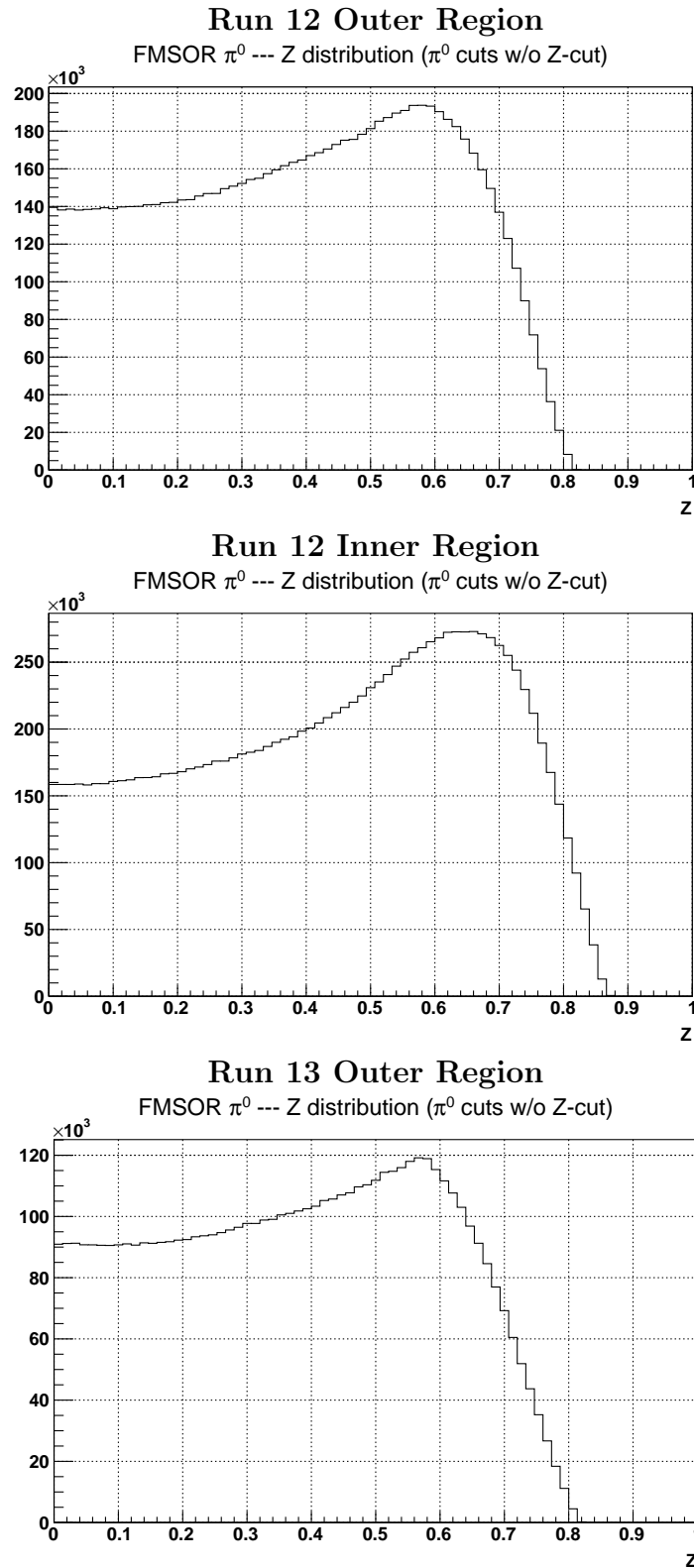


Figure 3.30: π^0 Z distribution ($Z < 0.8$ cut not applied) for Run 12 outer region (top), Run 12 inner region (middle) and Run 13 outer region (bottom)

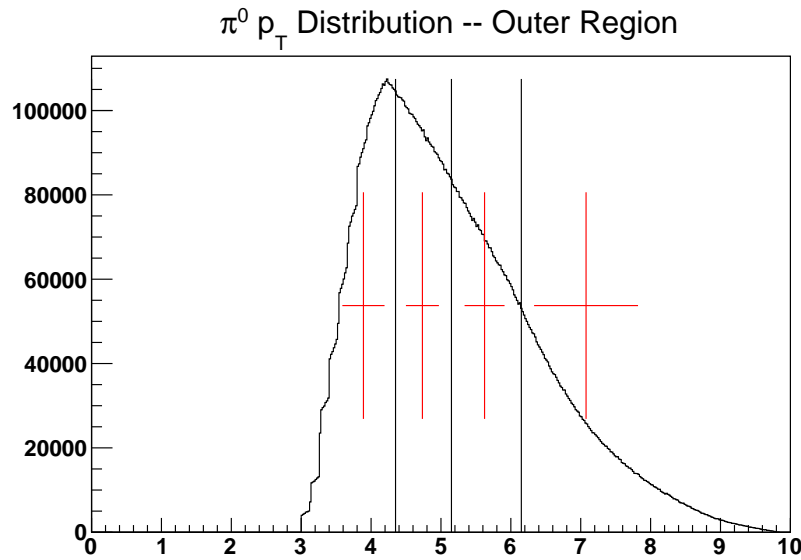


Figure 3.31: $\pi^0 p_T$ distribution for outer region. Tall black lines denote p_T bin boundaries. Horizontal positions of vertical red lines indicate p_T bin means. Lengths of horizontal red lines indicate bin RMS values. Note that this includes both Runs 12 and 13.

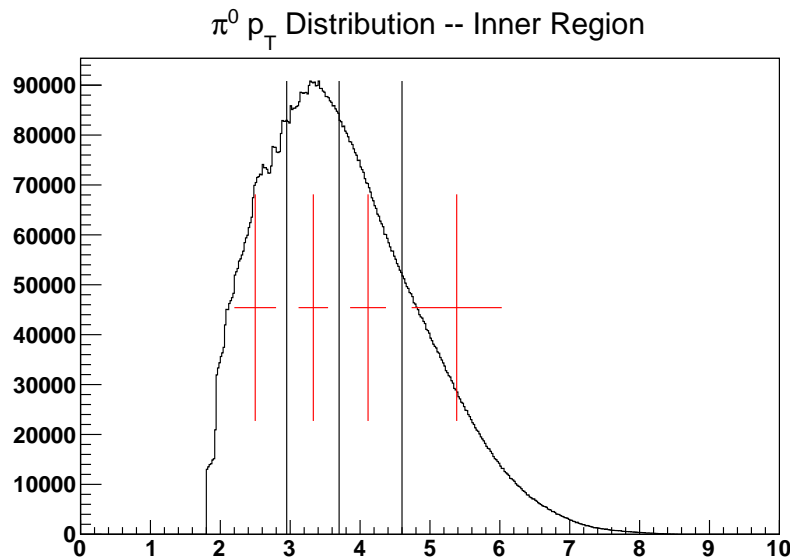


Figure 3.32: $\pi^0 p_T$ distribution for inner region. Note that this is Run 12 only.

Chapter 4

Relative Luminosity

The relative luminosity, as given in equation 1.6, is the ratio of luminosity from same-helicity bunch crossings to that from opposite-helicity bunch crossings:

$$R_3 = \frac{L_{++} + L_{--}}{L_{+-} + L_{-+}}. \quad (4.1)$$

Other relative luminosity ratios may be formed, which correspond to different kinds of asymmetries; see appendix B for the other combinations and associated details. This chapter presents the value of R_3 as well as various diagnostics on its determination and consistency.

Details of this analysis may be found on the following webpages:

- Run 12:

<http://www.star.bnl.gov/protected/spin/dilks/scalers2012/index.html>

- Run 13:

<http://www.star.bnl.gov/protected/spin/dilks/scalers2013/index.html>

4.1 Basic Computation Algorithm

The relative luminosity is typically measured by high-rate “scaler” detectors. At STAR, the scaler detectors are the Beam-Beam Counter (BBC), the Vertex Position Detector (VPD), and the Zero Degree Calorimeter (ZDC). Hits in the scaler detectors, which satisfy certain conditions such as $\text{ADC} > \text{threshold}$, are read out for every bunch crossing via the “scaler boards.” The number of hits for each initial proton helicity combination $h_a h_b$ can then be taken as the values of $L_{h_a h_b}$ in equation 4.1, since other factors such as efficiency and acceptance are cancelled in the ratio of luminosities.

In both Runs 12 and 13, there was a designated “luminosity scaler board” used for such analyses. In Run 12, scaler board number 12 read out 24-bit streams for every bunch crossing, whereas in Run 13, board number 4 read out 32-bit streams. In both Runs, the last 7 bits represented a bunch crossing number with possible values $0 - 127$, where a value of $0 - 119$ represented a STAR bunch crossing. With this bunch crossing numbering, the abort gaps in each beam were cogged at STAR to occupy bunch crossings $31 - 39$ (from yellow beam abort gap) and $111 - 119$ (from blue beam abort gap).

Most of the remaining bits read out in the luminosity scaler boards are true for a single scaler system readout, given certain conditions. Most typically, for each scaler detector, there were two singles bits (one for the east scaler, denoted by e , and one for the west, denoted by w) which fire if the ADC counts are above a threshold, as well as one coincidence bit, denoted by x , which fires if the east and west scaler ADC counts were both above threshold and occurred within a short time window. These three bits were available for all three detector subsystems in both Runs 12 and 13, except for the VPD x bit in Run 13.

The three scaler bits can be considered as one 3-bit unit, a tribit, written as $T = 4x + 2w + e$. In the most ideal setting, only one of four combinations of e, w, x should occur in each bunch crossing for each scaler detector: (1) only e fires, (2) only w fires, (3) all three e, w, x fire (since by definition, x only fires if both e and w fired), or (4) no bits fire. The first three of these tribits are called “logical” bit combinations (the fourth is trivially the zero combination), as opposed to the other four possible tribits, called “illogical” combinations, which should not occur in an ideal setting. An example illogical combination is x firing, but not e or w .

The possible non-zero tribits are given for Runs 12 and 13 in table 4.1. Tribits $T \in \{1, 2, 7\}$ are logical bit combinations, whereas $T \in \{3, 4, 5, 6\}$ are illogical. The seven tribits are then ORed together according to table 4.1 in order to form “raw scale counts” for each scaler detector for east singles, west singles, and coincidences; these raw scale counts are denoted with capital letters: E , W , and X , respectively. These ORs of tribits follow from [9].

Figure 4.1 shows the relative number of scaler bit combinations which fired. More logical tribits occurred than illogocal tribits, except for the case where w and e fired, but not x , which is on the same order as the logical tribits. From now on, only information on the ZDC and VPD will be shown for brevity, as the BBC was noted for having rather inconsistent relative luminosity measurements with high systematic uncertainties.

Run 12 Scaler Bit Combinations

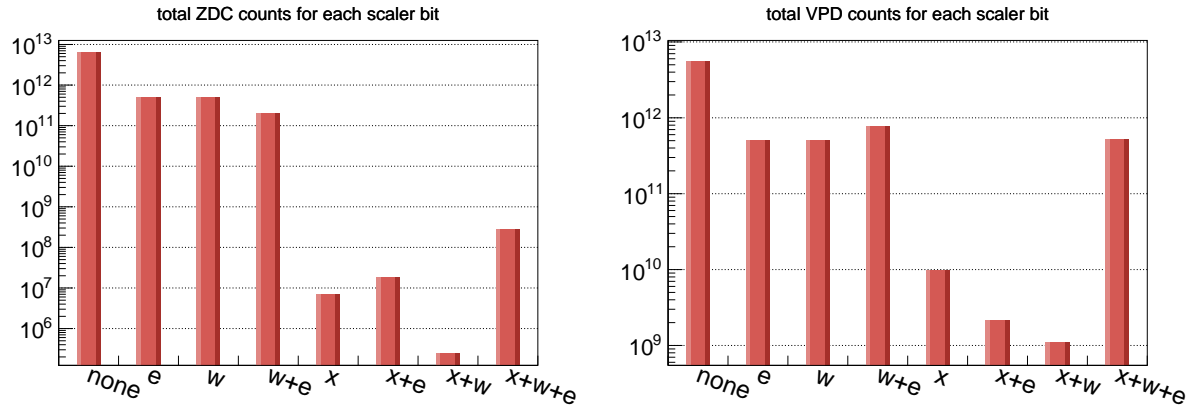
T	x	w	e	BBC			ZDC			VPD		
				E	W	X	E	W	X	E	W	X
1	0	0	1	•			•			•		
2	0	1	0		•			•			•	
7	1	1	1	•	•	•	•	•	•	•	•	•
3	0	1	1	•	•	•	•	•	•	•	•	•
4	1	0	0									
5	1	0	1	•			•			•		
6	1	1	0		•			•			•	

Run 13 Scaler Bit Combinations

T	x	w	e	BBC			ZDC			VPD		
				E	W	X	E	W	X	E	W	X
1	0	0	1	•			•			•		
2	0	1	0		•			•			•	
7	1	1	1	•	•	•	•	•	•	n/a	n/a	n/a
3	0	1	1	•	•	•	•	•	•	•	•	•
4	1	0	0							n/a	n/a	n/a
5	1	0	1	•			•			n/a	n/a	n/a
6	1	1	0		•			•		n/a	n/a	n/a

Table 4.1: Scaler bit recombinations. The left most column “T” is the decimal representation of the 7 combinations of the three scaler bits, x for coincidence, w and e for west and east singles. The logical bit combinations, $T \in \{1, 2, 7\}$, are bits which are expected to fire, *i.e.*, if the x bit fires, the e and w bits are also expected to fire; all other bit combinations are called illogical combinations: $T \in \{3, 4, 5, 6\}$. The E , W and X scale counts are then defined by ORing logical and illogical tribits marked with •’s in each column. Note that in Run 13, there was no VPD x -bit, so for example, VPDE is defined as $T = 1$ OR $T = 3$

Run 12 Scaler Bit Counts



Run 13 Scaler Bit Counts

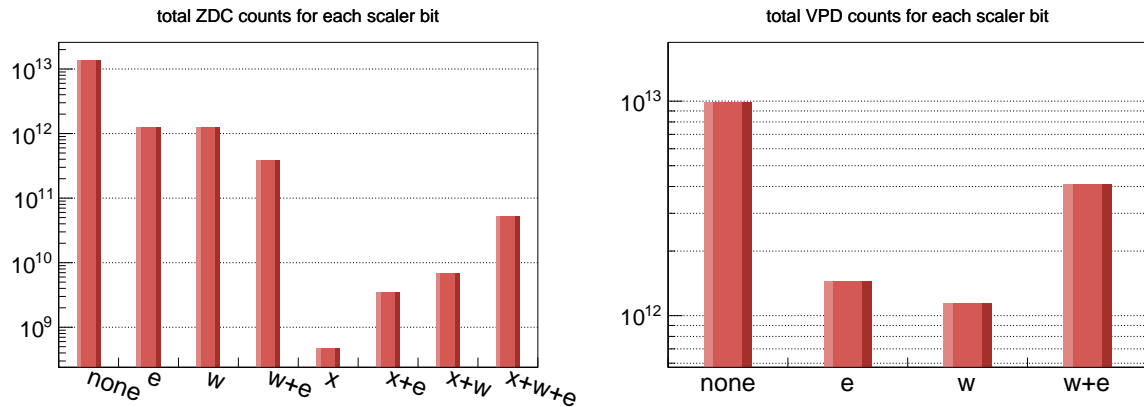


Figure 4.1: Scaler bit counts for ZDC (left) and VPD (right)

4.2 Accidentals and Multiples Corrections

Figure 4.2 shows a schematic of the possible types of interactions which can cause scale counts. The top row shows a normal single event and a normal coincidence event. The bottom row shows a sample of an accidental coincidence of two separate interactions and of an under-counted multiple interaction in one bunch crossing. Given this viewpoint, the combined scaler counts E, W, and X need to be corrected for these cases where there were accidental coincidences and under-countings of multiple interactions in a single bunch crossing. Two forms of the accidentals and multiples corrections are presented in this section: the “CDF corrections,” developed by the Collider Detector at Fermilab (CDF) collaboration [10], and the “rate-safe corrections,” developed by PHENIX [11].

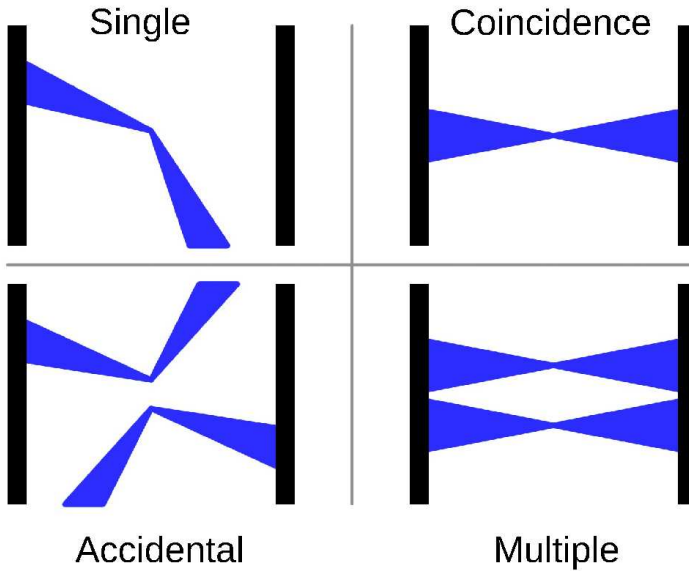


Figure 4.2: Types of events seen in scalers, showing the form of accidental coincidences and multiple interactions, to be corrected for in analysis. The vertical black lines represent scaler detectors (one for east and another for west) and the blue cones represent scaler count-producing particle trajectories.

4.2.1 CDF Accidentals Correction

The CDF corrections are implemented by considering event probabilities. Let \mathcal{P}_S denote the physical probability of an event which should fire scaler bit combination $S \in \{E, W, X\}$. Let P_S be the “scale probability” of scaler S , *i.e.*, the probability that S actually fires. Note that $P_S = N_S/N_{bx}$, where N_S is the number of times S fired and N_{bx} is the total number of bunch crossings. Note that N_S is a *raw* scale count, as opposed to a *corrected* scale count.

For the following argument, refer to figure 4.3. The scale probability P_E has contributions from physical probabilities \mathcal{P}_E and from \mathcal{P}_X , but we do not want to include the contribution where E and X would physically occur, that is, we omit the contribution of $\mathcal{P}_E \cap \mathcal{P}_X$ in P_E . Similarly for P_W , we include \mathcal{P}_W and \mathcal{P}_X , omitting $\mathcal{P}_W \cap \mathcal{P}_X$. For the coincidences, P_X naturally includes \mathcal{P}_X as well as the case $\mathcal{P}_E \cap \mathcal{P}_W$, but these two contributions are not disjoint: the case $\mathcal{P}_E \cap \mathcal{P}_W \cap \mathcal{P}_X$ is therefore omitted. In summary, the scale probabilities may be written in terms of the physical process probabilities as:

$$P_E = \mathcal{P}_E \cup \mathcal{P}_X \setminus (\mathcal{P}_E \cap \mathcal{P}_X) \Leftrightarrow \mathcal{P}_E + \mathcal{P}_X - \mathcal{P}_E \cdot \mathcal{P}_X \quad (4.2)$$

$$P_W = \mathcal{P}_W \cup \mathcal{P}_X \setminus (\mathcal{P}_W \cap \mathcal{P}_X) \Leftrightarrow \mathcal{P}_W + \mathcal{P}_X - \mathcal{P}_W \cdot \mathcal{P}_X \quad (4.3)$$

$$P_X = \mathcal{P}_X \cup (\mathcal{P}_E \cap \mathcal{P}_W) \setminus (\mathcal{P}_E \cap \mathcal{P}_W \cap \mathcal{P}_X) \Leftrightarrow \quad (4.4)$$

$$\Leftrightarrow \mathcal{P}_X + \mathcal{P}_E \cdot \mathcal{P}_W - \mathcal{P}_E \cdot \mathcal{P}_W \cdot \mathcal{P}_X$$

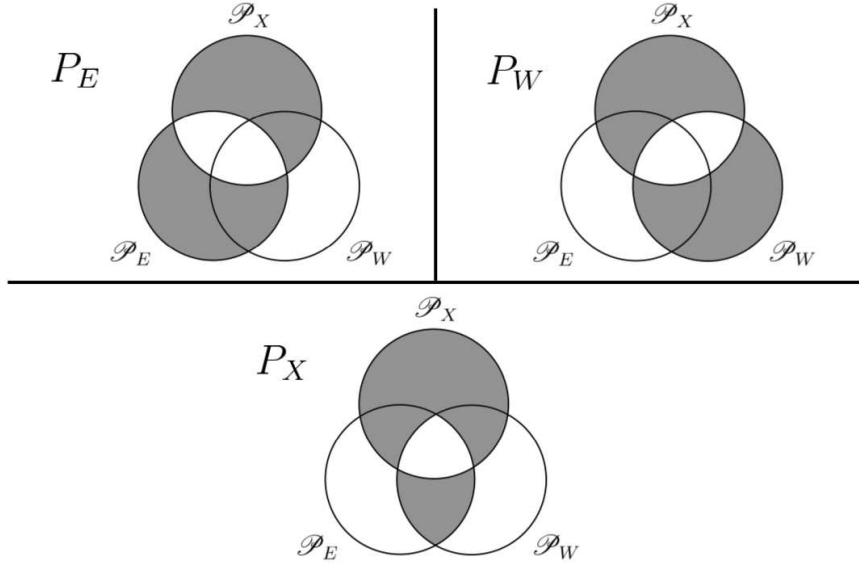


Figure 4.3: Scale probabilities as subsets of the union of physical process probabilities

The physical process probabilities may then be written in terms of the scale probabilities and subsequently in terms of the scale counts as

$$\mathcal{P}_E = \frac{N_E - N_X}{N_{bx} - N_W} \quad (4.5)$$

$$\mathcal{P}_W = \frac{N_W - N_X}{N_{bx} - N_E} \quad (4.6)$$

$$\mathcal{P}_X = \frac{N_X - N_E N_W / N_{bx}}{N_{bx} + N_X - N_E - N_W} \quad (4.7)$$

These are the accidentals-corrected probabilities; multiplying them by N_{bx} gives the accidentals-corrected scale counts.

4.2.2 CDF Multiple Interactions Correction

In order to correct for multiple interactions in a bunch crossing, the distribution of k interactions per bunch crossing, given λ as the “true” number of interactions in a bunch crossing, is modelled as a Poisson distribution:

$$\mathcal{P}(\lambda, k) = \frac{e^{-\lambda} \lambda^k}{k!} \quad (4.8)$$

The Poisson distribution is used since the bunch crossings occur at a constant rate and independently of each other. The probability for no interactions in a bunch crossing is

$$\mathcal{P}(\lambda, k = 0) = e^{-\lambda} = 1 - \mathcal{P}(\lambda, k \neq 0) \quad (4.9)$$

Assuming that $\mathcal{P}(\lambda, k \neq 0)$ represents the accidentals-corrected probabilities in equations 4.5-4.7, which are independent of λ , the probability of no interactions provides access to the “true” number of interactions per bunch crossing:

$$\lambda = -\ln [1 - \mathcal{P}(k \neq 0)] \quad (4.10)$$

The final CDF correction equations, which give the accidentals and multiples corrected counts \mathcal{N}_S in terms of the raw scale counts N_S , are therefore

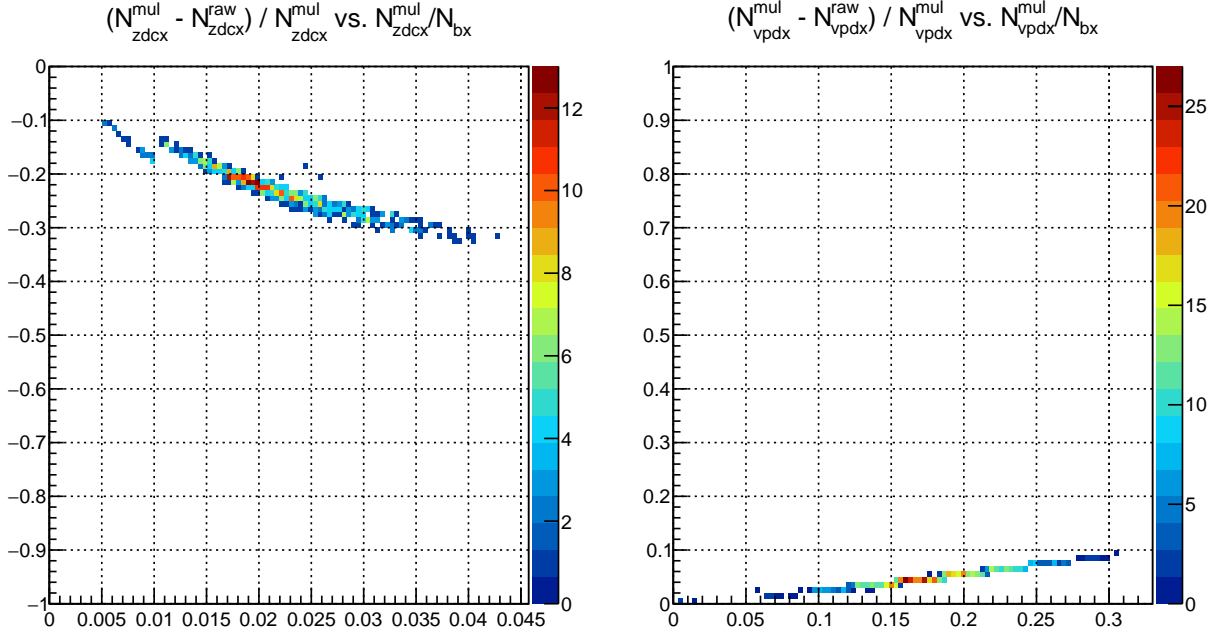
$$\mathcal{N}_E = -N_{bx} \cdot \ln \left(1 - \frac{N_E - N_X}{N_{bx} - N_W} \right) \quad (4.11)$$

$$\mathcal{N}_W = -N_{bx} \cdot \ln \left(1 - \frac{N_W - N_X}{N_{bx} - N_E} \right) \quad (4.12)$$

$$\mathcal{N}_X = -N_{bx} \cdot \ln \left(1 - \frac{N_X - N_E N_W / N_{bx}}{N_{bx} + N_X - N_E - N_W} \right) \quad (4.13)$$

Figure 4.4 shows the fractional deviation of the CDF corrected counts plotted vs. the corrected scale probability for coincidences. In other words, this is a plot of $(N_X^{CDF} - N_X^{raw}) / N_X^{CDF}$ vs. N_X^{CDF} / N_{bx} , where the superscript *CDF* indicates CDF-corrected counts and the superscript *raw* indicates the uncorrected counts. There is a strong dependence of this fractional deviation on the scale probability, which can be interpreted as a dependence of the correction on the rate.

Run 12 CDF Corrections



Run 13 CDF Corrections

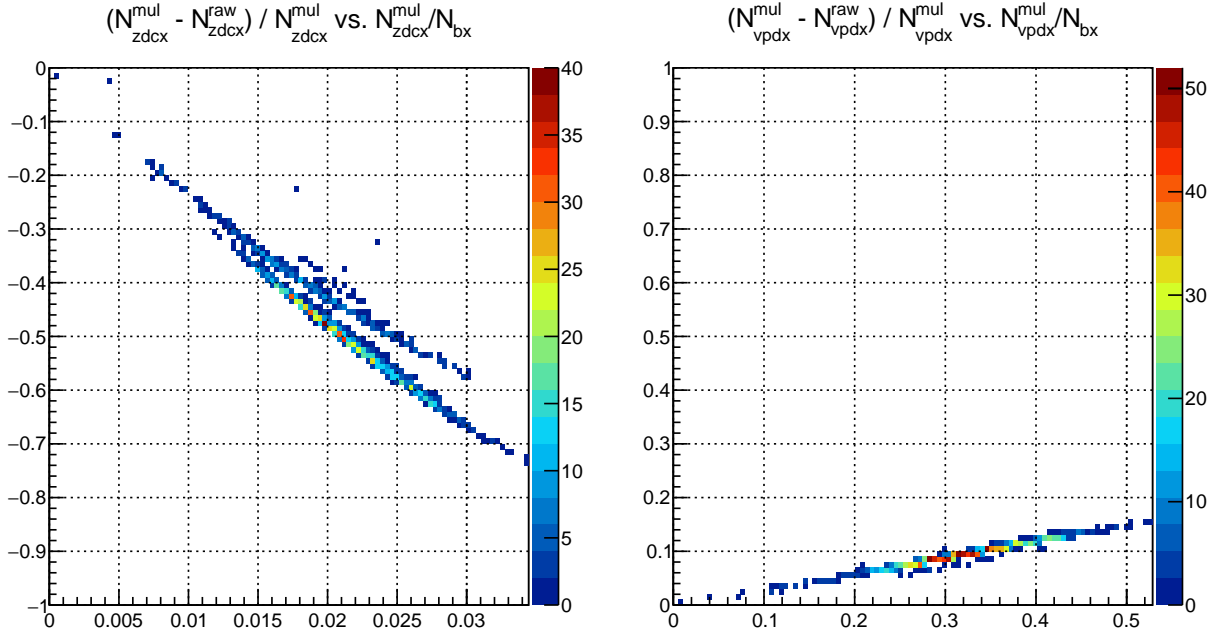


Figure 4.4: Fractional deviation of the CDF corrected counts vs. corrected scale probability for the ZDC (left) and VPD (right). Run 13 shows stronger scale probability dependence than Run 12.

4.2.3 Rate-Safe Accidentals and Multiples Corrections

PHENIX has developed an alternative method for applying scalar counts corrections for accidentals and multiples, called “rate-safe counting” (and sometimes also called the “pile-up correction”). Details may be found in section 4.3 of [11] and the associated analysis note [12]. This section contains a terse description of the method and the final correction equations used; the full derivation has been reproduced in appendix D.

Three “event classes” are considered: east single-sided (ESS), west single-sided (WSS), and double-sided (DS). The average number of times these events occur in a bunch crossing are denoted λ_E , λ_W , and λ , respectively. Each event class has a detection probability of k events, given by a Poisson distribution. These distributions factor in the E and W detector efficiency \times acceptance, denoted by ε_E and ε_W .

One then considers the following three probabilities, in terms of event class probabilities (which are subscripted the event class acronyms):

- Zero hits in E-scaler:

$$P(k_E = 0) = P_{DS}(k_E = 0) \cdot P_{ESS}(k_E = 0) = e^{-\varepsilon_E(\lambda + \lambda_E)} \quad (4.14)$$

- Zero hits in W-scaler:

$$P(k_W = 0) = P_{DS}(k_W = 0) \cdot P_{WSS}(k_W = 0) = e^{-\varepsilon_W(\lambda + \lambda_W)} \quad (4.15)$$

- Zero hits in either detector:

$$\begin{aligned} P(k_E = 0, k_W = 0) &= P_{DS}(k_E = 0, k_W = 0) \cdot P_{ESS}(k_E = 0) \cdot P_{WSS}(k_W = 0) = \\ &= e^{\varepsilon_W \varepsilon_E \lambda - \varepsilon_W \lambda - \varepsilon_E \lambda - \varepsilon_W \lambda_W - \varepsilon_E \lambda_E} \end{aligned} \quad (4.16)$$

These probabilities are combined into one expression by considering the probability that both detectors detect zero hits, given the condition that each of the single-sided detectors each detected zero hits. This probability, denoted P^* , is expressed as

$$P^* = \frac{P(k_E = 0, k_W = 0)}{P(k_E = 0) \cdot P(k_W = 0)} = e^{\Omega \lambda} \quad \text{where } \Omega := \varepsilon_W \varepsilon_E \quad (4.17)$$

Taking the logarithm of each side and writing each probability of detecting zero hits as unity minus the probability of detecting nonzero hits yields

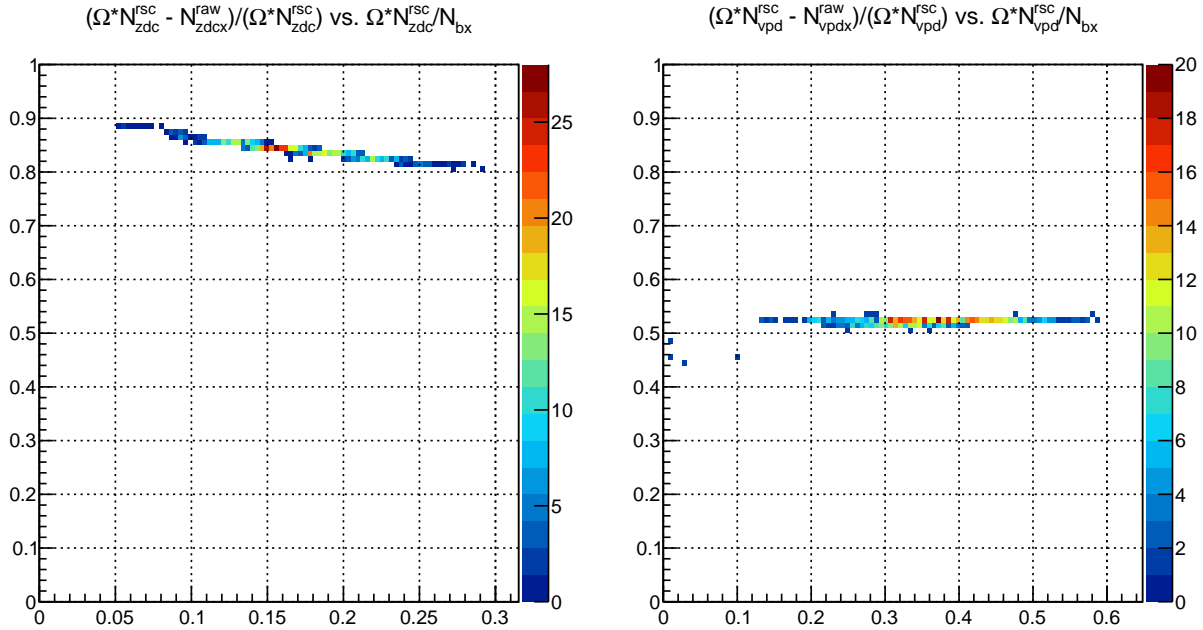
$$\Omega \lambda = \ln P^* = \ln \left[\frac{1 - P_X}{(1 - P_E)(1 - P_W)} \right] \quad (4.18)$$

The probability of detecting a hit can be written as $P_S = \langle N_S \rangle / N_{bx}$, where $S \in \{E, W, X\}$. Finally, the rate-safe corrected counts N_{rsc} (times efficiency and acceptance Ω , which is factored out in any relative luminosity computation), is written as

$$\Omega N_{rsc} = N_{bx} \cdot \ln \left[\frac{1 - \langle N_X \rangle / N_{bx}}{(1 - \langle N_E \rangle / N_{bx}) (1 - \langle N_W \rangle / N_{bx})} \right] \quad (4.19)$$

Figure 4.5 shows the fractional deviation of the rate-safe corrected counts (times efficiency and acceptance) plotted versus the ratio of this corrected number of counts to the number of bunch crossings. Denoting the efficiency times acceptance as Ω , this is a plot of $(\Omega N^{RSC} - N_X^{raw}) / \Omega N^{RSC}$ vs. $\Omega N^{RSC} / N_{bx}$, where the superscript *RSC* is for the rate-safe corrected counts and the superscript *raw* is for the uncorrected number of counts. Comparing this to figure 4.4 and interpreting the horizontal axis as a surrogate for the scale rate, one sees that this correction method depends much less on rate, hence the nomenclature “rate-safe correction method” is appropriate. Note that this comparison assumes that the raw counts in figure 4.5 includes a factor of Ω .

Run 12 Rate-Safe Corrections



Run 13 Rate-Safe Corrections

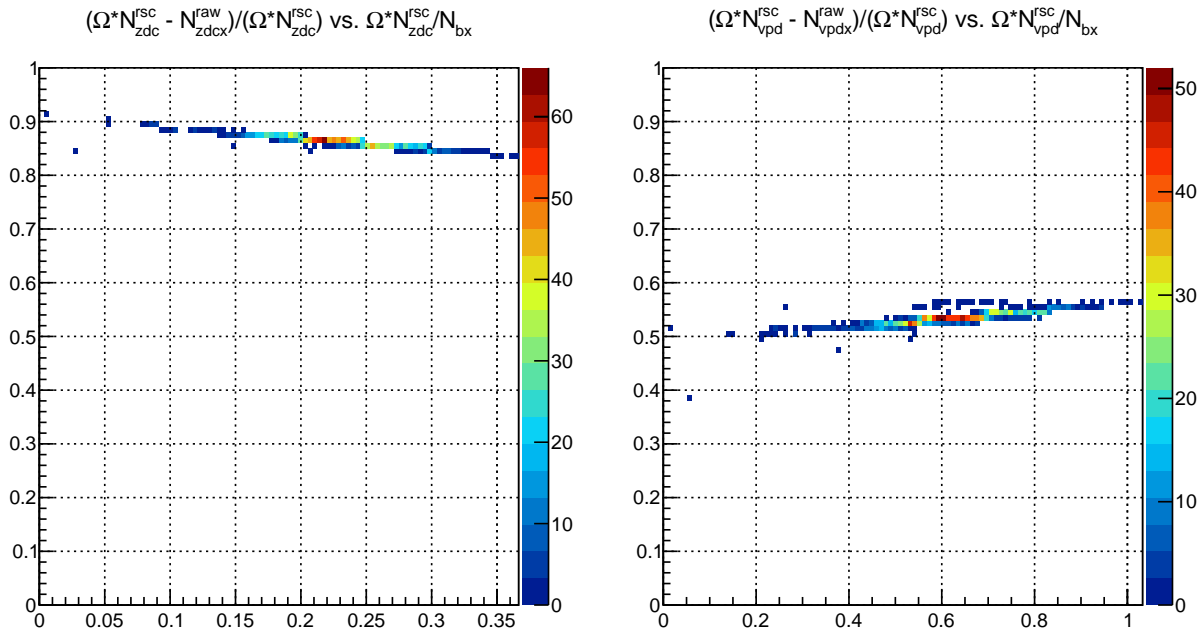


Figure 4.5: Fractional deviation of the rate-safe corrected counts vs. the ratio of the rate-safe counts (times efficiency and acceptance) to the number of bunch crossings for the ZDC (left) and VPD (right). This is a comparison to figure 4.4.

4.3 R_3 Results

Figures 4.6-4.9 show the R_3 values plotted vs. run index for the ZDC and VPD for both Runs 12 and 13. In each figure, four plots are shown. The first three use the CDF corrections equations and are, in order from top to bottom, R_3 for E, for W, and for X. The fourth plot is R_3 computed using the rate-safe corrections method, which makes use of all three E , W , and X raw counts.

The red lines in these figures show a constant fit and the fit results are quoted in the upper-right corner of each figure. The typical relative luminosity fluctuates between $\pm 4\%$ and remains approximately constant within each fill. Fluctuations up and down are from fill-to-fill and are due to the injected spin pattern. In Run 13, the first few fills had bunch crossings 69 – 70 empty, which explains the somewhat higher value of $|1 - R_3|$.

Statistical uncertainty bars are also plotted on these figures, although they are too small to be seen at this scale; the uncertainty is typically $\sim 0.5 - 1 \times 10^{-4}$, where the uncertainty propagation equations are given at the end of appendix D. For the CDF corrections method, the square root of the counts is used for the counts uncertainties; for the rate-safe method, the counts uncertainties are derived in appendix D.

Run 12 ZDC R_3 vs. Run Index

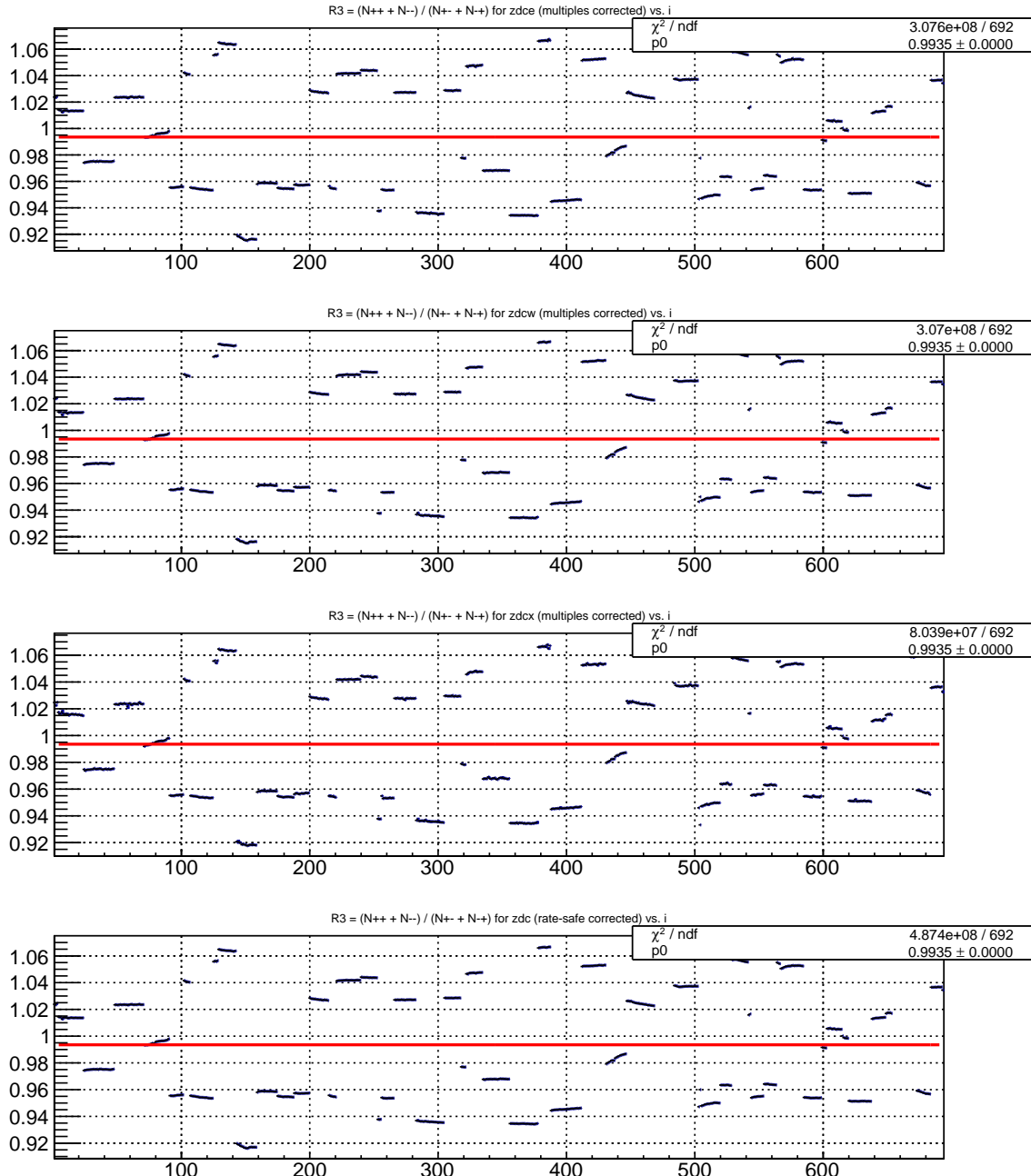


Figure 4.6: R_3 from ZDC for Run 12; from top to bottom: CDF corrected E, CDF corrected W, CDF corrected X, rate-safe corrected

Run 12 VPD R_3 vs. Run Index

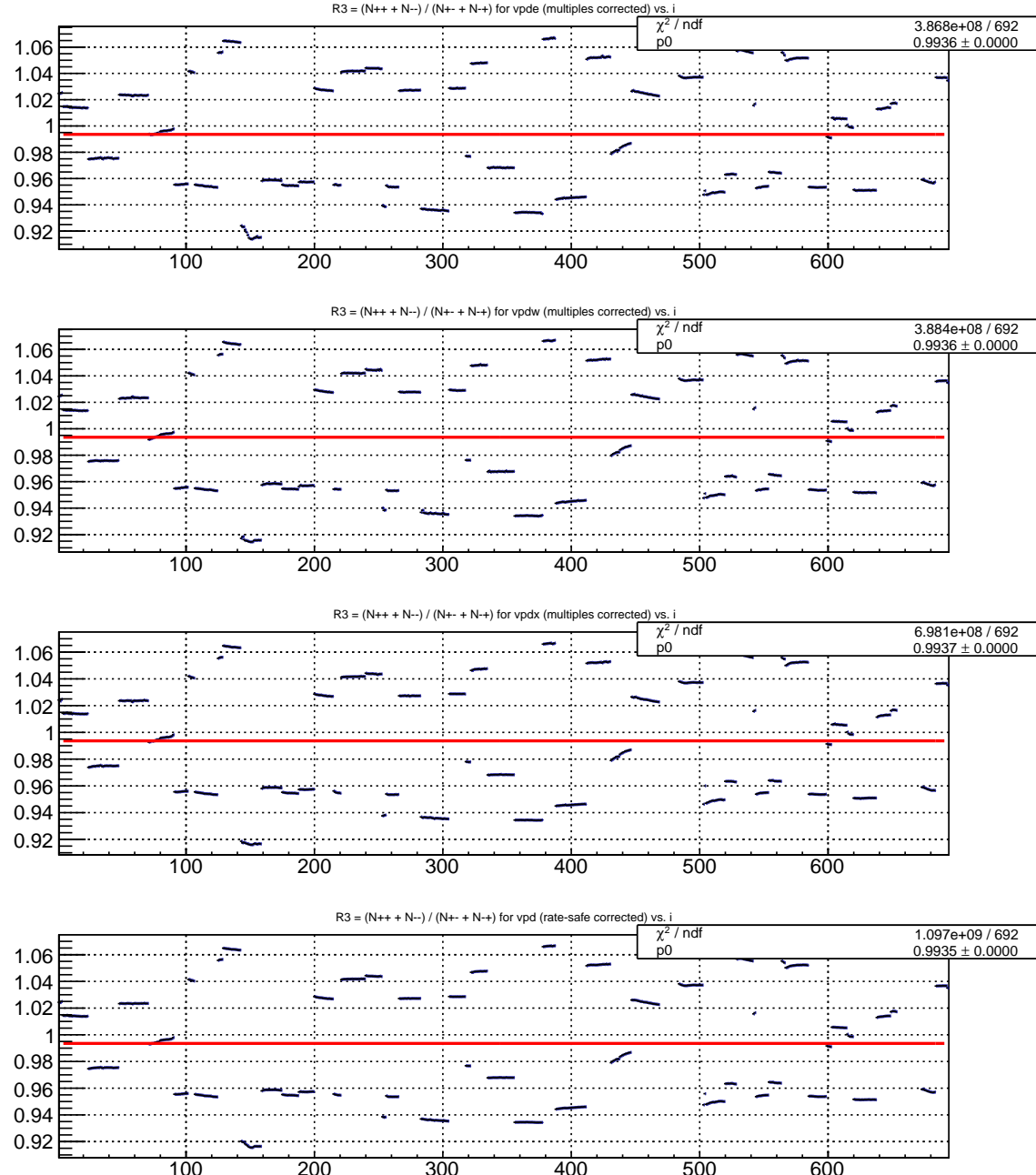


Figure 4.7: R_3 from VPD for Run 12

Run 13 ZDC R_3 vs. Run Index

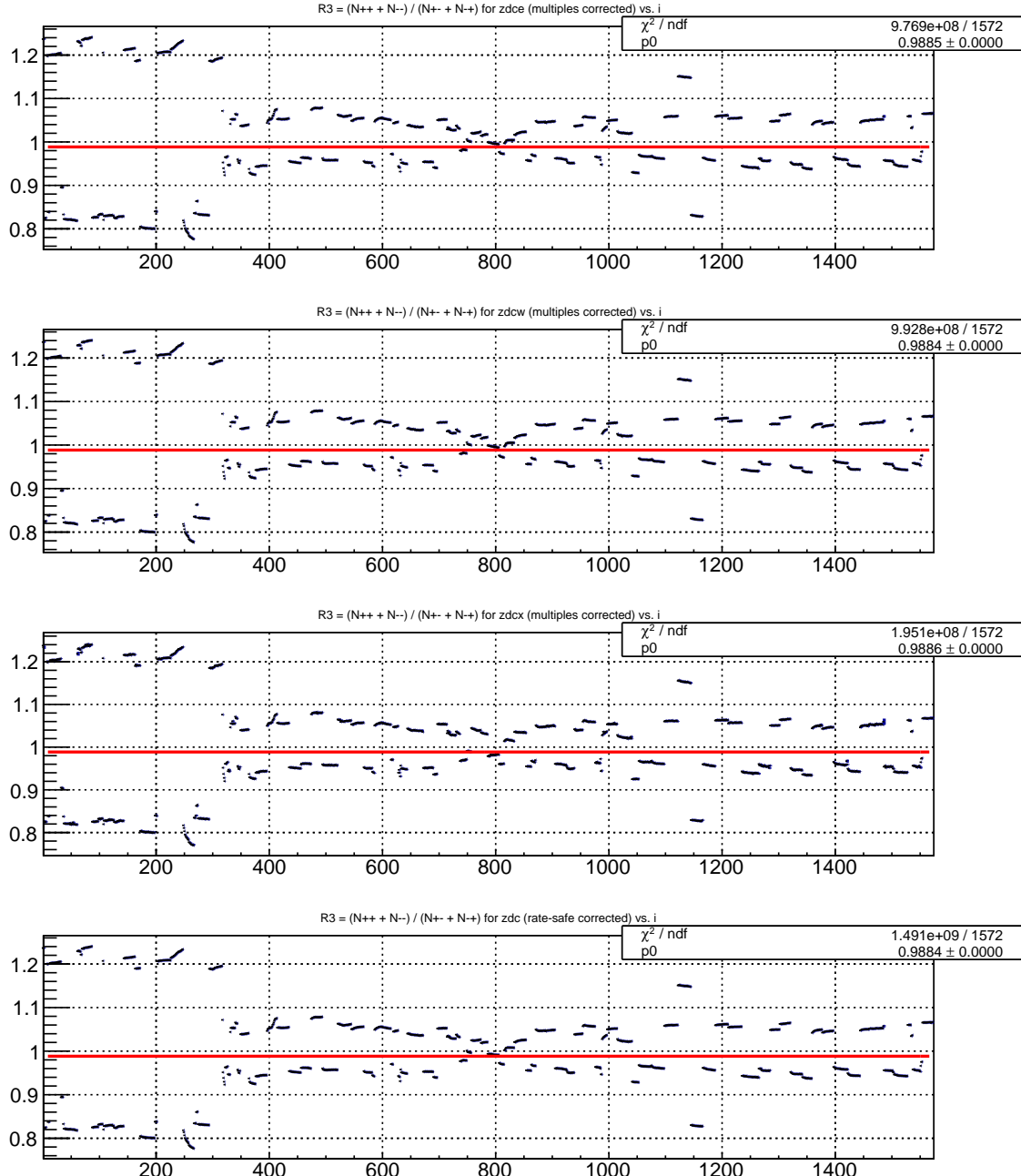


Figure 4.8: R_3 from ZDC for Run 13

Run 13 VPD R_3 vs. Run Index

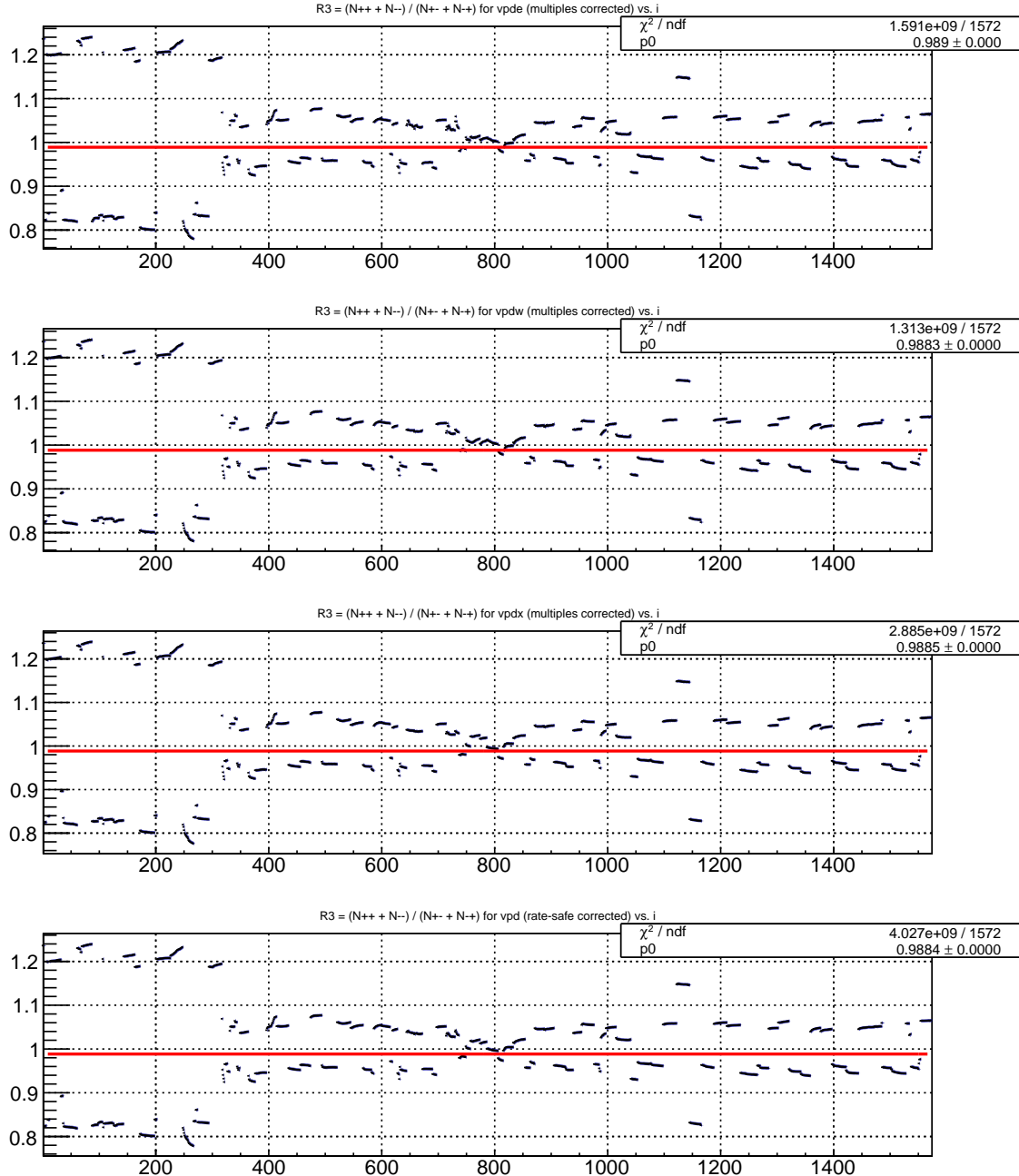


Figure 4.9: R_3 from VPD for Run 13

4.4 R_3 Cross-Checks

The following cross-checks have been employed to test the consistency of the relative luminosity measurement and to compare the two corrections methods:

- CDF vs. Rate-safe R_3 (figure 4.11)
- ZDC and VPD R_3 comparison (figure 4.13)
- CDF corrected E and W R_3 comparison (figure 4.15)
- CDF corrected E and X R_3 comparison (figure 4.17)
- CDF corrected W and X R_3 comparison (figure 4.19)

One important observation is that, although the difference between the R_3 measurement via the CDF corrections and the rate-safe corrections is rather small, the difference of the R_3 measurement between the ZDC and VPD is about half as big for the rate-safe method than for the CDF corrections method (see figures 4.12 and 4.13, bottom plot). This observation motivates a preference toward the use of the rate-safe corrections method since it provides better consistency between the ZDC and VPD.

Only runs which have “consistent” R_3 measurements are allowed in the full $A_{LL}^{\pi^0}$ analysis. Figures 4.13-4.19 are used to define the cuts for such consistent measurements. Furthermore, the duration of the DAQ run, denoted by t , is compared to the ratio between the total number of bunch crossings in the run and the bunch crossing rate; ideally t should be the same as this ratio, denoted by τ . The exact requirements for a consistent and good relative luminosity measurement are shown in table 4.2, which contains maximum allowed values of the absolute value of each metric given in the first column.

Run 12 $R_3^{\text{rate-safe}} - R_3^{\text{CDF}}$ vs. Run Index

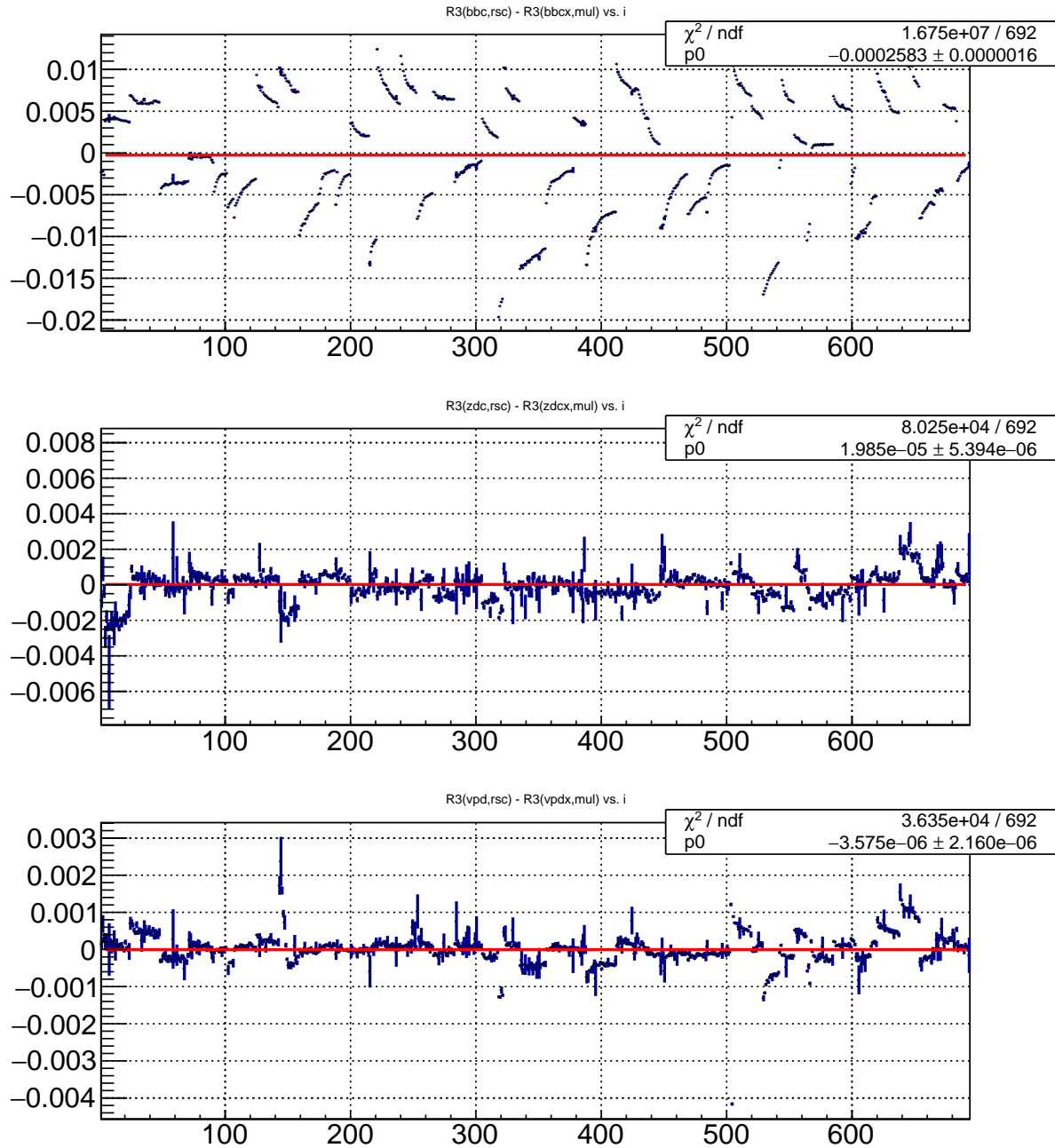


Figure 4.10: Run 12 R_3 from rate-safe corrections method minus R_3 from CDF corrections method vs. run index for BBC (top), ZDC (middle), and VPD (bottom)

Run 13 $R_3^{\text{rate-safe}} - R_3^{\text{CDF}}$ vs. Run Index

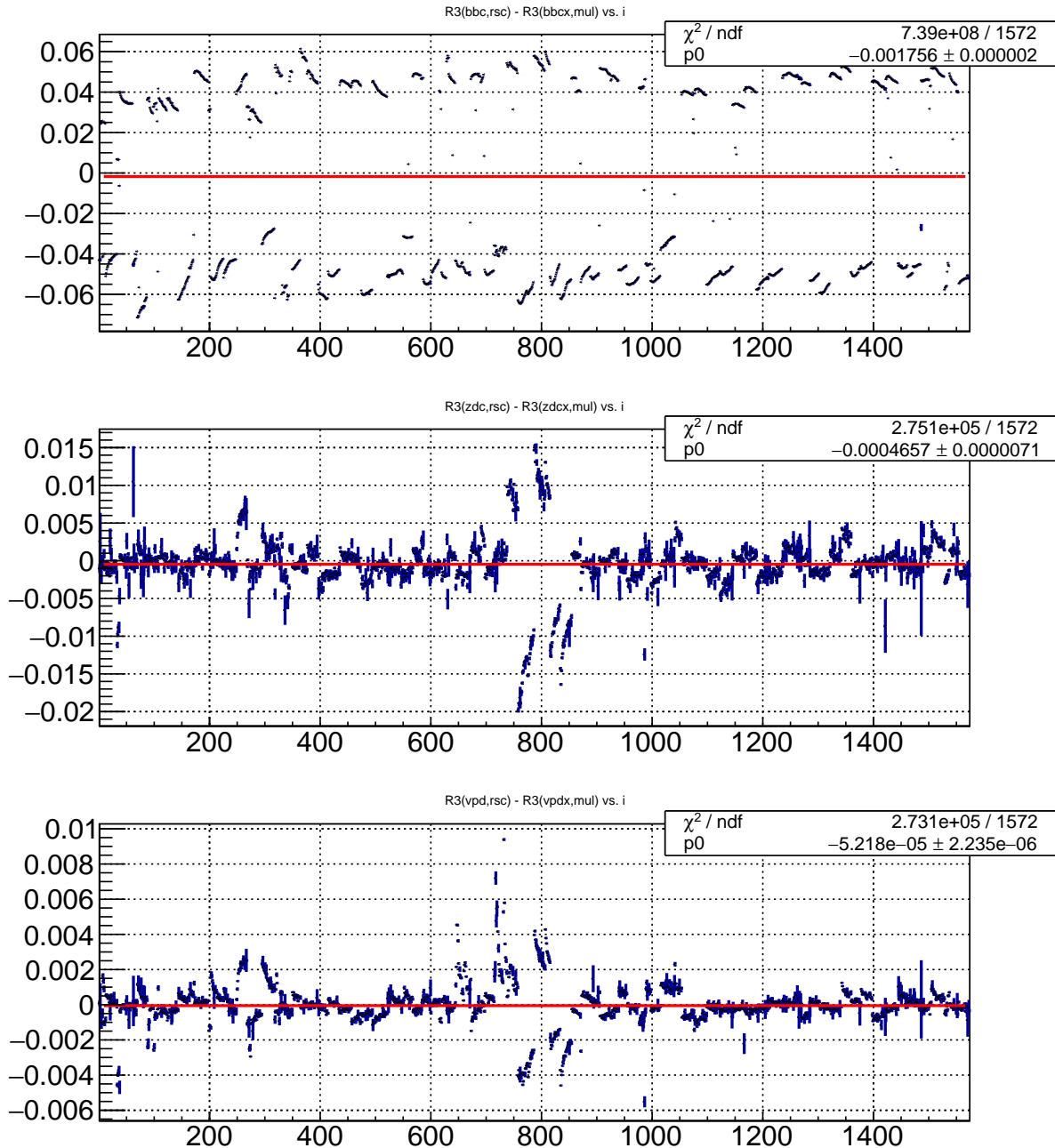


Figure 4.11: Run 13 R_3 from rate-safe corrections method minus R_3 from CDF corrections method vs. run index for BBC (top), ZDC (middle), and VPD (bottom)

Run 12 $R_3^{\text{ZDC}} - R_3^{\text{VPD}}$ vs. Run Index

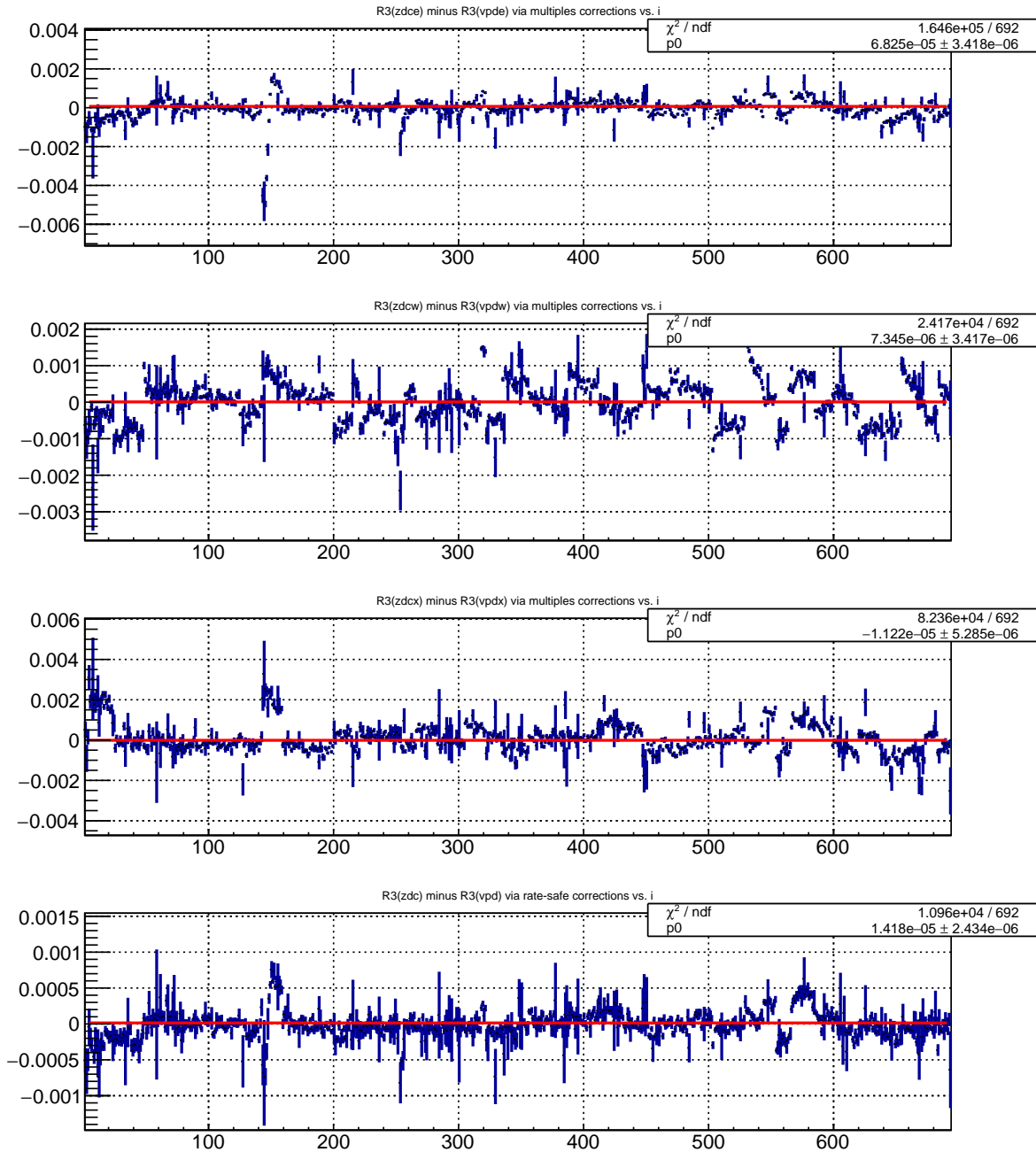


Figure 4.12: Run 12 R_3 from ZDC minus R_3 from VPD vs. run index; in order from top to bottom, the plots are for CDF corrected E, W, X, and rate-safe corrected

Run 13 $R_3^{\text{ZDC}} - R_3^{\text{VPD}}$ vs. Run Index

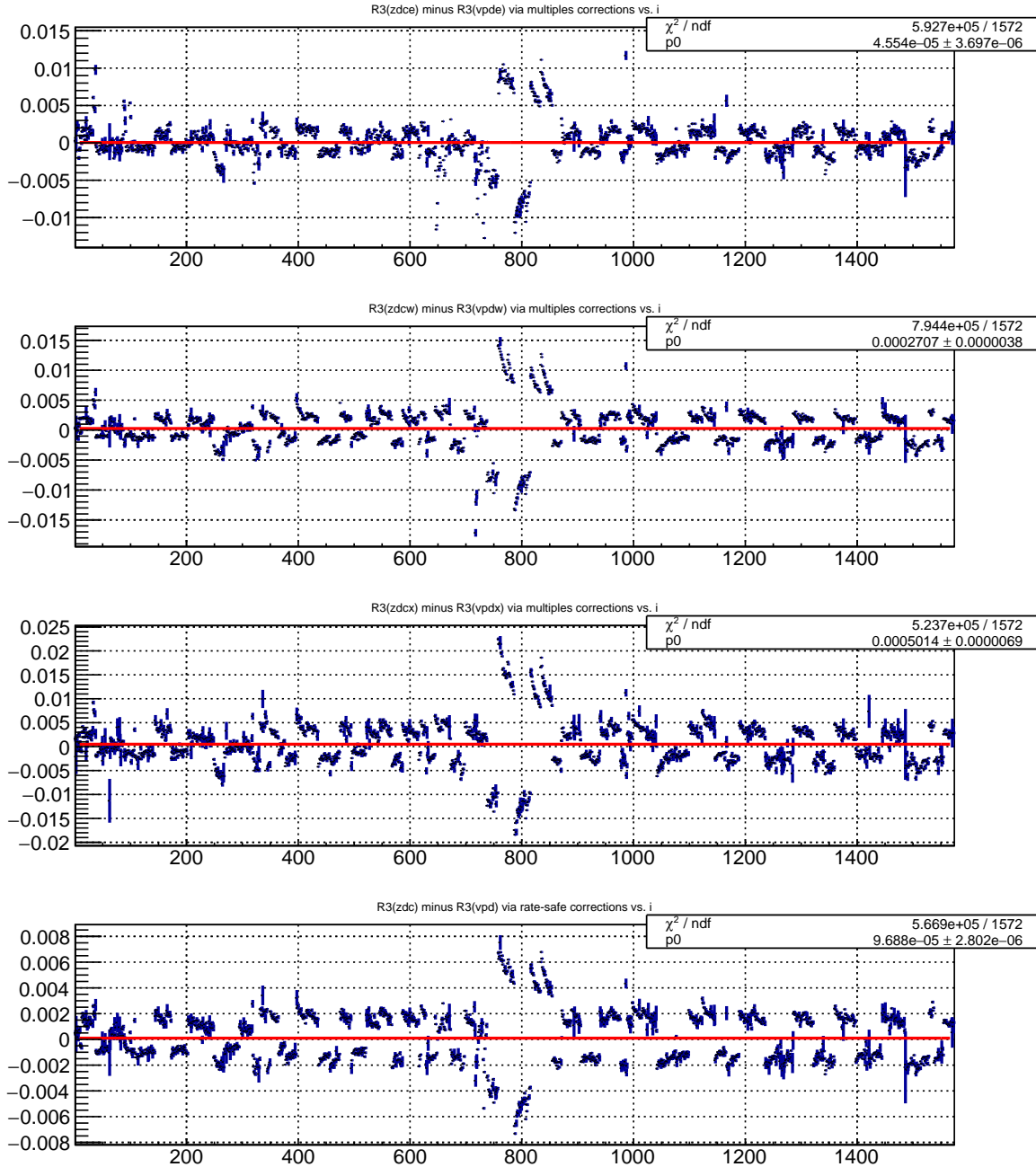


Figure 4.13: Run 13 R_3 from ZDC minus R_3 from VPD vs. run index; in order from top to bottom, the plots are for CDF corrected E, W, X, and rate-safe corrected

Run 12 $R_3^E - R_3^W$ vs. Run Index

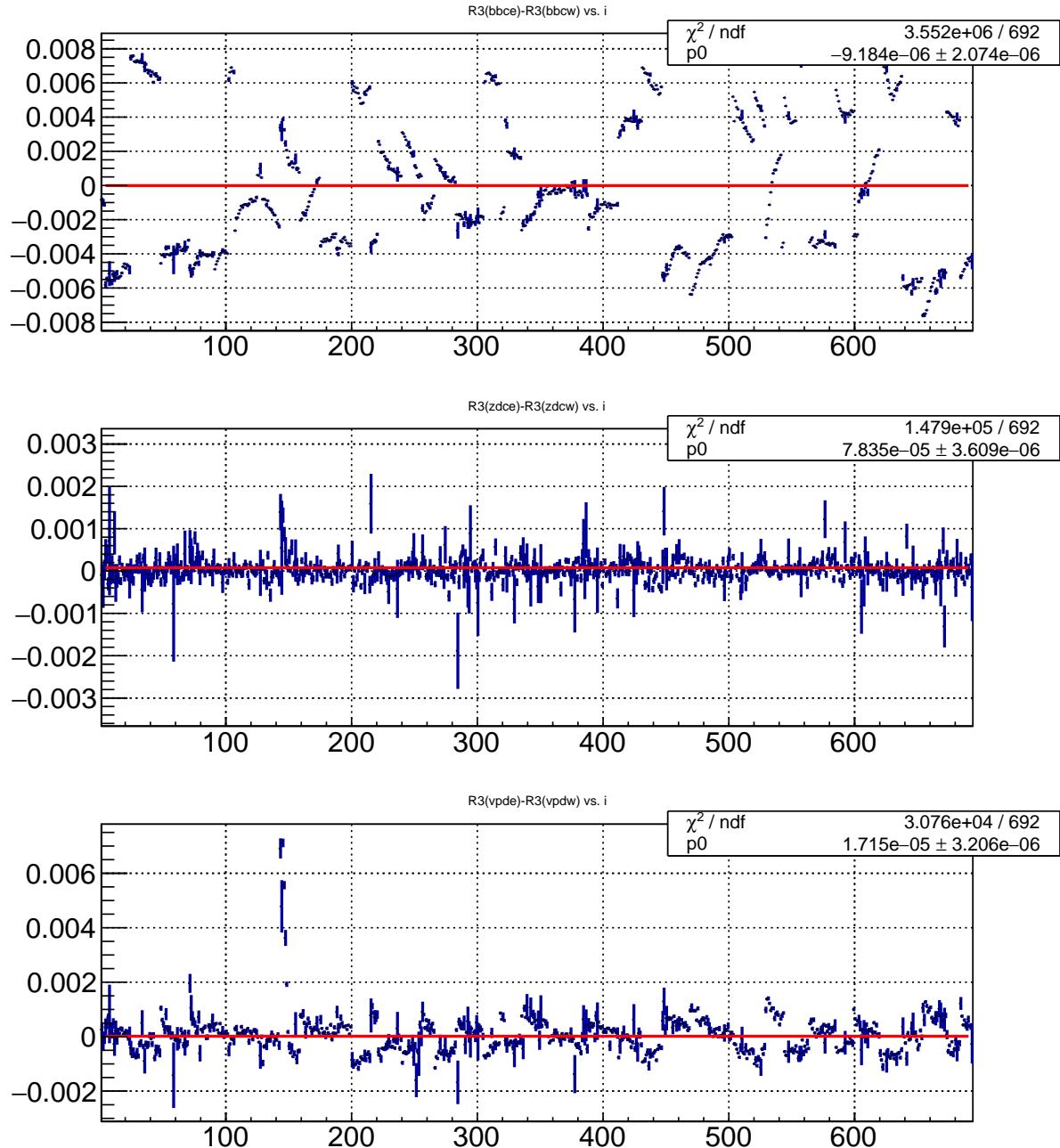


Figure 4.14: Run 12 R_3 from E minus R_3 from W vs. run index; in order from top to bottom, the plots are for CDF corrected BBC, ZDC, and VPD

Run 13 $R_3^E - R_3^W$ vs. Run Index

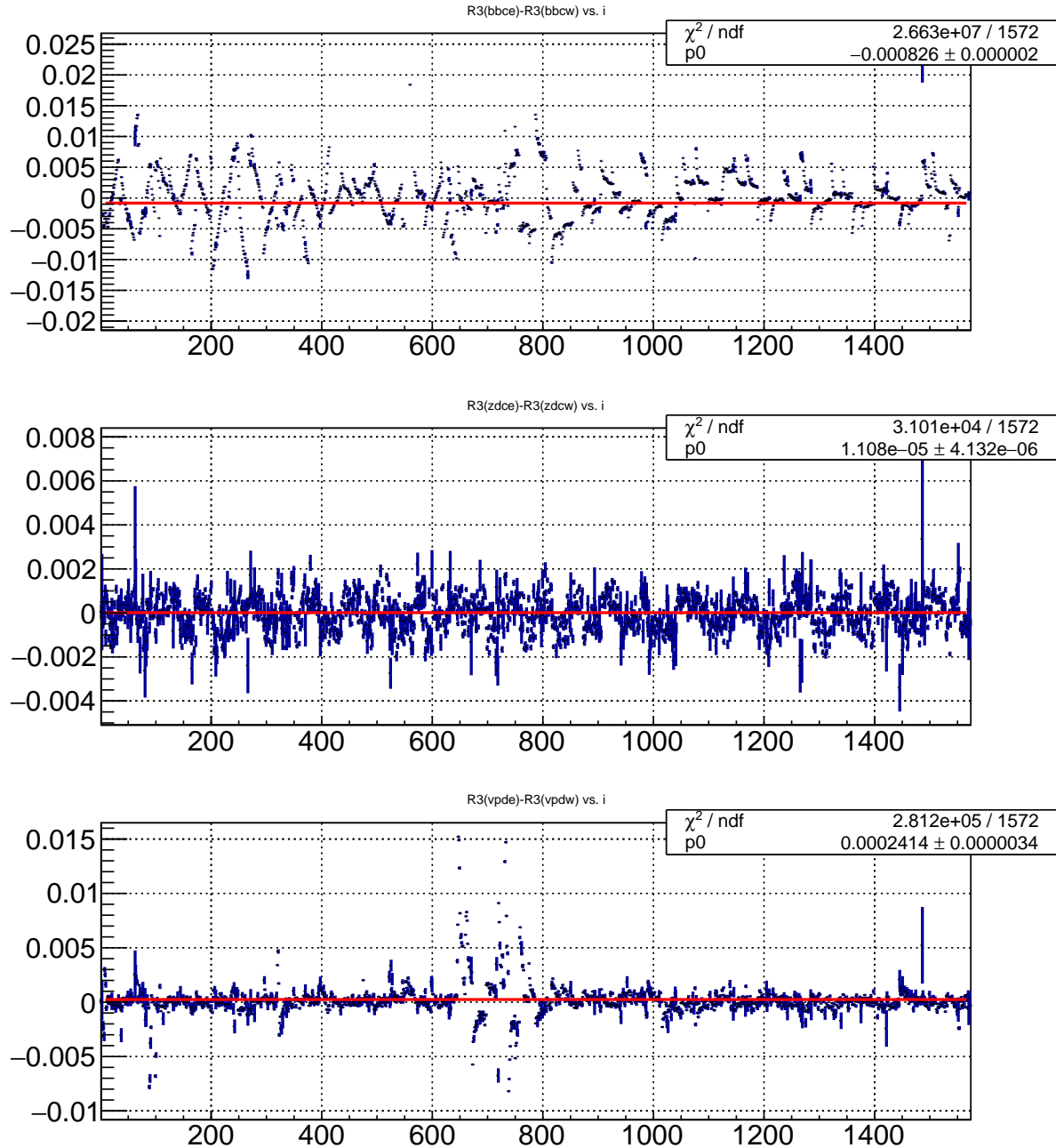


Figure 4.15: Run 13 R_3 from E minus R_3 from W vs. run index; in order from top to bottom, the plots are for CDF corrected BBC, ZDC, and VPD

Run 12 $R_3^E - R_3^X$ vs. Run Index

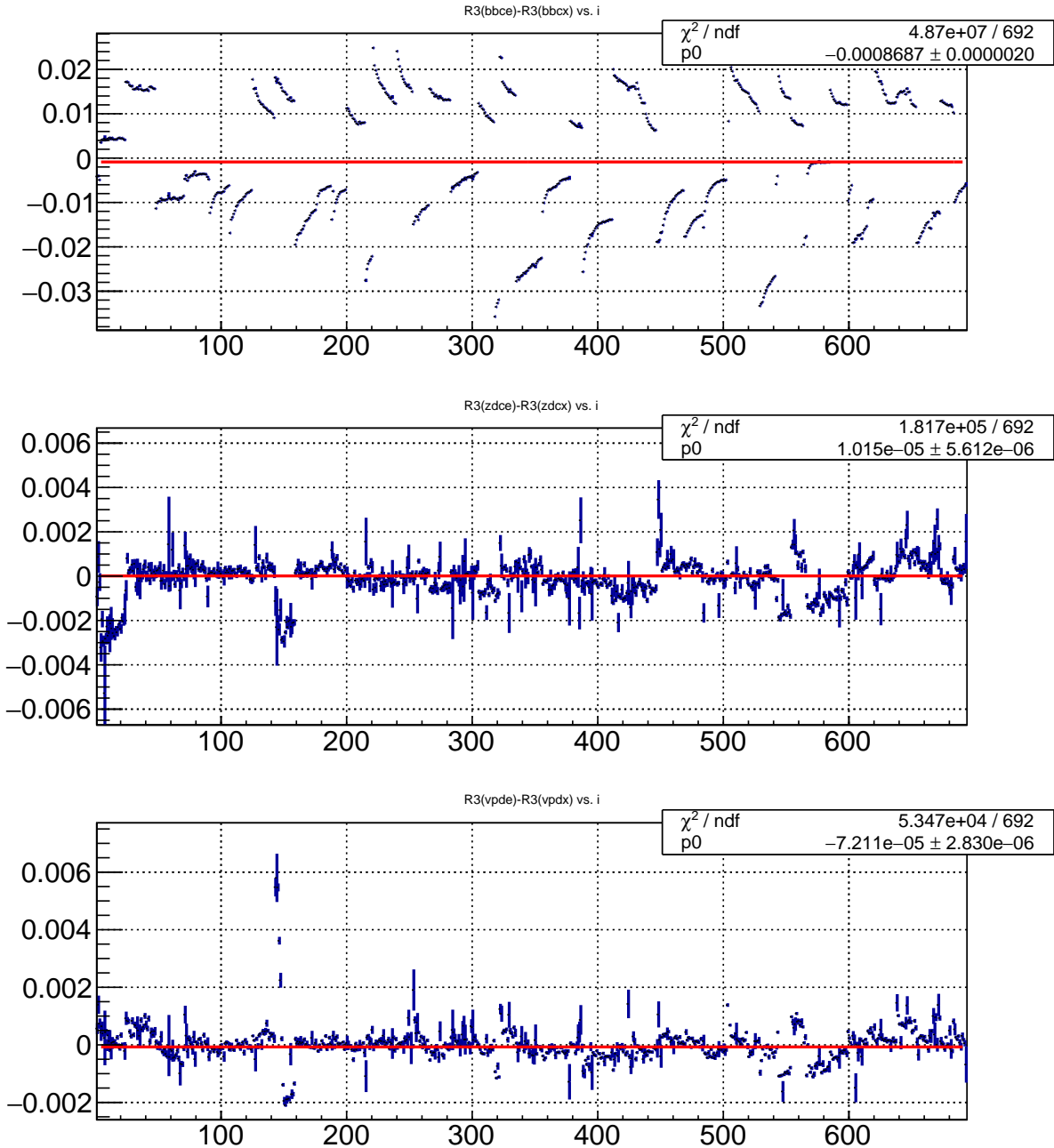


Figure 4.16: Run 12 R_3 from E minus R_3 from X vs. run index; in order from top to bottom, the plots are for CDF corrected BBC, ZDC, and VPD

Run 13 $R_3^E - R_3^X$ vs. Run Index

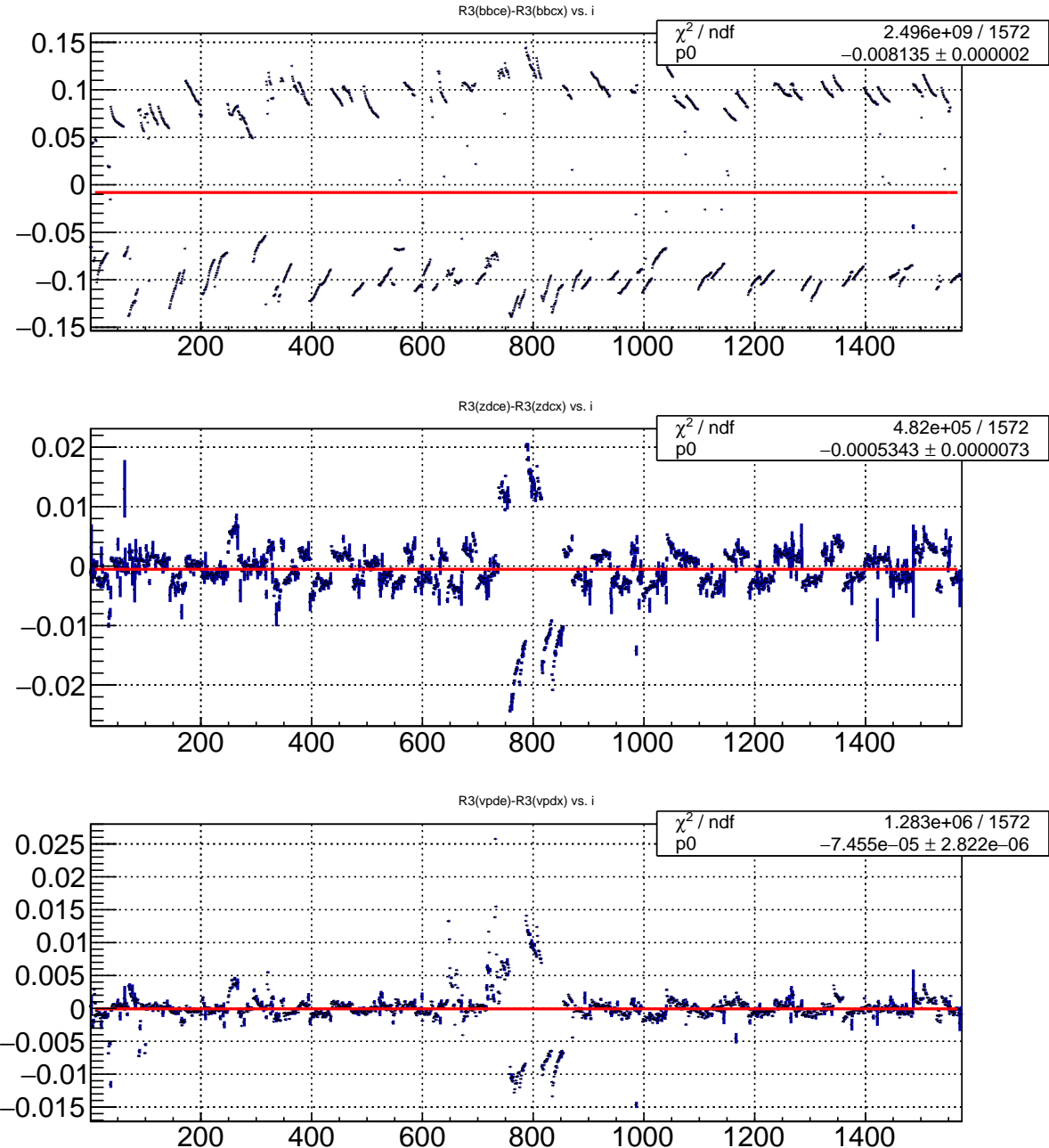


Figure 4.17: Run 13 R_3 from E minus R_3 from X vs. run index; in order from top to bottom, the plots are for CDF corrected BBC, ZDC, and VPD

Run 12 $R_3^W - R_3^X$ vs. Run Index

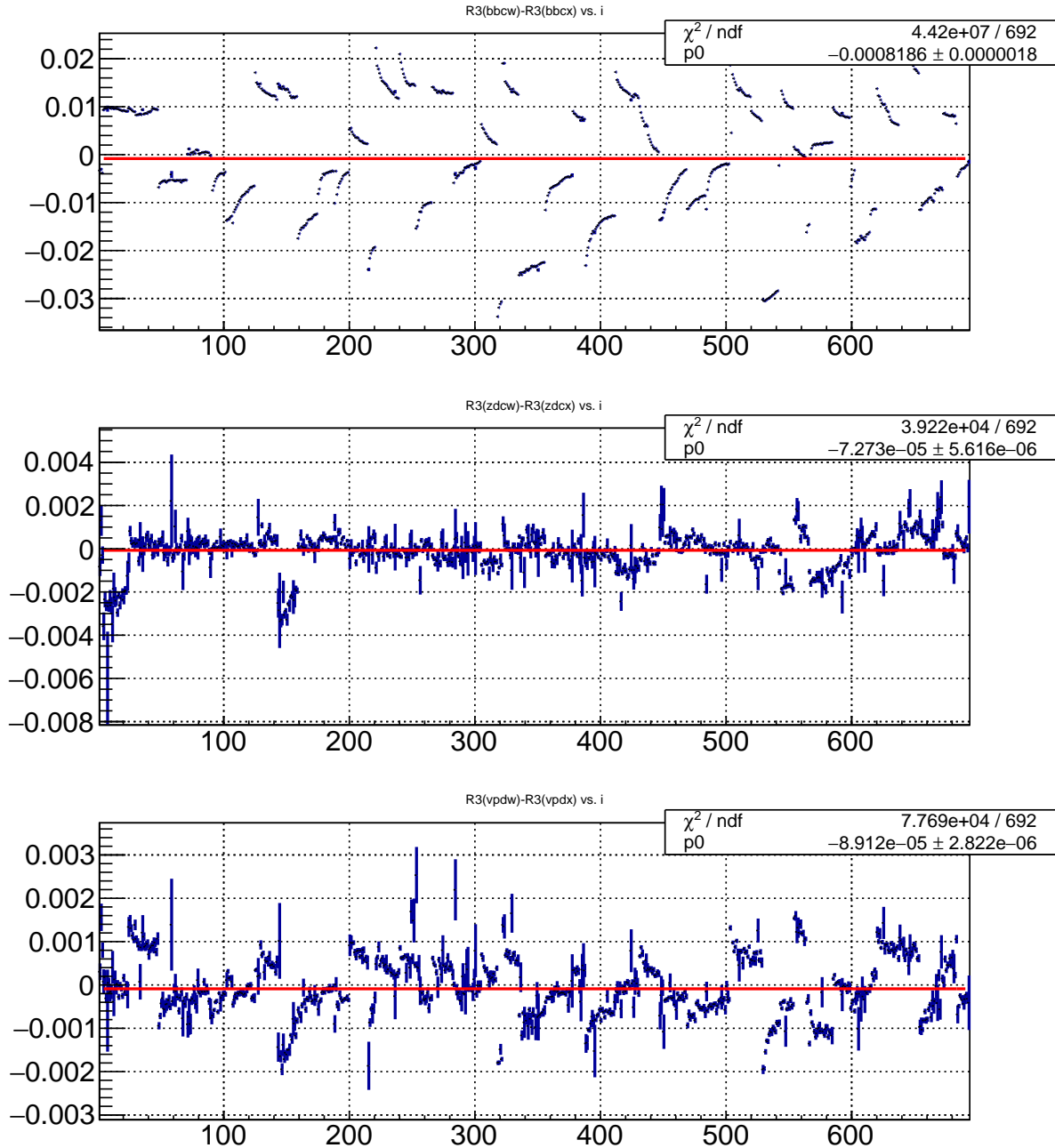


Figure 4.18: Run 12 R_3 from W minus R_3 from X vs. run index; in order from top to bottom, the plots are for CDF corrected BBC, ZDC, and VPD

Run 13 $R_3^W - R_3^X$ vs. Run Index

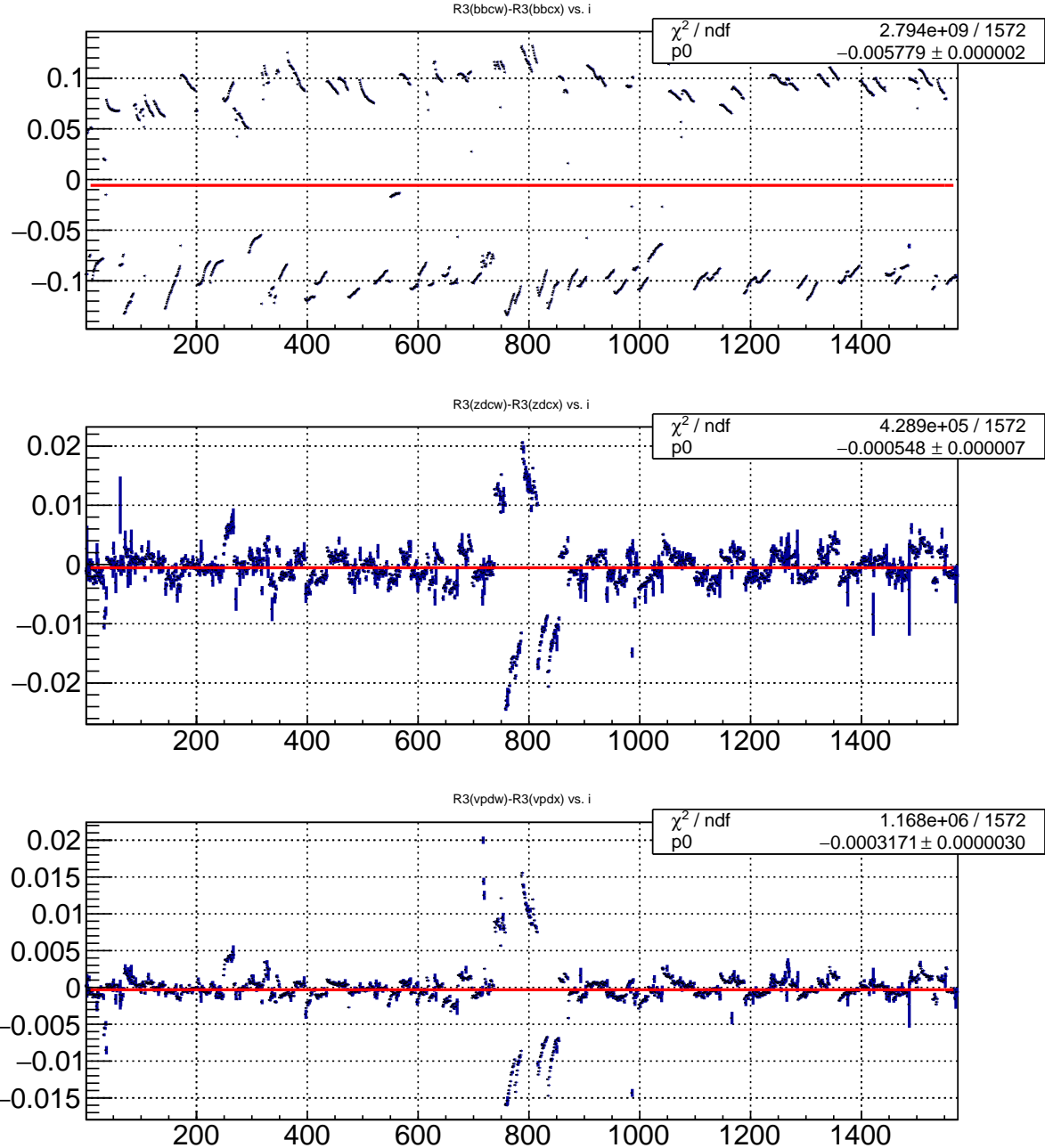


Figure 4.19: Run 13 R_3 from W minus R_3 from X vs. run index; in order from top to bottom, the plots are for CDF corrected BBC, ZDC, and VPD

Comparison	Run 12	Run 13
VPDE - ZDCE	0.005	0.006
VPDW - ZDCW	0.005	0.004
VPDX - ZDCX	0.005	0.008
VPDE - VPDW	0.003	0.005
VPDE - VPDX	0.002	0.006
VPDW - VPDX	0.003	0.004
ZDCE - ZDCW	0.002	0.002
ZDCE - ZDCX	0.004	0.008
ZDCW - ZDCX	0.004	0.007
t/τ	1.4	1.8

Table 4.2: Upper limits for various metrics for a DAQ run’s R_3 measurement to be self-consistent; DAQ runs which do not satisfy all of these requirements are omitted from analysis

4.5 Miscellaneous

4.5.1 Anomalous Bunch Crossings

For every fill, the number of corrected (and uncorrected) scaler counts was plotted as a function of bunch crossing number. Abort gaps were verified and any bunch crossings that had an anomalously low number of counts were omitted from the relative luminosity computation. Bxings which had no spin defined in CDEV were, by default, also omitted; this includes abort gaps as well as bunch crossings 69 and 70 for the first few fills analysed in Run 13.

Furthermore, for Run 13 fills 17512-17520, the first two bunch crossings coming out of each abort gaps had somewhat lower counts. These bunches were not filled with the normal number of protons, according to the wall-current monitors, and were also removed from analysis. Lists of omitted bunch crossings are found on the relative luminosity analysis webpages (links provided in the beginning of this chapter). Omitting bunch crossings from the relative luminosity analysis in turn omits their FMS π^0 s from the $A_{LL}^{\pi^0}$ analysis.

4.5.2 N_{bx} vs. Bunch Crossing

When plotting the number of bunch crossings N_{bx} as a function of bunch crossing number, an unexpected sigmoid-type function is observed. See figure 4.20 for an example, where the vertical axis is rescaled such that the highest point is at unity.

This effect negligibly small in the context of a relative luminosity analysis; it is on the order of 2×10^{-4} and enters the relative luminosity analysis via the corrections equations

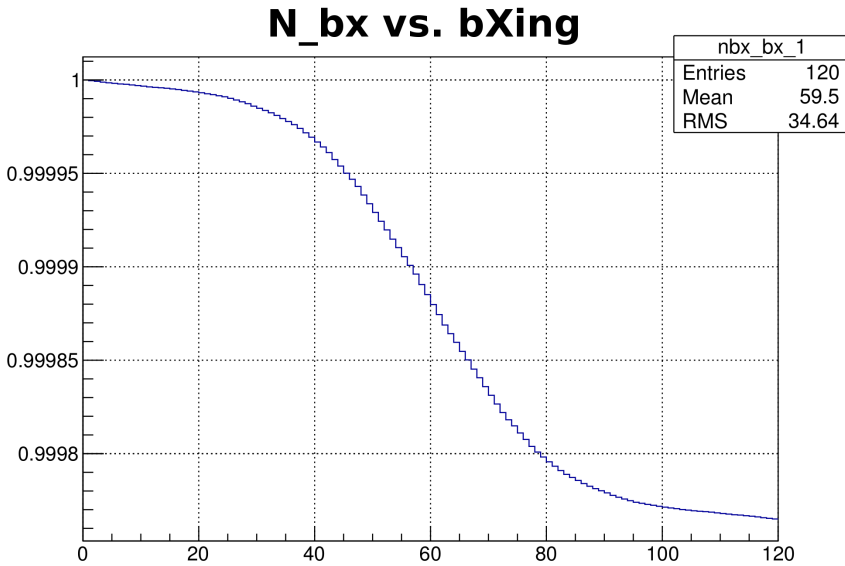


Figure 4.20: N_{bx} vs. bunch crossing number for an example run, showing the typical “sigmoid” behavior

(both CDF and rate-safe). It was finally solved near the beginning of Run 15: the issue was in the bunch counters as an “extra revolution tick reset.” Details of the solution and discussion thereof are found at the following hypernews thread:

<http://www.star.bnl.gov/HyperNews-star/protected/get/startrig/4814.html>

After the fix, a typical plot shows a spike at bunch crossing 0 coincident with the start up time for the DAQ run as well as a step of one count at the bunch crossing where the DAQ run ended. The first run taken during Run 15 which includes this fix is 16078055.

Chapter 5

Systematic Uncertainties

The overall uncertainty on $A_{LL}^{\pi^0}$ and on p_T , the kinematic variable in terms of which the $A_{LL}^{\pi^0}$ measurement is presented, must be assessed. This chapter presents systematic uncertainties on $A_{LL}^{\pi^0}$ which come from the relative luminosity and from a nonzero transverse component in the polarization, followed by a determination of the overall systematic uncertainty on p_T .

5.1 Relative Luminosity Systematic

The dominant systematic uncertainty for the $A_{LL}^{\pi^0}$ measurement is from the relative luminosity determination. Three schemes for determining this systematic have been explored: via direct comparison between VPD and ZDC, via scalar asymmetries from bunch-fitting, and via scalar subsystem self-consistency through transverse single-spin asymmetries. Additionally, A_{LL} as determined using R_3 from the VPD was compared to that from the ZDC.

Given the representation of A_{LL} in terms of yield and relative luminosity R_3 as in equation 1.5, one can propagate the uncertainty of R_3 to an uncertainty on A_{LL} :

$$\Delta_{A_{LL}}^2 = \left(\frac{\partial A_{LL}}{\partial R_3} \right)^2 \Delta_{R_3}^2 = \left(\frac{2(N_{++} + N_{--})(N_{+-} + N_{-+})}{P_B P_Y [(N_{++} + N_{--}) + R_3 (N_{+-} + N_{-+})]} \right)^2 \Delta_{R_3}^2 \quad (5.1)$$

With the approximation $N_{++} + N_{--} \approx R_3 (N_{+-} + N_{-+})$, the systematic uncertainty becomes

$$\Delta_{A_{LL}} = \frac{1}{2} \cdot \frac{1}{P_B P_Y} \cdot \frac{\Delta_{R_3}}{R_3} \quad (5.2)$$

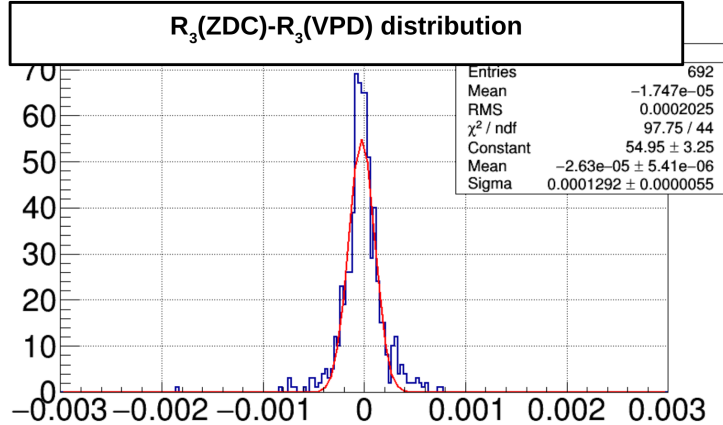


Figure 5.1: Run 12 rate-safe corrected $R_3^{\text{ZDC}} - R_3^{\text{VPD}}$ distribution with Gaussian fit

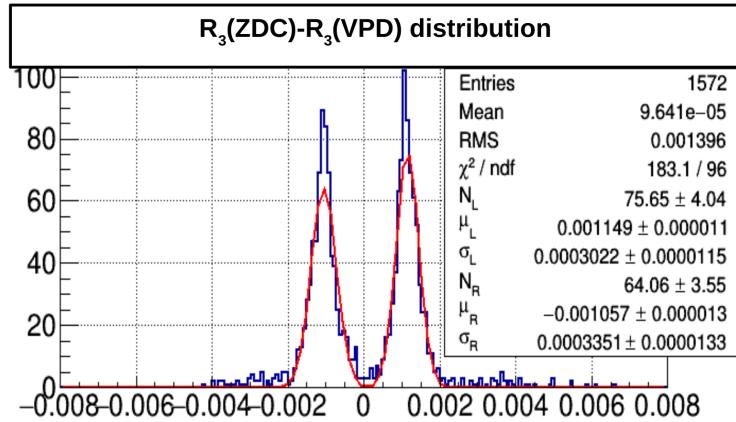


Figure 5.2: Run 13 rate-safe corrected $R_3^{\text{ZDC}} - R_3^{\text{VPD}}$ distribution with two Gaussian fits

5.1.1 Direct VPD and ZDC Comparison: Δ_{R_3} Method

One way to obtain a systematic uncertainty is to simply compare the R_3 value obtained from the ZDC to that obtained from the VPD; here we use a value of $R_3^{\text{ZDC}} - R_3^{\text{VPD}}$ as Δ_{R_3} in equation 5.2.

Figures 5.1 and 5.2 show the value of Δ_{R_3} for Runs 12 and 13, respectively. For Run 12, the RMS of the distribution is 2.0×10^{-4} and the standard deviation according to the Gaussian fit is 1.3×10^{-4} . Run 13, on the other hand, shows a bimodal distribution with standard deviations 3.0×10^{-4} for the lower peak and 3.4×10^{-4} for the higher peak and an overall RMS of 1.4×10^{-3} .

It turns out that the two separate Δ_{R_3} peaks in Run 13 correspond to two different spin patterns (see section 5.1.3.2, figures 5.6 and 5.7 for the 8 overall spin patterns for each Run). From the perspective of double-spin asymmetries there were two “classes” of spin patterns

in each of Run 12 and 13. Denoting a same-helicity bunch crossing as “S” and an opposite-helicity crossing as “O”, the double-spin pattern classes can be represented by listing the double-spin states of the first 8 bunch crossings; this is done for both Runs 12 and 13 in table 5.1.

Bunch Crossing # mod 8:	0	1	2	3	4	5	6	7
Run 12 Pattern Class A:	S	O	O	S	O	S	S	O
Run 12 Pattern Class B:	O	S	S	O	S	O	O	S
Run 13 Pattern Class A:	S	S	S	S	O	O	O	O
Run 13 Pattern Class B:	O	O	O	O	S	S	S	S

Table 5.1: Double-Spin Patterns, where “S” denotes same spins and “O” denotes opposite spins

The main difference between the Runs is that Run 12 alternates between “SOOS” and “OSSO” whereas Run 13 alternates between “SSSS” and “OOOO.” The maximum number of consecutive bunch crossings which have the same double-spin state “S” or “O” is 2 for Run 12 and 4 for Run 13; consequently, any biases introduced by having multiple consecutive bunch crossings with same double-spin state will be enhanced in Run 13 with respect to Run 12. This enhancement would only be seen, however, if there was some information from one bunch crossing spilling over into subsequent bunch crossings. As will be discussed in section 5.1.5, after-pulsing in the scaler systems is a likely culprit and the bimodality of Δ_{R_3} is a consequence.

In order to convert Δ_{R_3} into a systematic uncertainty on $A_{LL}^{\pi^0}$, equation 5.2 must be used. For the polarization, the overall average luminosity-weighted polarization (see section 6.2) from runs used in the $A_{LL}^{\pi^0}$ analysis was used: for Run 12 $P_B = 0.54$ and $P_Y = 0.56$ while for Run 13 $P_B = P_Y = 0.57$. The average R_3 values from the VPD is 0.9967 for Run 12 and 1.002 for Run 13. For Run 12, we use the standard deviation (σ) from the Gaussian fit as an estimate of Δ_{R_3} ; for Run 13, the standard deviations (σ_L and σ_R) of the two Gaussian distributions are averaged together. The resulting systematic uncertainty is:

- Run 12: $\Delta_{A_{LL}} [\Delta_{R_3}] = \frac{1}{2} \cdot \frac{1}{P_B P_Y} \cdot \frac{\sigma (\Delta_{R_3})}{\langle R_3 \rangle} = 2.1 \times 10^{-4}$
- Run 13: $\Delta_{A_{LL}} [\Delta_{R_3}] = \frac{1}{2} \cdot \frac{1}{P_B P_Y} \cdot \frac{[\sigma_L (\Delta_{R_3}) + \sigma_R (\Delta_{R_3})] / 2}{\langle R_3 \rangle} = 4.9 \times 10^{-4}$

5.1.2 Comparison of $A_{LL}^{\pi^0}$ via VPD and ZDC: $\delta_{A_{LL}}$ Method

Another idea to obtain a systematic on A_{LL} is to compare the nominal values of A_{LL} computed using the relative luminosity from the VPD to those from the ZDC. Figures 5.3-5.5 show $\delta_{A_{LL}}$, defined as A_{LL} with R_3 from ZDC minus A_{LL} with R_3 from VPD, for (approximately) each of the p_T bins used in the final analysis. A fit to a constant is also shown. Run 12 shows a $\delta_{A_{LL}}$ on the order of $5 - 8 \times 10^{-5}$ whereas Run 13 shows a $\delta_{A_{LL}}$ on the order of 1.5×10^{-4} . These differences are much smaller than any other method used to determine systematic uncertainties from relative luminosity.

The reason $\delta_{A_{LL}}$ is smaller in comparison to the aforementioned systematic uncertainty is because $\delta_{A_{LL}}$ is sensitive to the mean of Δ_{R_3} , not its standard deviation. To see this, consider using the maximum likelihood method for determining a value of $\delta_{A_{LL}}$. Following the same maximum likelihood method used for extracting $A_{LL}^{\pi^0}$ (appendix H), the maximum likely $\delta_{A_{LL}}$ is

$$\bar{\delta}_{A_{LL}} = \frac{\sum_{i=1}^N \delta_{A_{LL_i}} / \sigma_i^2}{\sum_{i=1}^N 1 / \sigma_i^2} \quad (5.3)$$

where the sums run over DAQ runs and σ_i is the statistical uncertainty on the i th run's $\delta_{A_{LL}}$. Working out the details, one finds that the numerator terms are $\delta_{A_{LL_i}} / \sigma_i^2 \propto 1 / \Delta_{R_3}$ and the denominator terms are $1 / \sigma_i^2 \propto 1 / \Delta_{R_3}^2$. Since the numerator terms are proportional to $1 / \Delta_{R_3}$ and Δ_{R_3} is centered around zero, up to means of 1.8×10^{-5} in Run 12 and 9.6×10^{-5} in Run 13, the overall value of $\delta_{A_{LL}}$ is expected to be within the same order of magnitude. Ultimately, this $\delta_{A_{LL}}$ method has been abandoned as a systematic uncertainty for this analysis.

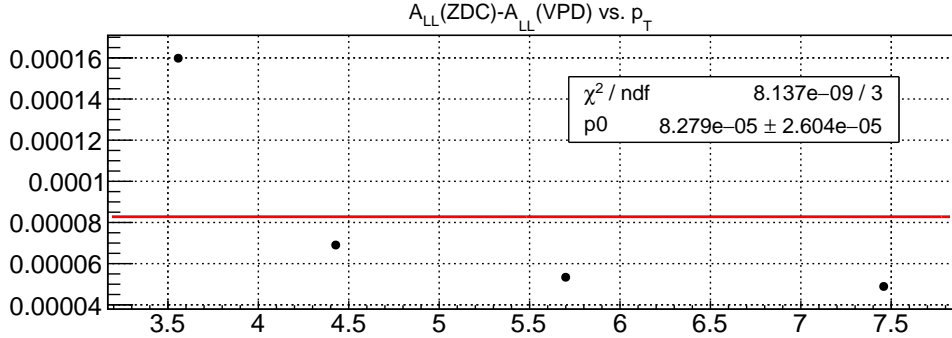


Figure 5.3: Run 12 outer region A_{LL} with R_3 from ZDC minus A_{LL} with R_3 from VPD, for each p_T bin

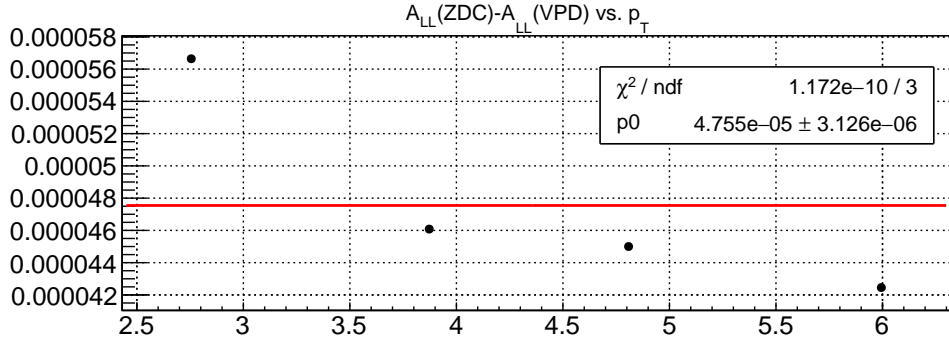


Figure 5.4: Run 12 inner region A_{LL} with R_3 from ZDC minus A_{LL} with R_3 from VPD, for each p_T bin

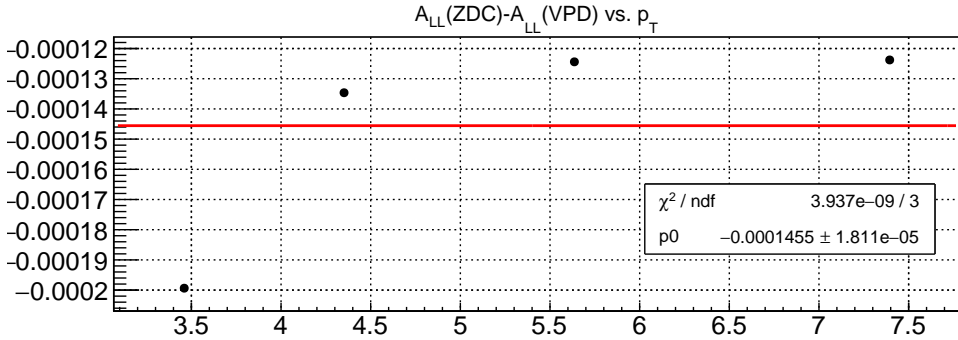


Figure 5.5: Run 13 outer region A_{LL} with R_3 from ZDC minus A_{LL} with R_3 from VPD, for each p_T bin

5.1.3 Intrinsic Scaler Double-Spin Asymmetries: $\Delta_{S_{LL}}$ Method

One can also evaluate systematic biases of $A_{LL}^{\pi^0}$ due to the relative luminosity measurement by measuring A_{LL} in one scaler detector while using another scaler detector to measure the relative luminosity. This method has been employed in various PHENIX analyses, e.g, as in chapter 4 of [11]. This “scaler asymmetry,” denoted here as S_{LL} , is extracted using the “bunch-fitting” technique, which is summarized below; more details are in appendix E.

In order to relate S_{LL} to a systematic uncertainty on $A_{LL}^{\pi^0}$, one must propagate uncertainties on the number of counts in both scaler detectors used in extracting S_{LL} . Referring to the appendix of [13], the systematic uncertainty is simply

$$\Delta_{A_{LL}} \approx \Delta_{S_{LL}}. \quad (5.4)$$

5.1.3.1 Bunch Fitting Algorithm

Consider S_{LL} as an asymmetry in scaler subsystem S measured while using scaler system MB for a “minimum-biased” relative luminosity measurement. It may be written as

$$S_{LL} = \frac{1}{P_B P_Y} \varepsilon_3 = \frac{1}{P_B P_Y} \frac{(N_S^{++} + N_S^{--}) - R_3^{MB} (N_S^{+-} + N_S^{-+})}{(N_S^{++} + N_S^{--}) + R_3^{MB} (N_S^{+-} + N_S^{-+})} \quad (5.5)$$

Writing out the relative luminosity R_3^{MB} in terms of yields in MB allows this asymmetry to be expressed as

$$S_{LL} = \frac{1}{P_B P_Y} \frac{(N_S^{++} + N_S^{--}) / (N_{MB}^{++} + N_{MB}^{--}) - (N_S^{+-} + N_S^{-+}) / (N_{MB}^{+-} + N_{MB}^{-+})}{(N_S^{++} + N_S^{--}) / (N_{MB}^{++} + N_{MB}^{--}) + (N_S^{+-} + N_S^{-+}) / (N_{MB}^{+-} + N_{MB}^{-+})} \quad (5.6)$$

This is just an asymmetry of the ratios of scaler counts from S to MB ; the raw asymmetry can therefore be extracted by minimizing the χ^2 of the following fit to the ratio as a function of bunch crossing number:

$$\frac{N_S^i}{N_{MB}^i} = c_3 (1 + h_B^i h_Y^i \cdot \varepsilon_3) \quad (5.7)$$

where the superscripts i indicate a bunch crossing number, $h_B, h_Y \in \{-1, 1\}$ are the initial proton helicities, and $\{c_3, \varepsilon_3\}$ are the fit parameters. The raw asymmetry ε_3 is then divided by the polarization product to obtain S_{LL} while the fit parameter c_3 is an overall scaling proportional to the cross-section. If $\varepsilon_3 \cdot \sum_{i=1}^{120} h_B^i h_Y^i \ll 120$, then c_3 is interpreted as the average of the ratio N_S^i / N_{MB}^i .

5.1.3.2 Scaler Asymmetry Measurement

Because ultimately the $A_{LL}^{\pi^0}$ analysis uses the VPD relative luminosity measurement, this section presents the VPD scaler asymmetry S_{LL} while treating the ZDC as a relative luminosity measurement; in the language of the bunch fitting algorithm this is a bunch fit to the ratio VPD/ZDC. The rate-safe corrected data is presented here; it turns out that with the CDF corrections applied, the S_{LL} distribution is more than twice as wide as the distribution derived using rate-safe corrections.

The distribution of S_{LL} was analysed for each spin pattern separately as well as for all spin patterns for an overall distribution. Figures 5.6 and 5.7 show the 8 different spin patterns used in Runs 12 and 13, respectively, where the colors are used in the S_{LL} distributions presented below. The B and Y brackets represent the spin state of the first 8 bunch crossings while the numerical subscript represents which of the 4 fill patterns are used. The double-spin pattern classes in terms of Ss and Os is also given; 4 bunch-crossing patterns are contained in each class.

Figures 5.8 and 5.9 show the S_{LL} distributions. Run 12 shows a single-mode distribution and all spin patterns agree; it is therefore fit with a single Gaussian with normalization constant N , mean μ , and standard deviation σ . Run 13, on the other hand, shows a bimodal distribution, revealing that S_{LL} is correlated to spin pattern; this is the same correlation seen in the aforementioned Δ_{R_3} distribution. This distribution is fit to the sum of two Gaussian functions, where the parameters are given subscripts L and R for left and right. Pattern class OOOOSSSS tends to have positive S_{LL} (mean $\mu_R = 1.6 \times 10^{-3}$) while pattern class SSSSOOOO tends to have negative S_{LL} (mean $\mu_L = -1.6 \times 10^{-3}$). The widths of the two classes agree: $\sigma_L = 4.0 \times 10^{-4}$ and $\sigma_R = 3.9 \times 10^{-4}$.

The $A_{LL}^{\pi^0}$ systematic uncertainty is, according to equation 5.4, approximately equal to $\Delta_{S_{LL}}$. Because S_{LL} is basically a double-spin asymmetry in the VPD, which could contribute to the $A_{LL}^{\pi^0}$ measurement, the absolute value of the mean S_{LL} is added to the standard deviation (from the fit) as a conservative estimate for the overall $\Delta_{A_{LL}}$. As in the Δ_{R_3} method, the two standard deviations from Run 13 are averaged together. The resulting systematic uncertainties are:

- Run 12: $\Delta_{A_{LL}} [\Delta_{S_{LL}}] = \sigma(S_{LL}) + |\langle S_{LL} \rangle| = 1.9 \times 10^{-4}$
- Run 13: $\Delta_{A_{LL}} [\Delta_{S_{LL}}] = \frac{\sigma_L(S_{LL}) + \sigma_R(S_{LL})}{2} + |\langle S_{LL} \rangle| = 4.1 \times 10^{-4}$

	$B_1[+ - + - - + - +] Y_3[+ + - - + + - -] (SOOSOSOSSO)$
	$B_1[+ - + - - + - +] Y_4[- - + + - - + +] (OSSOSOOS)$
	$B_2[- - + + - - + -] Y_3[+ + - - + + - -] (OSSOSOOS)$
	$B_2[- - + + - - + -] Y_4[- - + + - - + +] (SOOSOSOSSO)$
	$B_3[+ + - - + + - -] Y_1[+ - + - - + - +] (SOOSOSOSSO)$
	$B_3[+ + - - + + - -] Y_2[- - + + - - + +] (OSSOSOOS)$
	$B_4[- - + + - - + +] Y_1[+ - + - - + - +] (OSSOSOOS)$
	$B_4[- - + + - - + +] Y_2[- - + - - + - +] (SOOSOSOSSO)$

Figure 5.6: Run 12 spin patterns legend

	$B_1[+ + - - + + - -] Y_3[+ + - - - + +] (SSSSOOOO)$
	$B_1[+ + - - + + - -] Y_4[- - + + + + - -] (OOOOSSSS)$
	$B_2[- - + + - - + +] Y_3[+ + - - - + +] (OOOOSSSS)$
	$B_2[- - + + - - + +] Y_4[- - + + + + - -] (SSSSOOOO)$
	$B_3[+ + - - - + +] Y_1[+ + - - + + - -] (SSSSOOOO)$
	$B_3[+ + - - - + +] Y_2[- - + + - - + +] (OOOOSSSS)$
	$B_4[- - + + + + - -] Y_1[+ + - - + + - -] (OOOOSSSS)$
	$B_4[- - + + + + - -] Y_2[- - + + - - + +] (SSSSOOOO)$

Figure 5.7: Run 13 spin patterns legend

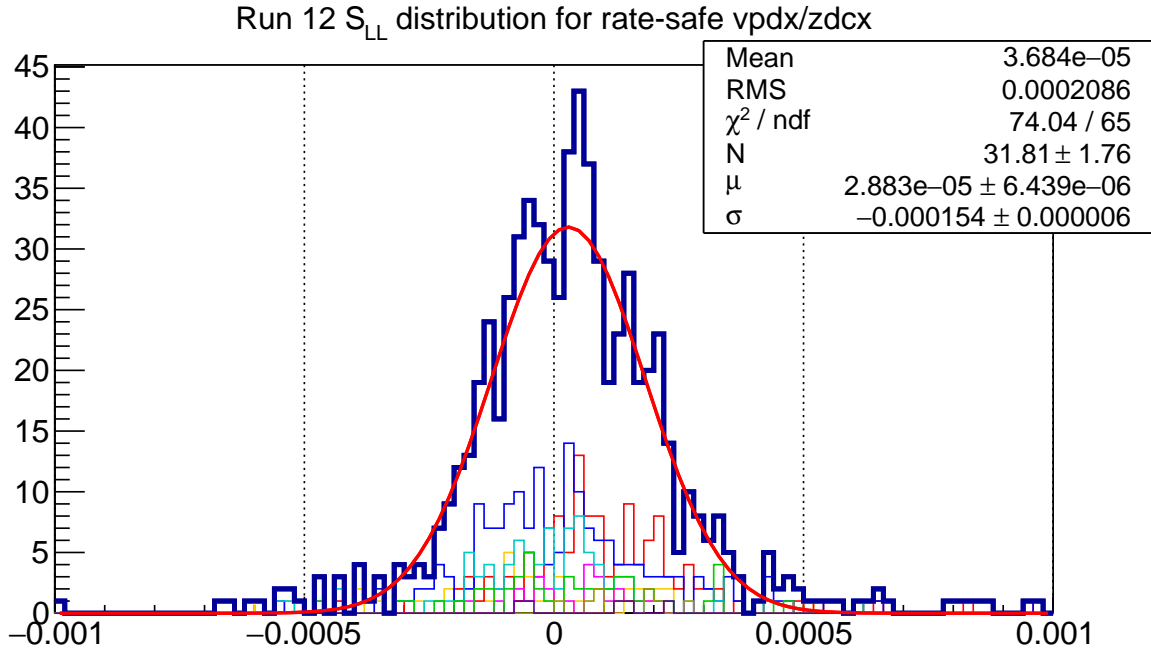


Figure 5.8: Run 12 S_{LL} for rate-safe VPD while treating rate-safe ZDC as a relative luminosity measurement

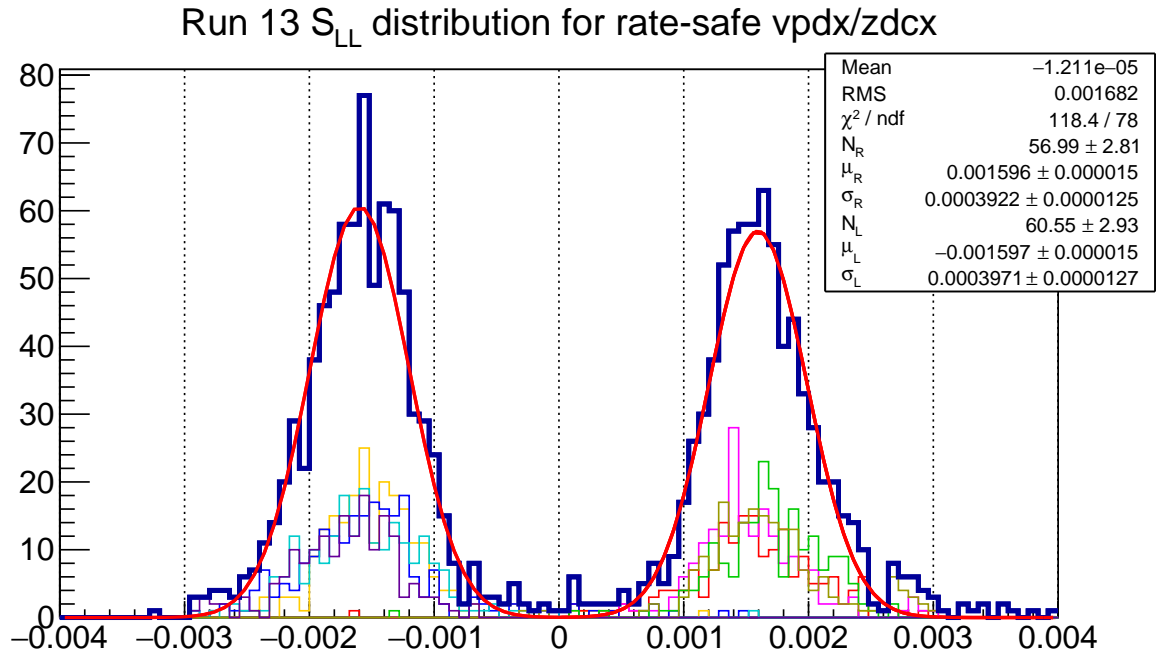


Figure 5.9: Run 13 S_{LL} for rate-safe VPD while treating rate-safe ZDC as a relative luminosity measurement

5.1.4 Scaler Self-Consistency via A_N Cross Ratio: Δ_{D_N} Method

A completely alternative method to compute a systematic uncertainty from the relative luminosity is to measure A_N in a scaler detector by two different methods: the “cross-ratio method”, which *does not* need a relative luminosity, and the standard method (similar to measuring A_{LL}), which *does* need a relative luminosity. The cross-ratio A_N can be compared to the A_N measured using the relative luminosity; a difference between the measurements indicates how much the asymmetry is biased by the relative luminosity.

The cross-ratio method (see, for example, [8]) exploits the following azimuthal symmetry in order to cancel out the need for a relative luminosity measurement. Let $N_{\uparrow(\downarrow)}$ be the π^0 yield for incoming spin-up(down) protons and let $\mathcal{L}_{\uparrow(\downarrow)}$ be the luminosity. Let Ω be the product of efficiency and acceptance for a detector. Now assume the detector is split left and right, and denote their yields, luminosities, and acceptance times efficiency by a superscript L for left and R for right. The assumed azimuthal symmetry is about a 180° rotation about the beam axis:

$$\frac{N_\downarrow^L}{\Omega^L \mathcal{L}_\downarrow} = \frac{N_\uparrow^R}{\Omega^R \mathcal{L}_\uparrow} \text{ and } \frac{N_\uparrow^L}{\Omega^L \mathcal{L}_\uparrow} = \frac{N_\downarrow^R}{\Omega^R \mathcal{L}_\downarrow} \quad (5.8)$$

By writing out the expression for A_N for both the L and R halves of the detector and uniting them via this symmetry, one can express A_N as the so-called “cross-ratio”, which is independent of a relative luminosity:

$$A_N^{(\text{cross-ratio})} = \frac{1}{P} \cdot \frac{\sqrt{N_\uparrow^L N_\downarrow^R} - \sqrt{N_\uparrow^R N_\downarrow^L}}{\sqrt{N_\uparrow^L N_\downarrow^R} + \sqrt{N_\uparrow^R N_\downarrow^L}}, \quad (5.9)$$

where P is the polarization of proton beam used to compute A_N .

A value of A_N can also be determined using the associated relative luminosity (R_1 for the yellow beam and R_2 for the blue beam, as defined in appendix B). Denoting the relative luminosity as $r \in \{R_1, R_2\}$, consider the difference of the A_N values:

$$D_N := A_N^{(\text{cross-ratio})} - \frac{1}{P} \cdot \frac{N_\uparrow - r N_\downarrow}{N_\uparrow + r N_\downarrow} \quad (5.10)$$

The uncertainty on r propagates as

$$\Delta_{D_N} = \left| \frac{\partial D_N}{\partial r} \right| \cdot \Delta_r = \frac{1}{2} \cdot \frac{1}{P} \cdot \frac{\Delta_r}{r} \quad (5.11)$$

The uncertainty on a measurement of D_N therefore is sensitive to a relative luminosity uncertainty, Δ_r/r ; however, this r is a relative luminosity used for a *single*-spin asymmetry.

Since A_N is not sensitive to polarization, a measurement of Δ_{D_N} is sensitive to how well the relative luminosity is in general, and can be used for A_{LL} as well, which just uses different combinations of incoming spin-states than A_N does. To see this more a bit more clearly, consider the statistical uncertainties on the relative luminosity (see appendix B); they are

$$\begin{aligned}\Delta_{R_1} &= \sqrt{\frac{(\sigma_{-+}^2 + \sigma_{++}^2)(\mathcal{L}_{--} + \mathcal{L}_{+-})^2 + (\sigma_{--}^2 + \sigma_{+-}^2)(\mathcal{L}_{-+} + \mathcal{L}_{++})^2}{(\mathcal{L}_{--} + \mathcal{L}_{+-})^4}} \\ \Delta_{R_2} &= \sqrt{\frac{(\sigma_{+-}^2 + \sigma_{++}^2)(\mathcal{L}_{--} + \mathcal{L}_{-+})^2 + (\sigma_{--}^2 + \sigma_{-+}^2)(\mathcal{L}_{+-} + \mathcal{L}_{++})^2}{(\mathcal{L}_{--} + \mathcal{L}_{-+})^4}} \\ \Delta_{R_3} &= \sqrt{\frac{(\sigma_{--}^2 + \sigma_{++}^2)(\mathcal{L}_{-+} + \mathcal{L}_{+-})^2 + (\sigma_{-+}^2 + \sigma_{+-}^2)(\mathcal{L}_{--} + \mathcal{L}_{++})^2}{(\mathcal{L}_{-+} + \mathcal{L}_{+-})^4}}\end{aligned}$$

where σ_{ab} is the statistical error on \mathcal{L}_{ab} . If the four luminosities are equal, then although the relative luminosities would all be equal to one, their errors would be equal to each other. Under this assumption, we would therefore have $\Delta_r/r \approx \Delta_{R_3}/R_3$.

Using the above assumption, equation 5.11 is similar to equation 5.2. If we assume polarization of each beam is the same, P , then comparing equation 5.11 and 5.2 reveals the approximating relation

$$\Delta_{A_{LL}} \approx \frac{1}{P} \Delta_{D_N} \quad (5.12)$$

For extracting A_{LL} , the VPD is used for a relative luminosity; therefore, D_N is measured in the VPD. The yields which go into the computation of D_N were taken from the VPD PMT scaler boards, which provide the azimuthal (and pseudorapidity) segmentation needed to compute an A_N . The R_1 and R_2 relative luminosity values appropriate for east and west were taken from the VPD rate-safe corrected counts. The ZDC-SMD detector, which has hodoscope-like segmentation (described in section 5.2), was also used to extract a value of D_N ; the D_N distributions in the ZDC are much wider than those in the VPD, however. The VPD is ultimately more self-consistent than the ZDC, and this is the primary reason the VPD is used for the relative luminosity in the overall $A_{LL}^{\pi^0}$ analysis.

In Run 12, the VPD PMTs were not read-out in any scaler system; only the overall VPD scaler counts were read-out. In Run 13, however, VPD PMT scaler counts were read-out, and thus the focus of this self-consistency analysis is constrained to the Run 13 VPD. Figure 5.10 shows D_N distributions for the east and west VPD systems. The dependence of D_N on spin patterns was also assessed by plotting the distributions for each spin pattern listed in figure 5.7, where the pattern number here is defined as 10 times the blue pattern number plus the yellow pattern number. In the east VPD, one can observe some mild correlation with spin patterns; this correlation is not nearly as strong in the west VPD,

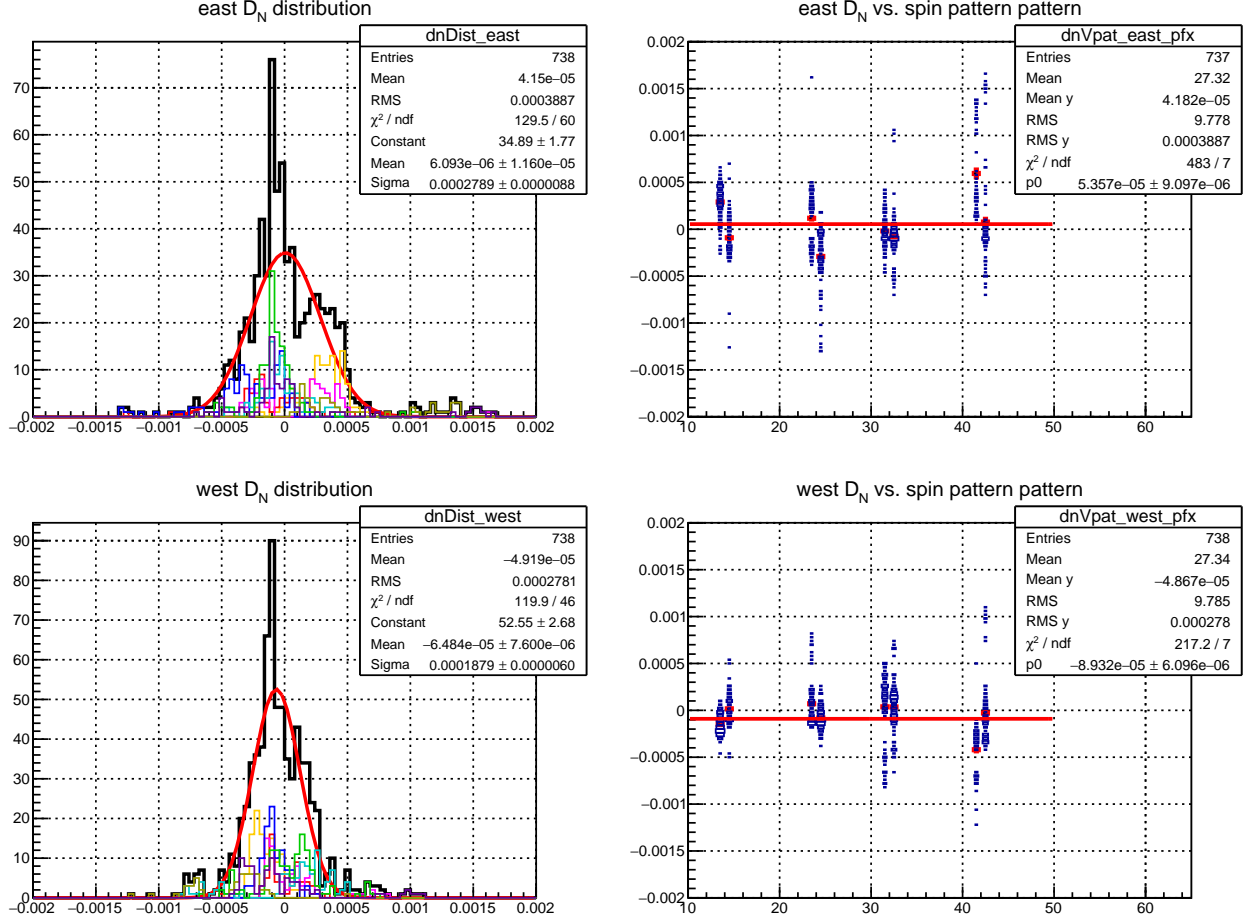


Figure 5.10: Top row is east VPD D_N data and bottom row is west VPD. Left column: D_N distribution; black is full distribution and the colors are for each spin pattern (legend in figure 5.7). A Gaussian fit to the total distribution is also drawn. Right column: D_N vs. spin pattern number; red crosses within each spin pattern indicate the pattern's D_N means and errors and the red horizontal line is an overall fit to those means

however.

The RMS of the east VPD D_N is 3.9×10^{-4} and for the west is 2.8×10^{-4} . The standard deviations from the Gaussian fits are 2.8×10^{-4} and 1.9×10^{-4} for the east and west, respectively; the higher width in the east VPD is attributed to its mild spin pattern correlation.

From equation 5.12, in order to obtain a systematic on $A_{LL}^{\pi^0}$ one needs to multiply by an additional factor of $1/P_B$ or $1/P_Y$; the correct factor is the polarization which is *not* already multiplied in D_N , e.g., use Δ_{D_N}/P_B for the east systematic since $D_N^{\text{east}} \propto 1/P_Y$. By using standard deviation from the fit as Δ_{D_N} , we have

- East: $\Delta_{A_{LL}} [\Delta_{D_N}] = \frac{\Delta_{D_N}^{\text{east}}}{P_B} = \frac{2.8 \times 10^{-4}}{0.57} = 4.9 \times 10^{-4}$

- West: $\Delta_{A_{LL}} [\Delta_{D_N}] = \frac{\Delta_{D_N}^{\text{west}}}{P_Y} = \frac{1.9 \times 10^{-4}}{0.57} = 3.3 \times 10^{-4}$
- Average over East and West: $\langle \Delta_{A_{LL}} [D_N] \rangle = 4.1 \times 10^{-4}$

5.1.5 Correlations of Run 13 Δ_{R_3} and S_{LL} with Spin Patterns

The exact origin of this Run 13 separation of Δ_{R_3} (or of S_{LL}) with respect to spin patterns remains under investigation. One possible cause of a correlation with spin patterns is scaler afterpulsing. Figure 5.11 shows the rate-safe corrected number of counts for all data in Run 13, normalized over all bunch crossings. The two usual abort gaps appear from bunch crossings 31-39 and 111-119. Furthermore, about 25% of the data had bunch crossings 69 and 70 empty, creating a divot in the distributions. The nominal counts vs. bunch crossing plot (bottom right of figure 5.11) shows what an ideal scaler counter would see, given each bunch crossing had a single collision and the bunches were also filled ideally; this nominal bunch crossing distribution will be referred to as the “kernel” distribution, where abort gaps have zero counts and the divot at bunch crossings 69-70 is set at 75% of the typical filled bunch crossing.

The first few bunch crossings after each abort gap, denoted as the “post-abort” bunch crossings, show a slow rise in the number of counts; this is much more evident in the BBC than in the ZDC or VPD. Furthermore, the BBC shows a complementary fall-off of the number of counts in the abort gaps (this is also seen in the ZDC and VPD, but the abort gap counts are down by a factor of 10,000 from the nominal number of counts). These abort gap and post-abort features are also seen in and after the 69-70 divot.

The most likely reason for this post-abort gap bunch crossing behavior is claimed to be afterpulsing somewhere in the scaler systems. In order to explore a possible afterpulsing effect, first let the pulse seen by scaler phototubes be $P(t)$, where t represents time and can be mapped to bunch crossing number b by multiplying by the bunch crossing rate (RHIC clock frequency) f_c . Let the pulse shape be defined by a single pulse confined to one bunch-crossing plus an “afterpulse” $A(b)$, which could perhaps be associated with dark current:

$$P(b) = \frac{1}{\sigma_P \sqrt{2\pi}} \cdot e^{-b^2/2\sigma_P^2} + A(b) \quad (5.13)$$

where σ_P is sufficiently small for the pulse to be confined to within one bunch crossing. Let $K(b)$ be the kernel distribution as defined above; this is the distribution one would see if $P(t)$ were ideal and there was no afterpulsing. The number of scaler counts per bunch crossing, denoted $N(b)$, is then modelled as a convolution of the pulse shape and the kernel

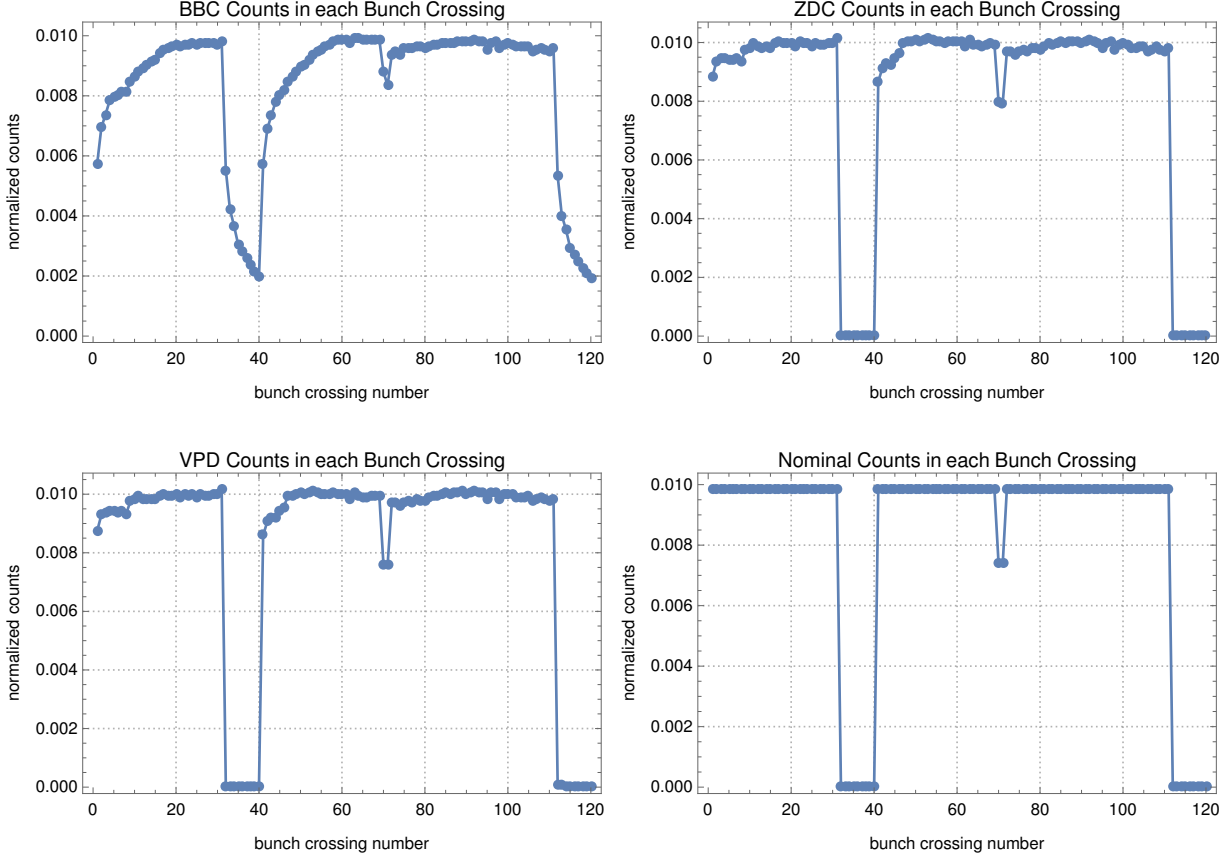


Figure 5.11: Rate-safe corrected number of counts vs. bunch crossing number for the BBC (top left), ZDC (top right), VPD (bottom left), and for an ideal scaler (bottom right). All plots are normalized.

distribution:

$$N(b) = (K * P)(b) = \int_{-\infty}^{\infty} d\beta K(\beta)P(b - \beta) \quad (5.14)$$

In an attempt to determine what might have been the original $P(b)$ for a given $N(b)$, several different deconvolution algorithms were tried. Most of them returned similar results, but with varying levels of noise and artifacts coming from noise in the $N(b)$ data, from the assumption of $K(b)$ and its comparison to the actual bunch filling quality, and from the deconvolution algorithm itself. The algorithm which resulted with $P(t)$ shapes with the least amount of noise was the Tikhonov regularization method in Mathematica; more details can be found in Mathematica documentation for the functions “ListDeconvolve” and “ImageDeconvolve”.

The deconvolved $P(b)$ results are shown in figure 5.12 for each of the three scaler systems, along with the deconvolved nominal pulse in order to test the algorithm. The horizontal axis is bunch crossing number, but the pulse begins at bunch crossing number 60; this is just a

consequence of the deconvolution algorithm and hence the horizontal axis numbers can be interpreted as the number of bunch crossings after the pulse, plus 60. Figure 5.13 shows a zoom in of the noise level on the deconvolved nominal pulse, which is at the 1% level. Clearly the BBC shows some afterpulsing effect, since $P(b)$ takes ~ 15 bunch crossings to settle to zero; the ZDC and VPD pulses decay to zero after 1 or 2 bunch crossings. The nominal pulse is as expected: a delta function at bunch crossing 61 plus noise.

The bunch-crossings with the least amount of afterpulsing effects are those which are just after the abort gaps, since they feel little-to-no afterpulsing from the preceding abort gap bunch crossings; however, these post-abort bunch crossings show a strong dependence on how far they are from the previous abort gap end. After sufficiently many post-abort gap bunch crossings, the after-pulsing effect is saturated and no more increase in the number of scaler counts per bunch crossing is observed. Because we are searching for a dependence on the relative luminosity systematics on spin patterns, we now turn our attention to spin patterns in the post-abort gap regions.

Table 5.2 shows the absolute value of the difference in the number of S crossings (N_S) and the number of O crossings (N_O) within N_{pa} bunch crossings after each abort gap; note that the spin pattern coming out of each abort gap is the same, since it is a pattern which repeats every 8 bunch crossings and the post-abort regions begin at bunch crossing 0 and at bunch crossing 40. In Run 12, the number of S crossings and O crossings balances out every other bunch crossing. In Run 13, however, the number of S crossings exceeds the number of O crossings by as much as 4 (and vice versa); if the observed afterpulsing effect occurs for ~ 4 bunch crossings, then we could see a bias in R_3 values which correlates to spin pattern classes A and B. For example, if the first four post-abort gap crossings are OOOO, then we have *less-than-nominal* O scale counts which would consequently bias R_3 toward higher values. If the strength of the effect is stronger in the ZDC with respect to the VPD (or vice versa), then the difference in their R_3 values becomes biased by spin pattern class; consequently so does the $A_{LL}^{\pi^0}$ systematic uncertainty from R_3 uncertainty.

The above ideas can be tested by omitting the first few post-abort gap bunch crossings and recomputing Δ_{R_3} . Figure 5.14 shows the Gaussian fit results of Δ_{R_3} distributions for the omission of N_{pa} post-abort gap bunch crossings, from 0 omitted up to 40. The blue points indicate two Gaussian fits were used to fit two separate peaks and the green points indicate one Gaussian fit to one peak. The open magenta points indicate a single Gaussian fit to what may actually be two peaks, but the two peak fit was too difficult to implement. The following features in this oscillation are observed:

- Nodes at approximately $N_{pa} \in \{4, 12, 20, 28, 36\}$ and anti-nodes in between

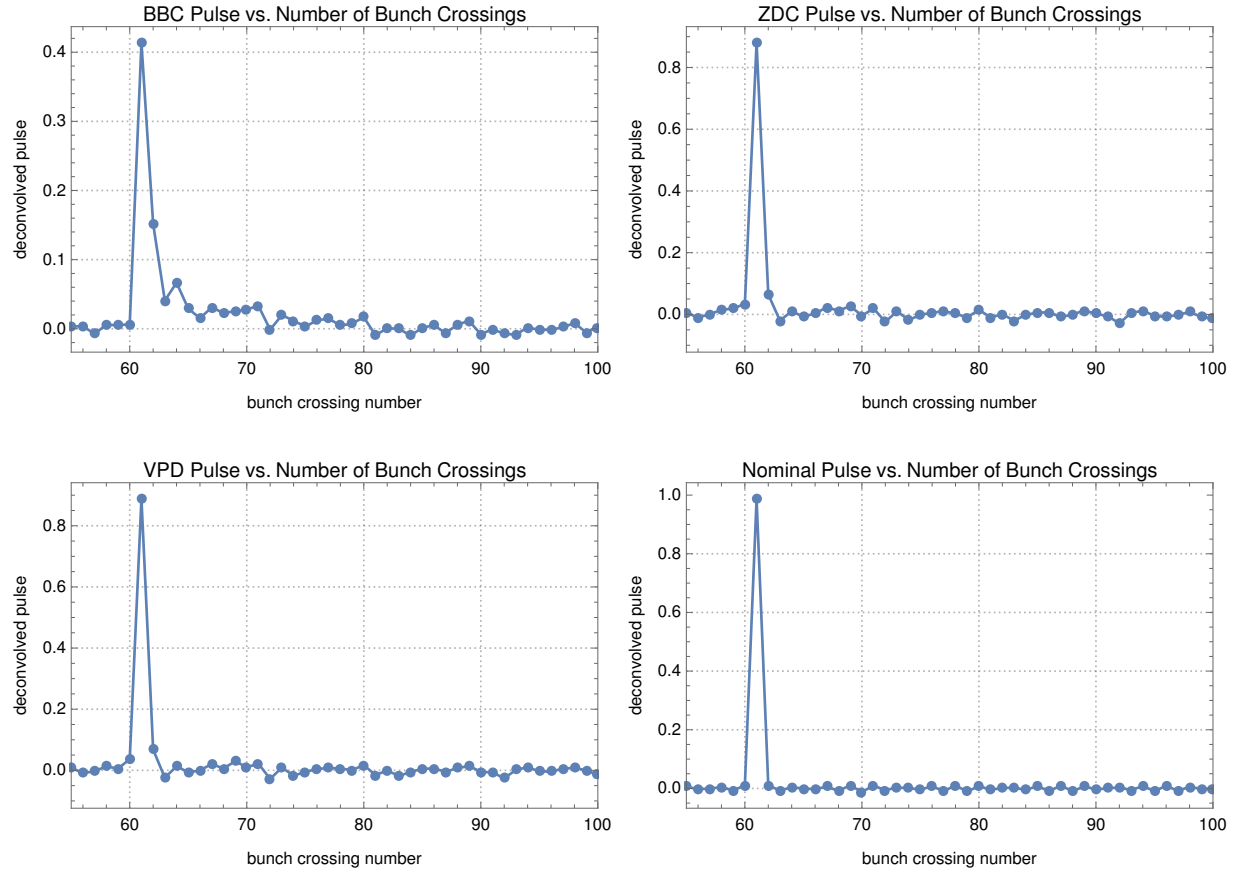


Figure 5.12: Deconvolved pulse $P(b)$ vs. bunch crossing number for the BBC (top left), ZDC (top right), VPD (bottom left), and for an ideal scaler (bottom right). The pulse is centered at bunch crossing 61.

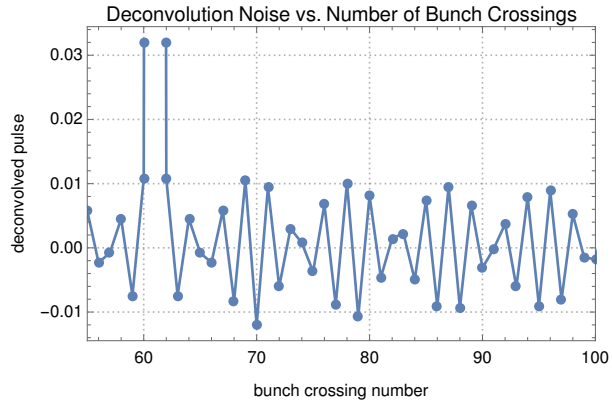


Figure 5.13: Deconvolved nominal pulse $P(b)$ vs. bunch crossing number, zoomed in to show the noise

N_{pa}	Run 12	Run 13
1	1	1
2	0	2
3	1	3
4	0	4
5	1	3
6	0	2
7	1	1
8	0	0
9	1	1
10	0	2
11	1	3
12	0	4

Table 5.2: Double-spin state differences $|N_S - N_O|$ within N_a bunch crossings after an abort gap

- The largest splitting of the peaks is in the $N_{pa} = 0$ case, that is, in the full data set.
- Slight damping, which is likely due to after-pulsing saturating the number of scaler counts
- The period is 8 bunch crossings, which is the same as that of the spin patterns
- The distance between any node and its nearest anti-node is 4, which is related to the pattern of 4 “S” bunch crossings followed by 4 “O” bunch crossings
- The amplitude is anti-correlated with the value of $|N_S - N_O|$ from table 5.2

As a complementary study, removal of N_{pa} pre-abort gap bunch crossings was tested. Figure 5.15 shows the result of the distribution fits. All distributions are bimodal, however, there is still sinusoidal behavior of the distribution means, with respect to N_{pa} . There is no value of omitted N_{pa} pre-abort gap bunch crossings for which the distributions merge; this property verifies that the observed bimodal structure is sensitive to only post-abort gap bunch crossings.

This test of omitting post-abort gap bunch crossings was also performed on S_{LL} , although only up to $N_{pa} = 8$. The results are similar and are given in figures 5.16-5.17; note that although the ZDCE/VPDX raw asymmetry with CDF corrections is shown here, the general result holds for the rate-safe corrected VPD/ZDC S_{LL} as well.

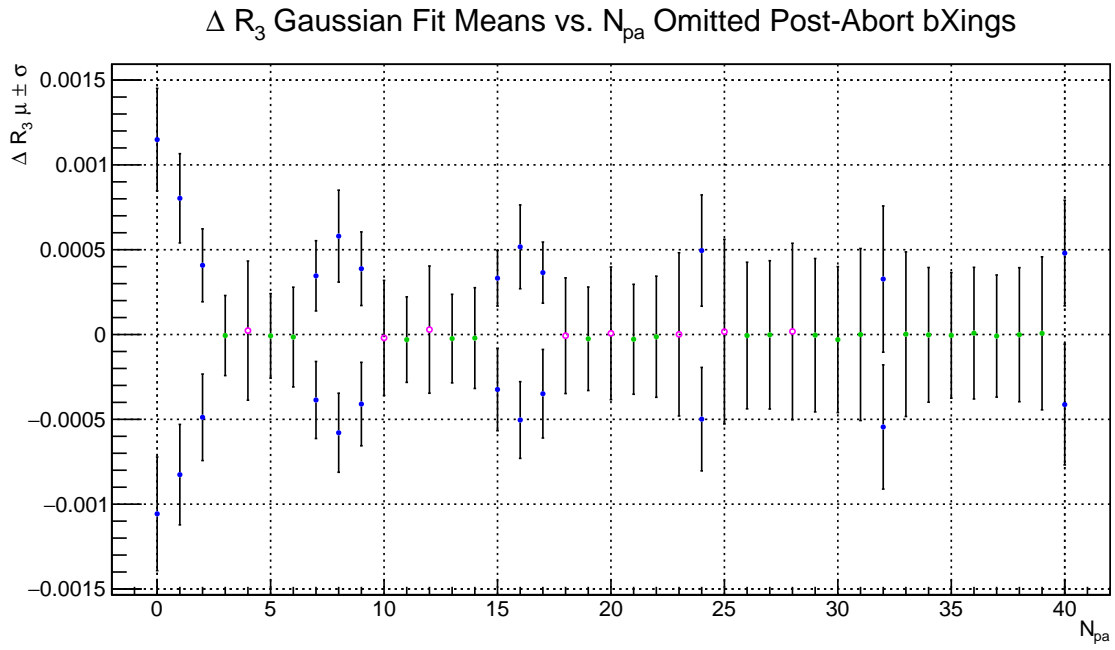


Figure 5.14: Gaussian fit results for ΔR_3 distributions as a function of number of omitted post-abort gap bunch crossings, N_{pa} . Blue: 2 peaks and 2 Gaussians; Green: 1 peak and 1 Gaussian; Open Magenta: possibly 2 peaks but 1 Gaussian.

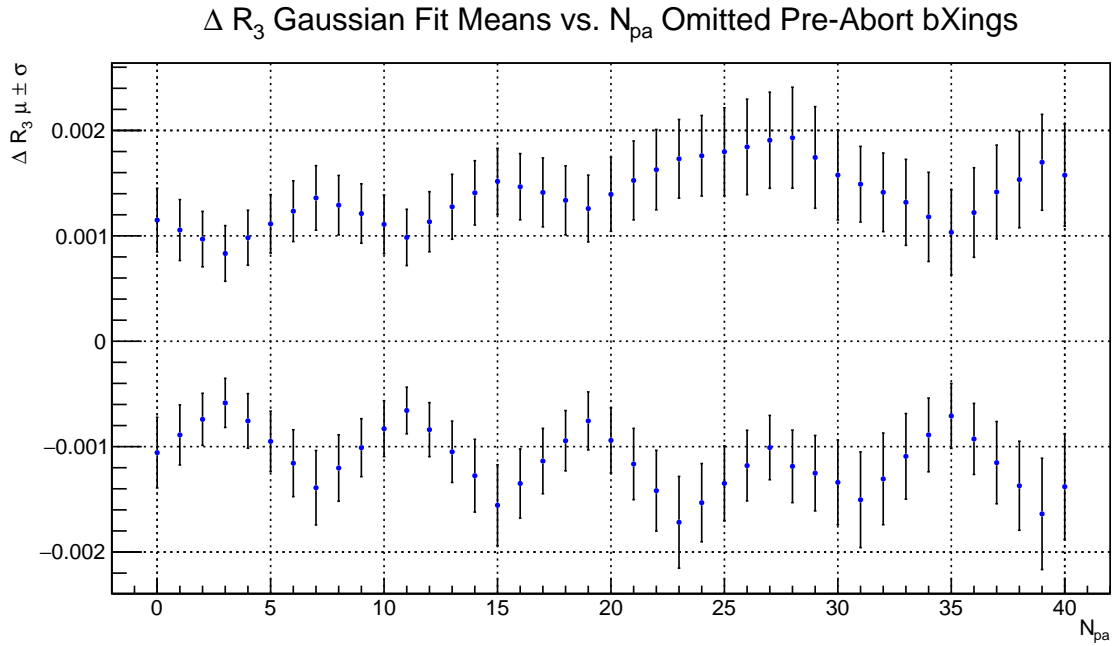


Figure 5.15: Gaussian fit results for ΔR_3 distributions as a function of number of omitted pre-abort gap bunch crossings, N_{pa} . In this case, all distributions were bimodal

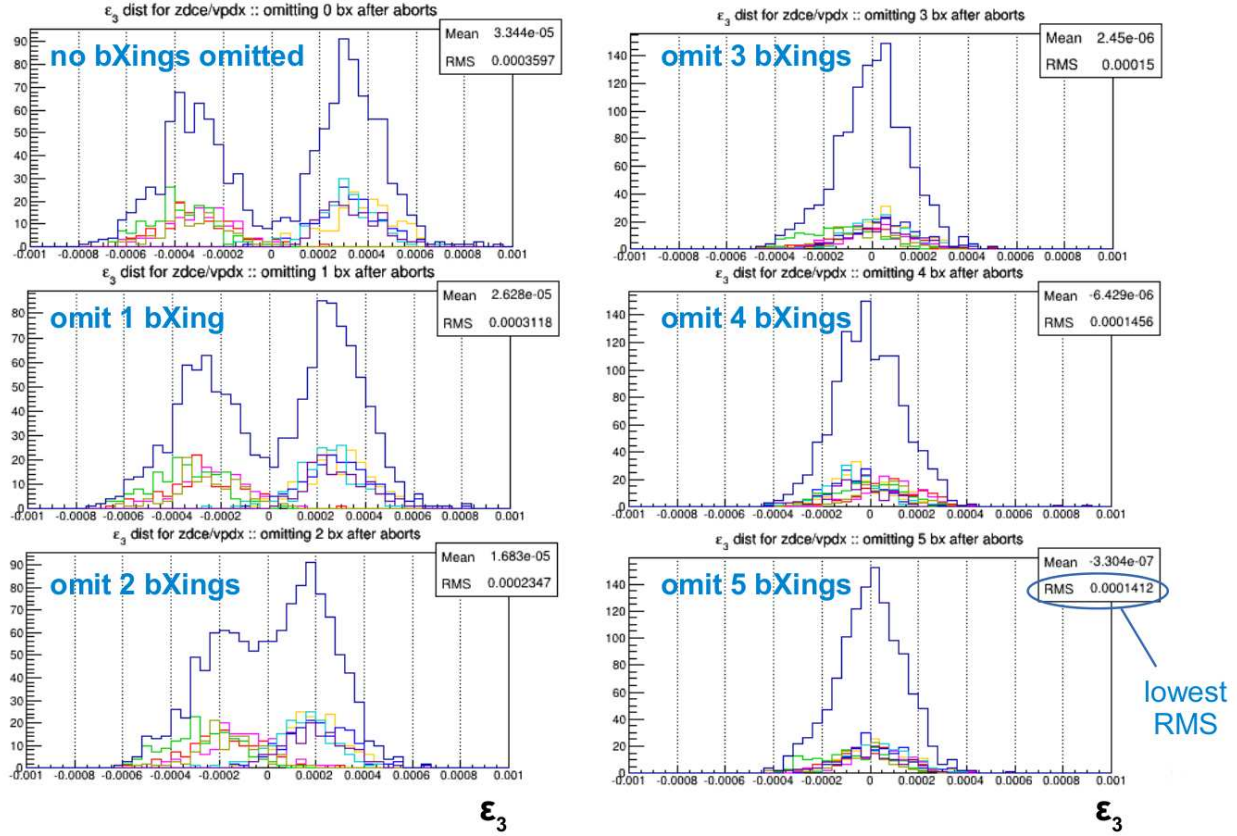


Figure 5.16: Raw ZDCE scaler asymmetry distributions with VPDX as relative luminosity; Run 13. Each panel is for a different number of bunch crossings after each abort gap omitted (0-5)

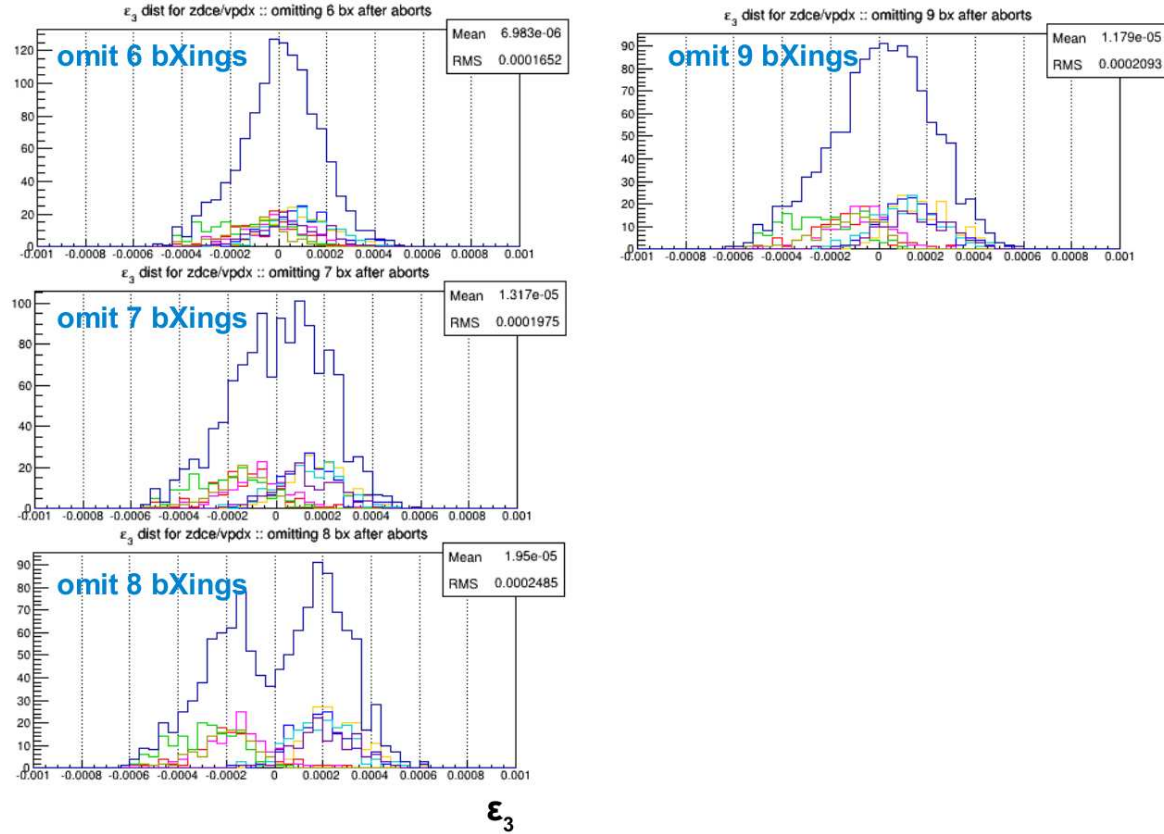


Figure 5.17: Raw ZDCE scaler asymmetry distributions with VPDX as relative luminosity; Run 13. Each panel is for a different number of bunch crossings after each abort gap omitted (6-9)

5.1.6 Summary of Relative Luminosity Systematics

Table 5.3 shows a summary of the systematic uncertainties on $A_{LL}^{\pi^0}$ from relative luminosity. While they are mostly consistent with each other, we have ultimately decided to use the $\Delta_{A_{LL}} [\Delta_{R_3}]$ values in order to be conservative and because it is the method with the simplest implementation and interpretation.

Method	Run 12	Run 13
$\Delta_{A_{LL}} [\Delta_{R_3}]$	2.1×10^{-4}	4.9×10^{-4}
$\Delta_{A_{LL}} [\Delta_{S_{LL}}]$	1.9×10^{-4}	4.1×10^{-4}
$\Delta_{A_{LL}} [\Delta_{D_N}]$	N/A	4.1×10^{-4}

Table 5.3: Summary of $A_{LL}^{\pi^0}$ systematic uncertainties from relative luminosity

This systematic uncertainty is the dominant shift systematic uncertainty on A_{LL} . It is still smaller than the statistical uncertainty, however, which is on the order of 10^{-3} for this analysis.

5.2 Polarization Transverse Component Systematic

While the protons are circulating through RHIC, a transverse polarization is maintained. In order to achieve collisions with longitudinal polarizations, the spin rotators are used to rotate the spin states from transverse to longitudinal when the protons enter the STAR hall, and back to transverse when they exit. This spin rotation may be imperfect, however. A nonzero transverse component of the polarization just before collision propagates as an additional systematic to the A_{LL} measurement.

The ZDC has a hodoscopic scintillator layer with 8 horizontal slats and 7 horizontal slats. This layer is called the Shower Maximum Detector (SMD) layer of the ZDC, or ZDC-SMD, and for Run 12 and 13 was used as the main local polarimeter. Transverse single-spin asymmetries A_N measured during a longitudinally polarized data-taking period can be compared to expected A_N values with transversely polarized collisions. The ratio between these asymmetries for each beam, along with an estimate of the transverse double-spin asymmetry, are all factors of the associated A_{LL} systematic, as will be shown below. We begin by discussing local polarimetry in general; for a more in-depth discussion of local polarimetry and asymmetries from a quantum mechanical point of view, see appendix C.

5.2.1 STAR Local Polarimetry

Consider a beam of protons, accelerated by a synchrotron, entering a local coordinate system such that the beam is along the z -axis, the y -axis is vertical, and the x -axis is parallel to the synchrotron radius. During a transverse polarization running period, let the incoming proton polarization vector be

$$\vec{P}_T = (0, P_T, 0), \quad (5.15)$$

assuming that longitudinal components are zero (*i.e.* negligible Thomas precession). During a longitudinal polarization running period, let the polarization vector be

$$\vec{P}_L = (P_x, P_y, P_z) \quad (5.16)$$

where $P_z \gg P_x, P_y$.

During a transverse run, the raw left/right transverse single-spin asymmetry is

$$\varepsilon_T = P_T A_N = \frac{\sqrt{N_L^\uparrow N_R^\downarrow} - \sqrt{N_R^\uparrow N_L^\downarrow}}{\sqrt{N_L^\uparrow N_R^\downarrow} + \sqrt{N_R^\uparrow N_L^\downarrow}} \quad (5.17)$$

where A_N is the transverse single-spin asymmetry (analysing power), and $N_{L,R}^{\uparrow,\downarrow}$ is the number of hits (e.g., BBC, ZDC, *et al*) which scatter to the left (L) or right (R) for incoming proton spin up (\uparrow) or down (\downarrow).

During a longitudinal run, given that the polarization vector can have arbitrary nonzero transverse components, one can look at two asymmetries: the raw left/right asymmetry

$$\varepsilon_{LR} = P_y A_N = \frac{\sqrt{N_L^+ N_R^-} - \sqrt{N_R^+ N_L^-}}{\sqrt{N_L^+ N_R^-} + \sqrt{N_R^+ N_L^-}} \quad (5.18)$$

and the raw up/down asymmetry

$$\varepsilon_{UD} = P_x A_N = \frac{\sqrt{N_U^+ N_D^-} - \sqrt{N_D^+ N_U^-}}{\sqrt{N_U^+ N_D^-} + \sqrt{N_D^+ N_U^-}}. \quad (5.19)$$

For the longitudinal running period, the notation for yields $N_{L,R,U,D}^{+,-}$ is a bit different: L and R again denote scattering left or right, U and D denote scattering up and down, but since the beam is ideally polarized along the beam axis, the notational superscripts $+$ and $-$ are used to indicate incoming polarization aligned and anti-aligned along the beam axis, respectively. If there is a nonzero transverse component to the polarization, either $+$ will select the transverse component “up” protons and $-$ will select the transverse component

“down” protons or vice versa. Therefore the signs of ε_{LR} and ε_{UD} will depend on the azimuth of the polarization vector; however, it turns out that this sign ambiguity does not matter in the determination of the final polarization vector angles.

Converting to polar coordinates, the longitudinal polarization vector becomes

$$P_x = P_L \sin \theta \cos \phi \quad (5.20)$$

$$P_y = P_L \sin \theta \sin \phi \quad (5.21)$$

where $P_L = \sqrt{P_x^2 + P_y^2 + P_z^2}$ can be measured by the polarimetry group by, for example, pC polarimeters.

Inserting equations 5.20 and 5.21 into equations 5.18 and 5.19 and using the value of A_N from equation 5.17 yields

$$\varepsilon_{LR} = \frac{P_L}{P_T} \varepsilon_T \sin \theta \sin \phi \quad (5.22)$$

$$\varepsilon_{UD} = \frac{P_L}{P_T} \varepsilon_T \sin \theta \cos \phi \quad (5.23)$$

The solution of which gives the polarization polar angle and azimuth:

$$\sin \theta = \frac{P_T}{P_L} \frac{\sqrt{\varepsilon_{LR}^2 + \varepsilon_{UD}^2}}{\varepsilon_T} \quad (5.24)$$

$$\tan \phi = \frac{\varepsilon_{LR}}{\varepsilon_{UD}} \quad (5.25)$$

Instead of measuring ε_{LR} and ε_{UD} , one can fit the single-spin asymmetry cross-ratio as a function of ϕ to the form $\varepsilon_L \sin(\phi + \phi_0)$, with fit parameters ε_L , the asymmetry, and ϕ_0 , a phase angle related to the azimuth of the transverse component of the polarization. This asymmetry is related to the U/D and L/R asymmetries via

$$\varepsilon_L = P_L^\perp A_N = \sqrt{P_x^2 + P_y^2} A_N = \sqrt{\varepsilon_{LR}^2 + \varepsilon_{UD}^2}$$

Since A_N is independent of polarization, we have

$$A_N = \frac{\varepsilon_T}{P_T} = \frac{\varepsilon_L}{P_L^\perp}, \quad (5.26)$$

which implies

$$\frac{\varepsilon_L}{\varepsilon_T} = \frac{P_L^\perp}{P_T} \quad (5.27)$$

Note that by equation 5.24 this verifies $\sin \theta = P_L^\perp / P_L$

5.2.2 Relating Local Polarimetry to A_{LL} Systematic

Let P_B and P_Y be the polarization vectors for two colliding longitudinally-polarized proton bunches. Define their product as $\rho = P_B P_Y$ as well as the products of their components as $\rho^\perp = P_B^\perp P_Y^\perp$ and $\rho^\parallel = P_B^\parallel P_Y^\parallel$.

In the ZDC, we can measure the raw transverse single-spin asymmetry (TSSA), ε_L , and compare it to ε_T , the raw TSSA during a period of transverse polarization with polarization P_T , with the same conditions under which ε_L was measured, such that $P_T^2 \approx P^\parallel{}^2 + P^\perp{}^2 = P^2$ (e.g., disable spin rotators which rotate transverse polarization into longitudinal polarization). Following equations 5.26 and 5.27, we have for each beam

$$\frac{\varepsilon_L}{P^\perp} = \frac{\varepsilon_T}{P} \quad (5.28)$$

Letting $N^{h_B h_Y}$ be the yield, given proton spin states $h_B, h_Y \in \{+, -\}$, and R_3 be the relative luminosity, the measured overall double-spin asymmetry (DSA), denoted \mathbb{A} , may be decomposed into contributions from A_{LL} and from the transverse DSA $A_{NN} = A_\Sigma + A_{TT} \cos 2\phi$ as

$$\mathbb{A} = \frac{1}{\rho} \cdot \frac{N^{++} + N^{--} - R_3(N^{+-} + N^{-+})}{N^{++} + N^{--} + R_3(N^{+-} + N^{-+})} = A'_{LL} + A'_{NN} \quad (5.29)$$

where $A'_{LL} = \varepsilon_{LL}/\rho$ is the measured longitudinal DSA, and $A'_{NN} = \varepsilon_{NN}/\rho$ is the measured transverse DSA (see appendix C for details). The primes denote that these asymmetries are measured with respect to the overall polarization; they can be compared to the “true” DSAs, $A_{LL} = \varepsilon_{LL}/\rho^\parallel$ and $A_{NN} = \varepsilon_{NN}/\rho^\perp$, allowing \mathbb{A} to be expressed as

$$\mathbb{A} = \frac{\rho^\parallel}{\rho} A_{LL} + \frac{\rho^\perp}{\rho} A_{NN} \quad (5.30)$$

By assuming $P^\perp \ll P$, we expand the factors of first term:

$$\frac{P^\parallel}{P} = \sqrt{\frac{P^2 - P^\perp{}^2}{P^2}} = \sqrt{1 - \left(\frac{P^\perp}{P}\right)^2} = 1 + O\left[\left(\frac{P^\perp}{P}\right)^2\right] \quad (5.31)$$

In the context of small asymmetries, the higher order terms can be ignored and we may safely assume $\rho^\parallel/\rho \approx 1$.

The systematic uncertainty then is just the difference between the measured asymmetry

and extracted “true” asymmetry:

$$\Delta_{A_{LL}} [P^\perp] := \mathbb{A} - A_{LL} = \frac{P_B^\perp}{P_B} \cdot \frac{P_Y^\perp}{P_Y} \cdot A_{NN} = \frac{\varepsilon_L^B}{\varepsilon_T^B} \cdot \frac{\varepsilon_L^Y}{\varepsilon_T^Y} \cdot A_{NN} \quad (5.32)$$

where equation 5.28 was used to write the fractional transverse polarization components as ratios of asymmetries measured in the ZDC.

5.2.3 Transverse Component Systematic Result

Figures 5.18-5.20 show the ZDC-SMD raw spin asymmetries, for each beam, plotted versus a run index. Transverse asymmetries ε_T are from two transverse fills’ worth of data taken at $\sqrt{s} = 510$ GeV during the Run 12 longitudinal startup running period; longitudinal asymmetries ε_L are from Runs 12 and 13 longitudinal. Constant fit lines are shown, which indicate the maximum-likely values of these asymmetries and are used in equation 5.32.

The transverse DSA decomposes as $A_{NN} = A_\Sigma + A_{TT} \cos 2\phi$. Both A_Σ and A_{TT} can be measured from Run 11 $\sqrt{s} = 500$ GeV transverse data, using a similar technique to extracting A_{LL} by making use of a relative luminosity. The relative luminosity measurement for Run 11 is very similar to that in Runs 12 and 13. The raw double spin asymmetry is then extracted for bins in p_T using the same Maximum Likelihood Method (MLM) as was used for A_{LL} ; however, this raw asymmetry must also be binned in azimuth. The azimuthal-dependence of the raw asymmetry is then scaled by polarization and fit to the functional form $A_\Sigma + A_{TT} \cos 2\phi$; in other words, A_Σ is an overall offset asymmetry and A_{TT} is the amplitude of its azimuthal modulation.

Regarding the systematic uncertainty on A_{LL} , only A_Σ matters since A_{TT} vanishes upon averaging over azimuth. Figure 5.21 shows the A_Σ result, where vertical error bars are statistical and horizontal error bars are the RMSs of the p_T bins. The p_T binning and η boundaries approximately match those in the $A_{LL}^{\pi^0}$ analysis. Because the transverse polarization component systematic is a sub-dominant systematic on A_{LL} , this rough estimate of A_Σ is sufficient; a conservative upper bound of $A_\Sigma < 0.008$ is used for evaluating the A_{LL} systematic.

Using the mean raw asymmetries from the 3 datasets in equation 5.32, the systematic uncertainty from each Run is:

$$\text{Run 12: } \Delta_{A_{LL}} [P^\perp] = \frac{0.0023}{0.055} \cdot \frac{0.0025}{0.048} \cdot 0.008 = 1.7 \times 10^{-5} \quad (5.33)$$

$$\text{Run 13: } \Delta_{A_{LL}} [P^\perp] = \frac{0.0020}{0.055} \cdot \frac{0.0019}{0.048} \cdot 0.008 = 1.2 \times 10^{-5} \quad (5.34)$$

In comparison to the relative luminosity systematic ($\sim 10^{-4}$) and statistical uncertainties,

this is a rather small contribution to the overall $A_{LL}^{\pi^0}$ uncertainty.

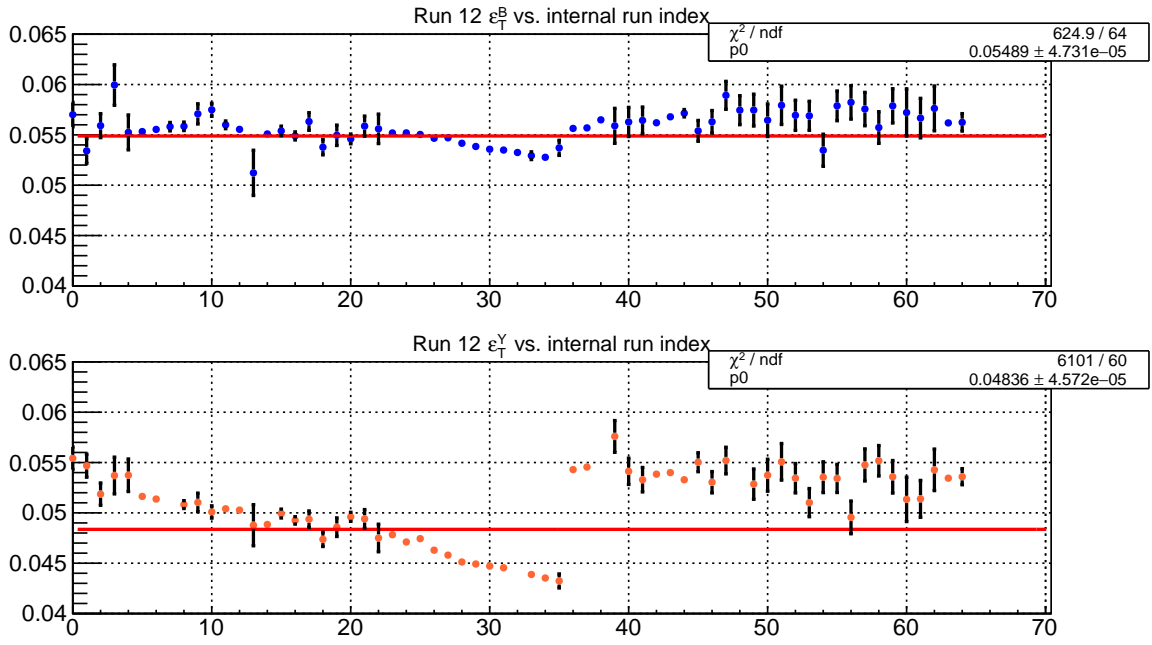


Figure 5.18: Raw single-spin asymmetries in the ZDC-SMD for transverse fills 16570 and 16578 during Run 12 ($\sqrt{s} = 510$ GeV) vs. an internal run index. The jump in asymmetries around run index 35 represents the separation between the two fills.

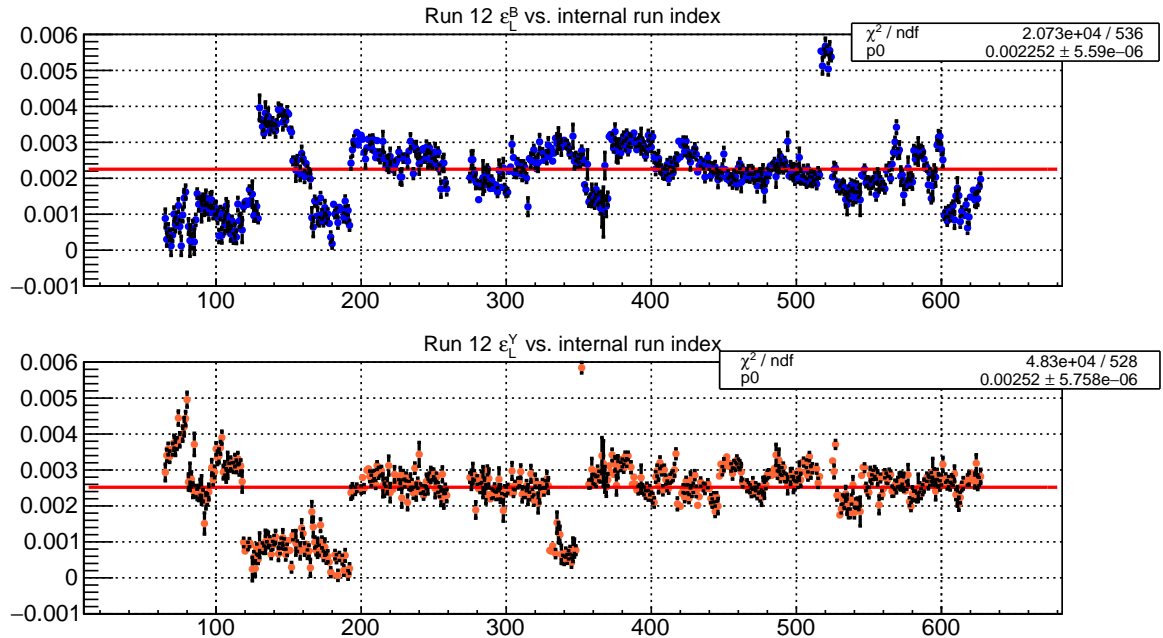


Figure 5.19: Raw single-spin asymmetries in the ZDC-SMD for all longitudinal fills during Run 12 vs. an internal run index.

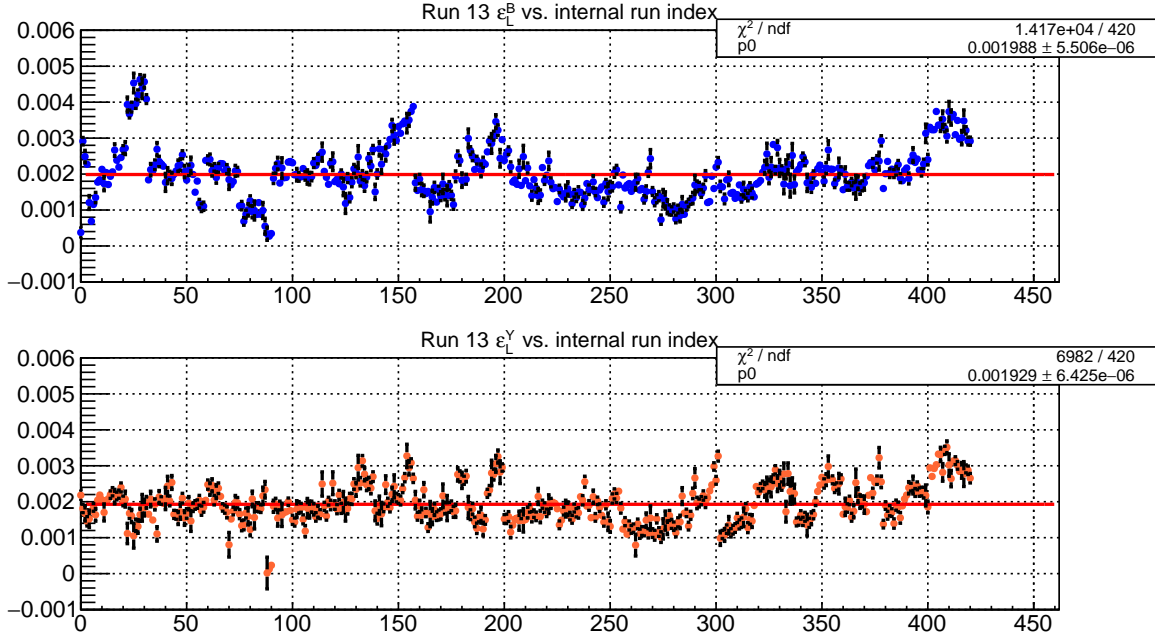


Figure 5.20: Raw single-spin asymmetries in the ZDC-SMD for all longitudinal fills during Run 13 vs. an internal run index.

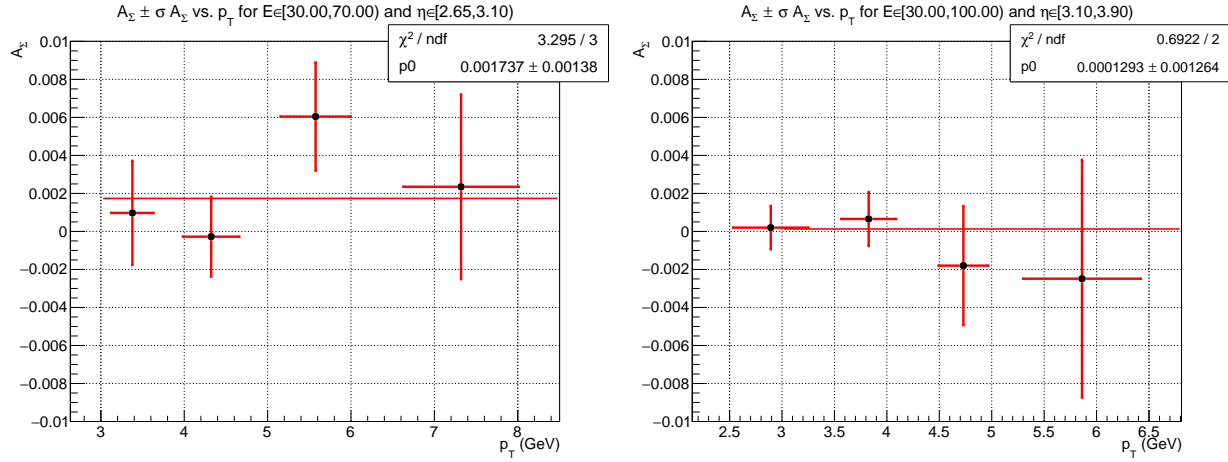


Figure 5.21: Transverse double-spin asymmetries A_Σ from Run 11 transverse data, binned in p_T , for outer η region on the left and inner η region on the right. Vertical error bars are statistical uncertainties and horizontal error bars are p_T bin RMSs.

5.3 p_T Uncertainty

The final $A_{LL}^{\pi^0}$ value will be plotted as a function of $\pi^0 p_T$, thus an estimate of the overall p_T uncertainty for each p_T bin must be assessed. This uncertainty has several contributions: energy uncertainty, vertex uncertainty, position uncertainty, and other systematic uncertainties arising from calibration studies. This section shows how the p_T uncertainty is composed of the different contributions, followed by a discussion of each.

Consider a π^0 with 4-momentum

$$p_{\pi^0} = (E, p_T \cos \phi, p_T \sin \phi, p_T \cot \theta) \quad (5.35)$$

which represents a π^0 scattered at polar angle θ and azimuth ϕ . Assume the longitudinal momentum is approximately equal to the energy, *i.e.*, $p_T \approx E \tan \theta$; this approximation is valid for the forward η range which the FMS occupies. Now consider the π^0 decay photons hitting the FMS a transverse distance of h from the beam, as in figure 5.22. Let R_z be the distance between the shower max plane and the nominal vertex, so that $\tan \theta = h/R_z$. Putting these relations together,

$$p_T(E, h, R_z) \approx \frac{Eh}{R_z} \quad (5.36)$$

The uncertainties on E and $\theta(h, R_z)$ propagate as

$$\frac{\sigma_{p_T}}{p_T} \approx \frac{\sigma_E}{E} \oplus \frac{\sigma_h}{h} \oplus \frac{\sigma_{R_z}}{R_z} \quad (5.37)$$

Thus σ_{p_T} is linear with respect to p_T . Energy resolution, nonlinear PMT response, and calibration uncertainties give σ_E , position uncertainty gives σ_h , and vertex uncertainty gives σ_{R_z} .

A more accurate determination of the p_T uncertainty can be made by making use of invariant mass and taking into account uncertainties on photon separation and energy imbalance; however, extra terms which correct equation 5.37, arising from considering the two photons' kinematics, are negligibly small (see appendix G).

One could also consider correlation terms in the p_T uncertainty. Because there are three uncertainty terms in equation 5.37, there are three possible correlation terms: energy with position, energy with vertex, and position with vertex. These terms are not included in the final p_T uncertainty calculation, for reasons which will be discussed in section 5.3.4.

For every π^0 which is used for determining A_{LL} , we know all quantities in equation 5.37 and consequently have a value of σ_{p_T} for each π^0 . For each p_T bin, we can assemble a

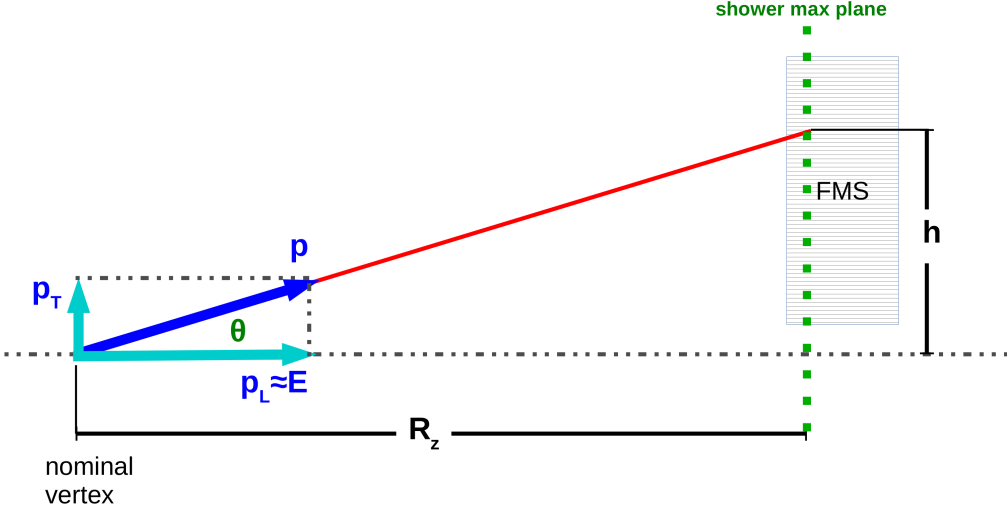


Figure 5.22: Diagram of geometry used to determine p_T uncertainty.

distribution of σ_{p_T} 's and from there determine an overall p_T uncertainty on each A_{LL} vs. p_T point. The following sections will now discuss in detail the contributing uncertainties: σ_E , σ_h , and σ_{R_z} .

5.3.1 Energy Uncertainty

The energy uncertainty can be broken into three major contributions: energy resolution, nonlinear response of the PMTs, and another from calibration. By far the most dominant contribution is from the nonlinear response and the calibration; furthermore, these contributions are dominant in the overall p_T uncertainty. Letting Q represent the energy resolution, G the uncertainty from nonlinear response, and C the uncertainty from calibration, the energy uncertainty is decomposed as

$$\frac{\sigma_E}{E} = \frac{Q}{\sqrt{E}} \oplus G \oplus C \quad (5.38)$$

5.3.1.1 Energy Resolution

The measured energy in a calorimeter is proportional to the number of particles in the electromagnetic shower, denoted N , which follows a Poisson distribution. Since the mean value of N is equal to its variance σ_N^2 , we have

$$\frac{\sigma_N}{N} = \frac{\sqrt{N}}{N} \propto \frac{1}{\sqrt{E}}. \quad (5.39)$$

Thus energy resolution is typically quoted in terms of \sqrt{E} :

$$\frac{\sigma_E}{E} = \frac{Q}{\sqrt{E}} \quad (5.40)$$

for $Q \in (0, 1)$, which depends on the calorimeter material, setup, and energy measurement.

While the energy of a pion is the sum of energies of its decay photons, the energy resolution of the pions is the same as that of the decay photons, because, given $E = \sum_i E_i$, we have

$$\sigma_E^2 = \sum_i \left(\frac{\partial E}{\partial E_i} \right)^2 \sigma_{E_i}^2 = \sum_i \sigma_{E_i}^2 = \sum_i Q^2 E_i = Q^2 E \quad (5.41)$$

An attempt to measure an estimated energy resolution for a single FMS cell was made at Fermilab, by making use of an electron beam which was being used for another test experiment for STAR calorimetry, experiment T1018. A single large FMS cell was wrapped in mylar and coupled to a PMT (radius 1.4 cm, *i.e.*, small cell sized), such that the coupling could be easily adjusted; the original purpose of this test was to determine the dependence of photo-electron yield and energy resolution on the optical coupling between the PMT and the Pb-glass, with the goal to select an optimal coupling for a proposed refurbishment of the FMS. The cell and coupled PMT were made light-tight, mounted on a remotely-controllable stage, and the setup was moved into electron beams with energies of 8 GeV and 16 GeV. Data were then acquired for several different PMT-Pb-glass couplings, in coincidence with several other monitoring detectors, such as a Cherenkov detector, beam hodoscope, and scaler counters.

The criteria used for event selection included a hodoscope geometry cut, which ensured centered electron incidence, as well as minimum ADC cuts on associated Cherenkov and scintillator detectors. The momentum spread of the beam was measured to be about 1.8%, however the cell's energy resolution measurement was heavily dominated by light leakage out of the sides of the cell; it would have been better to test a matrix of cells for an energy resolution measurement. We have therefore chosen to be conservative and to not try to deconvolve the “true” energy resolution from the beam momentum spread.

Because this test at Fermilab was not designed to measure the energy resolution and was focused more on optical couplings, it is not a good measurement of the energy resolution of the FMS; nonetheless, it is the only measurement available at the time of this analysis. Additionally, it was only done for a large cell and no tests were performed with a small cell. Fortunately, this p_T systematic contribution is sub-dominant when compared to the G and C terms in the overall energy uncertainty.

Figure 5.23 shows a plot of the measured energy resolution as a function of various air-

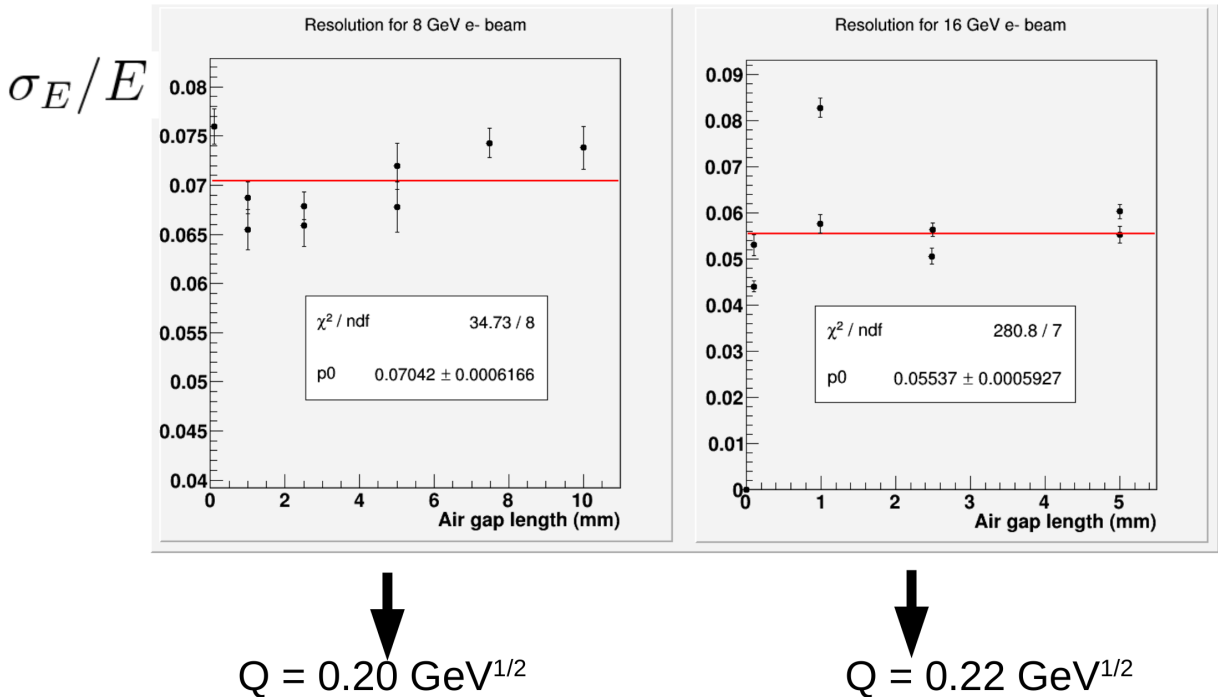


Figure 5.23: σ_E/E vs. PMT-to-Pb-glass airgap length for two different e^- beams; data from test conducted during beam time at Fermilab test experiment T1018

gap sizes between the Pb-glass and PMT; an air-gap size of 0.1 mm actually represents a test where the PMT and the Pb-glass were coupled with optical grease. No substantial dependence on optical coupling was observed in the energy resolution, therefore a fit to a constant is shown in order to estimate a value of $Q \sim 0.2$.

This estimate of $Q \sim 0.2$ is likely an overestimate, given the light leakage out of the sides of the cell as well as the momentum spread of the electron beam. Even at the estimated scale of Q , it represents a sub-dominant systematic uncertainty compared to the other contributions to the energy uncertainty. Furthermore, it is measuring an event-by-event smearing of the energy, not a bias, and therefore gets averaged out in the overall $A_{LL}^{\pi^0}$ measurement. Ultimately it was decided to *drop* this contribution to the p_T systematic uncertainty.

5.3.1.2 Calibration Anchor Point

The fit algorithm for π^0 s has a tendency to over-estimate the 2-photon opening angle at higher π^0 energies. Because of this over-estimation of opening angles, the reconstructed invariant two-photon mass depends on the total energy: a monotonic increase of the mass as a function of energy is observed. Calibration of the FMS based on π^0 masses therefore depends heavily on what range of π^0 energies are selected to calibrate with; this choice of

energy range is known as the “calibration anchor point.” The anchor point range was 28 ± 10 GeV for the large cells and 40 ± 10 GeV for the small cells.

Under the π^0 mass calibration scheme, the reconstructed π^0 mass is corrected to be at the ideal 135 Mev. If a different calibration anchor point energy were chosen, the overall calibration would shift. For relevant changes in the anchor point, the overall energies could change up to about 5%, which represents another possible systematic bias in p_T . Therefore, a value of $C = 5\%$ was adopted as a contribution to the p_T uncertainty, arising from the overall choice of calibration.

5.3.1.3 Nonlinear Response

The overall $A_{LL}^{\pi^0}$ analysis is performed with an implementation of the day-0 non-linear gain $g(E)$ correction applied (see section 3.4.2). The result is compared to a parallel analysis of the data with the day-D corrections applied, as well as a “control” analysis with the corrections disabled altogether. By comparing the p_T means, i.e., the plotted positions of the final $A_{LL}^{\pi^0}$ data points, for the day-0 case with the day-D case, the p_T systematic uncertainty contribution G is determined. The value of G is interpreted as the additional shift in p_T that would incur had we taken into account the increased nonlinearity caused by the radiation damage. The day-0 model is more well-understood as a basic nonlinear E -dependent gain correction, whereas the day-D model as an extention to include radiation damage effects is not as well-vetted; therefore, we have decided to assign the fractional difference between the day-0 and day-D p_T means as a value of G :

$$G = \frac{\langle p_{T_t}^{\text{day-}D} \rangle - \langle p_{T_t}^{\text{day-}0} \rangle}{\langle p_{T_t}^{\text{day-}0} \rangle} \quad (5.42)$$

Figure 5.24 shows a comparison of the day-0 p_T distribution in blue to the day-D distribution in red. The overall shape looks the same, hence the p_T means do not change by much. There are some additional events in the p_T peak region from the day-D model compared to the day-0 model; this is because all of the kinematics cuts apply to the $g(E)$ -corrected values (*i.e.*, not the uncorrected, observed values), which differ between the day-D and day-0 models. Some events which satisfy kinematic cuts after day-D corrections may not satisfy them after day-0 corrections. In fact, more events satisfy kinematic cuts for either day-0 or day-D corrections than for the case where no nonlinear correction is applied; this is because, in general, the $g(E)$ corrections tend to reduce E and p_T , and this reduction is stronger for higher values of E and p_T (see figures 3.13 and 3.14). More events near the upper limits of the cuts are being brought down in E and p_T into the accepted kinematic region; less

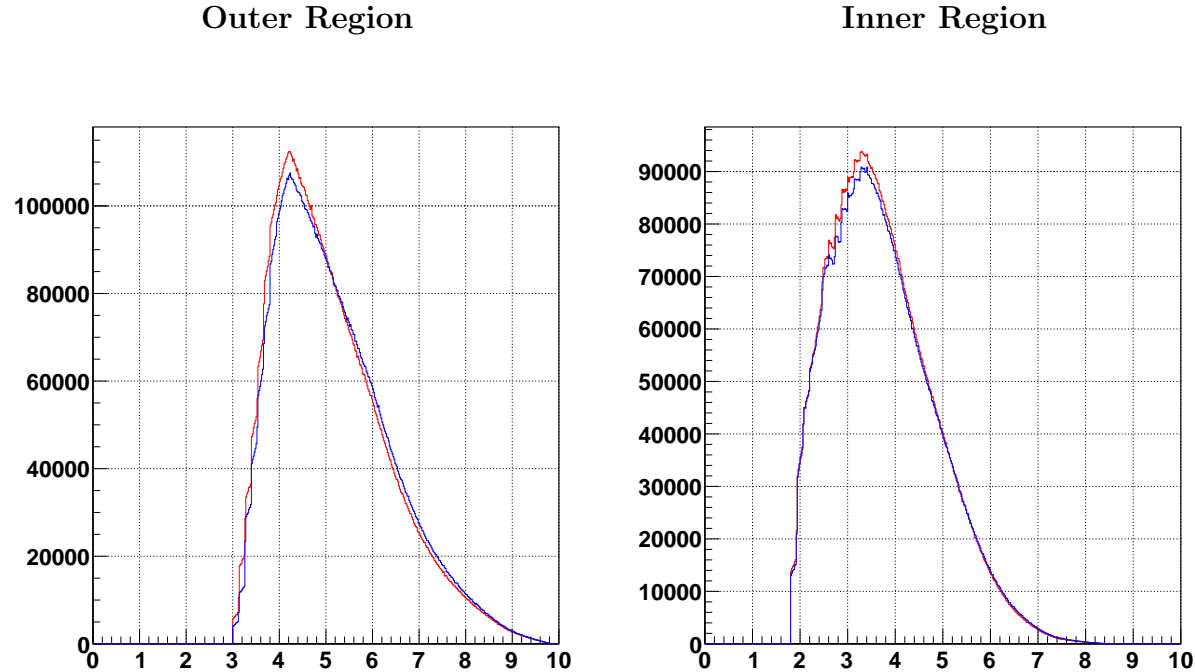


Figure 5.24: Comparison of p_T distributions between day-0 in blue and day- D in red. The day- D distribution has slightly more events, as explained in the text

events near the lower limits of the cuts are “falling” out of the accepted region. Thus overall, applying $g(E)$ corrections tends to increase the overall number of events which pass all cuts.

Table 5.4 lists the p_T means for each p_T bin in the $A_{LL}^{\pi^0}$ analysis for each of the three parallel analyses. The value of G is also listed; this contribution to the overall p_T systematic uncertainty is very small. Note that the fractional differences in p_T means from the control analysis are not very high either; this indicates that the net effect of the $g(E)$ correction on the p_T means is effectively washed out.

5.3.2 Position Uncertainty

Although position uncertainty is expected to be a sub-dominant contribution to the p_T uncertainty, it is nonetheless important estimate its magnitude. Consider a single photon cluster in the FMS. Let E_i denote the energy of the i th tower in the cluster and let (x_i, y_i) be the coordinates of that tower. Consider the photon position (\bar{x}, \bar{y}) as approximated by the energy-weighted mean of the towers:

$$\bar{x} = \frac{\sum_i x_i E_i}{\sum_i E_i} \quad (5.43)$$

p_T Bin		No $g(E)$	Day-0 $g(E)$	Day- D $g(E)$	G
Outer Region	$p_T^{\text{thresh}} - 4.35$	3.91	3.91	3.89	-0.41%
	4.35 – 5.15	4.73	4.73	4.73	-0.07%
	5.15 – 6.15	5.62	5.62	5.62	-0.09%
	$6.15 - p_T^{\max}$	7.08	7.08	7.07	-0.06%
Inner Region	$p_T^{\text{thresh}} - 2.95$	2.50	2.50	2.50	0.17%
	2.95 – 3.70	3.33	3.33	3.33	-0.04%
	3.70 – 4.60	4.11	4.11	4.11	-0.01%
	$4.60 - p_T^{\max}$	5.37	5.37	5.36	-0.29%

Table 5.4: Mean p_T values for each bin and for the cases of no $g(E)$ correction, day-0 $g(E)$, and day- D $g(E)$; the p_T systematic uncertainty contribution G is also given, which compares day-0 $g(E)$ to day- D $g(E)$ p_T means

Derivatives of \bar{x} with respect to each tower energy E_j are $(x_j - \bar{x}) / E$. Given that the energy resolution is $\sigma_{E_j} = Q^2 E_j$, the uncertainty is on the centroid is

$$\sigma_{\bar{x}}^2 = \frac{Q^2 \hat{\sigma}_x^2}{E} \quad (5.44)$$

where $\hat{\sigma}_x^2$ is the energy-weighted variance,

$$\hat{\sigma}_x^2 := \sum_i \frac{E_i (x_i - \bar{x})^2}{E} \quad (5.45)$$

Therefore the error on the photon position, approximated here by the cluster centroid, is proportional to $1/\sqrt{E}$, where the constant of proportionality will be henceforth denoted $W := Q\hat{\sigma}_x$.

In addition to the photon centroid, the penetration of the photon into the glass before the shower initializes must also be taken into account. If the photon has a polar angle θ from the vertex, then the projection of one radiation length X_0 to the front plane of the FMS is $X_0 \sin \theta$. This amount represents another possible uncertainty in the reconstructed transverse position of the photon, especially if the incident angle is high.

A value for W was determined in the RADPHI calorimeter at Jefferson Lab [14], which is an array of FMS small cells. This value can be extended to the large cells as well, by multiplying by a factor 6 cm / 4 cm, which is the approximate ratio of large to small cell transverse sizes. Radiation lengths were measured in other Pb-glass arrays which utilized the same glass; see [15] for large cells and [16] for small cells. Values of W and X_0 are given in table 5.5

Another contribution to the systematic uncertainty is due to the choice of shower shape

	Large Cell	Small Cell
W	$1.065 \text{ cm} \cdot \text{GeV}^{1/2}$	$0.71 \text{ cm} \cdot \text{GeV}^{1/2}$
X_0	3.2 cm	2.5 cm

Table 5.5: W and X_0 values for FMS Pb-glass, measured by RADPHI for small cells and extrapolated to large cells

model. As mentioned before in section 3.3.2, one can use an asymmetric shower shape model, which takes into account corrections from the incident photon angle. The symmetric shower shape model, which is independent of incident angle, is employed in this $A_{LL}^{\pi^0}$ analysis, therefore the possible bias from having not applied incident angle corrections must be taken into account.

At the highest angle of incidence accepted in the FMS, using the asymmetric shower shape returns a photon position a distance of, at the most, 0.5 cm from the position returned from the symmetric shower shape. This bias is another contribution to the overall position uncertainty, and is denoted as A .

Putting everything together, the full position uncertainty is

$$\sigma_h = \frac{W}{\sqrt{E}} \oplus X_0 \sin \theta \oplus A \quad (5.46)$$

Given typical values of E and θ , the typical contribution to the p_T systematic is $\sigma_h/h \sim 1\%$, which is sub-dominant, but not negligible.

5.3.3 Vertex Uncertainty

The offset in the vertex is another possible bias in the overall p_T of events seen in the FMS. This offset, denoted σ_{R_z} , contributes to the p_T systematic as σ_{R_z}/R_z , where R_z is the distance between the FMS and the nominal vertex position, 7.2 m. Figure 5.25 shows the vertex distribution in Run 13, along with distributions filtered by FMS trigger.

Since in Run 13, only the large cells were ultimately analyzed, the LgBS1 trigger is the most unbiased trigger selection on the vertex distribution, which would give a reasonable estimate of the vertex offset in the $A_{LL}^{\pi^0}$ data set. The mean of the LgBS1-filtered vertex distribution is about 9.8 cm, which gives a value of $\sigma_{R_z}/R_z = 1.4\%$; other trigger-filtered distributions give a very similar mean, so this choice of trigger is of little impact. Furthermore, the Run 12 distribution was similar, and therefore this value of 1.4% is used as an overall value for this p_T systematic contribution.

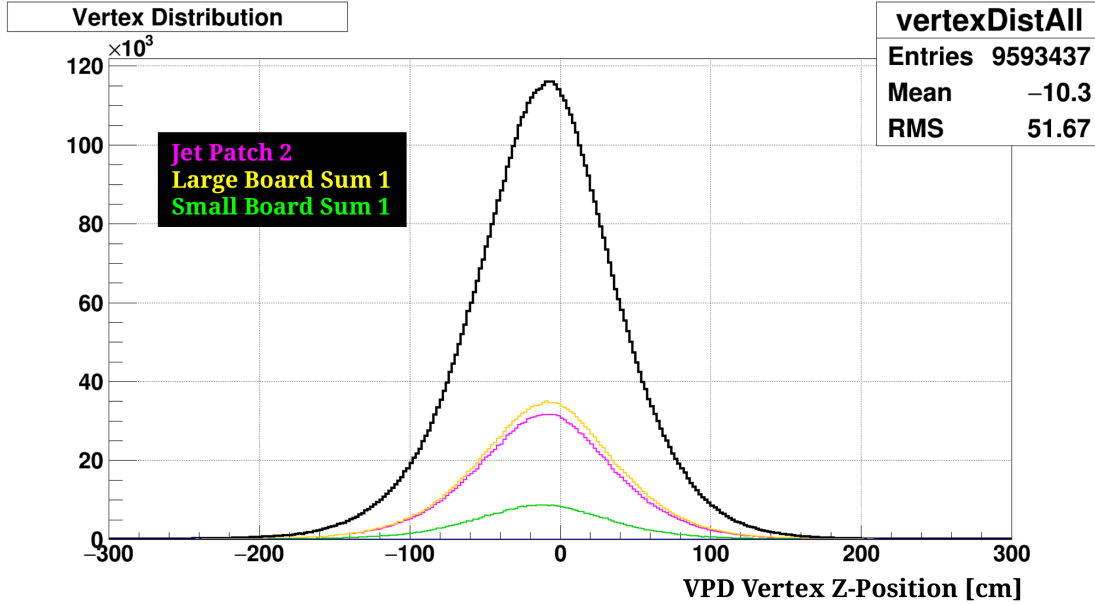


Figure 5.25: Vertex distribution, in particular, the z-position of the vertex as determined by the VPD. Black distribution is all events, magenta is for FMS-JP2, yellow for FMS-LgBS1, and green for FMS-SmBS1.

5.3.4 Correlation Terms in p_T Uncertainty

We now return to the question of including correlation terms: energy with position, energy with vertex, and position with vertex. The measured energy is physically not correlated with the vertex offset, therefore the energy and vertex term vanishes. The position uncertainty and vertex offset could be correlated, however this correlation term also includes factors for the position and vertex uncertainties themselves, both of which are small with respect to correlations involving energy uncertainty. Therefore, the position and vertex correlation term is omitted as negligible. Finally, regarding the energy with position term, the dominant energy uncertainty contribution, C , is from the calibration anchor point and is not correlated with position. The sub-dominant contribution, G , from including radiation damage considerations for the nonlinear gain correction, can be correlated with position and needs some careful thought.

Consider the case where the energy of a shower is underestimated, that is, $E_o < E_t$. This case occurs because the initial part of the shower was not detected, since it was effectively blocked by attenuation due to properties of the Pb-glass as well as radiation damage. The part of the shower that is detected, however, averages out in the transverse plane to a greater value of h than it would have had the entire shower been observed. Therefore, underestimating E leads to an overestimate of h and vice versa; the energy and position

uncertainties are thus anti-correlated. The derivatives of $p_T(E, h, R_z)$ with respect to E and h are both positive, so the anti-correlation therefore makes the overall energy and position correlation term negative and would serve to reduce the overall p_T uncertainty. Because this correlation is based on the sub-dominant p_T uncertainty contribution G , it is expected to be small. Therefore, neglecting this term altogether returns an overall p_T uncertainty which is a slight overestimate. Ultimately, the more-conservative path was chosen and this correlation term was omitted altogether.

5.3.5 p_T Uncertainty Result

To summarize the above discussions, the full p_T systematic uncertainty is

$$\frac{\sigma_{p_T}}{p_T} = [G \oplus C] \oplus \frac{1}{h} \left[\frac{W}{\sqrt{E}} \oplus X_0 \sin \theta \oplus A \right] \oplus \left[\frac{\sigma_{R_z}}{R_z} \right] \quad (5.47)$$

where the contributions from energy, position, and vertex uncertainties have been respectively bracketed. The overall contribution from energy uncertainty ranges 5 – 6%, and is dominant and also dependent on which p_T bin is considered. The position and vertex uncertainties contribute about 1% and 1.5%, respectively, and when added in quadrature with the energy uncertainty, give an overall σ_{p_T}/p_T of approximately 5 – 6%.

The σ_{p_T} value is plotted as a function of p_T , for all π^0 events in the $A_{LL}^{\pi^0}$ analysis. The p_T binning can be seen in the small discontinuities at the p_T bin boundaries, where the slope increases slightly when proceeding to higher p_T .

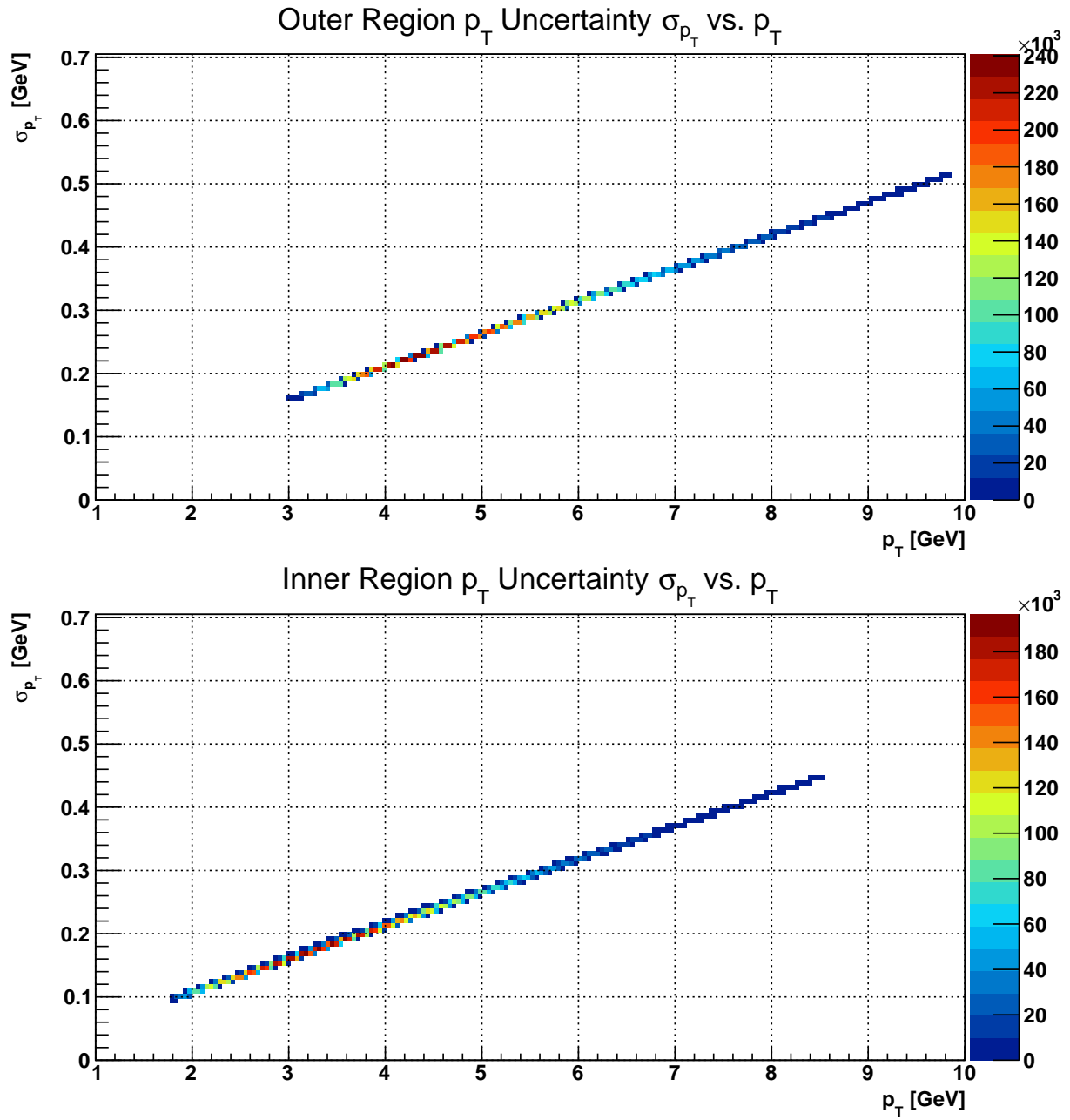


Figure 5.26: Full p_T uncertainty vs. p_T for outer region (top) and inner region (bottom).

5.4 Summary of Systematic Uncertainties

Table 5.6 shows a summary of all of the systematic uncertainties which are included in the $A_{LL}^{\pi^0}$ analysis. They are organized by type and origin, indicated in the classification column; approximate typical values for each uncertainty are given in the rightmost column.

Uncertainty	Symbol	Classification	Typical Value
Relative Luminosity	$\Delta_{ALL} [\Delta_{R_3}]$	$A_{LL}^{\pi^0}$ Shift	$2 - 5 \times 10^{-4}$
Polarization Transverse Component	$\Delta_{ALL} [P^\perp]$	$A_{LL}^{\pi^0}$ Shift	$1 - 2 \times 10^{-5}$
Overall Polarization	$\sigma_{\mathbb{P}_B \mathbb{P}_Y} / \mathbb{P}_B \mathbb{P}_Y$	$A_{LL}^{\pi^0}$ Scale	6.7%
Calibration Bias	C	p_T Bias (from σ_E)	5%
Nonlinear Gain Correction	G	p_T Bias (from σ_E)	< 0.4%
Energy Bias in Position	$W/h\sqrt{E}$	p_T Bias (from σ_h)	< 0.5%
Position Uncertainty from Shower Depth	$X_0 \sin \theta/h$	p_T Bias (from σ_h)	< 0.5%
Position Bias from Shower Shapes	A/h	p_T Bias (from σ_h)	< 1%
Vertex Offset	σ_{R_z}/R_z	p_T Bias (from σ_{R_z})	1.4%

Table 5.6: Summary of $A_{LL}^{\pi^0}$ systematic uncertainties

Chapter 6

$A_{LL}^{\pi^0}$ Analysis

6.1 Kinematic Binning and Means

η Region	p_T Bin	p_T Range (Gev)	E Range (GeV)	η Range
Outer Region	1	$p_T^{\text{thresh}} - 4.35$	30 – 70	2.65 – 3.15
	2	4.35 – 5.15		
	3	5.15 – 6.15		
	4	6.15 – p_T^{\max}		
Inner Region	1	$p_T^{\text{thresh}} - 2.95$	30 – 100	3.15 – 3.90
	2	2.95 – 3.70		
	3	3.70 – 4.60		
	4	4.60 – p_T^{\max}		

Table 6.1: Kinematic bin ranges for the $A_{LL}^{\pi^0}$ analysis. Two η regions were used, each divided into four p_T bins.

Table 6.1 shows the kinematic bins used in the $A_{LL}^{\pi^0}$ analysis. Two η regions are defined: an outer region which has mostly large cells and an inner region with mostly small cells. The η -ring between the regions is set at 3.15 as a rounded value which appropriately separates the large cells and small cells calibration scheme, as presented in the M vs. η plot back in figure 3.2. For the large cells region, both Runs 12 and 13 are analysed; on the other hand, only Run 12 is analyzed for the small cells region, because the small cells were heavily radiation-damaged during Run 13. Furthermore, only the first half of Run 13 was ultimately analyzed because of the accumulating radiation damage.

Four p_T bins are defined separately in the two η regions. Their boundaries were determined by approximately equalizing the π^0 yields within each bin, given the full p_T distribution of the π^0 s considered in $A_{LL}^{\pi^0}$. The value p_T^{thresh} is a time-dependent p_T threshold, which was discussed in section 3.6.2; the lowest kinematically-allowed value of p_T , given

by $p_T^{\min} \approx E^{\min}/\cosh\eta^{\max}$, is less than p_T^{thresh} for both η regions. The upper limit of p_T is $p_T^{\max} \approx E^{\max}/\cosh\eta^{\min}$, which gives a value of $p_T^{\max} = 9.8$ GeV for the outer region and 8.6 GeV for the inner region.

Table 6.2 lists the means of the kinematic variables p_T , E , and η for each of the p_T bins. Note that the p_T means quoted here are the values at which the $A_{LL}^{\pi^0}$ data points are plotted; these p_T means are background corrected (see section 6.4.1), but they are negligibly different from the uncorrected values. The E and η values are not background-corrected. These kinematic means are needed in order to initialize the global fit analysis for which this $A_{LL}^{\pi^0}$ measurement is a key piece.

η Region	p_T Bin	$\langle p_T \rangle$ (GeV)	$\langle E \rangle$ (GeV)	$\langle \eta \rangle$
Outer Region	1	3.91	36.8	2.92
	2	4.73	42.7	2.88
	3	5.62	49.9	2.87
	4	7.08	58.6	2.80
Inner Region	1	2.50	41.2	3.49
	2	3.33	52.7	3.44
	3	4.11	63.8	3.42
	4	5.37	79.2	3.38

Table 6.2: Kinematic bin means for the $A_{LL}^{\pi^0}$ analysis.

6.2 Polarization

The polarization of the proton bunches is measured by an independent set of polarimeters which are located in the RHIC ring, diametrically opposite STAR. They are maintained by the CNI Polarimetry Group at RHIC. For further details of the polarimetry measurement, see [17] and references therein.

For each fill, the polarimetry group provides two numbers along with their uncertainties: the initial polarization at the beginning of a fill, P_0 , and the time dependence of the polarization, $P_1 = dP/dt$. For a given run which occurs T seconds after the beginning of a fill, the polarization is

$$P(T) = P_0 + P_1 T \quad (6.1)$$

The value of T for each run in this analysis is taken from the *middle* of the run.

These polarization measurements are then taken together within each fill and combined into a luminosity-weighted average, returning one value of the polarization for each fill; the FMS JP2 trigger was used for the luminosity measurement. Statistical and systematic errors

were also propagated on a run-by-run and fill-by-fill basis; details can be found in appendix F as well as the polarimetry group’s analysis note, [17].

Figures 6.1 and 6.2 show the polarizations for the blue and yellow beams as well as the polarization product, as a function of a run index. Both the time-dependent polarization $P(t)$ (in blue) and the luminosity-weighted average $P(t)$ (in magenta) are plotted. The data shown in these figures are all the runs which are used in the $A_{LL}^{\pi^0}$ analysis. For scaling the raw double-helicity asymmetry to $A_{LL}^{\pi^0}$, the luminosity-weighted average polarizations are used on a fill-by-fill basis.

For the entire set of runs which are used in this $A_{LL}^{\pi^0}$ analysis, the overall luminosity-weighted polarizations and their errors were also computed. These numbers are given in table 6.3.

	Run 12	Run 13	Runs 12+13
\mathbb{P}_B	0.54 ± 0.019	0.57 ± 0.019	0.55 ± 0.019
\mathbb{P}_Y	0.56 ± 0.019	0.57 ± 0.019	0.56 ± 0.020
$\mathbb{P}_B\mathbb{P}_Y$	0.31 ± 0.020	0.32 ± 0.021	0.31 ± 0.021
L_{int}	57.4 pb^{-1}	6.0 pb^{-1}	63.4 pb^{-1}

Table 6.3: Overall luminosity-weighted average polarizations with uncertainties; blue beam, yellow beam, and product polarizations are shown, as well as the overall integrated luminosity. See appendix F for details.

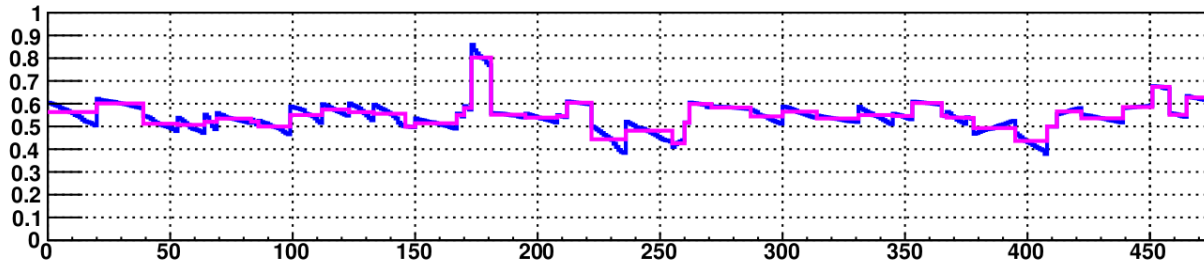
6.2.1 Scale Systematic on $A_{LL}^{\pi^0}$

The final value of A_{LL} is a measured raw double-spin asymmetry ε_{LL} scaled by the polarization product: $A_{LL} = \varepsilon_{LL}/\mathbb{P}_B\mathbb{P}_Y$. Because of this scale, an additional scale systematic on $A_{LL}^{\pi^0}$ is assigned. Table 6.3 indicates this scale systematic for Runs 12 and 13 combined is $\sigma_{\mathbb{P}_B\mathbb{P}_Y}/\mathbb{P}_B\mathbb{P}_Y = 6.7\%$. This is a scale systematic uncertainty on $A_{LL}^{\pi^0}$ that is independent of all the aforementioned shift systematic uncertainties. Furthermore, the aforementioned shift systematic uncertainties define an uncertainty of the overall offset from zero; on the other hand, the polarization scale systematic uncertainty defines an uncertainty in the overall scale of the asymmetry. In the case of $A_{LL}^{\pi^0}$, an asymmetry consistent with zero was measured, therefore this uncertainty is not as meaningful as it would be for a nonzero asymmetry.

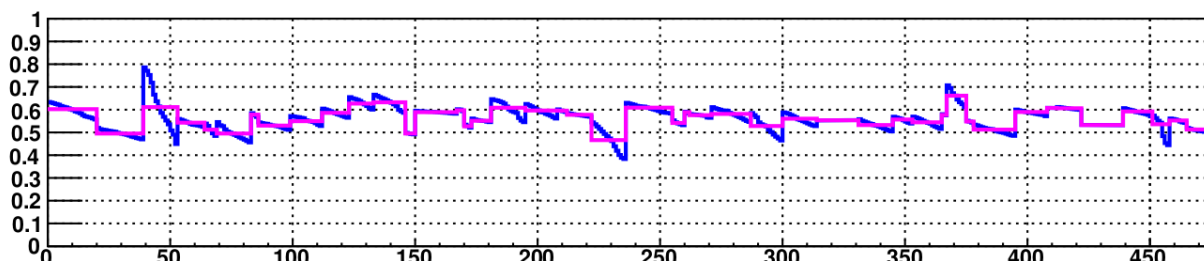
6.3 Maximum Likelihood Method A_{LL} Computation

Data at STAR is typically taken in half-hour periods called “DAQ runs.” In order to combine the data into a single measurement, a Maximum Likelihood Method (MLM) is employed.

Run 12 Blue Beam Polarization vs. Run Index



Run 12 Yellow Beam Polarization vs. Run Index



Run 12 Polarization Product vs. Run Index

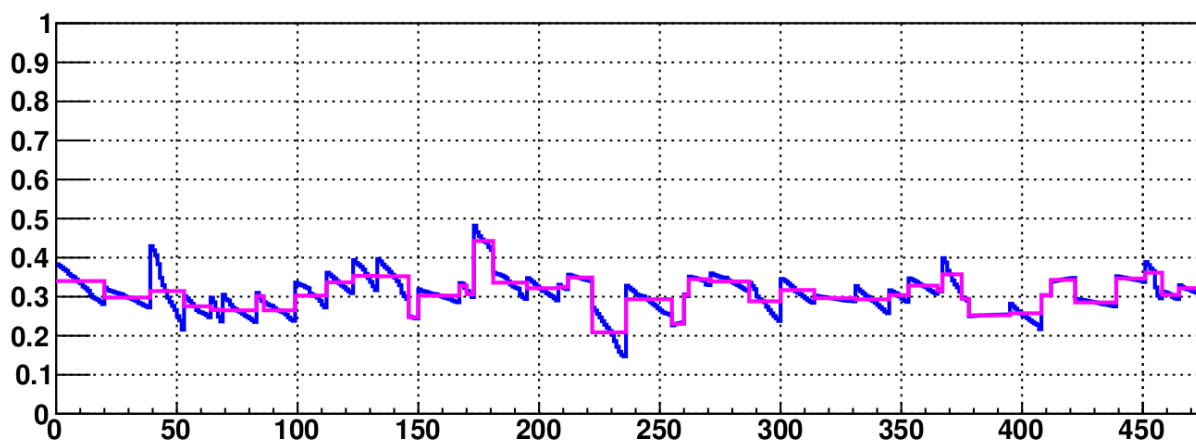
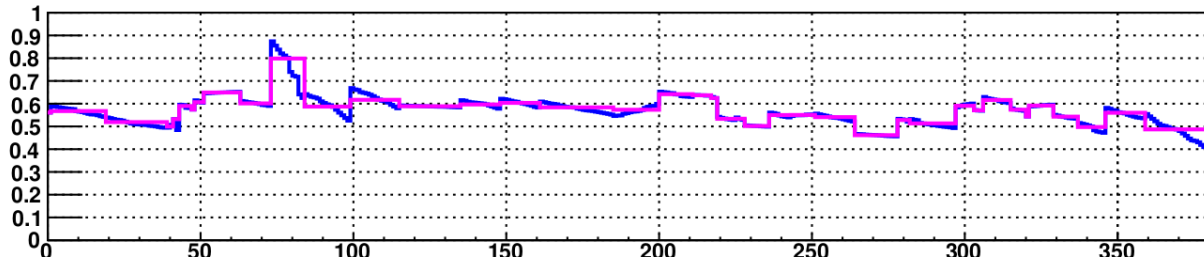
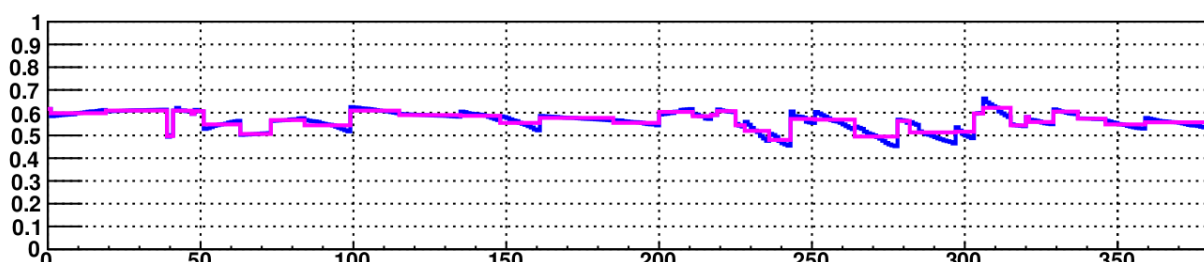


Figure 6.1: Polarizations vs. run index for Run 12; blue line is $P(t)$ and magenta line is the luminosity-weighted average of $P(t)$ within each fill.

Run 13 Blue Beam Polarization vs. Run Index



Run 13 Yellow Beam Polarization vs. Run Index



Run 13 Polarization Product vs. Run Index

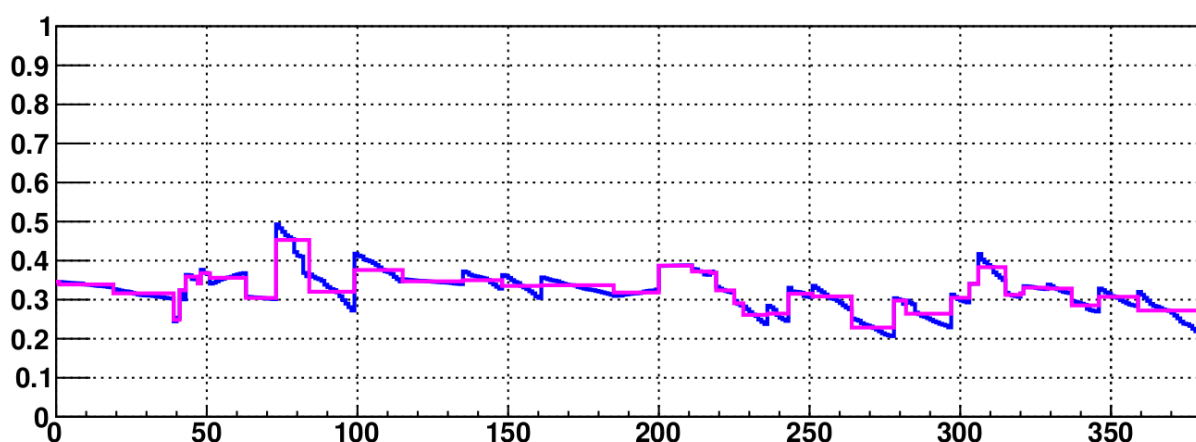


Figure 6.2: Polarizations vs. run index for Run 13; blue line is $P(t)$ and magenta line is the luminosity-weighted average of $P(t)$ within each fill.

See appendix H for the full derivation; only the final formulae are presented in this section.

Let i represent a single DAQ run. Let

$$\begin{aligned} S_i &:= N_i^{++} + N_i^{--} \\ D_i &:= N_i^{+-} + N_i^{-+} \\ P_i &:= P_i^B P_i^Y \end{aligned} \tag{6.2}$$

where $N^{h_B h_Y}$ is the number of π^0 s with the initial proton spin states as h_B and h_Y . Let R_i be the relative luminosity R_3 for run i . The maximum likely A_{LL} , denoted by \bar{A}_{LL} , is

$$\bar{A}_{LL} = \frac{\sum_i P_i (S_i - R_i D_i)}{\sum_i P_i^2 (S_i + R_i D_i)} \tag{6.3}$$

Letting \bar{P} be the average polarization product P_i and $N = \sum_i (S_i + D_i)$, the simplified statistical uncertainty is

$$\sigma_{\bar{A}_{LL}} \approx \frac{1}{\bar{P} \sqrt{N}} \tag{6.4}$$

6.4 Background Corrections

Any measured asymmetry of any signal could be influenced by a possible nonzero asymmetry in the background under the signal. Given measurements of both the signal+background asymmetry and the background asymmetry alone, the signal asymmetry can be extracted from the signal+background asymmetry. Such a procedure is called the “background correction” to the asymmetry and it is applied to $A_{LL}^{\pi^0}$, given a background A_{LL} measurement from the mass window sideband region discussed in section 3.6.3.

6.4.1 Implementation

Let A_M be a measured asymmetry in some mass signal window, with a nonzero background. Let A_B be the asymmetry of the background and let A_S be the signal asymmetry, which we are trying to extract. Let F be the signal purity, defined as the fraction of the events over which A_M is measured that are signal events; thus $1 - F$ is the fraction of events which are from the background. The measured asymmetry is then decomposed as

$$A_M = F A_S + (1 - F) A_B \tag{6.5}$$

The signal asymmetry, corrected by the background asymmetry, is therefore

$$A_S = \frac{1}{F} A_M - \frac{1-F}{F} A_B \quad (6.6)$$

The uncertainties of A_M , A_B , and F , written σ_{A_M} , σ_{A_B} , and σ_F , propagate to the uncertainty of A_S as

$$\sigma_{A_S}^2 = \left(\frac{1}{F}\right)^2 \sigma_{A_M}^2 + \left(\frac{F-1}{F}\right)^2 \sigma_{A_B}^2 + \left(\frac{A_B - A_M}{F^2}\right)^2 \sigma_F^2 \quad (6.7)$$

Typically asymmetries are measured as a function of a kinematic variable $v \in \{\eta, p_T, E\}$ or a set of such variables. The mean v in each measurement bin, denoted by $\langle v \rangle$, also needs to be corrected by the background. Its correction and uncertainty can easily be obtained by replacing the A 's in equations 6.6 and 6.7 by $\langle v \rangle$'s. The final asymmetry plot is of $A_{LL}^{\pi^0}$ vs. p_T and we use $A_{LL}^{\pi^0} = A_S$, $A_{LL}^{\text{tot}} = A_M$, and $A_{LL}^{\text{BG}} = A_B$, as well as similar notation for the mean p_T values. The background correction is then

$$A_{LL}^{\pi^0} = \frac{1}{F} \cdot A_{LL}^{\text{tot}} - \frac{1-F}{F} \cdot A_{LL}^{\text{BG}} \quad (6.8)$$

$$\langle p_T^{\pi^0} \rangle = \frac{1}{F} \cdot \langle p_T^{\text{tot}} \rangle - \frac{1-F}{F} \cdot \langle p_T^{\text{BG}} \rangle \quad (6.9)$$

In practice, the shift in asymmetry due to the background correction is smaller than the statistical uncertainty, but sometimes larger than the systematic uncertainty; the shift in $\langle p_T \rangle$ is typically smaller than 0.01 GeV and is negligible, but nonetheless implemented. A correction on the p_T uncertainty is not implemented here, since the correction itself is negligible and the final p_T uncertainty given in the $A_{LL}^{\pi^0}$ measurement plots represents an overall systematic uncertainty anyway.

Regarding the background-corrected uncertainty, σ_{A_S} from equation 6.7, one can gain an understanding of how large the increase in statistical uncertainty will be, which arises from including the lower-statistics background asymmetry A_B determination along with the higher-statistics A_M in order to produce A_S , which is of less statistics than A_M . Let N_M and N_B be the number of events used for A_M and A_B , respectively. Then, with P the polarization product,

$$\sigma_{A_B} = \frac{1}{P\sqrt{N_B}} = \frac{1}{P\sqrt{N_M(1-F)}} = \sigma_{A_M} \frac{1}{\sqrt{1-F}} \quad (6.10)$$

Inserting this relation into equation 6.7 and assuming $A_B \approx A_M$ gives the ratio of background

corrected uncertainty to the original uncertainty as

$$\frac{\sigma_{A_S}}{\sigma_{A_M}} \approx \frac{\sqrt{2-F}}{F} \quad (6.11)$$

This ratio falls toward 1 as F increases; for $F > 0.75$, the gain in uncertainty is less than a factor of 1.5.

For each runset, contributions to A_{LL}^{tot} and to A_{LL}^{BG} are included in the MLM sums of equation 6.3. The final maximum likely values of these asymmetries are those which are used in equation 6.6 and equation 6.7 is used as the corrected statistical uncertainty. We now turn to a determination of the signal purity, F .

6.4.2 Signal and Background Fitting

Let m be invariant mass. The π^0 (or η) signal is modelled by a skewed Gaussian,

$$G(m) = \exp \left[-\frac{1}{2} \left(\frac{m-\mu}{\omega} \right)^2 \right] \times \left\{ 1 + \operatorname{erf} \left[\frac{\alpha}{\sqrt{2}} \cdot \frac{m-\mu}{\omega} \right] \right\} \quad (6.12)$$

where the fit parameters are μ , the expected and un-skewed signal mass, ω , the signal width, and α , which is related to the skewness. The background is modelled with a linear combination of Chebyshev polynomials of the first kind:

$$B(m) = 1 + \sum_{k=1}^n b_k T_k(m) \quad \text{where } T_k(\cos \theta) = \cos(k\theta) \quad (6.13)$$

The degree used here is $n = 3$ and the coefficients $\{b_k\}$ are the fit parameters. Typical values of $\{b_1, b_2, b_3\}$ obtained from fitting are typically around $\{1.5 \text{ to } 2, -0.5 \text{ to } 0.5, 1 \text{ to } 1.5\}$ for the outer region and $\{-1.5 \text{ to } -1, -3 \text{ to } -0.5, 1 \text{ to } 1.5\}$ for the inner region

Now define the following additional fit parameters: the estimated number of pions N_π , η -mesons N_η , and background events N_B . These additional fit parameters define the relative amounts of meson signals relative to the background. Letting $G_\pi(m)$ and $G_\eta(m)$ be the skewed Gaussians for the pions and η -mesons, respectively, the full fit model $M(m)$ is

$$M(m) = N_\pi G_\pi(m) + N_\eta G_\eta(m) + N_B B(m) \quad (6.14)$$

The summand fit functions $\{G_\pi, G_\eta, B\}$ are considered as probability density functions and are normalized over the full mass range of 0 to 1 GeV. Consequently, the total number of

events as determined by the fit algorithm is

$$\int_0^1 M(m)dm = N_\pi + N_\eta + N_B \quad (6.15)$$

The signal range, S_π , over which the purity is calculated is determined using an algorithm similar to that used in determining the E -dependent π^0 mass window, described in section 3.6.3. The same idea of starting from the fit maximum and sliding left and right of the peak to a fraction of the maximum is used in order to establish a similarly defined signal range. The endpoints of S_π are used as boundaries of integrals used to calculate the π^0 purity.

Using the mass histogram $H(m)$, the pion purity F , defined as the fraction of events in the signal range S_π which are pions, is

$$F = N_\pi \cdot \frac{I_{G_\pi}}{I_H} \quad (6.16)$$

where the notation “ I_f ” for a given a function of mass, $f(m)$, is defined as

$$I_f := \int_{m \in S_\pi} f(m)dm$$

Note that for the case of I_H , the integral is replaced by a sum, since $H(m)$ is a histogram. In practice, it is better to use the background fit $B(m)$ compared to the data histogram $H(m)$ to determine the pion purity:

$$F = 1 - N_B \cdot \frac{I_B}{I_H} - N_\eta \cdot \frac{I_{G_\eta}}{I_H} \quad (6.17)$$

Note that the η -meson contribution is included in case S_η , corresponding to $G_\eta(m)$, overlaps into the signal region S_π ; this usually does not happen and for the purpose of discussion can be ignored.

The fully propagated uncertainty on F is

$$\sigma_F^2 = \left(\frac{\partial F}{\partial N_B} \right)^2 \sigma_{N_B}^2 + \left(\frac{\partial F}{\partial I_H} \right)^2 \sigma_{I_H}^2 + \sum_{j=1}^n \sum_{k=1}^n \frac{\partial F}{\partial b_j} \frac{\partial F}{\partial b_k} \sigma_{b_j b_k} + 2 \sum_{k=1}^n \frac{\partial F}{\partial N_B} \frac{\partial F}{\partial b_k} \sigma_{b_k N_B} \quad (6.18)$$

where the covariances $\sigma_{f_1 f_2}$ can be written in terms of correlation coefficients $\rho_{f_1 f_2}$ via $\sigma_{f_1 f_2} = \rho_{f_1 f_2} \sigma_{f_1} \sigma_{f_2}$. The uncertainties $\{\sigma_{N_B}, \sigma_{b_k}\}$ and correlation coefficients may all be determined

from the fit, and $\sigma_{I_H} = \sqrt{I_H}$. Putting everything together, the uncertainty is

$$\begin{aligned}\sigma_F^2 = \frac{1}{I_H^2} & \left[I_B^2 \sigma_{N_B}^2 + \frac{N_B^2 I_B^2}{I_H} + \sum_{j=1}^n \sum_{k=1}^n N_B^2 I_{T_j} I_{T_k} \rho_{b_j b_k} \sigma_{b_j} \sigma_{b_k} \right. \\ & \left. + 2 \sum_{k=1}^n I_B N_B I_{T_k} \rho_{b_k N_B} \sigma_{b_k} \sigma_{N_B} \right]\end{aligned}\quad (6.19)$$

This uncertainty is useful for determining the fit quality, but it does not impact $A_{LL}^{\pi^0}$ significantly, since σ_F is scaled by a factor of $(A_B - A_M)/F^2$ in equation 6.7 and is typically small.

Figures 6.3 and 6.4 show sample fits for the outer and inner regions, respectively. The fit algorithm was performed runset-by-runset for all p_T bins used in $A_{LL}^{\pi^0}$. The fits were to data in a “fit window,” defined between a lower mass bound of typically 0.06-0.1 GeV up to an upper bound of 0.6-0.75 GeV. The exact boundaries chosen depended on the shape of the mass distribution and the performance of the fit algorithm; the algorithm would tend to be successful for various fit window boundaries, but after a relative limit, the fit would fail if the window was too wide. Consequently, the fit window boundaries were chosen to push toward that limit, in order to maximize the subset of data considered in the fit. The lowest three p_T bins of the outer region included an η -meson fit; all other p_T bins did not show enough of an η -signal to warrant an η -meson fit attempt.

The signal peak fit height does not match the data peak height as well as one would hope, especially at higher p_T . This weakness justifies the preference toward using the background fit and data histogram integrals to calculate F (via equation 6.17), rather than making use of the signal fit integral. The sideband regions, along with the η -meson, seem to be reasonably well-fit for almost all of the runsets, therefore the background fit is more reliable than the signal fit for providing a measurement of F .

6.4.3 Purity Results

Figures 6.5-6.8 show plots of pion purity F as a function of runset as well as a distribution, for each p_T bin for both η regions. The error bars are from equation 6.19. There is some slight time-dependence observed in some of the F values. In practice, one could background-correct each runset’s $A_{LL}^{\pi^0}$ value, use each runset’s value of F , and form an enhanced MLM sum; however, this would require a good measurement of the background asymmetry for each runset, which is not the case since the background (sideband) sample size is much smaller than the signal sample size. Therefore, a single maximum-likely value of F for each p_T bin used in $A_{LL}^{\pi^0}$ is obtained instead; correcting for time-dependent F would not improve the

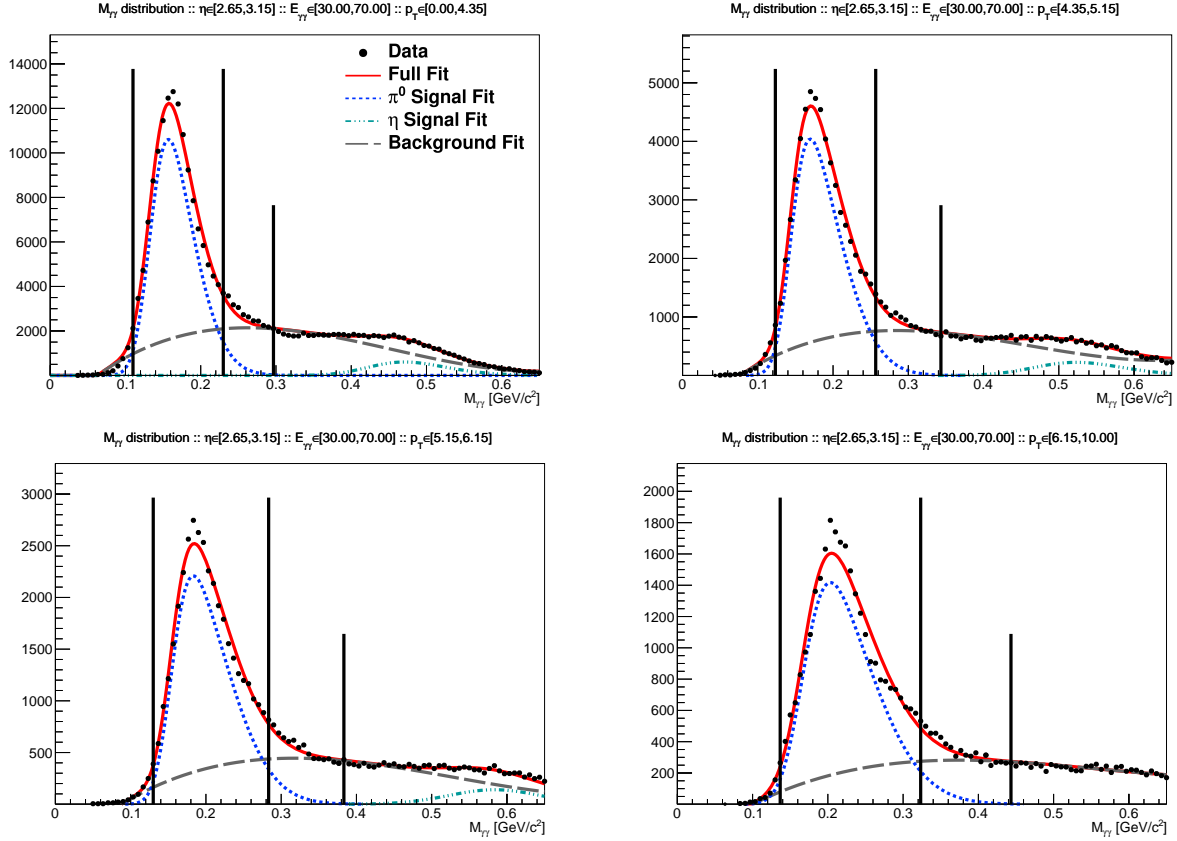


Figure 6.3: Sample fit results for each of the four p_T bins of the outer region. The fit legend in the first panel. Tall vertical lines denote signal window S_π boundaries, and the short vertical line indicates the upper boundary of the sideband region (which is not used in the fit or calculation of F)

$A_{LL}^{\pi^0}$ result much, given the context of the error bars on F . These maximum likely values are indicated by the red constant fit lines.

Figure 6.9 shows a plot of the maximum likely F values for each of the p_T bins used in $A_{LL}^{\pi^0}$. The error bars are from equation 6.7. The background level is 20 – 25% for the outer region and 10 – 15% for the inner region.

One might ask if there is a systematic uncertainty on $A_{LL}^{\pi^0}$ associated to this background correction. Already, according to equation 6.7, there is an increase in statistical uncertainties from making this correction. On the other hand, it is reasonable to investigate the $A_{LL}^{\pi^0}$ values for different choices of F . It turns out that for changes in F within its uncertainty, changes in $A_{LL}^{\pi^0}$ are no more than 3×10^{-4} , which is comparable to the relative luminosity systematic uncertainty and well below the gain in statistical uncertainties. We have therefore left the uncertainty associated to the background correction to be taken into account via the increased statistical uncertainties.

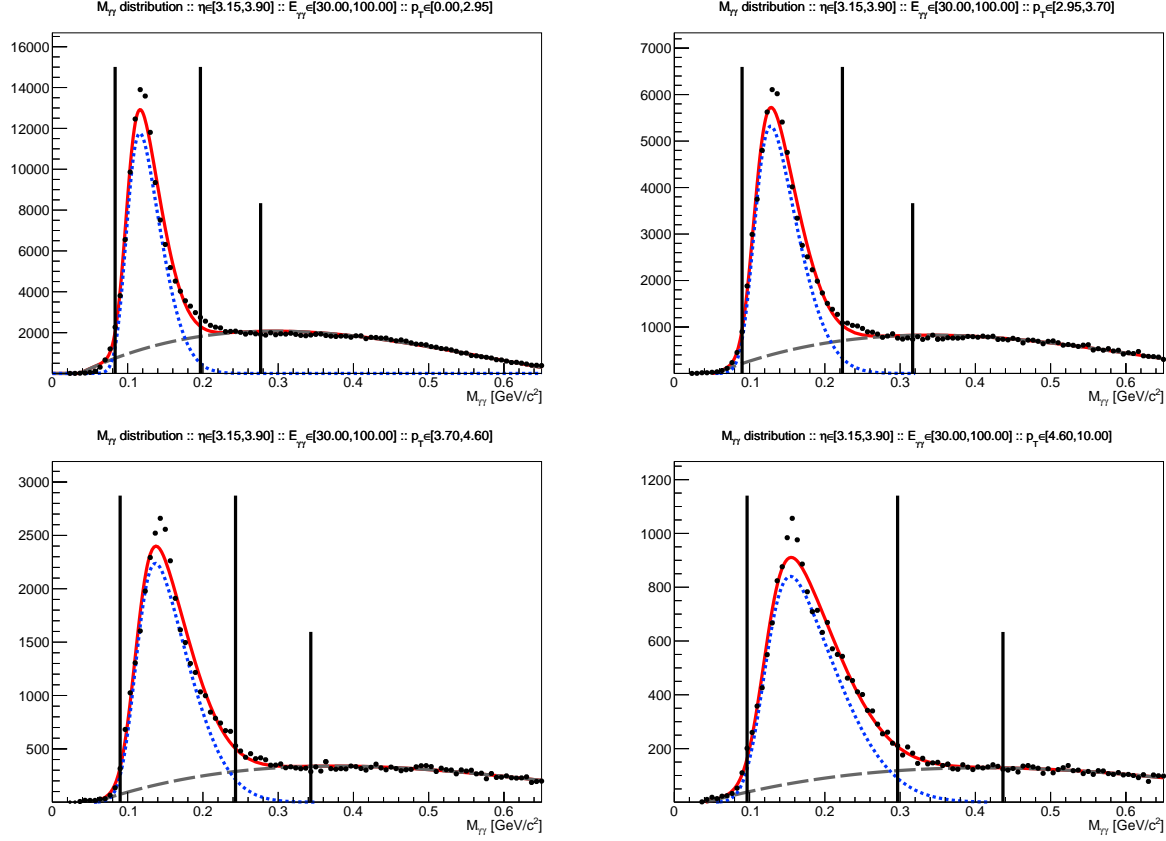


Figure 6.4: Sample fit results for each of the four p_T bins of the inner region.

The application of the background correction is shown in figures 6.10 and 6.11. The top-left panel of each figure shows a comparison in the signal+background A_{LL} in red, that is A_M , to the background asymmetry, A_B , in blue; these asymmetries are plotted versus their p_T bin means, the vertical uncertainties are statistical and the horizontal uncertainties are p_T bin RMS values. The bottom-left panel shows the difference $A_M - A_B$ versus corrected p_T means, with error bars representing their propagated uncertainties (since A_M and A_B are taken from separate parts of the M distribution, the uncertainty on their difference is the quadrature sum of their uncertainties). A fit line is drawn, showing the difference between A_M and A_B is no more than one standard deviation. The top-right panel shows the extracted, background-corrected signal asymmetry A_S in green compared to A_M in red. The bottom-right panel shows $A_S - A_M$ on the vertical axis versus $\langle p_T \rangle_S - \langle p_T \rangle_M$ on the horizontal axis; vertical error bars are not uncertainties, but differences in the uncertainties of the asymmetries, $\sigma_{A_S} - \sigma_{A_M}$. Differences between A_S and A_M range from 2×10^{-4} to 1.5×10^{-3} .

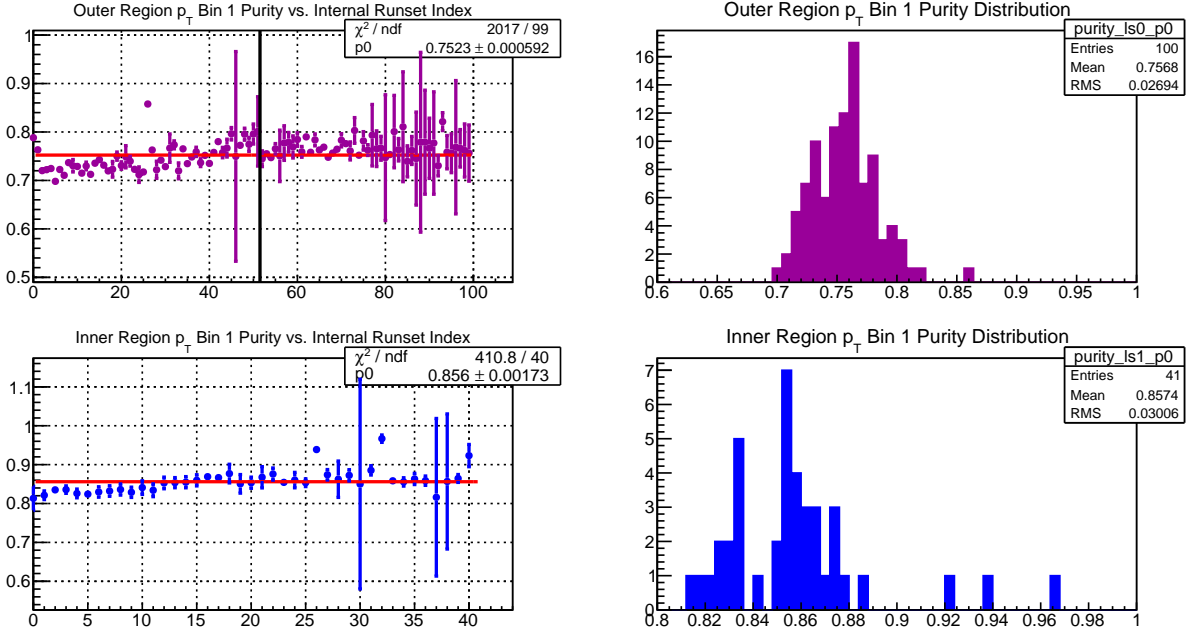


Figure 6.5: Left plots show the π^0 purity vs. a runset index, and right plots show the distributions of purities. The outer region (top plots) includes both Runs 12 and 13, and there is a vertical black line in the top-left plot showing the boundary between the Runs. The inner region (bottom plots) does not include Run 13. This is for p_T bin 1.

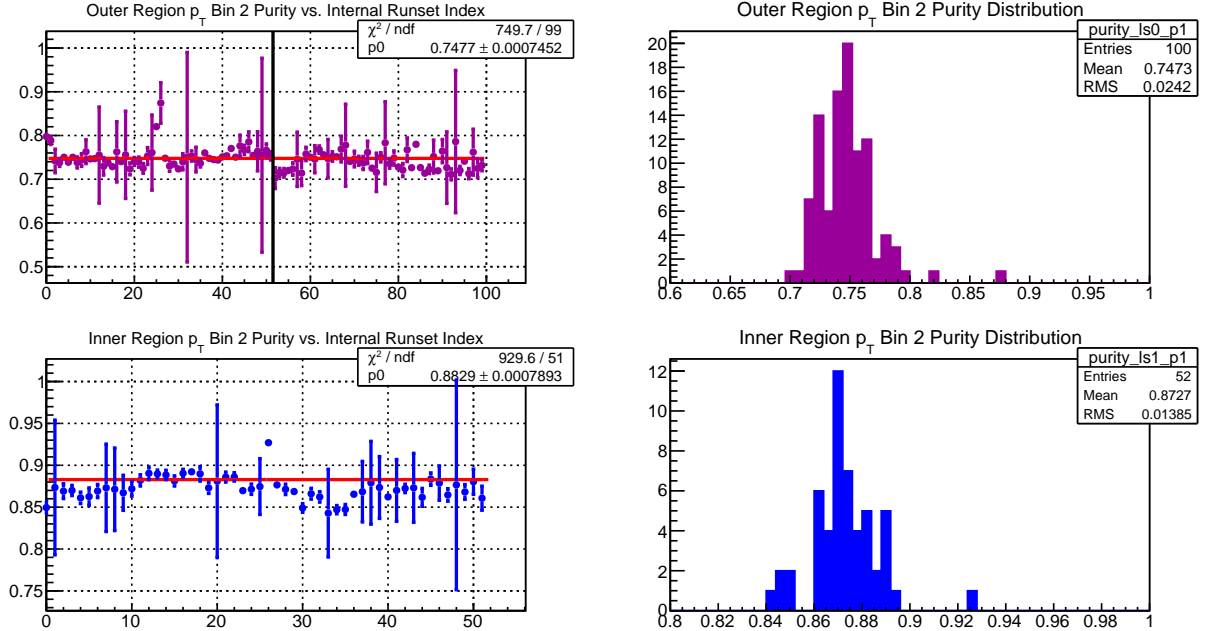


Figure 6.6: π^0 purities for p_T bin 2. Note that for p_T bins 2-4, there are more runsets plotted; this is because a few late runsets are completely cut out of p_T bin 1 via the time-dependent p_T threshold cut.

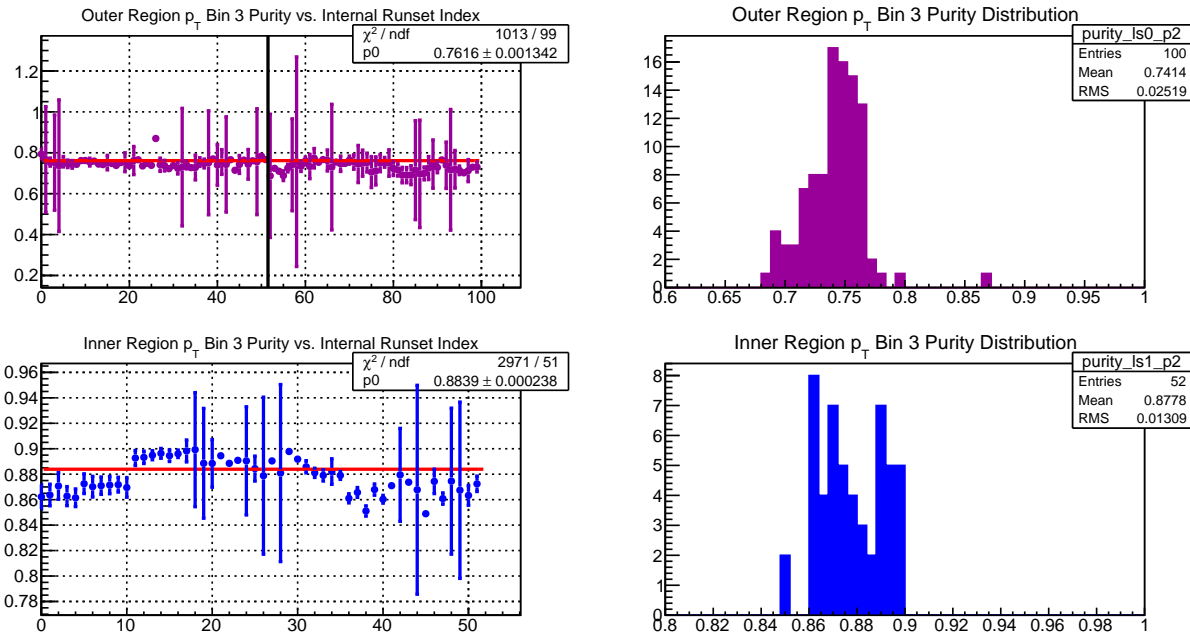


Figure 6.7: π^0 purities for p_T bin 3

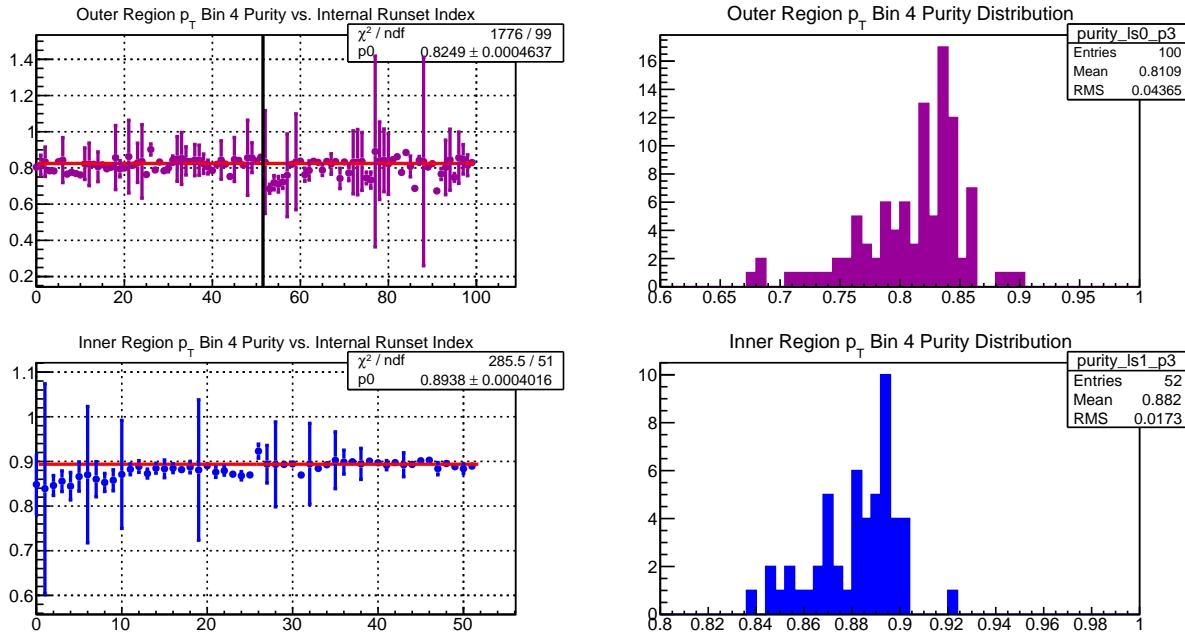


Figure 6.8: π^0 purities for p_T bin 4

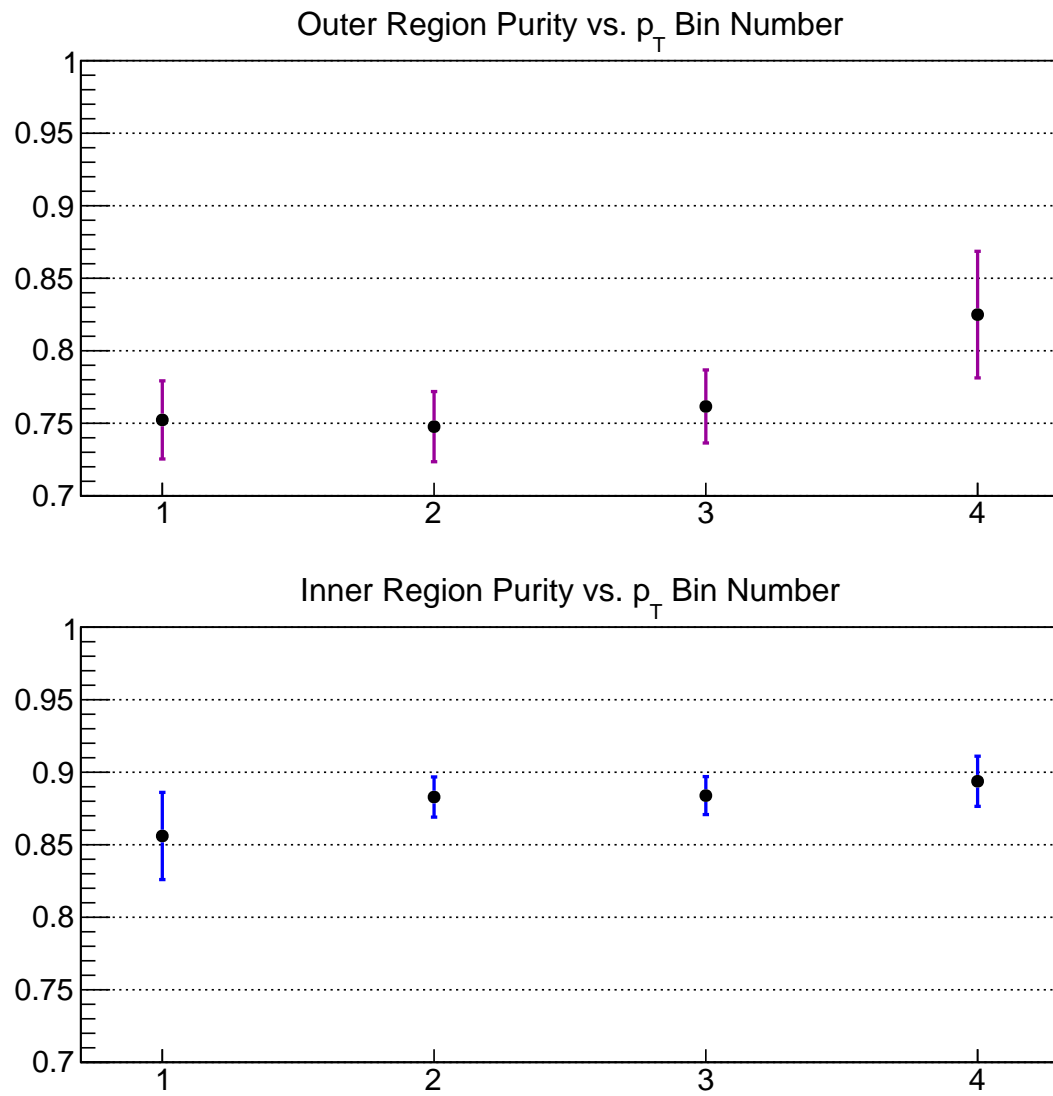


Figure 6.9: π^0 purities F for each p_T bin used in $A_{LL}^{\pi^0}$ for outer region (top) and inner region (bottom)

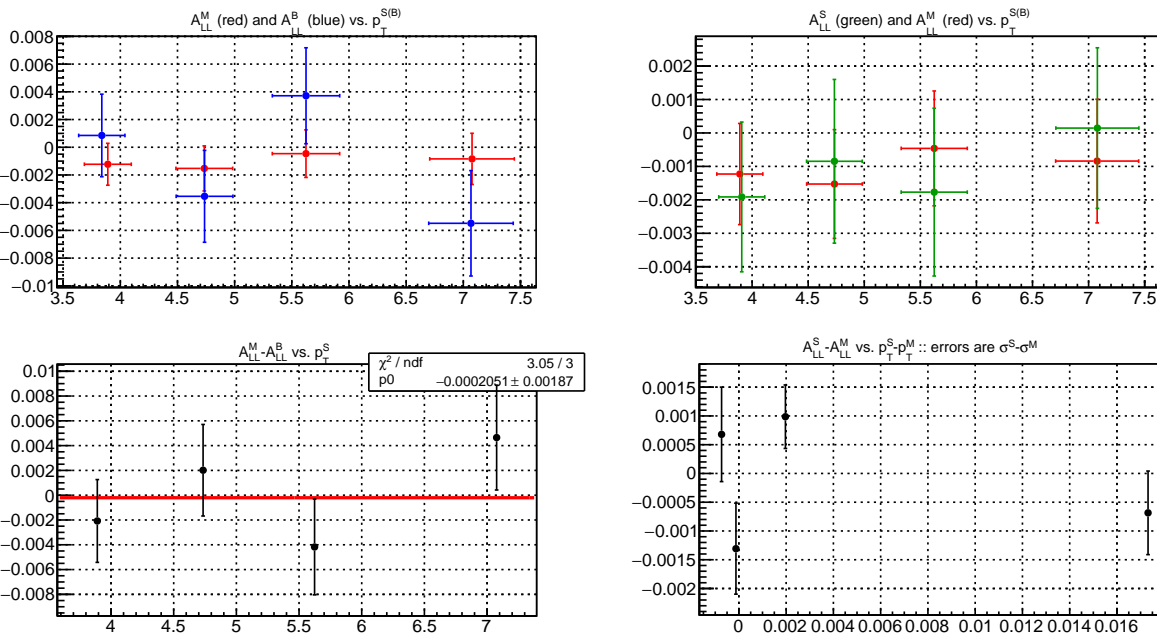


Figure 6.10: Background corrections implementation for outer region; see text for description of plots

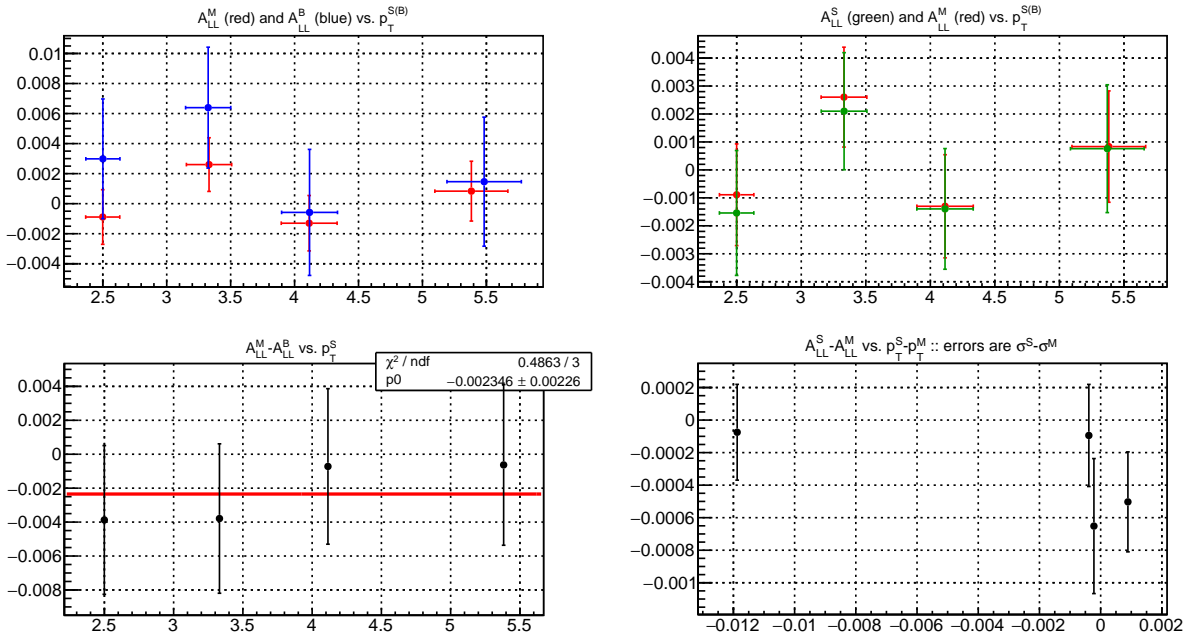


Figure 6.11: Background corrections implementation for inner region; see text for description of plots

6.5 Preliminary $A_{LL}^{\pi^0}$ Results

The relative luminosity used for the preliminary plots was measured by averaging the R_3 obtained from the VPDE, VPDW, VPDX using the CDF corrections. Since the preliminary plots were released before the rate-safe corrections were implemented, the CDF corrections were used. Consistency was checked between the R_3 measurement from the ZDC and from the VPD; any runs which had very inconsistent measurements were excluded.

Figures 6.12 and 6.13 show $A_{LL}^{\pi^0}$ plotted vs. E and p_T , respectively. The vertical lines are statistical uncertainties, horizontal lines are bin RMSs, and the vertical size of the shading represents the systematic uncertainty. Red markers are for 35 mrad π^0 isolation, and blue markers are for 100 mrad isolation. The asymmetry is consistent with zero given the present statistical and systematic uncertainties. Furthermore, the statistical uncertainty is approaching the systematic uncertainty.

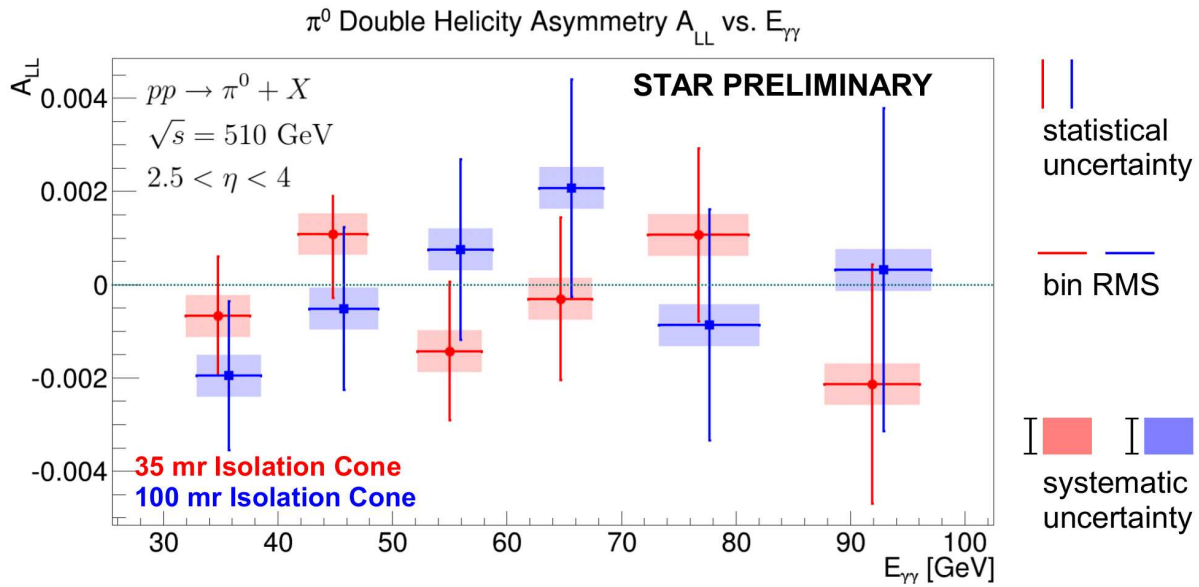


Figure 6.12: Preliminary Measurement of $A_{LL}^{\pi^0}$ vs. E

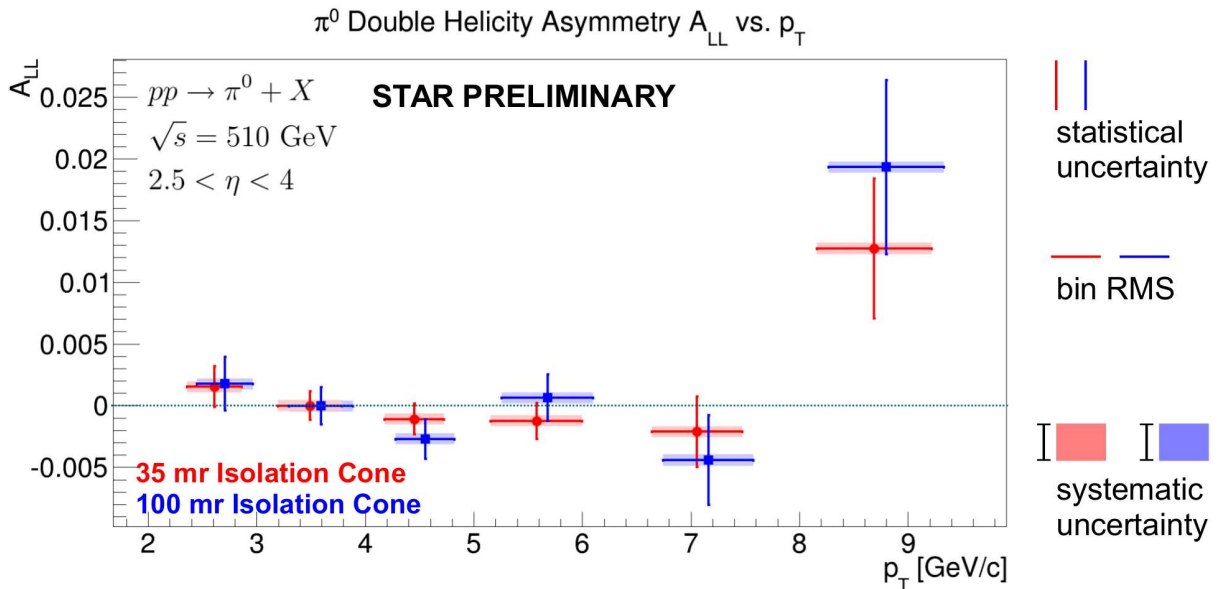


Figure 6.13: Preliminary Measurement of $A_{LL}^{\pi^0}$ vs. p_T

6.6 Final $A_{LL}^{\pi^0}$ Results

The final version of the $A_{LL}^{\pi^0}$ measurement is done as a function of p_T , for the outer and inner η regions (see table 6.1). Theory curves produced by DSSV and NNPDF have been included; further documentation on these is found at:

- http://www.star.bnl.gov/protected/spin/trent/fms_theory/theory.html

The final plot is not included in this document, however, it can be found in the most recent version of the paper draft.

Appendices

Appendix A

Decay Kinematics of $\pi^0 \rightarrow \gamma + \gamma$

A.1 Invariant Mass

Consider the decay of a π^0 with momentum along the z -axis into two photons spanning the xz -plane with 4-momenta

$$k_1 = (E_1, E_1 \sin \alpha_1, 0, E_1 \cos \alpha_1) \quad (\text{A.1})$$

$$k_2 = (E_2, -E_2 \sin \alpha_2, 0, E_2 \cos \alpha_2) \quad (\text{A.2})$$

The invariant mass squared is

$$M^2 = (k_1 + k_2)^2 = 2k_1 k_2 = 4E_1 E_2 \sin^2 \frac{\alpha}{2} \quad (\text{A.3})$$

where $\alpha = \alpha_1 + \alpha_2$ is the photon opening angle. Let $E = E_1 + E_2$ be the total energy and let $Z = |E_1 - E_2|/E$ be the photon energy imbalance. The invariant mass is then

$$M = 2\sqrt{E_1 E_2} \cdot \sin \frac{\alpha}{2} \approx \sqrt{E_1 E_2} \cdot \alpha \quad (\text{A.4})$$

$$= E\sqrt{1 - Z^2} \cdot \sin \frac{\alpha}{2} \approx \frac{E}{2}\sqrt{1 - Z^2} \cdot \alpha \quad (\text{A.5})$$

The opening angle can be thought of as a function of E_1 and E_2 or of E and Z , given a fixed value of M :

$$\alpha = 2 \arcsin \left(\frac{M}{2\sqrt{E_1 E_2}} \right) \approx \frac{M}{\sqrt{E_1 E_2}} \quad (\text{A.6})$$

$$= 2 \arcsin \left(\frac{M}{E\sqrt{1 - Z^2}} \right) \approx \frac{2M}{E\sqrt{1 - Z^2}} \quad (\text{A.7})$$

Note that the opening angle spans approximately $z\alpha/w$ cells, where z is the distance to the interaction point and w is the cell width. For $z = 7$ m, a 10 mrad opening angle spans 7 cm, which is just over 1 large cell width or just under 2 small cell widths.

In order to explore the inter-dependencies of the kinematic variables, next few pages show various planes cut from the $M(E, Z, \alpha)$ and $M(E_1, E_2, \alpha)$ hypersurfaces.

- Figure A.1 shows M -contours in the α vs. E plane for fixed values of Z , as described by equation A.7. These plots show the energy-dependence of the opening angle: higher energy pions ($M = 0.135$ GeV) have smaller opening angles than those with lower energy, and the more massive η -mesons ($M = 0.55$ GeV) have much larger opening angles than pions.
- Figure A.2 shows α -contours in the M vs. E plane for fixed values of Z , as described by equation A.4. For constant opening angles, the invariant mass rises as a function of energy. If the opening angle as a function of energy is overestimated, then data will tend to show an increase in the mass as a function of energy. In other words, the observation of a positive linear dependence of the invariant mass on the energy is evidence of an overestimation of the photon separation at higher energies.
- Figure A.3 shows α -contours in the M vs. Z plane for fixed values of E . At higher Z , the mass decreases for fixed values of α . This decrease is more extreme at higher energies. *N.b.*, the uncertainty on Z becomes much greater as the photon separation decreases and approaches the region where it is difficult to distinguish 1-photon clusters from those with 2 photons.
- Figures A.4-A.5 show contours of $\alpha(E_1, E_2)$ and $\alpha(E, Z)$ given M fixed at the π^0 mass and at the η mass. Placing an upper limit on a π^0 opening angle, a consequence of an isolation cone, helps reduce contributions from low energy “soft” photons.

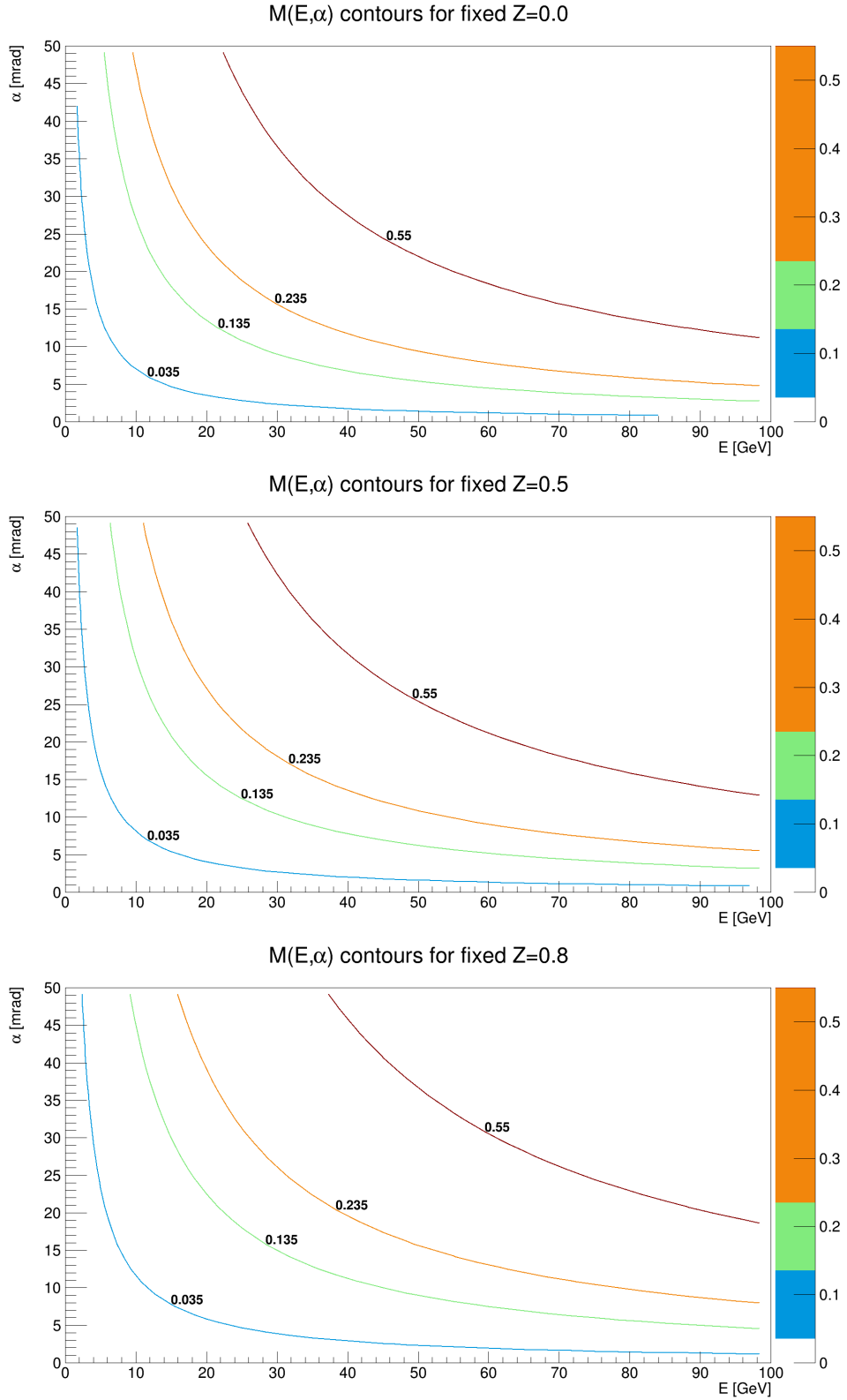


Figure A.1: α vs. E plane with M contours for fixed $Z = 0$ (top), $Z = 0.5$ (middle), and $Z = 0.8$ (bottom)

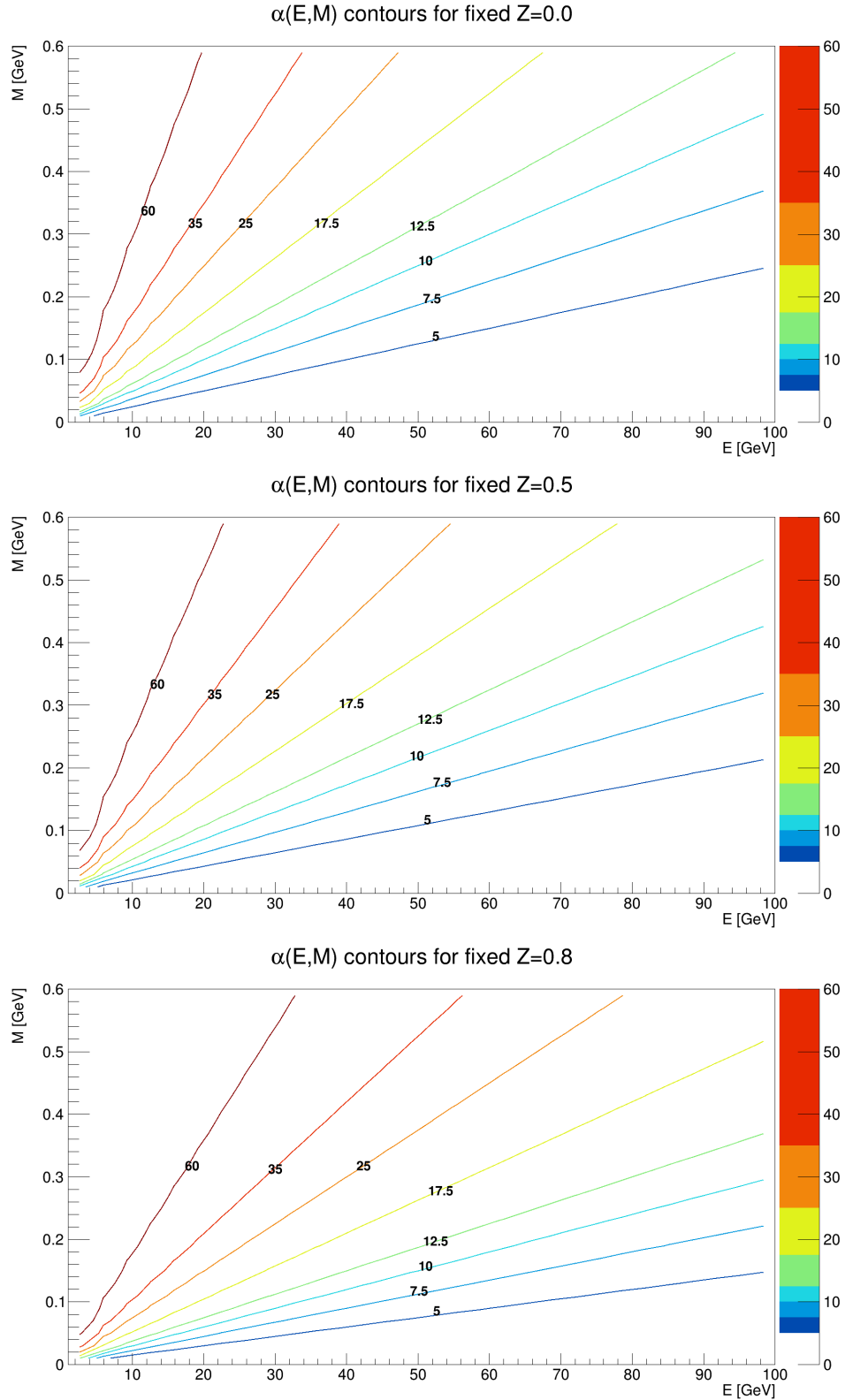


Figure A.2: M vs. E plane with α contours for fixed $Z = 0$ (top), $Z = 0.5$ (middle), and $Z = 0.8$ (bottom)

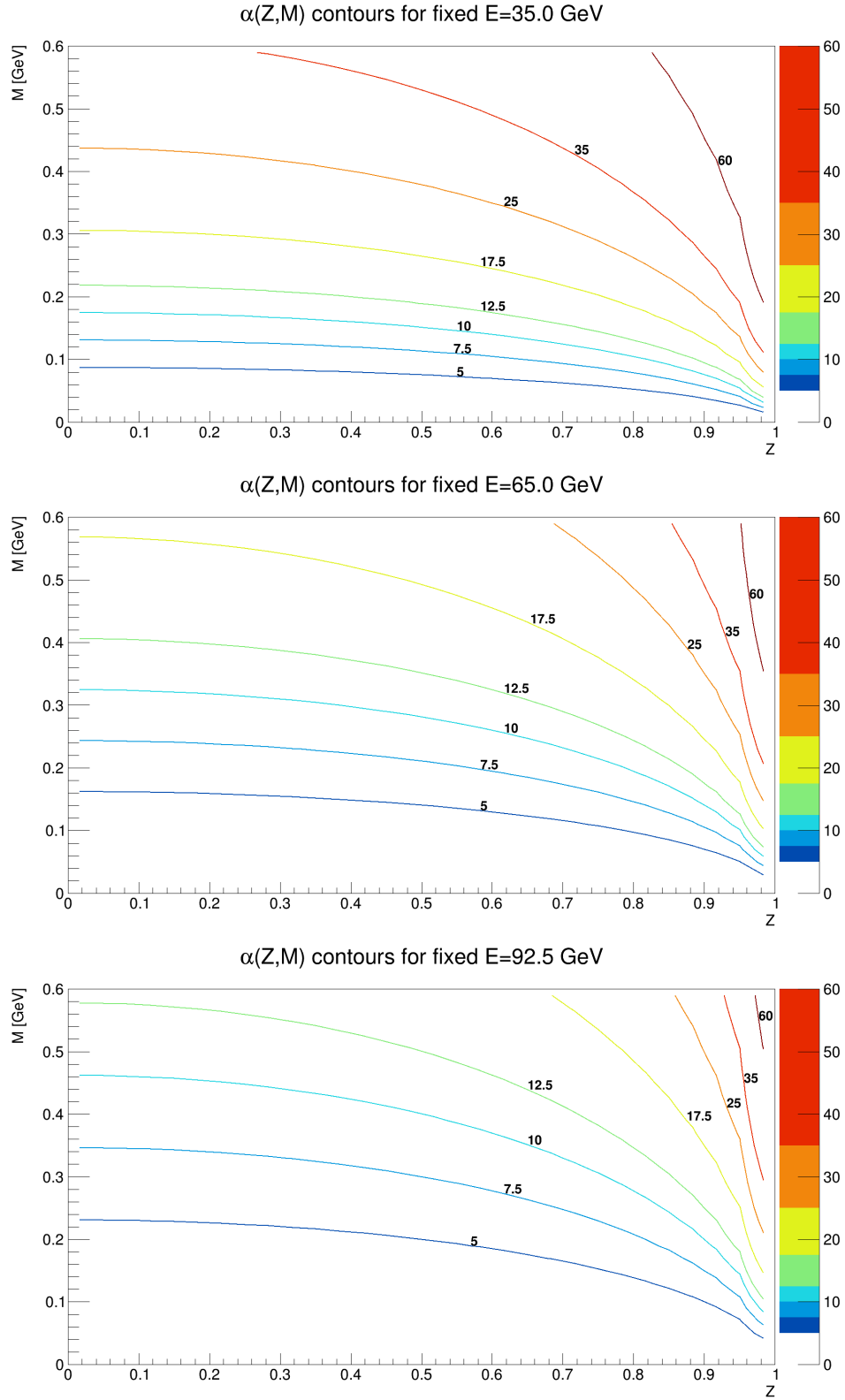


Figure A.3: M vs. Z plane with α contours for fixed $E = 35$ GeV (top), $E = 65$ GeV (middle), and $E = 92.5$ GeV (bottom)

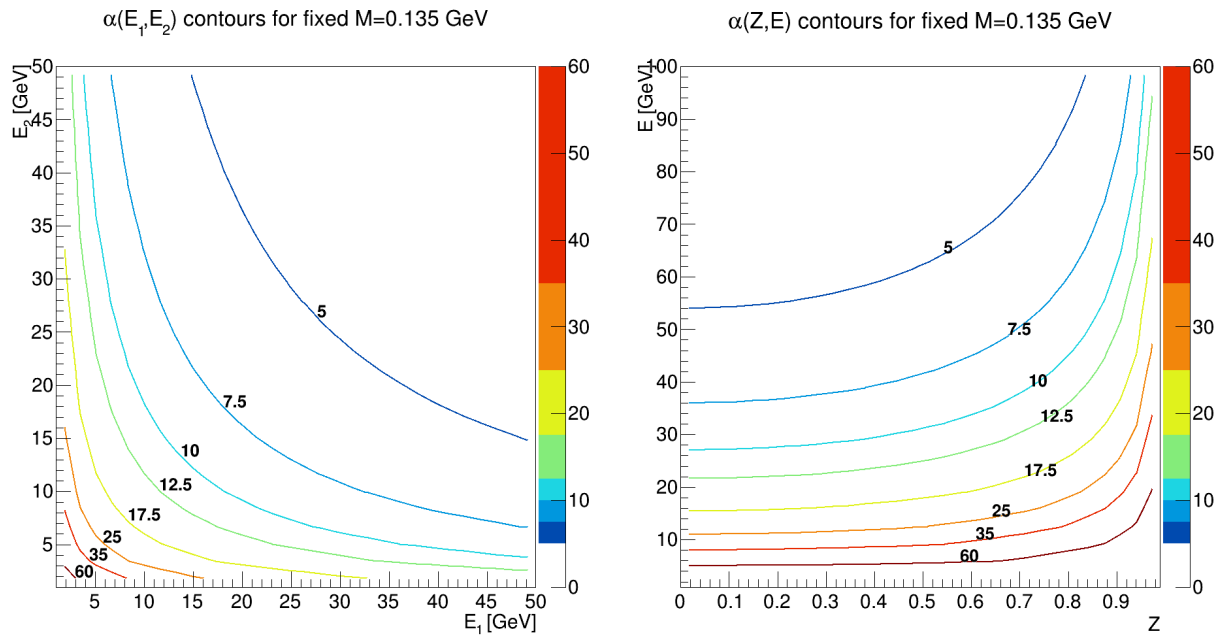


Figure A.4: E_2 vs. E_1 plane (left) and E vs. Z plane (right) with α contours for M fixed at π^0 mass

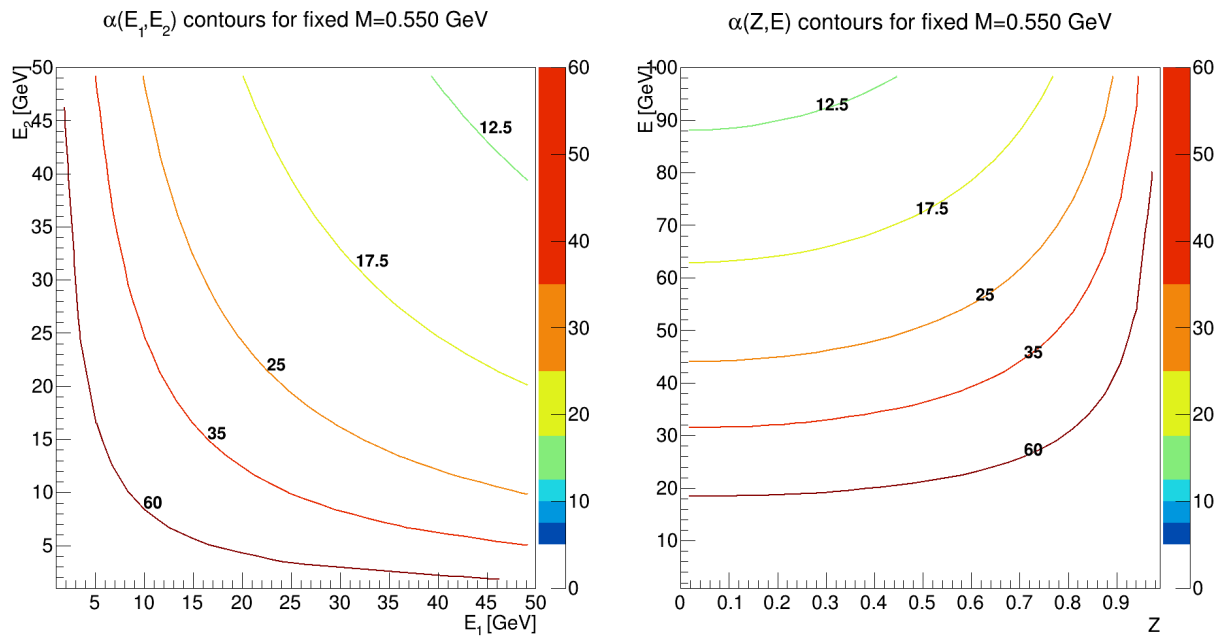


Figure A.5: E_2 vs. E_1 plane (left) and E vs. Z plane (right) with α contours for M fixed at η -meson mass

A.2 Note on Small Angles from π^0 Decay Cones

Consider a 30 GeV π^0 decaying toward the FMS. Typically it will decay into a pair of photons with an opening angle of 10 mrad. Assuming the decay can happen with any azimuthal orientation, the space of possible photon trajectories forms a 10 mrad cone, which intersects the FMS front plane in an ellipse, since the cone axis is at an angle with respect to the normal vector of the FMS front plane. Let this angle, which is the π^0 scattering angle θ , be 70 mrad, corresponding to photon hits detected 0.5 m away from where the beam pipe intersects the FMS front plane. The eccentricity of the projected ellipse is then

$$\varepsilon = \frac{\sin 0.070}{\cos 0.010/2} = 0.07 \quad (\text{A.8})$$

The ratio of the ellipse's minor axis length to the major axis length is then $\sqrt{1 - \varepsilon^2} = 0.9975$, which is too small to be noticeable with respect to the position resolution of the FMS. Thus π^0 opening angles are small enough such that ellipticity corrections are not needed in the determination of opening angles based solely on distance between photon hits.

Appendix B

Spin Asymmetries and their Relative Luminosities

B.1 Notation

a = asymmetry number (following STAR relative luminosity convention)

h_B = blue (west) beam proton helicity

h_Y = yellow (east) beam proton helicity

ε_a = raw asymmetry

$\sigma^{\text{sign}(h_B)\text{sign}(h_Y)}$ = proton helicity-dependent cross section

R_a = relative luminosity

$L^{\text{sign}(h_B)\text{sign}(h_Y)}$ = proton helicity-dependent integrated luminosity

H_a = helicity factor (see appendix E)

$H_a = +1$ for helicity combo in R_a numerator

$H_a = -1$ for helicity combo in R_a denominator

B.2 Nine Asymmetries and Relative Luminosities

a	ε_a	R_a	H_a	comment
1	$\frac{(\sigma^{++} + \sigma^{-+}) - (\sigma^{+-} + \sigma^{--})}{(\sigma^{++} + \sigma^{-+}) + (\sigma^{+-} + \sigma^{--})}$	$\frac{L^{++} + L^{-+}}{L^{+-} + L^{--}}$	h_Y	yellow SSA
2	$\frac{(\sigma^{++} + \sigma^{+-}) - (\sigma^{-+} + \sigma^{--})}{(\sigma^{++} + \sigma^{+-}) + (\sigma^{-+} + \sigma^{--})}$	$\frac{L^{++} + L^{+-}}{L^{-+} + L^{--}}$	h_B	blue SSA
3	$\frac{(\sigma^{++} + \sigma^{--}) - (\sigma^{+-} + \sigma^{-+})}{(\sigma^{++} + \sigma^{--}) + (\sigma^{+-} + \sigma^{-+})}$	$\frac{L^{++} + L^{--}}{L^{+-} + L^{-+}}$	$h_B h_Y$	DSA
4	$\frac{\sigma^{++} - \sigma^{--}}{\sigma^{++} + \sigma^{--}}$	$\frac{L^{++}}{L^{--}}$	$\frac{h_B + h_Y}{2}$	like sign asym
5	$\frac{\sigma^{-+} - \sigma^{--}}{\sigma^{-+} + \sigma^{--}}$	$\frac{L^{-+}}{L^{--}}$	$\frac{(1 - h_B) h_Y}{2}$	
6	$\frac{\sigma^{+-} - \sigma^{--}}{\sigma^{+-} + \sigma^{--}}$	$\frac{L^{+-}}{L^{--}}$	$\frac{(1 - h_Y) h_B}{2}$	
7	$\frac{\sigma^{++} - \sigma^{+-}}{\sigma^{++} + \sigma^{+-}}$	$\frac{L^{++}}{L^{+-}}$	$\frac{(1 + h_B) h_Y}{2}$	
8	$\frac{\sigma^{-+} - \sigma^{+-}}{\sigma^{-+} + \sigma^{+-}}$	$\frac{L^{-+}}{L^{+-}}$	$\frac{h_Y - h_B}{2}$	unlike sign asym
9	$\frac{\sigma^{++} - \sigma^{-+}}{\sigma^{++} + \sigma^{-+}}$	$\frac{L^{++}}{L^{-+}}$	$\frac{(1 + h_Y) h_B}{2}$	

Note that all asymmetries can also be defined for transverse polarized collisions as well. The naming conventions for physics asymmetries are usually as follows (given $a = 1$ corresponds to the RHIC yellow beam and $a = 2$ to blue):

- Single-Spin

- Longitudinal: $A_L^Y = \frac{1}{P_Y} \varepsilon_1$ Transverse: $A_n^Y = \frac{1}{P_Y} \varepsilon_1 = A_N^Y \cos \phi$
- Longitudinal: $A_L^B = \frac{1}{P_B} \varepsilon_2$ Transverse: $A_n^B = \frac{1}{P_B} \varepsilon_2 = A_N^B \cos \phi$

- Double-Spin

- Longitudinal: $A_{LL} = \frac{1}{P_B P_Y} \varepsilon_3$ Transverse: $A_{nn} = \frac{1}{P_B P_Y} \varepsilon_3 = A_{TT} + A_\Sigma \cos 2\phi$

Assuming the scalar uncertainties of L_z are σ_z , the relative luminosity uncertainties are:

$$\begin{aligned}\sigma_{R_1} &= \sqrt{\frac{(\sigma_{-+}^2 + \sigma_{++}^2)(L_{--} + L_{+-})^2 + (\sigma_{--}^2 + \sigma_{+-}^2)(L_{-+} + L_{++})^2}{(L_{--} + L_{+-})^4}} \\ \sigma_{R_2} &= \sqrt{\frac{(\sigma_{+-}^2 + \sigma_{++}^2)(L_{--} + L_{-+})^2 + (\sigma_{--}^2 + \sigma_{-+}^2)(L_{+-} + L_{++})^2}{(L_{--} + L_{-+})^4}} \\ \sigma_{R_3} &= \sqrt{\frac{(\sigma_{--}^2 + \sigma_{++}^2)(L_{-+} + L_{+-})^2 + (\sigma_{-+}^2 + \sigma_{+-}^2)(L_{--} + L_{++})^2}{(L_{-+} + L_{+-})^4}} \\ \sigma_{R_4} &= \sqrt{\frac{\sigma_{++}^2 L_{--}^2 + \sigma_{--}^2 L_{++}^2}{L_{--}^4}} \\ \sigma_{R_5} &= \sqrt{\frac{\sigma_{-+}^2 L_{--}^2 + \sigma_{--}^2 L_{-+}^2}{L_{--}^4}} \\ \sigma_{R_6} &= \sqrt{\frac{\sigma_{+-}^2 L_{--}^2 + \sigma_{--}^2 L_{+-}^2}{L_{--}^4}} \\ \sigma_{R_7} &= \sqrt{\frac{\sigma_{++}^2 L_{+-}^2 + \sigma_{+-}^2 L_{++}^2}{L_{+-}^4}} \\ \sigma_{R_8} &= \sqrt{\frac{\sigma_{+-}^2 L_{-+}^2 + \sigma_{-+}^2 L_{+-}^2}{L_{-+}^4}} \\ \sigma_{R_9} &= \sqrt{\frac{\sigma_{++}^2 L_{-+}^2 + \sigma_{-+}^2 L_{++}^2}{L_{-+}^4}}\end{aligned}$$

Appendix C

Decomposing Cross-Sections in terms of Spin Asymmetries

C.1 Longitudinal Components

Consider a particle, described by state $|\psi\rangle$, heading in the z direction. Let its spin be in the $x - z$ plane, such that it makes an angle α with the z -axis. That is, the spin vector is

$$\vec{P} = (P \sin \alpha, 0, P \cos \alpha)$$

(the label P stands for polarization, which is more properly defined for an ensemble of particles, but P is chosen instead of S to avoid confusion with spin operators). Consider the two helicity states: spin along the $+z$ -axis, described by $|+\rangle$ and spin along the $-z$ -axis, described by $|-\rangle$. These states form a basis

$$\left\{ |+\rangle = \begin{pmatrix} 1 \\ 0 \end{pmatrix}, |-\rangle = \begin{pmatrix} 0 \\ 1 \end{pmatrix} \right\}$$

which span the space on which the spin-1/2 representation of the spin operators act. The linear maps S_i associated to the spin operators can be expanded as follows:

$$S_z = \frac{1}{2} \begin{pmatrix} 1 & 0 \\ 0 & -1 \end{pmatrix} = \frac{1}{2} \left(|+\rangle\langle+| - |-\rangle\langle-| \right) \quad (\text{C.1})$$

$$S_x = \frac{1}{2} \begin{pmatrix} 0 & 1 \\ 1 & 0 \end{pmatrix} = \frac{1}{2} \left(|+\rangle\langle-| + |-\rangle\langle+| \right) \quad (\text{C.2})$$

$$S_y = \frac{1}{2} \begin{pmatrix} 0 & -i \\ i & 0 \end{pmatrix} = \frac{i}{2} \left(|-\rangle\langle+| - |+\rangle\langle-| \right) \quad (\text{C.3})$$

Note that since $S_z|\pm\rangle = \pm\frac{1}{2}|\pm\rangle$, we have the following expectation values:

$$\begin{aligned} \langle\psi|S_x|\psi\rangle &= \sin(\alpha)/2 \\ \langle\psi|S_y|\psi\rangle &= 0 \\ \langle\psi|S_z|\psi\rangle &= \cos(\alpha)/2 \end{aligned}$$

Let's expand $|\psi\rangle$ in the $\{|+\rangle, |-\rangle\}$ basis:

$$|\psi\rangle = c_+|+\rangle + c_-|-\rangle$$

Acting with S_z yields

$$S_z|\psi\rangle = \frac{1}{2}c_+|+\rangle - \frac{1}{2}c_-|-\rangle$$

and hence the expectation value,

$$\langle\psi|S_z|\psi\rangle = \left(c_+|+\rangle + c_-|-\rangle \right) \left(\frac{1}{2}c_+|+\rangle - \frac{1}{2}c_-|-\rangle \right) = \frac{1}{2} (c_+^2 - c_-^2),$$

together with equation C.1, implies the relation

$$c_+^2 - c_-^2 = \cos \alpha \quad (\text{C.4})$$

The S_x operator yields a similar relation:

$$\langle\psi|S_x|\psi\rangle = \left(c_+|+\rangle + c_-|-\rangle \right) \left(\frac{1}{2}c_+|-\rangle + \frac{1}{2}c_-|+\rangle \right) = c_+c_-,$$

and thus

$$2c_+c_- = \sin \alpha \quad (\text{C.5})$$

Simultaneously solving equations C.4 and C.5 for c_{\pm} allows us to express the state in terms of its spin vector angle:

$$|\psi\rangle = \sqrt{\frac{1 + \cos \alpha}{2}}|+\rangle + \sqrt{\frac{1 - \cos \alpha}{2}}|-\rangle \quad (\text{C.6})$$

Now consider two colliding particles a and b with spin vector angles α and β , described as:

$$\begin{aligned} |a\rangle &= \sqrt{\frac{1 + \cos \alpha}{2}}|a_+\rangle + \sqrt{\frac{1 - \cos \alpha}{2}}|a_-\rangle \\ |b\rangle &= \sqrt{\frac{1 + \cos \beta}{2}}|b_+\rangle + \sqrt{\frac{1 - \cos \beta}{2}}|b_-\rangle \end{aligned}$$

The scattering cross-section may be written as:

$$\begin{aligned} 4\sigma_{ab} = 4 \cdot \langle ab|\sigma|ab\rangle &= (1 + \cos \alpha)(1 + \cos \beta)\sigma_{++} + (1 + \cos \alpha)(1 - \cos \beta)\sigma_{+-} + \\ &\quad (1 - \cos \alpha)(1 + \cos \beta)\sigma_{-+} + (1 - \cos \alpha)(1 - \cos \beta)\sigma_{--} \\ &= (\sigma_{++} + \sigma_{+-} + \sigma_{-+} + \sigma_{--}) + \cos \alpha(\sigma_{++} + \sigma_{+-} - \sigma_{-+} - \sigma_{--}) + \\ &\quad \cos \beta(\sigma_{++} - \sigma_{+-} + \sigma_{-+} - \sigma_{--}) + \cos \alpha \cos \beta(\sigma_{++} - \sigma_{+-} - \sigma_{-+} + \sigma_{--}) \end{aligned}$$

where

$$\sigma_{\pm\pm} := \langle a_{\pm}b_{\pm}|\sigma|a_{\pm}b_{\pm}\rangle$$

and

$$\sigma = \sigma_{++} + \sigma_{+-} + \sigma_{-+} + \sigma_{--}$$

Defining the following asymmetries

$$\begin{aligned} A_L^a &= \frac{(\sigma_{++} + \sigma_{+-} - \sigma_{-+} - \sigma_{--})}{\sigma} \\ A_L^b &= \frac{(\sigma_{++} + \sigma_{-+} - \sigma_{+-} - \sigma_{--})}{\sigma} \\ A_{LL} &= \frac{(\sigma_{++} + \sigma_{--} - \sigma_{+-} - \sigma_{--})}{\sigma} \end{aligned}$$

allows one to write the cross-section as

$$\sigma_{ab} = \frac{\sigma}{4} (1 + A_L^a \cos \alpha + A_L^b \cos \beta + A_{LL} \cos \alpha \cos \beta) \quad (\text{C.7})$$

C.2 Transverse Components

We now rotate the basis to the transverse basis:

$$\begin{aligned} |+\rangle &= \frac{1}{\sqrt{2}}(|\uparrow\rangle + |\downarrow\rangle) \\ |-\rangle &= \frac{1}{\sqrt{2}}(|\uparrow\rangle - |\downarrow\rangle) \end{aligned}$$

In this basis, the spin operators transform to:

$$\begin{aligned} S_x &= \frac{1}{2}(|\uparrow\rangle\langle\uparrow| - |\downarrow\rangle\langle\downarrow|) \\ S_y &= \frac{i}{2}(|\uparrow\rangle\langle\downarrow| - |\downarrow\rangle\langle\uparrow|) \\ S_z &= \frac{1}{2}(|\uparrow\rangle\langle\downarrow| + |\downarrow\rangle\langle\uparrow|) \end{aligned}$$

Expand the state in this basis as

$$|\psi\rangle = c_{\uparrow}|\uparrow\rangle + c_{\downarrow}|\downarrow\rangle$$

Expectation values give rise to the following relations:

$$\begin{aligned} \langle\psi|S_x|\psi\rangle &= \frac{1}{2}(c_{\uparrow}^2 - c_{\downarrow}^2) = \frac{1}{2}\sin\alpha \\ \langle\psi|S_z|\psi\rangle &= c_{\uparrow}c_{\downarrow} = \frac{1}{2}\cos\alpha \end{aligned}$$

Solving this system yields

$$|\psi\rangle = \sqrt{\frac{1+\sin\alpha}{2}}|\uparrow\rangle + \sqrt{\frac{1-\sin\alpha}{2}}|\downarrow\rangle \quad (\text{C.8})$$

Similar to the longitudinal case, one can define the following asymmetries, which are azimuthally modulated:

$$\begin{aligned} A_P^a &= \frac{\sigma_{\uparrow\uparrow} + \sigma_{\uparrow\downarrow} - \sigma_{\downarrow\uparrow} - \sigma_{\downarrow\downarrow}}{\sigma} = R^a + A_N^a \cos\phi \\ A_P^b &= \frac{\sigma_{\uparrow\uparrow} + \sigma_{\downarrow\uparrow} - \sigma_{\uparrow\downarrow} - \sigma_{\downarrow\downarrow}}{\sigma} = R^b + A_N^b \cos\phi \\ A_{PP} &= \frac{\sigma_{\uparrow\uparrow} + \sigma_{\downarrow\downarrow} - \sigma_{\uparrow\downarrow} - \sigma_{\downarrow\uparrow}}{\sigma} = A_{\Sigma} + A_{TT} \cos(2\phi) \end{aligned}$$

where ϕ is the azimuth of the measured particle or jet and R is related to the relative luminosity. The cross-ratio single-spin asymmetry can be used for A_P , negating the need for the offsets R , and hence we can assume $R = 0$ if A_N is properly measured. Finally, the cross-section may be written as

$$\sigma_{ab} = \frac{\sigma}{4} \left\{ 1 + A_N^a \sin \alpha \cos \phi + A_N^b \sin \beta \cos \phi + [A_\Sigma + A_{TT} \cos(2\phi)] \sin \alpha \sin \beta \right\} \quad (\text{C.9})$$

C.3 Application: Systematic Uncertainty on A_{LL} due to Nonzero Transverse Polarization

The full cross-section, after averaging over azimuth, assuming parity conservation ($A_L = 0$), and assuming $\cos \alpha = \cos \beta \approx 1$ is

$$\begin{aligned} \sigma_{ab} &\propto 1 + A_{LL} \cos \alpha \cos \beta + A_\Sigma \sin \alpha \sin \beta \\ &\approx 1 + A_{LL} + A_\Sigma \sin \alpha \sin \beta \end{aligned}$$

Therefore, the systematic uncertainty is

$$\delta A_{LL} = |A_\Sigma \cdot \sin \alpha \cdot \sin \beta| \quad (\text{C.10})$$

This is the same as equation 5.32 when we average that over azimuth (so $A_{nn} = A_\Sigma$) and use $\sin \theta = P^\perp/P$ where $\theta \in \{\alpha, \beta\}$. If we allow a and b to have a nonzero azimuth, equation C.10 becomes

$$\delta A_{LL} = |A_\Sigma \cdot \sin \alpha \cdot \sin \beta \cdot \cos(\phi_a - \phi_b)| \quad (\text{C.11})$$

but since ϕ_a and ϕ_b are typically hard to measure, the most conservative estimate of $\cos(\phi_a - \phi_b) = 1$, which gives equation C.10, suffices.

Appendix D

Rate-Safe Counting Derivation

D.1 Event Classes

Assume that there can be multiple collisions per bunch crossing; typically there are ~ 1 collisions / bunch crossing. We define two classes of collisions, called “event classes”:

1. Double-sided events (DS): collisions which will trigger a coincidence
 - DS events occur an average of λ times / bunch crossing
2. Single-sided events (SS): collisions which will trigger a single hit but not a coincidence
 - East Single-sided events (ESS) occur an average of λ_E times / bunch crossing
 - West Single-sided events (WSS) occur an average of λ_W times / bunch crossing

D.2 Hit Probabilities

- DS events

The probability for detecting k_E hits in the E-scaler from DS events, given that the E-scaler has efficiency \times acceptance = ε_E is

$$P_{DS}(k_E) = \frac{(\varepsilon_E \lambda)^{k_E} e^{-\varepsilon_E \lambda}}{k_E!} \quad (\text{D.1})$$

Likewise, the probability for detecting k_W hits in the W-scaler from DS events, given that the W-scaler has efficiency \times acceptance = ε_W is

$$P_{DS}(k_W) = \frac{(\varepsilon_W \lambda)^{k_W} e^{-\varepsilon_W \lambda}}{k_W!} \quad (\text{D.2})$$

The joint probability that the E-scaler detects k_E hits AND the W-scaler detects k_W hits from DS events is

$$P_{DS}(k_E, k_W) = P_{DS}(k_W|k_E) \cdot P_{DS}(k_E) \quad (\text{D.3})$$

where $P_{DS}(k_W|k_E)$ is the probability that the W-scaler detected k_W hits, given that the E-scaler detected k_E hits.

Let i denote the number of collisions. After a bit of effort (see Manion's references above), one can show that this joint probability distribution may be written as

$$P_{DS}(k_E, k_W) = \sum_{i \geq \max(k_E, k_W)} \binom{i}{k_W} \binom{i}{k_E} \varepsilon_W^{k_W} \varepsilon_E^{k_E} (1 - \varepsilon_W)^{i-k_W} (1 - \varepsilon_E)^{i-k_E} \frac{\lambda^i e^{-\lambda}}{i!} \quad (\text{D.4})$$

- SS events

The probability for detecting k_E hits in the E-scaler from SS events is

$$P_{ESS}(k_E) = \frac{(\varepsilon_E \lambda_E)^{k_E} e^{-\varepsilon_E \lambda_E}}{k_E!} \quad (\text{D.5})$$

Likewise, the probability for detecting k_W hits in the W-scaler from SS events is

$$P_{WSS}(k_W) = \frac{(\varepsilon_W \lambda_W)^{k_W} e^{-\varepsilon_W \lambda_W}}{k_W!} \quad (\text{D.6})$$

D.3 Probabilities for Detecting Zero Hits

Consider the following three probability distributions:

1. Zero hits in E-scaler

$$P(k_E = 0) = P_{DS}(k_E = 0) \cdot P_{ESS}(k_E = 0) = e^{-\varepsilon_E(\lambda + \lambda_E)} \quad (\text{D.7})$$

2. Zero hits in W-scaler

$$P(k_W = 0) = P_{DS}(k_W = 0) \cdot P_{WSS}(k_W = 0) = e^{-\varepsilon_W(\lambda + \lambda_W)} \quad (\text{D.8})$$

3. Zero hits in 2-sided detector

$$\begin{aligned} P(k_E = 0, k_W = 0) &= P_{DS}(k_E = 0, k_W = 0) \cdot P_{ESS}(k_E = 0) \cdot P_{WSS}(k_W = 0) = \\ &= e^{\varepsilon_W \varepsilon_E \lambda - \varepsilon_W \lambda - \varepsilon_E \lambda - \varepsilon_W \lambda_W - \varepsilon_E \lambda_E} \end{aligned} \quad (\text{D.9})$$

Let P^* denote the probability that the 2-sided detector detects zero hits in both E and W scalers, given the condition that the single-sided detectors each detected zero hits. Using the Kolmogorov definition of conditional probability, P^* is expressed as

$$P^* = \frac{P(k_E = 0, k_W = 0)}{P(k_E = 0) \cdot P(k_W = 0)} = e^{\Omega \lambda} \quad \text{where } \Omega := \varepsilon_W \varepsilon_E \quad (\text{D.10})$$

Let $P_{E(W)}$ be the probability of detecting at least 1 E(W)-scaler single, and P_X be the probability of detecting at least 1 coincidence. These probabilities are used to rewrite the above three probability distributions for detecting zero hits in the form of

$$(\text{probability of zero hits}) = 1 - (\text{probability of at least 1 hit})$$

D.4 Rate-Safe Correction Equation

Take the logarithm of P^* to obtain

$$\Omega \lambda = \ln P^* = \ln \left[\frac{1 - P_X}{(1 - P_E)(1 - P_W)} \right] \quad (\text{D.11})$$

Assume the probability distributions of detecting $N_{E(W)}$ hits in the $E(W)$ -scaler and N_X coincidences are all binomial, given a total of N_{bx} bunch crossings. Manion argues that binomial distributions are needed since the probability of a trigger is significant for all filled bunch crossings. Denoting the mean of these binomial distributions by $\langle \cdot \rangle$, we thus have

$$P_S = \frac{\langle N_S \rangle}{N_{bx}} \quad \text{where } S \in \{E, W, X\} \quad (\text{D.12})$$

Finally, the product of E and W acceptances and efficiencies times the rate-safe counts N_{rsc} is written in terms of the raw scaler counts $\{N_E, N_W, N_X\}$ and total number of bunch crossings N_{bx} as

$$\boxed{\Omega N_{rsc} = N_{bx} \cdot \ln \left[\frac{1 - \langle N_X \rangle / N_{bx}}{(1 - \langle N_E \rangle / N_{bx})(1 - \langle N_W \rangle / N_{bx})} \right]} \quad (\text{D.13})$$

where the subscript “rsc” stands for “rate-safe correction”.

D.5 Note on Accidentals

1. For bunch crossings with 1 collision, we either have a true coincidence from a DS-event or a single hit from a SS-event
 - No accidental coincidences can occur in this case
2. For bunch crossings with more than 1 collision, we have the following possibilities:
 - Detection of coincidence event: either one or both of the following cases must occur:
 - At least 1 DS-collision – occurs an average of λ times / bunch crossing
 - At least 1 ESS-collision and 1 WSS-collision – occurs an average of λ_E and λ_W times / bunch crossing, respectively
 - Detection of single event
 - DS-event contribution
 - All SS-events in the bunch crossing are toward one detector – occurs an average of λ_E or λ_W times / bunch crossing

Claim: P^* only depends on λ , but not on λ_E or λ_W . Thus the above equation for N_{rsc} only counts “true coincidences,” eliminating the need to consider “accidental coincidences.”

D.6 Statistical Uncertainty Propagation

Define the function f , through which the counts uncertainties will be propagated:

$$f(N_X, N_E, N_W) := \Omega \cdot N_{rsc}(N_X, N_E, N_W) \quad (\text{D.14})$$

For a general function $Y = g(X_1, \dots, X_n) \in C^\infty$ such that $\mu_i := \langle X_i \rangle$, the uncertainty of the variables $\{X_i\}$ propagates to Y via a Taylor series expansion to first order, yielding

$$\sigma_Y^2 = \sum_{i=1}^n a_i^2 \underbrace{E[(X_i - \mu_i)^2]}_{=\sigma_{X_i}^2 \text{ (variance)}} + \sum_{i \neq j} a_i a_j \underbrace{E[(X_i - \mu_i)(X_j - \mu_j)]}_{=\sigma_{X_i X_j} \text{ (covariance)}} \quad (\text{D.15})$$

where

$$a_i := \frac{\partial}{\partial X_i} f(X_1 = \mu_1, \dots, X_n = \mu_n) \quad (\text{D.16})$$

and $E[X]$ denotes the expectation value of X .

Applying this expansion to equation D.14, the uncertainty in $\{N_X, N_E, N_W\}$ is propagated to an uncertainty in $\Omega \cdot N_{rsc}$ as

$$\begin{aligned}\sigma_{\Omega \cdot N_{rsc}}^2 &= \left(\frac{\partial f}{\partial N_X} \right)^2 \sigma_{N_X}^2 + \left(\frac{\partial f}{\partial N_E} \right)^2 \sigma_{N_E}^2 + \left(\frac{\partial f}{\partial N_W} \right)^2 \sigma_{N_W}^2 + \\ &\quad + 2 \left[\frac{\partial f}{\partial N_X} \frac{\partial f}{\partial N_E} \sigma_{N_X N_E} + \frac{\partial f}{\partial N_X} \frac{\partial f}{\partial N_W} \sigma_{N_X N_W} + \frac{\partial f}{\partial N_E} \frac{\partial f}{\partial N_W} \sigma_{N_E N_W} \right]\end{aligned}\quad (\text{D.17})$$

where all derivatives are evaluated at $N_S = \langle N_S \rangle$ with $S \in \{X, E, W\}$. Since the scalar counts $\{N_S\}$ are given by binomial distributions, the variances are

$$\begin{aligned}\sigma_{N_S}^2 &= N_{bx} P_S (1 - P_S) \\ &= \langle N_S \rangle \left(1 - \frac{\langle N_S \rangle}{N_{bx}} \right) \\ &= \langle N_S \rangle \cdot \zeta(N_S)\end{aligned}\quad (\text{D.18})$$

where

$$\zeta(N_S) := 1 - \frac{\langle N_S \rangle}{N_{bx}} \quad (\text{D.19})$$

The covariances, $\sigma_{S_1 S_2}$, can be obtained from 2D histograms. The derivatives of f evaluate to

$$\frac{\partial f}{\partial N_X} = \frac{-1}{\zeta(N_X)} \quad \text{and} \quad \frac{\partial f}{\partial N_{E,W}} = \frac{1}{\zeta(N_{E,W})} \quad (\text{D.20})$$

Inserting the variances, covariances, and derivatives yields the propagated uncertainty:

$$\begin{aligned}\sigma_{\Omega \cdot N_{rsc}}^2 &= \frac{\langle N_X \rangle}{\zeta(N_X)} + \frac{\langle N_E \rangle}{\zeta(N_E)} + \frac{\langle N_W \rangle}{\zeta(N_W)} - \\ &\quad - \frac{2\sigma_{N_X N_E}}{\zeta(N_X) \zeta(N_E)} - \frac{2\sigma_{N_X N_W}}{\zeta(N_X) \zeta(N_W)} + \frac{2\sigma_{N_E N_W}}{\zeta(N_E) \zeta(N_W)}\end{aligned}\quad (\text{D.21})$$

In practice, however, it is better to use the Pearson correlation coefficients, which are covariances normalized by the product of the variances: $\rho_{S_1 S_2} := \sigma_{S_1 S_2} / \sigma_{S_1} \sigma_{S_2}$. Typically, these correlation coefficients are close to unity for the present analyses.

Inserting the expression of the variances, the propagated uncertainty can be rewritten

using the Pearson correlation coefficients as

$$\boxed{\sigma_{\Omega \cdot N_{rsc}}^2 = \frac{\langle N_X \rangle}{\zeta(N_X)} + \frac{\langle N_E \rangle}{\zeta(N_E)} + \frac{\langle N_W \rangle}{\zeta(N_W)} - 2\rho_{N_X N_E} \sqrt{\frac{\langle N_X \rangle \langle N_E \rangle}{\zeta(N_X) \zeta(N_E)}} \\ - 2\rho_{N_X N_W} \sqrt{\frac{\langle N_X \rangle \langle N_W \rangle}{\zeta(N_X) \zeta(N_W)}} + 2\rho_{N_E N_W} \sqrt{\frac{\langle N_E \rangle \langle N_W \rangle}{\zeta(N_E) \zeta(N_W)}}} \quad (\text{D.22})$$

Equations D.13 and D.22 represent the quantity used for computing the relative luminosity and its statistical uncertainty. The statistical uncertainty in equation D.22 is further propagated into the nine relative luminosity equations.

Let L_z denote the quantity which we are using to compute the relative luminosity, where $z \in \{--, -, +, ++\}$ are the initial spin states. In this case, $L_z = \Omega \cdot N_{rsc,z}$, where Ω is assumed to be the same for all initial spin states. In this way, Ω cancels out of any relative luminosity considered.

Appendix E

Bunch-Fitting Algorithm

Refer to chapter 4 of [11] for the method used to compute ε_3 , the double-spin asymmetry. Let r^i be a quantity defined for bunch crossing $i \in B$, where B is the set of bunch crossing numbers under consideration. The objective is to fit r^i to the following equation:

$$r^i = c_a (1 + H_a^i \varepsilon_a) \text{ where } H_a^i = \begin{cases} h_Y^i, & \text{if } a = 1 \\ h_B^i, & \text{if } a = 2 \\ h_B^i h_Y^i, & \text{if } a = 3 \end{cases} \quad (\text{E.1})$$

The fit parameters are c_a and ε_a , for each asymmetry number $a \in \{1, \dots, 9\}$, where additional asymmetry numbers are defined in the table above. The yellow (east-facing) and blue (west-facing) single spin asymmetries are ε_1 and ε_2 ; the double spin asymmetry is ε_3 . The parameter c_a is approximately the average value of r^i for the case where $\varepsilon_a \sum_{i \in B} H_a^i \ll |B|$.

The bunch fitting algorithm determines the pair of parameters (c_a, ε_a) , which minimizes the χ_a^2 of the fit for asymmetry number a , given by

$$\chi_a^2 = \sum_{i \in B} \left[\frac{c_a (1 + H_a^i \varepsilon_a) - r^i}{\sigma_{r^i}} \right]^2, \quad (\text{E.2})$$

where $\sigma_{r^i}^2$ is the variance of r^i . The summand expands such that

$$\chi_a^2 = c_a^2 (1 + \varepsilon_a^2) \Sigma(1) - 2c_a \Sigma(r^i) + 2c_a^2 \varepsilon_a \Sigma(H_a^i) - 2c_a \varepsilon_a \Sigma(H_a^i r^i), \quad (\text{E.3})$$

where for a bunch crossing-dependent quantity x^i , the function $\Sigma(x^i)$ is defined as

$$\Sigma(x^i) := \sum_{i \in B} \frac{x^i}{\sigma_{r^i}^2}. \quad (\text{E.4})$$

The pair (c_a, ε_a) which minimises equation E.3 is the solution to the system

$$\begin{cases} 0 = \frac{\partial \chi_a^2}{\partial \varepsilon_a} = 2c_a^2 \varepsilon_a \Sigma(1) + 2c_a^2 \Sigma(H_a^i) - 2c_a \Sigma(H_a^i r^i) \\ 0 = \frac{\partial \chi_a^2}{\partial c_a} = 2c_a (1 + \varepsilon_a^2) \Sigma(1) - 2\Sigma(r^i) + 4c_a \varepsilon_a \Sigma(H_a^i) - 2\varepsilon_a \Sigma(H_a^i r^i) \end{cases} \quad (\text{E.5})$$

The solution, which can be expressed solely in terms of the summations $\Sigma(x^i)$ is:

$$\varepsilon_a = \frac{\Sigma(H_a^i) \Sigma(r^i) - \Sigma(1) \Sigma(H_a^i r^i)}{\Sigma(H_a^i) \Sigma(H_a^i r^i) - \Sigma(1) \Sigma(r^i)} \quad (\text{E.6})$$

$$c_a = \frac{\Sigma(H_a^i) \Sigma(H_a^i r^i) - \Sigma(1) \Sigma(r^i)}{\Sigma(H_a^i)^2 - \Sigma(1)^2} \quad (\text{E.7})$$

Propagation of uncertainty of each r^i gives the uncertainties on the fit parameters:

$$\sigma_{\varepsilon_a}^2 = \sum_{k \in B} \left(\frac{\partial \varepsilon_a}{\partial r^k} \sigma_{r^k} \right)^2 \quad (\text{E.8})$$

$$\sigma_{c_a}^2 = \sum_{k \in B} \left(\frac{\partial c_a}{\partial r^k} \sigma_{r^k} \right)^2 \quad (\text{E.9})$$

The derivative of the function $\Sigma(x^i)$ is nonzero if x^i is dependent on r^i , e.g., for $x^i = f(r^i)$,

$$\frac{\partial}{\partial r^k} \Sigma \circ f(r^i) = \sum_{i \in B} \frac{1}{\sigma_{r^i}^2} \frac{\partial}{\partial r^k} f(r^i) = \frac{1}{\sigma_{r^k}^2} \frac{\partial}{\partial r^k} f(r^k) \quad (\text{E.10})$$

Derivatives of the χ_a^2 -minimizing fit parameters are then

$$\frac{\partial \varepsilon_a}{\partial r^k} = \frac{1}{\sigma_{r^k}^2} \frac{[\Sigma(H_a^i)^2 - \Sigma(1)^2] [\Sigma(H_a^i r^i) - H_a^k \Sigma(r^i)]}{[\Sigma(H_a^i) \Sigma(H_a^i r^i) - \Sigma(1) \Sigma(r^i)]^2} \quad (\text{E.11})$$

$$\frac{\partial c_a}{\partial r^k} = \frac{1}{\sigma_{r^k}^2} \frac{H_a^k \Sigma(H_a^i) - \Sigma(1)}{\Sigma(H_a^i)^2 - \Sigma(1)^2} \quad (\text{E.12})$$

The propagated uncertainties are therefore

$$\sigma_{\varepsilon_a}^2 = \sum_{k \in B} \left[\frac{1}{\sigma_{r^k}^2} \frac{[\Sigma(H_a^i)^2 - \Sigma(1)^2] [\Sigma(H_a^i r^i) - H_a^k \Sigma(r^i)]}{[\Sigma(H_a^i) \Sigma(H_a^i r^i) - \Sigma(1) \Sigma(r^i)]^2} \right]^2 \quad (\text{E.13})$$

$$\sigma_{c_a}^2 = \sum_{k \in B} \left[\frac{1}{\sigma_{r^k}^2} \frac{H_a^k \Sigma(H_a^i) - \Sigma(1)}{\Sigma(H_a^i)^2 - \Sigma(1)^2} \right]^2 \quad (\text{E.14})$$

The above procedure can be used to extract raw asymmetries ε_a from a scalar system S ,

given a minimum-bias relative luminosity measured by detector MB by choosing

$$r^i = \frac{N_S^i}{N_{MB}^i},$$

where N_D^i is the number of scaler counts for bunch crossing i , measured by scaler D . The fractional error on r^i is given by propagation of uncertainty, assuming N_S^i and N_{MB}^i are uncorrelated:

$$\frac{\sigma_{r^i}}{r^i} = \sqrt{\frac{1}{N_S^i} + \frac{1}{N_{MB}^i}}. \quad (\text{E.15})$$

Let $N_D^{+(-)}$ be the total number of scaler counts seen by D , summed over bunch crossings with like (unlike) proton helicities. Then, for example, the raw double spin asymmetry extracted with the above definition of r^i is

$$\varepsilon_3 = \frac{N_S^+/N_{MB}^+ - N_S^-/N_{MB}^-}{N_S^+/N_{MB}^+ + N_S^-/N_{MB}^-} = \frac{N_S^+ - R_3^{MB}N_S^-}{N_S^+ + R_3^{MB}N_S^-}, \quad (\text{E.16})$$

where the minimum bias relative luminosity is $R_3^{MB} := N_{MB}^+/N_{MB}^-$. This asymmetry is then seen as a raw double spin asymmetry in scaler detector S with respect to a minimum bias scaler detector MB . Including the beam polarizations allows the definition of the scaler spin asymmetries (with respect to MB) as

$$\begin{cases} S_L^Y := \varepsilon_1/P_Y \\ S_L^B := \varepsilon_2/P_B \\ S_{LL} := \varepsilon_3/P_B P_Y \end{cases} \quad (\text{E.17})$$

Appendix F

Polarization Uncertainties

This appendix is a summary of polarization uncertainty propagation from the analysis note written by the CNI Polarimetry Group at RHIC [17], but with details specific to the Run 12 and 13 double-spin analysis.

This appendix begins with a discussion of polarization for a single beam, followed by a section which outlines how the polarization product is calculated, along with its uncertainty propagation. Finally, details concerning combining uncertainties for Runs 12 and 13 are presented.

F.1 Single Beam Polarization

Let $r \in \{1, \dots, N_r\}$ denote a single run number and $f \in \{1, \dots, N_f\}$ denote a single fill number, where N_r and N_f are the total number of runs and fills, respectively. Let F_r represent the fill (*i.e.*, set of runs) which contains run r , and denote its fill number by $f(r)$; similarly, let F_f represent fill f .

The CNI Polarimetry Group provides polarimetry parameters for each fill F_r as a pair of parameters $\{P_{f(r)}^0, P_{f(r)}^1\}$ along with their uncertainties $\{\sigma_{P_{f(r)}^0}, \sigma_{P_{f(r)}^1}\}$. Letting t_r be the time of run r since the beginning of its fill F_r , the time-dependent polarization for one beam is

$$P_r = P_{f(r)}^0 + P_{f(r)}^1 \cdot t_r \quad (\text{F.1})$$

For each fill, we may compute a luminosity-weighted average, given the luminosity of run r is L_r :

$$\langle P \rangle_f^{\text{LW}} = \frac{1}{L_f} \sum_{r \in F_f} L_r P_r = P_f^0 + \frac{P_f^1}{L_f} \sum_{r \in F_f} L_r t_r \quad \text{where} \quad L_f := \sum_{r \in F_f} L_r \quad (\text{F.2})$$

The uncertainties on the polarimetry parameters, $\{\sigma_{P_f^0}, \sigma_{P_f^1}\}$, propagate to an uncertainty

on $\langle P \rangle_f^{\text{LW}}$, along with a relative fill-to-fill systematic uncertainty on the pC polarization, $\sigma_{\text{sys}(P)}/P$, as

$$\sigma_{\langle P \rangle_f^{\text{LW}}} = \sigma_{P_f^0} \oplus \frac{\sigma_{P_f^1}}{L_f} \sum_{r \in F_f} L_r t_r \oplus \langle P \rangle_f^{\text{LW}} \cdot \frac{\sigma_{\text{sys}(P)}}{P} \quad (\text{F.3})$$

The symbol “ \oplus ” denotes quadrature summation. Values of $\sigma_{\text{sys}(P)}/P$ are obtained from table 4 in [17]:

- Run 12: 0% for blue, 3.1% for yellow
- Run 13: 2.8% for blue, 1.4% for yellow

We may now combine the fill-by-fill luminosity-weighted average polarizations into an overall polarization, \mathbb{P} , by luminosity-averaging $\langle P \rangle_f^{\text{LW}}$ over each fill:

$$\mathbb{P} = \frac{1}{\mathbb{L}} \sum_{f=1}^{N_f} L_f \langle P \rangle_f^{\text{LW}} \quad \text{where} \quad \mathbb{L} := \sum_{f=1}^{N_f} L_f \quad (\text{F.4})$$

The uncertainties $\sigma_{\langle P \rangle_f^{\text{LW}}}$ from equation F.3 propagate as

$$\sigma_{\mathbb{P}} = \frac{1}{\mathbb{L}} \bigoplus_{f=1}^{N_f} L_f \sigma_{\langle P \rangle_f^{\text{LW}}} \quad (\text{F.5})$$

There are two additional systematic uncertainties to consider: uncertainty from overall polarization scale and uncertainty from the profile correction. The overall scale uncertainties $\sigma_{\text{scale}}(P)/P$, which originate from H-jet and pC scale uncertainties and are summarized in table 5 of [17], are:

- Run 12: 3.4% for P_B , 3.4% for P_Y , and 6.6% for $P_B P_Y$
- Run 13: 3.2% for P_B , 3.3% for P_Y , and 6.4% for $P_B P_Y$

The uncertainty due to profile correction, $\sigma_{\text{profile}}(P)/P$ is

- For single beam: $2.2\%/\sqrt{N_f}$
- For both beams together: $3.1\%/\sqrt{N_f}$

At this point, one must be careful not to double-count uncertainties. The uncertainty $\sigma_{\mathbb{P}}$ in equation F.5 actually already contributes to $\sigma_{\text{scale}}(P)/P$. If N_T is the total number of

fills used to obtain the polarimetry A_N and, in turn, $\sigma_{\text{scale}}(P)/P$, then we can approximately correct $\sigma_{\mathbb{P}}$ by using a factor:

$$\sigma_{\mathbb{P}} \rightarrow \sigma_{\mathbb{P},\text{corr}} = \sigma_{\mathbb{P}} \cdot \text{Re} \sqrt{1 - \frac{N_f}{N_T}} \quad (\text{F.6})$$

For the case where more fills were analyzed N_f than were used to obtain polarimetry A_N , then $N_f > N_T$ implies $\sigma_{\sigma_{\mathbb{P},\text{corr}}} = 0$ and the scale systematic is completely double-counted. On the other hand, if $N_f < N_T$, then $\sigma_{\sigma_{\mathbb{P},\text{corr}}}$ accounts for the extra statistical uncertainty from having analyzed less than N_T fills. The values of N_T are (from table 6 in [17]):

- Run 12: 49 for blue, 49 for yellow
- Run 13: 138 for blue, 139 for yellow

All of the above uncertainties are combined together to form a total uncertainty on the \mathbb{P} for a single beam as

$$\sigma_{\mathbb{P}}^{\text{Tot}} = \sigma_{\mathbb{P},\text{corr}} \oplus \mathbb{P} \cdot \frac{\sigma_{\text{scale}}(P)}{P} \oplus \mathbb{P} \cdot \frac{\sigma_{\text{profile}}(P)}{P} \quad (\text{F.7})$$

which can be written as a relative uncertainty on \mathbb{P} as

$$\frac{\sigma_{\mathbb{P}}^{\text{Tot}}}{\mathbb{P}} = \frac{\sigma_{\mathbb{P},\text{corr}}}{\mathbb{P}} \oplus \frac{\sigma_{\text{scale}}(P)}{P} \oplus \frac{\sigma_{\text{profile}}(P)}{P} \quad (\text{F.8})$$

F.2 Beam Polarization Product

Equation F.7 represents the uncertainty of the overall polarization of one beam, but the $A_{LL}^{\pi^0}$ analysis uses the product of polarizations from each beam. Let us now consider the polarizations of two beams, denoted P and Q . The product of polarizations for one run r is

$$P_r Q_r = (P_{f(r)}^0 + P_{f(r)}^1 \cdot t_r) (Q_{f(r)}^0 + Q_{f(r)}^1 \cdot t_r) \quad (\text{F.9})$$

and the luminosity-weighted average for one fill f expands to

$$\langle PQ \rangle_f^{\text{LW}} = P_f^0 Q_f^0 + \frac{1}{L_f} \left[(P_f^0 Q_f^1 + P_f^1 Q_f^0) \sum_{r \in F_f} L_r t_r + P_f^1 Q_f^1 \sum_{r \in F_f} L_r t_r^2 \right] \quad (\text{F.10})$$

The statistical uncertainty, including fill-to-fill systematic uncertainties, is

$$\begin{aligned} \sigma_{\langle PQ \rangle_f^{\text{LW}}} &= \frac{\sigma_{P_f^0}}{L_f} \left(Q_f^0 L_f + Q_f^1 \sum_{r \in F_f} L_r t_r \right) \oplus \frac{\sigma_{P_f^1}}{L_f} \left(Q_f^0 \sum_{r \in F_f} L_r t_r + Q_f^1 \sum_{r \in F_f} L_r t_r^2 \right) \oplus \\ &\oplus \frac{\sigma_{Q_f^0}}{L_f} \left(P_f^0 L_f + P_f^1 \sum_{r \in F_f} L_r t_r \right) \oplus \frac{\sigma_{Q_f^1}}{L_f} \left(P_f^0 \sum_{r \in F_f} L_r t_r + P_f^1 \sum_{r \in F_f} L_r t_r^2 \right) \oplus \langle PQ \rangle_f^{\text{LW}} \cdot \frac{\sigma_{\text{sys}}(PQ)}{PQ} \end{aligned} \quad (\text{F.11})$$

where $\sigma_{\text{sys}}(PQ)/PQ = \sigma_{\text{sys}}(P)/P \oplus \sigma_{\text{sys}}(Q)/Q = 3.1\%$ for both Runs 12 and 13. The overall luminosity-weighted average polarization product is then

$$\mathbb{PQ} = \frac{1}{\mathbb{L}} \sum_{f=1}^{N_f} L_f \langle PQ \rangle_f^{\text{LW}} \quad (\text{F.12})$$

and the statistical uncertainty is

$$\sigma_{\mathbb{PQ}} = \frac{1}{\mathbb{L}} \bigoplus_{f=1}^{N_f} L_f \sigma_{\langle PQ \rangle_f^{\text{LW}}} \quad (\text{F.13})$$

The double-counting correction is

$$\sigma_{\mathbb{PQ}} \rightarrow \sigma_{\mathbb{PQ},\text{corr}} = \sigma_{\mathbb{PQ}} \cdot \text{Re} \sqrt{1 - \frac{N_f}{\text{Min}(N_T^P, N_T^Q)}} \quad (\text{F.14})$$

where the lesser of N_T^P and N_T^Q is used, since that would be the number of fills one would need in order to calculate a polarimetry double-spin asymmetry. Finally,

$$\sigma_{\mathbb{PQ}}^{\text{Tot}} = \sigma_{\mathbb{PQ},\text{corr}} \oplus \mathbb{PQ} \cdot \frac{\sigma_{\text{scale}}(PQ)}{PQ} \oplus \mathbb{PQ} \cdot \frac{\sigma_{\text{profile}}(PQ)}{PQ} \quad (\text{F.15})$$

where the scale and profile systematic uncertainties are

- $\sigma_{\text{scale}}(PQ)/PQ = 6.6\%$ for Run 12, 6.4% for Run 13
- $\sigma_{\text{profile}}(PQ)/PQ = 3.1\%/\sqrt{N_f}$ for both Runs together

F.3 Combining Uncertainties over Two Run Periods

If the analyzed data include polarizations from two RHIC Run periods, there will be two sets of polarimetry uncertainties to propagate, in order to determine an overall polarization uncertainty. This section demonstrates how to combine the two sets of uncertainties from Runs 12 and 13; altogether, four uncertainties need to be considered:

1. The fill-to-fill systematic uncertainty, $\sigma_{\text{sys}}(PQ)/PQ$, is trivial to combine since it enters each term of the quadrature sum in equation F.11.
2. The profile correction uncertainty, $\sigma_{\text{profile}}(PQ)/PQ$ is also straightforward, since it is the same for both Runs 12 and 13.
3. For the scale uncertainty, $\sigma_{\text{scale}}(PQ)/PQ$, [17] suggests to use the larger uncertainty between the two RHIC Runs.
4. For the double-counting correction, adding together the number of fills involved gives the correction factor

$$\sigma_{PQ} \rightarrow \sigma_{PQ,\text{corr}} = \sigma_{PQ} \cdot \text{Re} \cdot \sqrt{1 - \frac{N_{f,12} + N_{f,13}}{\text{Min}(N_{T,12}^P, N_{T,13}^Q) + \text{Min}(N_{T,12}^P, N_{T,13}^Q)}} \quad (\text{F.16})$$

F.4 Results

RUN 12

$$L_{int} = 57.4036 \text{ pb}^{-1}$$

$$\mathbb{P}_B = 0.5434 \quad \sigma_{\mathbb{P}_B} = 0.0187$$

$$\mathbb{P}_Y = 0.5641 \quad \sigma_{\mathbb{P}_Y} = 0.0194$$

$$\mathbb{P}_B \mathbb{P}_Y = 0.3069 \quad \sigma_{\mathbb{P}_B \mathbb{P}_Y} = 0.0204$$

$$\sigma_{\mathbb{P}_B, (\text{fill-to-fill scale})} = Re \left[\sqrt{1 - 45/49} \right] \cdot [0.0066] = 0.0019$$

$$\sigma_{\mathbb{P}_Y, (\text{fill-to-fill scale})} = Re \left[\sqrt{1 - 45/49} \right] \cdot [0.0078] = 0.0022$$

$$\sigma_{\mathbb{P}_Y, (\text{fill-to-fill scale})} = Re \left[\sqrt{1 - 45/49} \right] \cdot [0.0058] = 0.0017$$

$$\mathbb{P}_B \cdot \sigma_{scale}(P_B) / P_B = 0.5434 \cdot 0.0340 = 0.0185$$

$$\mathbb{P}_Y \cdot \sigma_{scale}(P_Y) / P_Y = 0.5641 \cdot 0.0340 = 0.0192$$

$$\mathbb{P}_B \mathbb{P}_Y \cdot \sigma_{scale}(P_B P_Y) / P_B P_Y = 0.3069 \cdot 0.0660 = 0.0203$$

$$\mathbb{P}_B \cdot \sigma_{profile}(P_B) / P_B = 0.5434 \cdot 0.0033 = 0.0018$$

$$\mathbb{P}_Y \cdot \sigma_{profile}(P_Y) / P_Y = 0.5641 \cdot 0.0033 = 0.0018$$

$$\mathbb{P}_B \mathbb{P}_Y \cdot \sigma_{profile}(P_B P_Y) / P_B P_Y = 0.3069 \cdot 0.0046 = 0.0014$$

RUN 13

$$L_{int} = 6.0140 \text{ pb}^{-1}$$

$$\mathbb{P}_B = 0.5688 \quad \sigma_{\mathbb{P}_B} = 0.0192$$

$$\mathbb{P}_Y = 0.5656 \quad \sigma_{\mathbb{P}_Y} = 0.0194$$

$$\mathbb{P}_B \mathbb{P}_Y = 0.3225 \quad \sigma_{\mathbb{P}_B \mathbb{P}_Y} = 0.0212$$

$$\sigma_{\mathbb{P}_B, (\text{fill-to-fill scale})} = Re \left[\sqrt{1 - 40/138} \right] \cdot [0.0067] = 0.0056$$

$$\sigma_{\mathbb{P}_Y, (\text{fill-to-fill scale})} = Re \left[\sqrt{1 - 40/139} \right] \cdot [0.0057] = 0.0048$$

$$\sigma_{\mathbb{P}_Y, (\text{fill-to-fill scale})} = Re \left[\sqrt{1 - 40/138} \right] \cdot [0.0054] = 0.0045$$

$$\mathbb{P}_B \cdot \sigma_{scale}(P_B)/P_B = 0.5688 \cdot 0.0320 = 0.0182$$

$$\mathbb{P}_Y \cdot \sigma_{scale}(P_Y)/P_Y = 0.5656 \cdot 0.0330 = 0.0187$$

$$\mathbb{P}_B \mathbb{P}_Y \cdot \sigma_{scale}(P_B P_Y)/P_B P_Y = 0.3225 \cdot 0.0640 = 0.0206$$

$$\mathbb{P}_B \cdot \sigma_{profile}(P_B)/P_B = 0.5688 \cdot 0.0035 = 0.0020$$

$$\mathbb{P}_Y \cdot \sigma_{profile}(P_Y)/P_Y = 0.5656 \cdot 0.0035 = 0.0020$$

$$\mathbb{P}_B \mathbb{P}_Y \cdot \sigma_{profile}(P_B P_Y)/P_B P_Y = 0.3225 \cdot 0.0049 = 0.0016$$

RUNS 12 + 13

$$L_{int} = 63.4177 \text{ pb}^{-1}$$

$$\mathbb{P}_B = 0.5458 \quad \sigma_{\mathbb{P}_B} = 0.0191$$

$$\mathbb{P}_Y = 0.5642 \quad \sigma_{\mathbb{P}_Y} = 0.0199$$

$$\mathbb{P}_B \mathbb{P}_Y = 0.3083 \quad \sigma_{\mathbb{P}_B \mathbb{P}_Y} = 0.0208$$

$$\sigma_{\mathbb{P}_B, (\text{fill-to-fill scale})} = Re \left[\sqrt{1 - 85/187} \right] \cdot [0.0060] = 0.0044$$

$$\sigma_{\mathbb{P}_Y, (\text{fill-to-fill scale})} = Re \left[\sqrt{1 - 85/188} \right] \cdot [0.0071] = 0.0052$$

$$\sigma_{\mathbb{P}_Y, (\text{fill-to-fill scale})} = Re \left[\sqrt{1 - 85/187} \right] \cdot [0.0053] = 0.0039$$

$$\mathbb{P}_B \cdot \sigma_{scale}(P_B) / P_B = 0.5458 \cdot 0.0340 = 0.0186$$

$$\mathbb{P}_Y \cdot \sigma_{scale}(P_Y) / P_Y = 0.5642 \cdot 0.0340 = 0.0192$$

$$\mathbb{P}_B \mathbb{P}_Y \cdot \sigma_{scale}(P_B P_Y) / P_B P_Y = 0.3083 \cdot 0.0660 = 0.0204$$

$$\mathbb{P}_B \cdot \sigma_{profile}(P_B) / P_B = 0.5458 \cdot 0.0024 = 0.0013$$

$$\mathbb{P}_Y \cdot \sigma_{profile}(P_Y) / P_Y = 0.5642 \cdot 0.0024 = 0.0013$$

$$\mathbb{P}_B \mathbb{P}_Y \cdot \sigma_{profile}(P_B P_Y) / P_B P_Y = 0.3083 \cdot 0.0034 = 0.0010$$

Appendix G

Including Photon Uncertainties in p_T Uncertainty

The p_T uncertainty was approximated in equation 5.37, rewritten here:

$$\frac{\sigma_{p_T}}{p_T} \approx \frac{\sigma_E}{E} \oplus \frac{\sigma_h}{h} \oplus \frac{\sigma_{R_z}}{R_z} \quad (\text{G.1})$$

A more accurate determination of the p_T uncertainty can be made by making use of invariant mass and taking into account uncertainties on photon separation and energy imbalance; however, it will be shown that the additional terms which correct equation G.1 are suppressed. Given a π^0 with the 4-momentum given in equation 5.35, its invariant mass is

$$M^2 = E^2 - p_T^2 \csc^2 \theta \quad (\text{G.2})$$

Defining Z as the photon energy imbalance and α as the decay opening angle, the two-photon system invariant mass is

$$M^2 = E^2 (1 - Z^2) \sin^2 \frac{\alpha}{2} \quad (\text{G.3})$$

Let R be the distance between the nominal vertex and the point on the FMS plane at which the π^0 would have struck had it not decayed. Let D be the transverse distance between the detected photon hits. Then

$$\tan \frac{\alpha}{2} = \frac{D}{2R} = \frac{D \cos \theta}{2R_z} =: T(D, \theta) \quad (\text{G.4})$$

Now take $\alpha(D, \theta)$ from equation G.4, insert it into equation G.3 and equate the result to equation G.2:

$$E^2 (1 - Z^2) \frac{T^2}{1 + T^2} = E^2 - p_T^2 \csc^2 \theta \quad (\text{G.5})$$

Solving for p_T gives

$$p_T(E, Z, \theta, D) = E \sin \theta \cdot \sqrt{\frac{1 + T^2 Z^2}{1 + T^2}} \quad (\text{G.6})$$

The uncertainty propagates as

$$\sigma_{p_T} = \frac{\partial p_T}{\partial E} \sigma_E \oplus \frac{\partial p_T}{\partial Z} \sigma_Z \oplus \frac{\partial p_T}{\partial \theta} \sigma_\theta \oplus \frac{\partial p_T}{\partial D} \sigma_D \quad (\text{G.7})$$

By defining X as

$$X := D \cdot \frac{\partial p_T}{\partial D} = E \sin \theta \cdot \frac{(Z^2 - 1) T^2}{(1 + T^2)^{3/2} \sqrt{1 + Z^2 T^2}} \quad (\text{G.8})$$

the derivatives in equation G.7 are then

$$\frac{\partial p_T}{\partial E} = \frac{p_T}{E} \quad (\text{G.9})$$

$$\frac{\partial p_T}{\partial Z} = \frac{(1 + T^2) ZX}{Z^2 - 1} \quad (\text{G.10})$$

$$\frac{\partial p_T}{\partial \theta} = p_T \cot \theta - X \tan \theta \quad (\text{G.11})$$

$$\frac{\partial p_T}{\partial D} = \frac{X}{D} \quad (\text{G.12})$$

Because $\tan \theta = h/R_z$,

$$\sigma_\theta^2 = \sin^2 \theta \cos^2 \theta \left[\left(\frac{\sigma_h}{h} \right)^2 + \left(\frac{\sigma_{R_z}}{R_z} \right)^2 \right] \quad (\text{G.13})$$

It is also easy to show that, given $Z = (E_1 - E_2)/E$ and $\sigma_{E_1}/E_1 = \sigma_{E_2}/E_2 = \sigma_E/E$,

$$\sigma_Z = \frac{1 - Z^2}{\sqrt{2}} \cdot \frac{\sigma_E}{E} \quad (\text{G.14})$$

It turns out that X is quite small when compared to other contributions to σ_{p_T} . If we set $X = 0$, the σ_Z and σ_D terms drop out. The σ_θ term is then the same as that in equation G.1, up to a factor of $\cos^2 \theta$, which is within 2% of unity for relevant values of θ . Since the E term is the same as that in equation G.1, the determinations of σ_{p_T} in equations G.1 and G.7 should be within about 2% agreement.

Appendix H

Maximum Likelihood Method for A_{LL} Measurement

H.1 Gaussian probability distributions

This derivation begins with the general maximum likelihood method (MLM). Let $f(x_i, \alpha)$ be the probability of measuring x_i in the i th measurement, where α represents the actual value of the measurement. Such a probability is often a Gaussian distribution, *i.e.*,

$$f(x_i, \alpha) = \frac{1}{\sigma\sqrt{2\pi}} \exp\left[-\frac{(x_i - \alpha)^2}{2\sigma^2}\right] \quad (\text{H.1})$$

Define the likelihood function L as the product of the probability distributions for N measurements:

$$L = \prod_{i=1}^N f(x_i, \alpha) \quad (\text{H.2})$$

The maximum likely value, denoted $\bar{\alpha}$, is the α such that L is maximized, *i.e.*, $\bar{\alpha}$ is the solution to

$$0 = \frac{\partial L}{\partial \alpha} \Big|_{\alpha=\bar{\alpha}} \quad (\text{H.3})$$

Because L is a product, it is simpler to evaluate the maximum value of its logarithm:

$$0 = \frac{\partial \ln L}{\partial \alpha} \Big|_{\alpha=\bar{\alpha}} = \sum_{i=1}^N \frac{\partial \ln f(x_i, \alpha)}{\partial \alpha} \Big|_{\alpha=\bar{\alpha}} \quad (\text{H.4})$$

With $f(x_i, \alpha)$ as a Gaussian distribution, the likelihood function is

$$L = \left(\frac{1}{\sigma \sqrt{2\pi}} \right)^N \exp \left[-\frac{1}{2\sigma^2} \sum_{i=1}^N (x_i - \alpha)^2 \right] \quad (\text{H.5})$$

Differentiating the logarithm of L with respect to α yields

$$\begin{aligned} \frac{\partial \ln L}{\partial \alpha} \Big|_{\alpha=\bar{\alpha}} &= \frac{\partial}{\partial \alpha} \left[N \ln \left(\frac{1}{\sigma \sqrt{2\pi}} \right) - \frac{1}{2\sigma^2} \sum_{i=1}^N (x_i - \alpha)^2 \right] \Big|_{\alpha=\bar{\alpha}} = \\ &= \frac{1}{\sigma^2} \sum_{i=1}^N (x_i - \bar{\alpha}) \end{aligned} \quad (\text{H.6})$$

Setting this to zero returns the solution

$$\bar{\alpha} = \frac{1}{N} \sum_{i=1}^N x_i \quad (\text{H.7})$$

Now consider the same Gaussian probability distribution, but allow for the width σ to vary from measurement-to-measurement, denoted as σ_i . The modified distribution is

$$f(x_i, \alpha) = \frac{1}{\sigma_i \sqrt{2\pi}} \exp \left[-\frac{(x_i - \alpha)^2}{2\sigma_i^2} \right] \quad (\text{H.8})$$

Differentiating $\ln L$ gives

$$\begin{aligned} \frac{\partial \ln L}{\partial \alpha} \Big|_{\alpha=\bar{\alpha}} &= \frac{\partial}{\partial \alpha} \ln \left\{ \prod_{i=1}^N \left(\frac{1}{\sigma_i \sqrt{2\pi}} \right) \cdot \exp \left[-\sum_{i=1}^N \frac{(x_i - \alpha)^2}{2\sigma_i^2} \right] \right\} \Big|_{\alpha=\bar{\alpha}} = \\ &= -\frac{\partial}{\partial \alpha} \sum_{i=1}^N \frac{(x_i - \alpha)^2}{2\sigma_i^2} \Big|_{\alpha=\bar{\alpha}} = \\ &= \sum_{i=1}^N \frac{x_i - \bar{\alpha}}{\sigma_i^2} \end{aligned} \quad (\text{H.9})$$

Setting this equal to zero yields $\bar{\alpha}$ as a weighted average:

$$\bar{\alpha} = \frac{\sum_{i=1}^N x_i / \sigma_i^2}{\sum_{i=1}^N 1 / \sigma_i^2} \quad (\text{H.10})$$

H.2 MLM value for A_{LL}

The above MLM can be used to extract a maximum likely value of the asymmetry A_{LL} , denoted \bar{A}_{LL} . Let i represent a single DAQ run. Let

$$\begin{aligned} S_i &:= N_i^{++} + N_i^{--} \\ D_i &:= N_i^{+-} + N_i^{-+} \\ P_i &:= P_i^B P_i^Y \end{aligned} \tag{H.11}$$

where $N^{\text{sign}(h_B)\text{sign}(h_Y)}$ is the number of π^0 s with the initial proton spin states as h_B and h_Y . Let R_i be the relative luminosity R_3 for run i . For a single run, the measurement of A_{LL_i} is written

$$A_{LL_i} = \frac{1}{P_i} \cdot \frac{S_i - R_i D_i}{S_i + R_i D_i} \tag{H.12}$$

The probability for measuring A_{LL_i} in the i th DAQ run, given maximum likely value \bar{A}_{LL} , is modelled as a Gaussian with run-dependent uncertainty σ_i :

$$f(A_{LL_i}, \bar{A}_{LL}) \propto \exp \left[-\frac{(A_{LL_i} - \bar{A}_{LL})^2}{2\sigma_i^2} \right] \tag{H.13}$$

Using the MLM technique above, the maximum likely value is

$$\bar{A}_{LL} = \frac{\sum_{i=1}^N A_{LL_i} / \sigma_i^2}{\sum_{i=1}^N 1 / \sigma_i^2} \tag{H.14}$$

The task is to now compute $\sigma_i =: \sigma_{A_{LL_i}}$, which is the uncertainty of A_{LL_i} . From now on, we suppress the i subscripts for brevity. We also assume that statistical uncertainties of R_i and P_i are negligibly small when compared to the statistical uncertainties of the yield (and the statistical uncertainty on P_i is already accounted for in the calculation of the overall polarization uncertainty in appendix F). The uncertainty in A_{LL_i} is

$$\begin{aligned} \sigma_{A_{LL}}^2 &= \left(\frac{\partial A_{LL}}{\partial S} \right)^2 \sigma_S^2 + \left(\frac{\partial A_{LL}}{\partial D} \right)^2 \sigma_D^2 = \\ &= \frac{(1 - A_{LL} P)^2 \sigma_S^2 + (1 + A_{LL} P)^2 R^2 \sigma_D^2}{P^2 (S + RD)^2} \end{aligned} \tag{H.15}$$

Assume that the raw asymmetry $A_{LL} P \ll 1$ and can be neglected in the calculation of $\sigma_{A_{LL}}$. Also let $\sigma_S = \sqrt{S}$ and $\sigma_D = \sqrt{D}$, because the yield distributions are assumed to be

Poissonian. The uncertainty becomes

$$\sigma_{A_{LL}}^2 = \frac{S + R^2 D}{P^2 (S + RD)^2} \quad (\text{H.16})$$

If the relative luminosity is close to unity, then the assumption $R^2 \sim R$ can be made and the numerator cancels a factor in the denominator, returning

$$\sigma_{A_{LL}}^2 \approx \frac{1}{P^2 (S + RD)} \quad (\text{H.17})$$

Substituting equation H.17 into equation H.14 gives the MLM value of A_{LL} used in this analysis:

$$\boxed{\bar{A}_{LL} = \frac{\sum_{i=1}^N P_i (S_i - R_i D_i)}{\sum_{i=1}^N P_i^2 (S_i + R_i D_i)}} \quad (\text{H.18})$$

It remains to propagate statistical uncertainty of S and D to \bar{A}_{LL} . It is

$$\sigma_{\bar{A}_{LL}}^2 = \sum_{i=1}^N \left[\left(\frac{\partial \bar{A}_{LL}}{\partial S_i} \right)^2 \sigma_{S_i}^2 + \left(\frac{\partial \bar{A}_{LL}}{\partial D_i} \right)^2 \sigma_{D_i}^2 \right] \quad (\text{H.19})$$

The derivatives with respect to S_i and D_i are

$$\frac{\partial \bar{A}_{LL}}{\partial S_i} = \frac{P_i - P_i^2 \bar{A}_{LL}}{\sum_{k=1}^N P_k^2 (S_k + R_k D_k)} \quad (\text{H.20})$$

$$\frac{\partial \bar{A}_{LL}}{\partial D_i} = \frac{-R_i P_i - R_i P_i^2 \bar{A}_{LL}}{\sum_{k=1}^N P_k^2 (S_k + R_k D_k)} \quad (\text{H.21})$$

Assuming that $P_i^2 \bar{A}_{LL}$ is negligible, inserting these derivatives into equation H.19 gives

$$\sigma_{\bar{A}_{LL}} = \sqrt{\frac{\sum_{i=1}^N P_i^2 (S_i + R_i^2 D_i)}{\sum_{i=1}^N P_i^2 (S_i + R_i D_i)}} \quad (\text{H.22})$$

Making the approximation $P_i = \bar{P}$, the average polarization, as well as $R_i = 1$, the uncertainty becomes simply

$$\sigma_{\bar{A}_{LL}} \approx \frac{1}{\bar{P} \sqrt{N}} \quad (\text{H.23})$$

where $N = \sum_{i=1}^N (S_i + D_i)$. It turns out that equation H.23 is extremely close to the value determined from equation H.22; ultimately equation H.22 is used for the statistical uncertainty on $A_{LL}^{\pi^0}$.

Appendix I

Curing Radiation Damage in the FMS

I.1 Sunlight Exposure

After Run 13 the FMS was unstacked and all cells were exposed to 48 hours of sunlight. During the exposure time, transverse transmittance spectra were measured at three longitudinal depths along a cell. Figure I.1 shows the spectrum of light used for the transmittance measurement; the spike at 656 nm is due to deuterium emission from the light source. Figure I.2 shows the transmittance spectra for a clear (not damaged) large cell, clear small cell, and damaged large and small cells; the colors indicate three longitudinal measurements: one near the front face (green), one in the center (red), and one near the back (blue). The vertical axis is a transmittance *relative* to the average transmittance for wavelengths greater than 900 nm. For the large cell, the front measurement shows the most damage, whereas for a small cell, the middle measurement shows the most; for both cells, the back measurement shows the least amount of damage.

Figure I.3 shows the ratio of transmittance of the damaged cell to that of the clear cell, given no sunlight exposure, 15 hours of exposure, and 40 hours of exposure, respectively for each row of plots in the figure. The clear cell was exposed in tandem with the damaged cell exposure. After 40 hours of exposure, the cells were 90-95% cured.

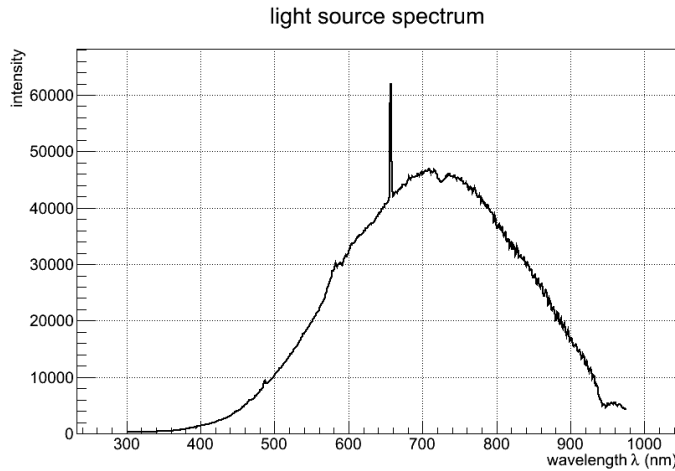


Figure I.1: Light source spectrum used for Pb-glass transmission spectra

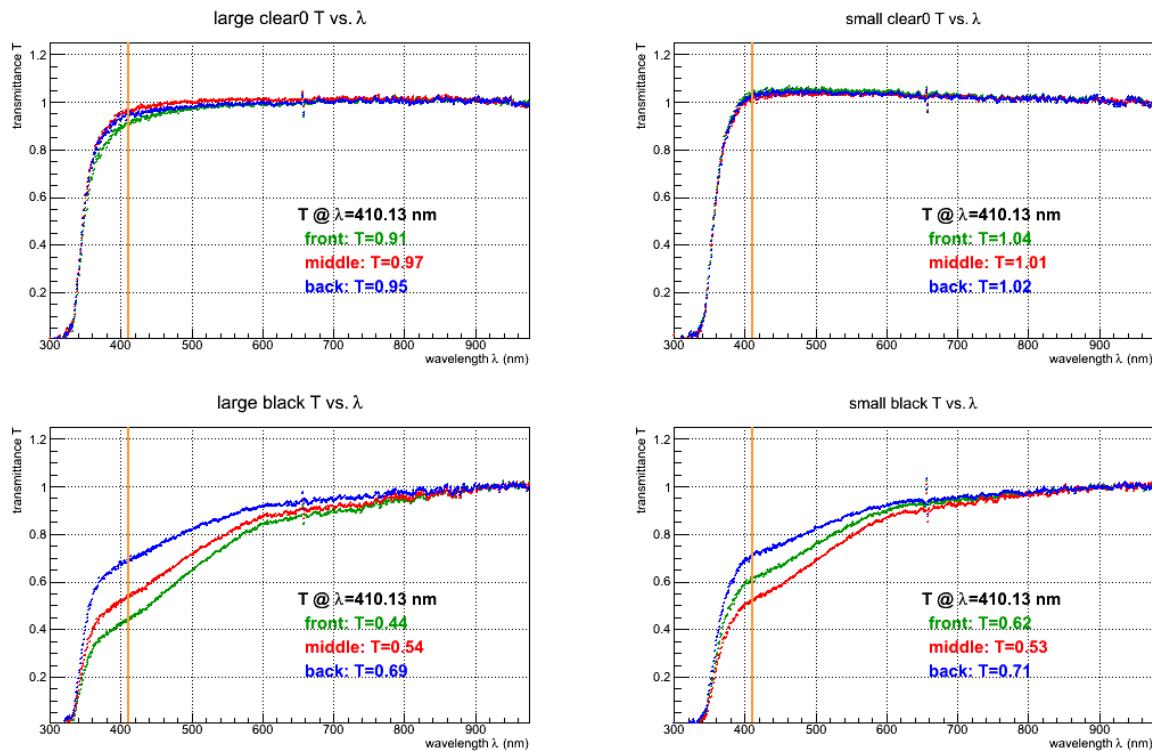
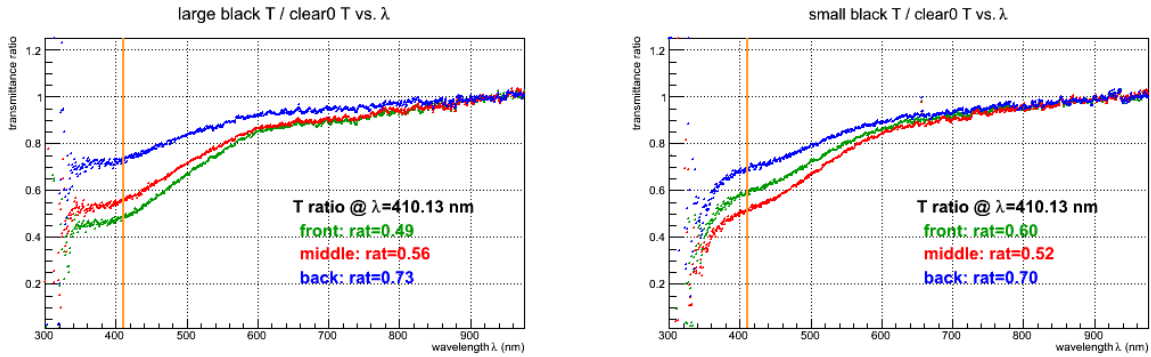
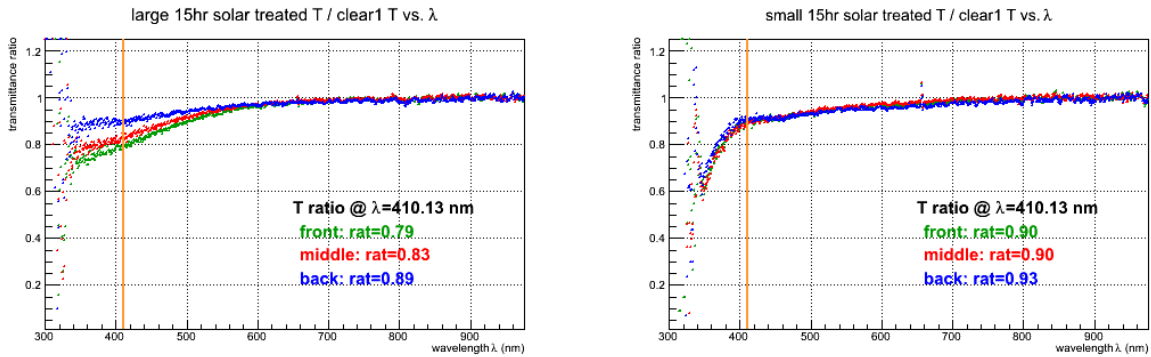


Figure I.2: Transmittance spectra for a large clear (not damaged) cell (top-left), small clear cell (top-right), damaged large cell (bottom-left) and damaged small cell (bottom-right). The colors indicate three longitudinal depths at which the transverse transmittance was measured: near the front (green), near the middle (red), and near the back, where the PMT would be (blue). Relative transmittance at 410 nm is written on each plot.

No Sunlight Exposure



After 15 Hours Exposure



After 40 Hours Exposure

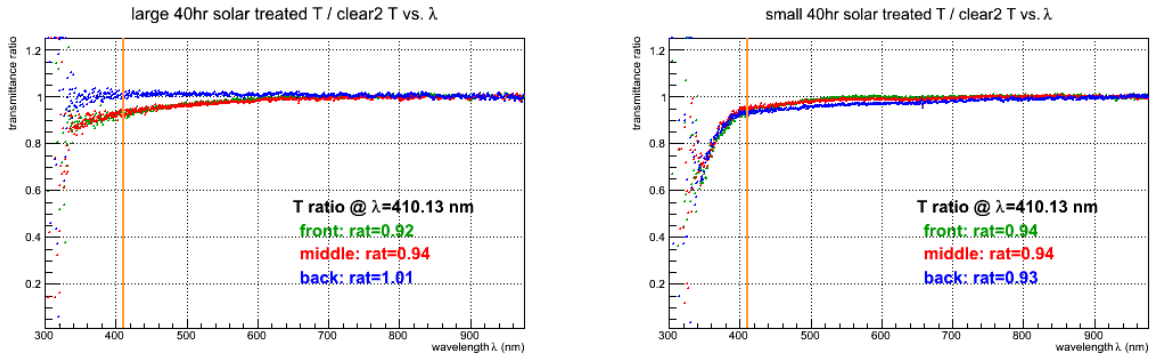


Figure I.3: Ratios of transmittance spectra for a large cell (left) and small cell (right) for 0 hours exposure (top), 15 hours (middle), and 40 hours (bottom). Transmittance ratios at 410 nm are written on each plot.

I.2 UV-LED Curing

After Run 16, the FMS Pb-glass was radiation damaged enough to once again necessitate curing. Since unstacking the FMS again and exposing all cells to sunlight is a formidable and time-consuming task, an alternative idea was employed. After testing multiple UV sources, we settled on UV-LEDs and therefore constructed a thin UV-LED array to sit in front of

the FMS glass. This array was designed to be turned on for a few hours per day during Run 17 in order to combat the radiation damage and attempt to keep the glass relatively clear.

A variety of UV-region wavelengths were tested. Figure I.4 shows the relative transmission in a small cell as a function of time (in hours) for 3 different wavelengths of light; the fastest curing is from the lowest wavelength: 375-380 nm. Thus an array of this wavelength of UV-LEDs was constructed.

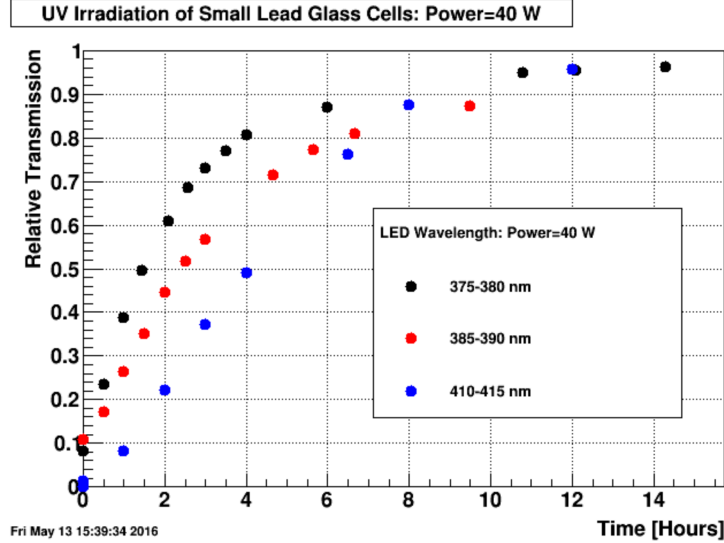


Figure I.4: Relative transmission of a small cell as a function of UV-LED exposure time (hours) for three different wavelengths: 410-415 nm (blue, slowest), 385-390 nm (red, middle), and 375-380 nm (black, fastest)

Due to design restrictions, the UV-LED array needed to be built in pieces and also needed to be as flat as possible so it could fit in the region in front of the FMS. Since the UV-LEDs ran rather hot, a method of keeping them cool was needed. The LEDs were mounted on aluminum plates, embedded with copper pipes which carried chilled water; these plates not only served as heat-sinks for the array, but also allowed the array itself to be segmented into small enough pieces such that installation was streamlined. Ultimately during operation, the temperature of the FMS rose only a couple of degrees and returned back to normal about 15 minutes after the UV-LED array was powered down.

Figure I.5 shows the effect of radiation damage as a function of pseudorapidity; the vertical axis is the ratio of flasher LED amplitudes between the end and the beginning of a 47 pb^{-1} period of $\sqrt{s} = 200 \text{ GeV}$ pp collisions. The damage is seen to be more severe at higher pseudorapidities, therefore the density of the UV-LEDs in the array was made to increase as a function of pseudorapidity. Figure I.6 shows a diagram of one quadrant of the UV-LED array, where the beam pipe passes through the bottom left corner. The distribution

of UV-LEDs is shown, along with the 7 aluminum plates that make up the array quadrant; the aluminum plates cover the majority of the large and small cells within the quadrant.

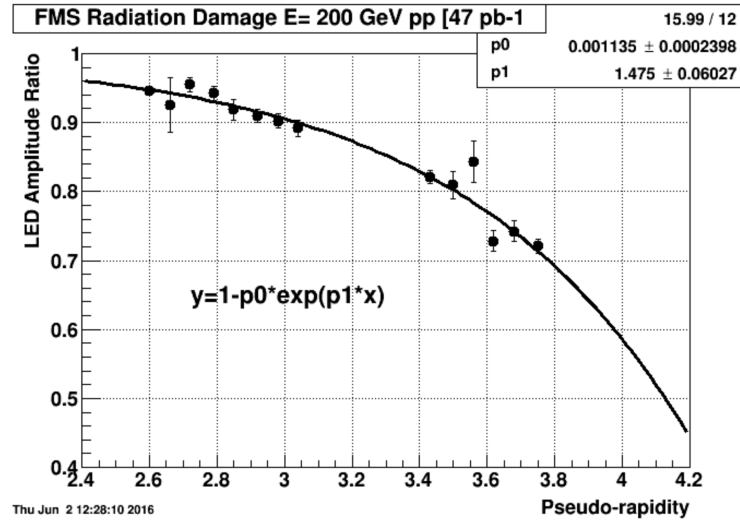


Figure I.5: Ratio of LED flasher amplitudes between end and beginning of a period of radiation damage accumulation, as a function of pseudorapidity.

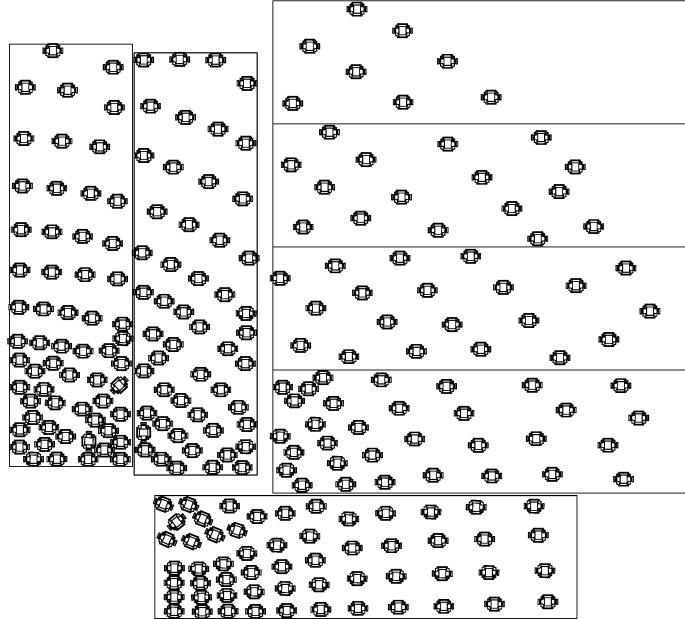


Figure I.6: One quadrant of the UV-LED array, showing the distribution of LEDs and their associated aluminum plates. The UV-LEDs were wired in groups of four (wiring not drawn).

Each UV-LED needed 10 W of power, supplied by a voltage drop of 10 V per LED and 1 A of current. Only 1 W of UV radiation power was emitted per LED; the rest was dissipated

as heat. Given that there are approximately 768 UV-LEDs, multiple power supplies were used. The power is first distributed to the power supplies via a 3-phase Power Distribution Unit (PDU); one PDU was used for the north half and another for the south half. Each PDU is connected to a 208 V input and contains 3 banks with 4 power supplies attached to each. On each power supply, there were 2 circuits containing 4 parallel strings of UV-LEDs, each with 4 UV-LEDs in series along with a fuse. Figure I.7 shows a diagram of this power distribution setup.

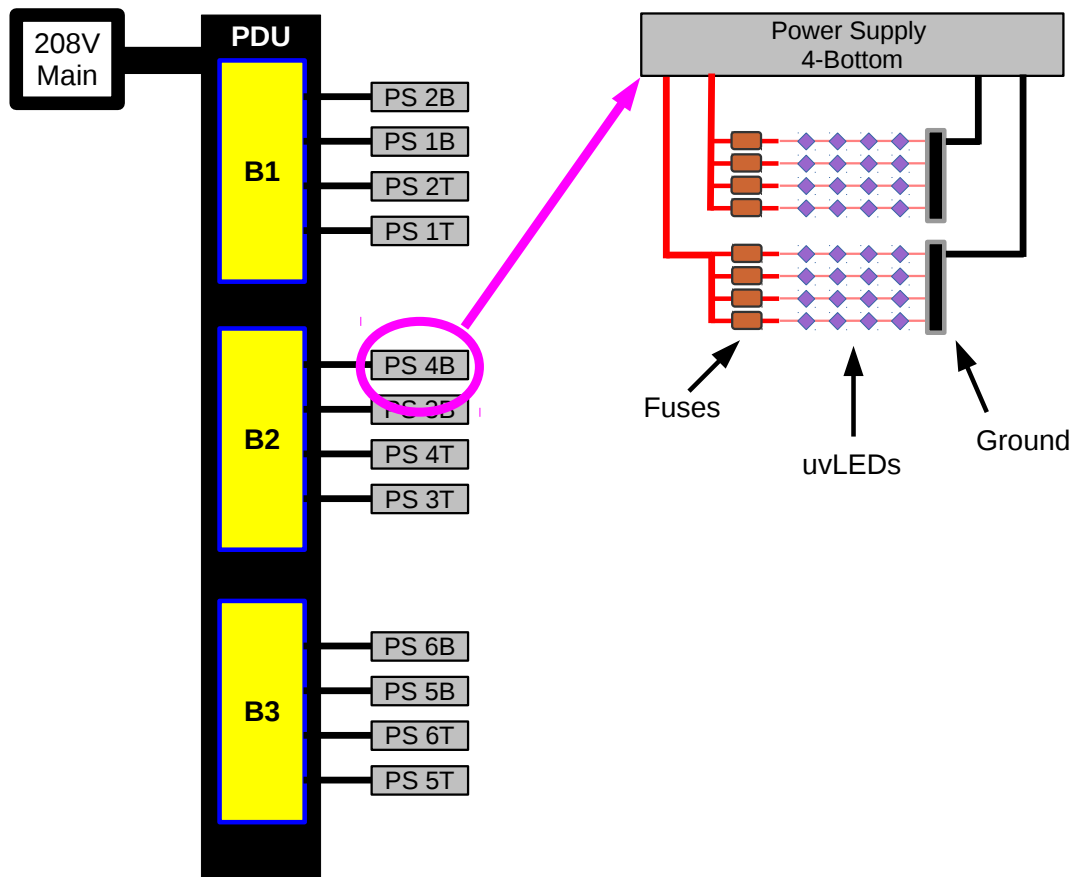


Figure I.7: Diagram of power distribution to the UV-LED array

Both PDUs were connected to the local intranet as well as directly linked to the control room via a fiber optic connection. Since both the PMT HV and UV-LED array were remotely controllable, a graphical user interface was designed in order to simplify operations. The graphical interface also served as a software interlock between the UV-LED array and the PMT HV system, since having both on at the same time could possibly damage the PMTs. Figure I.8 shows a screenshot of the control system.

FMS Control GUI:

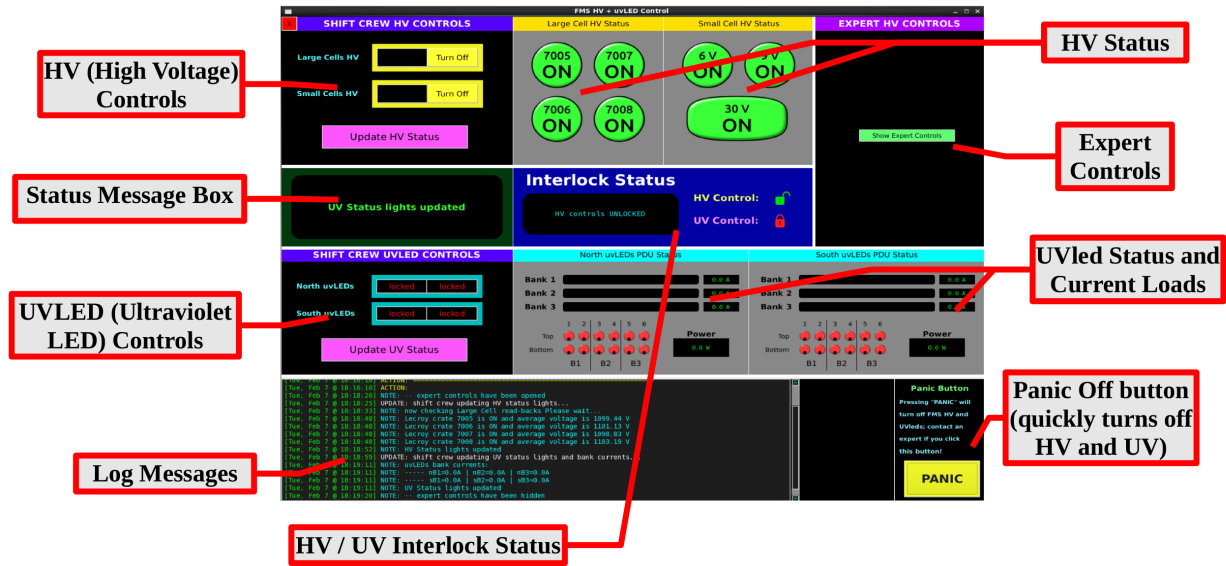


Figure I.8: Screenshot of the FMS HV and UV-LED graphical control interface, as well as software interlock.

Figure I.9 shows the ratio of flasher LED amplitudes for a 43 hour exposure of the FMS to the UV-LED array; this ratio is plotted as a function of pseudorapidity. Overall the UV-LED array successfully cleared the Pb-glass and it was used daily for a few hours per day during Run 17 to maintain glass transparency and a relatively constant trigger rate throughout the entire Run.

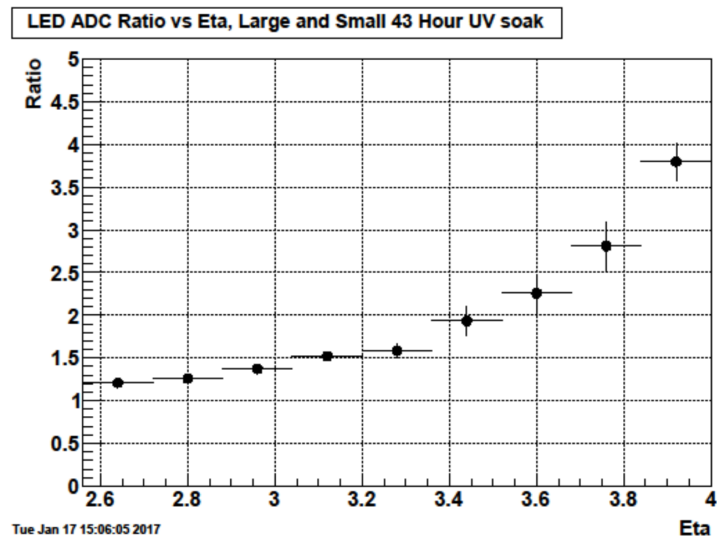


Figure I.9: LED amplitude after 43 hour exposure to UV-LED array divided by LED amplitude before exposure, vs. pseudorapidity. Radiation-hard cells were omitted from this diagram, as well as cells with misbehaving PMTs.

Bibliography

- [1] DE FLORIAN, D., R. SASSOT, M. STRATMANN, and W. VOGELSANG (2014) “Evidence for Polarization of Gluons in the Proton,” *Phys. Rev. Lett.*, **113**, p. 012001.
- [2] ADAMS, J. *et al.* [STAR COLLABORATION] (2006) “Forward neutral pion production in p+p and d+Au collisions at $\sqrt{s_{NN}} = 200$ GeV,” *Phys. Rev. Lett.*, **97**, p. 152302.
- [3] PATRIGNANI, C. ET AL. (2016) “Review of Particle Physics,” *Chin. Phys.*, **C40**(10), p. 100001.
- [4] EUN, L. (2012) “Transverse Single Spin Asymmetries and Cross-Sections for Forward π^0 and η Mesons at Large x_F in $\sqrt{s} = 200$ GeV $p^\uparrow + p$ Collisions at STAR,” Ph.D. thesis.
- [5] BIESER, F.S. *et al.* (2003) “The STAR trigger,” *Nucl. Instr. and Meth. A*, **499**(2), pp. 766 – 777.
- [6] LANDGRAF, J. (2013) “Overview and Evolution of the DAQ and Trigger Systems for the STAR Experiment at RHIC,” Presentation at *Triggering Discoveries in High Energy Physics*.
URL <https://indico.cern.ch/event/246374/contributions/542896/>
- [7] LEDNEV, A. (1995) “Electron shower transverse profile measurement,” *Nucl. Instr. and Meth. A*, **366**(2), pp. 292–297.
- [8] WANG, Y. (2004) “Measurement of Inclusive Forward Neutral Pion Production in 200 GeV Polarized Proton-Proton Collisions at RHIC,” Ph.D. thesis.
- [9] HAYS-WEHLE, J., J. SEELE, H. SPINKA, and B. SURROW (2012) “Relative Luminosity Analysis for run9 pp 200 GeV Running,” STAR Analysis Note.
- [10] CRONIN-HENNESSY, D., A. BERETVAS, and P. DERWENT (2000) “Luminosity monitoring and measurement at CDF,” *Nucl. Instr. and Meth. A*, **443**(1), pp. 37–50.

- [11] MANION, A. (2014) “Double Longitudinal Helicity Asymmetries in Pion Production from Proton Collisions, Studies of Relative Luminosity Determination, and the Impact on Determination of the Gluon Spin in the Proton,” Ph.D. thesis.
- [12] MANION, A. (2011) “Method for Determining Relative Luminosity from Detection Probabilities (Run9 200 GeV),” PHENIX Analysis Note.
- [13] FUKAO, Y. (2007) “Double helicity asymmetry for π^0 production in polarized $p + p$ collisions at $\sqrt{s} = 200$ GeV : Implications for the polarized gluon distribution in the proton,” Ph.D. thesis.
- [14] JONES, R.T. *et al.* (2006) “A bootstrap method for gain calibration and resolution determination of a lead-glass calorimeter,” *Nucl. Instr. and Meth. A*, **566**(2), pp. 366 – 374.
- [15] BARTOSZEK L. *et al.* (1991) “The E760 lead-glass central calorimeter: design and initial test results,” *Nucl. Instr. and Meth. A*, **301**(1), pp. 47 – 60.
- [16] BLAND, L. C. *et al.* (2008) “An electromagnetic shower profile in the lead-glass calorimeter in the energy range of 3–23 GeV,” *Instruments and Experimental Techniques*, **51**(3), pp. 342–350.
- [17] THE RHIC CNI POLARIMETRY GROUP (2016) “RHIC Polarization for Runs 9-15,” . URL https://wiki.bnl.gov/rhicspin/upload/e/e4/Pol_resultsMay2016.pdf